Functional Nucleic Acids for Ultrasound-Controlled Release and Targeted Cancer Theranostics

Von der Fakultät für Mathematik und Naturwissenschaften der RWTH Aachen University zur Erlangung des akademischen Grades eines Doktors der Naturwissenschaften genehmigte Dissertation

vorgelegt von

Wolfgang Hubertus Rath

Master of Science

aus

Aachen, Deutschland

Berichter: Univ.-Prof. Dr. rer. nat. Andreas Herrmann

Univ.-Prof. Dr. rer. nat. Andrij Pich

Tag der mündlichen Prüfung: 10.12.2025

DECLARATION OF AUTHORSHIP

I, Wolfgang Hubertus Rath, declare that this thesis and the work presented in it are my own and has been generated by me as the result of my own original research. I do solemnly swear that:

1. This work was done wholly or mainly while in candidature for the doctoral degree at this faculty and university;

2. Where any part of this thesis has previously been submitted for a degree or any other qualification at this university or any other institution, this has been clearly stated;

3. Where I have consulted the published work of others or myself, this is always clearly attributed;

4. Where I have quoted from the work of others or myself, the source is always given. This thesis is entirely my own work, with the exception of such quotations;

5. I have acknowledged all major sources of assistance;

6. Where the thesis is based on work done by myself jointly with others, I have made clear exactly what was done by others and what I have contributed myself;

7. Parts of this work have been published before as:

Research internships, bachelor and master thesis:

[1] “Development of DNA-labels for highly sensitive, targeted Magnetic Resonance Imaging”, master’s thesis, Xinpei Li, September 2024.

Publications:

[1] W.H. Rath, R. Göstl, A. Herrmann, “Mechanochemical Activation of DNAzyme by Ultrasound” **2024**, *Adv. Sci.*, 11 (8), 2306236. DOI: 10.1002/advs.202306236

Date Signature

Acknowledgements

First, I would like to thank my supervisor Prof. Andreas Herrmann for giving me my biggest challenge so far and supplying me with all the tools to overcome it. Through the work in his group, I was exposed to many different scientific concepts ranging from synthetic chemistry to cell biology, which greatly expanded my horizon. His ideas and input have been invaluable for the completion of this work and most importantly, the network he built at DWI provided the environment for me and others to learn and thrive. In the same vein, I would like to thank my second examiner Prof. Andrij Pich for being an integral pillar of DWI and for fostering both scientific excellence and community spirit. Special thanks also go to Prof. Robert Göstl, for being a great mentor and always going the extra mile to get things done.

Next, I'd like to thank my collaboration partners and DWI staff who helped with the completion of this work. Thanks to Sabri Sahnoun for doing a lot of work on the drug delivery project, and for giving me a lot of insight into pre-clinical research. I'd like to thank Dr. Jens Köhler and Janko Stoffels for advising me on multiple occasions and for designing and synthesizing the Click label for the PHIP project. I'd also like to thank Dr. Meike Emondts for her great advice regarding NMR measurements and the planning of the PHIP project. Thanks also go to Dr. Gurudas Chakraborty for his advice and for pushing my writing skills forward. Special thanks go out to Mark Loznik for doing a massive amount of work behind the curtains and for helping out with DNA synthesis. Thanks also go to Tina-Marie Thomas for doing a lot of work for the group, for example organizing barbeques and other activities. I'd like to thank Marion Conolly and Petra Esser for taking care of MALDI and ESI samples and for always keeping the spirits high.

Most importantly I would like to thank my colleagues, many of which have become great friends over the last years. I think it's appropriate to name Philippe first, since he has been around since week one 1 of the Bachelor studies. Thanks for all the great memories at Kaktus, skiing and occasionally at work. Melina might not be my oldest friend, but certainly my best and I'd like to thank her for her invaluable support and the many creative impulses she always provides. I'd like to thank Oliver for being a great mentor during my Master studies and for remaining a good friend afterwards. I want to thank Johannes, Fabi and Marcus for the excellent scientific discussions and for being the heart of every party, especially at Seaminar. I want to thank Christiane for suffering through the worst parts of the past 4 years together with me and for giving hope to those who still have to suffer. And of course I want to thank Thomas for providing the group with an endless supply of dad jokes.

I'd like to thank my climbing group Melina, Christiane, Tizzle, Karla and Shannon for never dropping me from 15 meters and for helping me to continually push myself physically and mentally. I want to express my appreciation for all my international colleagues, and I hope that through science we can uphold the spirit of international cooperation, even in the face of rising political tensions. I want to thank Ria and Diptendu for their hospitality, and I wish them all the best for their future. I also want to thank Chuanjiang, Xiaolong, Lumi, Kuan and Jilin for being great colleagues, for their contributions to the scientific discussions and for inspiring everybody through their tireless work ethic.

Summary

This thesis explores how functional nucleic acids (FNAs) can be used to construct ultrasound-responsive release systems and theranostic applications for the diagnosis and therapy of cancer. In contrast to synthetic polymers, FNAs offer powerful sequence programmability, the ability to form defined secondary and tertiary structures and can directly interface with biological systems. Another outstanding feature of FNAs is that they can easily be chemically modified. In particular, this thesis highlights two versatile techniques that can be used to generate multifunctional NAs: rolling circle amplification and copper-free Click reaction. RCA is an isothermal amplification technique that generates polynucleotides with very large molar mass. Due to their size, RCA products can be used to construct US-responsive systems. They are also a useful tool in the context of drug delivery, since they exhibit high nuclease stability and slow renal clearance. The copper-free Click reaction is one of the most important biolabeling reactions, which can be used to functionalize NAs with a variety of labels to facilitate imaging or therapeutic applications.

Chapter 1 of this thesis summarizes the necessary scientific context for this work. Firstly, the fundamentals of FNAs and their applications in the context of cancer drug delivery are summarized. The most common reactions for the chemical modification of NAs, as well as different labeling strategies for FNAs to facilitate various imaging techniques are discussed. Furthermore, the basics of polymer mechanochemistry, and how they can be applied to NAs in order to generate biocompatible mechanochemical systems are introduced.

In **chapter 2**, a mechanoresponsive system for the US mediated activation of an RNA-cleaving DNAzyme is presented. This system is based on a large DNA strand generated through RCA, onto which the DNAzyme is hybridized to deactivate it. The DNAzyme can then be released through US and subsequently cleave its substrate which is monitored by fluorescence.

Chapter 3 presents an RCA based drug delivery system for the treatment of glioblastoma using an *in ovo* model. For this purpose, the AS1411 aptamer sequence is encoded onto the RCA strand, providing a glioblastoma targeting function. Additionally, a chelator for radiolabeling is attached to the RCA strand through Click chemistry and the anticancer drug Doxorubicin is loaded onto the DNA via non-covalent interactions. In combination, these elements form a flexible theranostic platform for positron emission tomography using ^{68}Ga, and the co-delivery of Dox and ^{177}Lu for combined chemo- and radiotherapy.

Chapter 4 introduces an aptamer Click labeling strategy to generate targeted contrast agents for magnetic resonance imaging. The enhancement in MRI contrast is achieved through para-hydrogen induced polarization (PHIP). When conjugated with an aptamer, these PHIP tags are promising tools for targeted cancer imaging with MRI at low magnetic fields, for example in portable MRI machines.

The final section summarizes this work and gives some outlook on potential future research topics.

Zusammenfassung

Diese Arbeit untersucht die Nutzung von funktionalen Nukleinsäuren (FNS) für das Design von Ultraschall-responsiven Systemen zur Wirkstofffreisetzung und für die Entwicklung von theranostischen Systemen zur Diagnose und Behandlung von Krebs. Im Gegensatz zu synthetischen Polymeren bieten FNS effektive Sequenz-Programmierbarkeit, sowie die Fähigkeit definierte Sekundär- und Tertiär-Strukturen zu bilden und direkt mit biologischen Systemen zu interagieren. Ein weiterer Vorteil von FNS ist, dass sie einfacher chemisch modifiziert werden können. In dieser Arbeit werden zwei vielseitige Techniken zur Entwicklung von multifunktionalen FNS hervorgehoben: Rolling Circle Amplification und die kupferfreie Click-Reaktion. RCA ist eine isothermale Amplifikations-Methode, wobei Polynukleotide mit sehr hoher Molmasse generiert werden. Durch diese hohe Masse eignen sich RCA-Produkte zur Konstruktion von US-responsiven Systemen. Sie sind ebenfalls nützlich als Wirkstofftransport-System, da sie hohe Nuklease-Stabilität besitzen und nur langsam über die Nieren ausgeschieden werden. Die kupferfreie Click-Reaktion ist eine der wichtigsten Biokonjugations-Reaktionen, und kann verwendet werden, um FNS mit verschiedenen Labels für Bildgebungs- oder Therapie-Anwendungen zu funktionalisieren.

Kapitel 1 fasst den wissenschaftlichen Kontext dieser Arbeit zusammen. Die Grundlegenden Eigenschaften von FNS und ihre Anwendung im Wirkstofftransport für Krebstherapie werden erklärt. Außerdem werden die häufigsten Reaktionen zur chemischen Modifikation von FNS und Labeling-Strategien für verschieden Bildgebungs-Anwendungen diskutiert. Zusätzlich werden die Grundlagen der Polymer-Mechanochemie und ihre Anwendung zur Konstruktion von biokompatiblen mechanochemischen Systemen erläutert.

Kapitel 2 präsentiert ein System für die US-Aktivierung eines RNA-spaltenden DNAzyms. Dieses System basiert auf einem großen DNA-Strang, der durch RCA generiert wird, und anschließend mit dem DNAzym hybridisiert wird, um dessen katalytische Aktivität auszuschalten. Das DNAzym kann dann durch US freigesetzt werden und anschließend sein Substrat spalten, was durch Fluoreszenz beobachtet werden kann.

Kapitel 3 präsentiert ein auf RCA basierendes Wirkstofftransportsystem für die Behandlung von Glioblastoma in einem *in ovo* Modell. Hierzu wird die AS1411 Aptamer-Sequenz auf den RCA-Strang kodiert, was eine Ziel-Funktion für Glioblastoma-Zellen bereitstellt. Zusätzlich wird ein Chelator-Molekül für Radiolabeling durch Click Chemie an den RCA-Strang konjugiert, und das Krebsmedikament Doxorubicin wird durch Interkalation auf den RCA-Strang geladen. In Kombination bilden diese Elemente eine flexible theranostische Plattform für Positronen-Emissions-Tomographie mit ^{68}Ga oder den Co-Transport von ^{177}Lu und Dox für kombinierte Radio- und Chemotherapie.

Kapitel 4 stellt eine Click-Labeling-Strategie zur Synthese eines gezielten Kontrastmittels für Magnet-Resonanz-Tomographie vor. Die Erhöhung des MRT-Kontrasts wird in diesem Fall durch Para-Wasserstoff induzierte Polarisation (PHIP) erzielt. Aptamere, die mit diesen PHIP-Labels konjugiert werden, sind ein erfolgsversprechendes Kontrastmittel für gezielte Tumorbildgebung durch MRT bei niedriger Magnetfeldstärke, z.B. in portablen MRT-Geräten. Der letzte Abschnitt fasst die erzielten Ergebnisse zusammen und stellt potenzielle darauf aufbauende Forschungsthemen vor.

Table of Contents

Acknowledgements ii
Summary iii
Zusammenfassung iv
Aim and motivation 1
1. Introduction 3
1.1 Functional Nucleic Acids 3
1.1.1 Base Pairing Interactions 3
1.1.2 SELEX 4
1.1.3 Aptamers 5
1.1.4 DNAzymes 7
1.1.5 Rolling Circle Amplification 9
1.2 Polymer Mechanochemistry 10
1.2.1 Ultrasound and Cavitation 11
1.2.2 Mechanophores 12
1.2.3 Soft Mechanochemistry 12
1.2.4 Chemical Ultrasound vs. Medical Ultrasound 13
1.2.5 Towards Biocompatible Mechanochemistry 13
1.3 Cancer Drug Delivery 14
1.3.1 Historic Development of Chemotherapy 14
1.3.2 Tumor Microenvironment 15
1.3.3 Drug Resistance 16
1.3.4 Glioblastoma and the Blood Brain Barrier 16
1.3.5 Targeted Drug Delivery 17
1.3.6 AS1411 Aptamer 18
1.3.7 Glioblastoma Targeting 18
1.3.8 Chicken Embryo Model 19
1.4 DNA Functionalization 20
1.4.1 Bottom-up Synthesis of Nucleic Acids 20
1.4.2 Post-synthetic Modification 21
1.4.3 Backbone Complexation 21
1.5 Chelator Labels 22
1.6 Hyperpolarization 24
1.6.1 Nuclear magnetic resonance basics 24
1.6.2 MRI contrast agents 26
1.6.3 Para-hydrogen 26
1.6.4 PHIP 27
1.6.5 Biocompatible PHIP 28
1.6.6 Targeted MRI 29
2. Mechanochemical Activation of DNAzyme by Ultrasound 30

2.1 Aim and Motivation 30
2.2 Results....31
2.2.1 DNA Sequence Design and RCA Optimization....31
2.2.2 Controlling DNAzyme Kinetics by RCA....33
2.2.3 Mechanochemical Release of DNAzyme by Ultrasound....36
2.3 Discussion and Outlook 41
2.4 Experimental....42
3. Click-functionalized DNFs for Targeted Cancer Theranostics....44
3.1 Aim and Motivation 44
3.2 Results....45
3.2.1 Synthesis of Azide-modified ^{Apt}DNFs 45
3.2.2 Click-Functionalization of ^{Apt}DNFs 47
3.2.3 Dox Loading 51
3.2.4 Radiochemical Purity and Stability....51
3.2.5 *In vitro* Cell Uptake 52
3.2.6 *In ovo* Biodistribution 54
3.2.7 *In vitro* Cell Toxicity 56
3.3 Discussion and Outlook 58
3.4 Experimental....60
4. DNA Click-Functionalization with Hyperpolarizable Labels 63
4.1 Aim and Motivation 63
4.2 Results....64
4.2.1 DBCO functionalization of mPEG-DNA complexes....64
4.2.2 DBCO functionalization of DDAB-DNA complexes 66
4.2.3 Design and synthesis of PHIP labels 70
4.2.4 Click-functionalization of DNA with PHIP label....71
4.3 Discussion and Outlook 74
4.4 Experimental....76
5. Conclusion 78
6. Appendix 79
6.1 List of Abbrevations 79
6.2 List of Figures 80
6.3 List of Schemes 84
6.4 List of Tables 84
7. References....85

Aim and motivation

Cancers are still some of the most life-threatening diseases with a notoriously high recurrence rate after traditional treatments, due to the formation of metastases. Current chemo- and radiotherapy are also accompanied by heavy side-effects, while many cancer types are able to develop resistance towards these treatments. In order to increase the patient survival rate, methods to diagnose cancer earlier and to increase the therapeutic efficacy of drugs need to be developed. Modern technologies allow these modalities to be combined into theranostic systems, which allow real-time monitoring of the therapeutic progress and enable cancer treatments to be heavily personalized.[1]

An important aspect of theranostic systems is their targeting ability, which facilitates their accumulation at the cancer site after systemic application. This is achieved by conjugating a targeting moiety either directly to the drug/tracer molecule, or to the surface of carrier systems, for example nanoparticles. On the diagnostic side, this allows for the early detection of metastases, increases contrast between healthy and diseased tissue and therefore makes it possible to accurately assess the disease state. Therapeutic applications also benefit from a targeting function, since it increases the local drug concentration at the tumor site, leading to increased therapeutic efficacy and reduced side-effects.[2]

Commonly used targeting moieties are antibodies, cell specific metabolites or a class of functional nucleic acids (FNAs) called aptamers.[3] These are synthetic DNA or RNA oligonucleotides that fold into specific 3D structures, which gives them the ability to bind target molecules or receptors with high affinity and specificity. Among targeting ligands, aptamers stand out, since they offer low immunogenicity and are cheap to synthesize. NAs can easily be chemically modified compared to other biomacromolecules like proteins. This allows aptamers to be conjugated with different labels for various imaging applications or with drugs for targeted therapy. *In vivo* applications of aptamers still suffer from low circulation times, due to renal clearance and nuclease degradation, but modern systems try to address this by increasing the molecular weight of the conjugates and through the use of chemically modified oligonucleotides.[4]

While the use of targeting ligands greatly boosts the efficacy of theranostic agents, off-target effects still occur. To further increase the specificity, stimuli-responsive systems have been developed.[5] Compared to traditional “always-on” systems, they offer higher signal to noise ratio and a lower limit of detection during diagnostic applications, as well as reduced drug toxicity for therapeutic applications. Tumor-related stimuli, for example high amounts of reactive oxygen species (ROS) or low pH, can act as convenient triggers to activate these systems, but external stimuli like light can also be used.

A notable external stimulus is ultrasound (US), which is already widely used in clinical practice for non-invasive imaging or cancer therapy due to its high tissue penetration depth. Polymer mechanochemistry is a research field that explores how mechanical forces, including US, can be exploited to induce chemical transformations in polymers.[6] Traditionally, mechanochemical systems use strong cavitational US that is not biocompatible, since the energy barrier for activation is quite high. However, more sophisticated mechanochemical systems can be designed based on non-covalent interactions, which lowers the activation barrier and makes them responsive to lower energy US.[7] These systems might form the basis for the development of theranostic systems, which are activatable with clinical US.

This thesis explores how nucleic acid (NA) based systems can act as a platform to overcome these diverse challenges for the design of stimuli-responsive theranostic applications. Their sequence programmability allows for easy incorporation of a targeting moiety through an aptamer sequence. Other functional sequences can be incorporated that directly interface with biological systems, for example DNAzymes. Due to their ability to form supramolecular interactions, NAs also exhibit some unique mechanoresponsive properties that can be exploited for the design of US-activated systems. Lastly, this thesis demonstrates how the functionality of NAs can be vastly expanded through Click-labeling to facilitate various imaging modalities and targeted therapy.

1. Introduction

1.1 Functional Nucleic Acids

1.1.1 Base Pairing Interactions

NAs are composed of the nucleobases adenine, guanine, cytosine, thymine (only DNA) and uracil (only RNA), which are attached to a ribose unit (2'-desoxyribose for DNA) and connected through phosphate groups between the sugar units. These structural features enable multiple supramolecular interactions, including electrostatic interactions at the phosphate groups, hydrogen bonding at the amine groups of the nucleobases and stacking interactions with the π-systems of the nucleobases. Two very important binding modes, which lead to the formation of DNA secondary structures, are Watson-Crick base pairing[8] and Hoogsteen base pairing.[9] Both base pairing types are stabilized through hydrogen bonds with opposing nucleobases and π-stacking with adjacent nucleobases. Other factors impacting the thermodynamic stability of base pairing are the reduction in entropy caused by the base pairing, counterion concentration and hydration.[10]

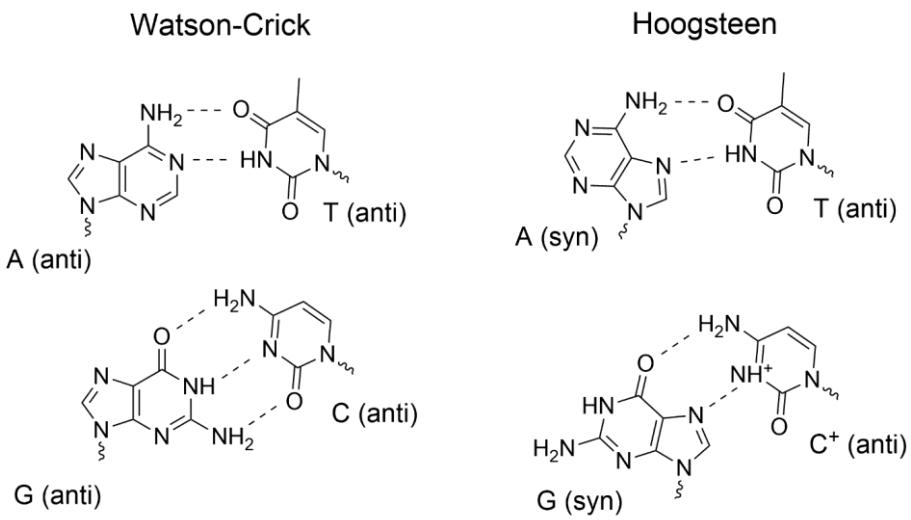

Figure 1. Watson-Crick and Hoogsteen base pairing modes.

The most famous NA secondary structure is the DNA double helix (B-DNA), which consists of two DNA strands coupled through Watson-Crick base pairing.[8] B-DNA is best known for its function of storing genetic information in eukaryotic cells and several bacteria and viruses. Hoogsteen base pairing is responsible for the formation of other secondary structures like triplexes, G-quadruplexes and i-motifs. In the genome, these non-canonical secondary structures are often found in promoter regions and play a role in regulating gene expression through the binding of transcription factors[11-12] or the inhibition of nucleosome formation.[13-14] These secondary structures are also prone to mutations and are often involved in the development of diseases.[15-16] Beyond these simple base pairing modes, nucleic acids can also form a variety of non-canonical base pairs like wobble pairs, reversed Watson-Crick and Hoogsteen pairing, sheared conformations or multiplets.[17] These interactions can form long range tertiary contacts, and are therefore responsible for the folding of NA secondary structures into tertiary structures. In the cell, these complex structures are typically formed by RNA which enables it to perform a large variety of functions, for example tRNA, ribosomes, ribozymes or riboswitches. Even though DNA generally exhibits lower structural diversity than RNA, it still has the potential to form functional tertiary structures.

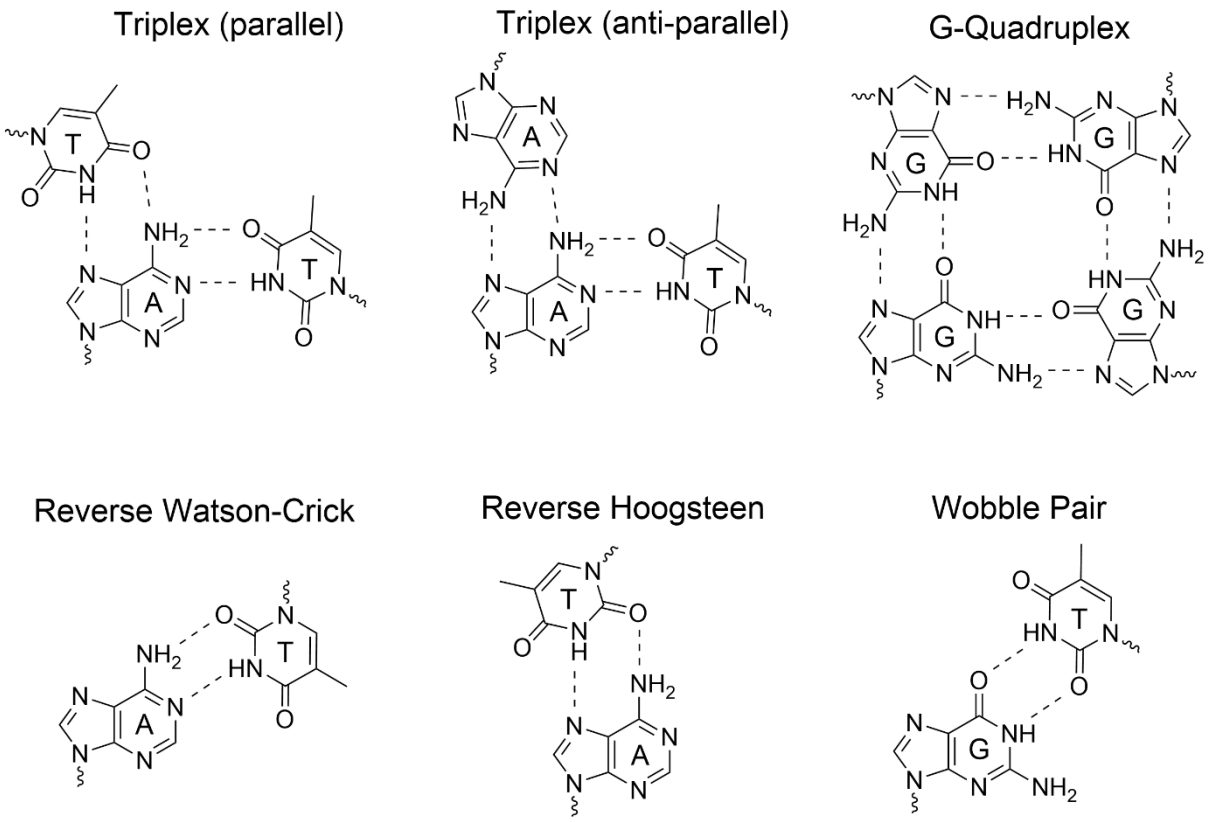

Figure 2. Examples of non-canonical base pairing modes.

1.1.2 SELEX

This chapter focuses on two classes of functional DNAs: DNAzymes (catalytically active DNA oligonucleotides) and aptamers (oligonucleotides which bind targets with high affinity and specificity). These are not found in nature but through an *in vitro* enrichment process called "systematic evolution of ligands by exponential enrichment" (SELEX).[18-19] During this process, functional NAs are selected from a library of random oligonucleotides, which are obtained through phosphoramidite synthesis, followed by *in vitro* transcription in the case of RNA. These oligonucleotides typically contain a random sequence in the middle and two defined primer binding sites at the ends to enable polymerase chain reaction (PCR). During aptamer SELEX, this library is then incubated with the immobilized target molecule, non-binding oligonucleotides are washed off, and the binding oligonucleotides are amplified through PCR to obtain an enriched library. This process is then repeated up to 20 times to obtain the oligonucleotides with the highest affinity for the target. Since its inception in 1990, this process has been optimized by developing new methods for the design of libraries and the separation of bound oligonucleotides (electrophoretic mobility, magnetic beads), by using more complex targets (cell & *in vivo* SELEX) and by improving the post-selection evaluation and modification process.[20] SELEX for ribozymes follows the same principles, but separating the catalytically active sequences from the library is a bit more complicated. To solve this problem, Silverman and colleagues have pioneered product-capturing strategies, which couple the reaction product with another oligonucleotide in a follow-up reaction. Due to its increased molecular weight, this construct can then be separated from the library through gel-electrophoresis.[21] Since SELEX is a time consuming procedure, *in silico* methods are becoming increasingly relevant in the process of finding new aptamers and ribozymes.[22]

1.1.3 Aptamers

Aptamers are synthetic oligonucleotides which fold into tertiary structures that can bind targets with high affinity and specificity. The first aptamer was found in 1990 by Ellington and Szostak, which was an RNA aptamer with the ability to bind anthraquinone dyes.[18] They also coined the term aptamer, which is derived from the Latin word "*aptus*" (to fit) and the Greek word "*mers*" (particle). Due to their function, aptamers are often compared to antibodies, but since they are NAs they have some inherent advantages over proteins, including cheaper and faster synthesis, higher thermal stability and higher chemical modifiability. The size of aptamers usually ranges from 35 to 100 nt, which means they can either act as a receptor for small organic molecules and metal ions or as a ligand for larger molecules (e.g. proteins). Their selective binding ability has been exploited in different diagnostic and sensing applications. For these systems, aptamers can be combined with different readout mechanisms in a modular fashion, which include optical methods (fluorescence, colorimetry), electrochemical methods (potentiometry, impedimetry, voltammetry) and mass sensitive methods (quartz crystal microbalance, microcantilever).[23-24] One big category of applications for these sensors is the detection of pathogens, which include bacteria (e.g. *Staphylococcus aureus* [25], *Mycobacterium tuberculosis*[26]), viruses (e.g. HIV[27], Influenza[28]), and parasites (e.g. Plasmodium and Trypanosoma[29]). Another area of application is the detection of environmental pollutants like antibiotics[30], bisphenol A[31], heavy metals[32] and pesticides.[33] Aptamer sensors are also used to detect biomarkers for the early diagnosis of cardiovascular and neurological diseases, as well as cancer.[34] Cancer cells can also be targeted directly through specific receptors on their surface, which can help in the detection of metastases.

Beyond detection, aptamers are a popular tool for the treatment of cancers, since their targeting ability can greatly reduce side effects and boost therapeutic efficacy of chemotherapeutic drugs. For the purpose of cancer therapy aptamers have been conjugated with different therapeutic agents, for example nucleic acids like siRNA, miRNA or shRNA, which can suppress the expression of a variety of disease-related genes. These chimeric RNAs are typically synthesized through *in vitro* transcription, with a DNA template containing the aptamer and siRNA sequence connected with a few spacer nucleotides.[35-36] Both RNA fragments can also be assembled through non-covalent interactions like Watson-Crick base pairing[37] or biotin-streptavidin coupling.[38] Aptamers can also be coupled with small organic drug molecules like Doxorubicin (Dox) or Paclitaxel, which are commonly used in chemotherapy. Covalent conjugation with drugs can be achieved through different reactions, including N-hydroxy succinimide (NHS) coupling[39], thiol-maleimide Michael-addition[40], or formaldehyde mediated coupling of two amine groups.[41] Chemotherapeutics, for example 5-fluorouracil, can also be directly incorporated into aptamers through phosphoramidite chemistry.[42] Some drugs can form non-covalent interactions with aptamers, for example Dox can be loaded onto NA double helixes through intercalation.[43] Instead of conjugating aptamers directly to drug molecules, they can be used to decorate the surface of particle based drug delivery systems (DDSs). Popular carrier systems include polymer particles, e.g. poly(lactic acid)/polyethylene glycol (PLA/PEG)[44], gold nanoparticles[45] or lipid nanoparticles.[46] Due to their receptor binding ability, aptamers can also act as therapeutics themselves, by either acting as an agonist activating a receptor or an antagonist blocking a receptor. One example of an aptamer antagonists is the NX1838 aptamer, which binds the vascular endothelial growth factor (VEGF)[47] and therefore has potential to combat pathological angiogenesis during the proliferation of tumors. Aptamer agonists are generally rarer than antagonists, but one example is the 4-1BB aptamer, which stimulates T-cell activation for cancer immunotherapy.[48]

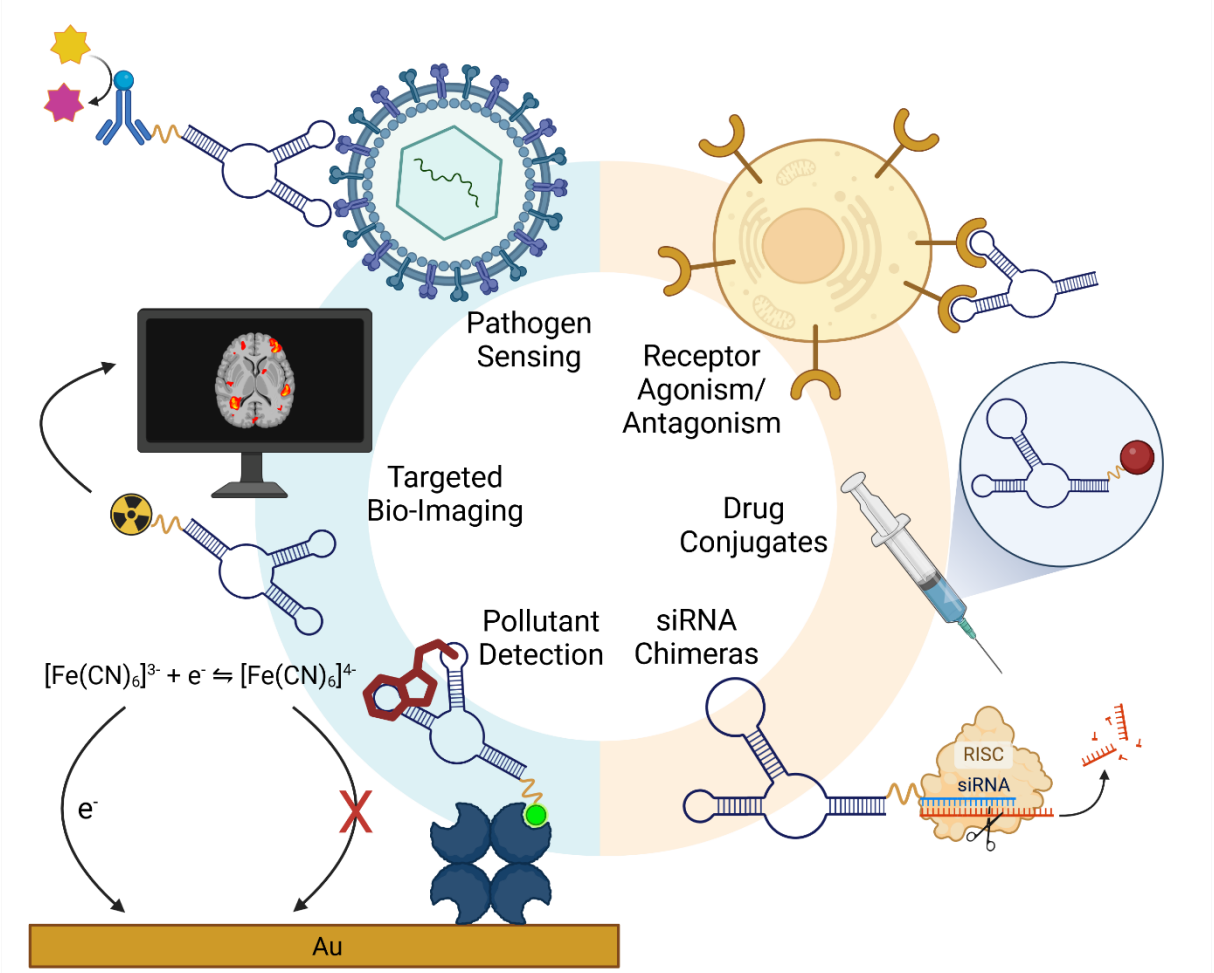

Figure 3. Examples of aptamer-based systems for imaging (left) and therapeutic (right) applications. Created in BioRender. Rath, W. (2025) https://BioRender.com/s17w753.

The biggest factor limiting the potential of aptamers for *in vivo* applications is their short half-life, caused by nuclease degradation and renal clearance. In order to avoid nuclease degradation, aptamers can be modified at the sugar unit with a 2'-amino, 2'-fluoro or 2'-O-methyl function.[49] Locked nucleic acids (LNAs) have also been utilized as backbone modification.[50] Alternatively, chemical modifications can be implemented at the nucleobases, for example 2'-fluoropyrimidines.[49] Additionally, an inverted deoxythymidine nucleotide can be inserted at the 3'-end to further enhance nuclease stability.[51] Ideally these chemical modifications are already applied during the SELEX process, since post-SELEX modification of aptamers can reduce their target affinity.[52] To avoid renal clearance, the molecular weight of aptamers has to be increased above the renal filter threshold (30-50 kDa). To achieve this, aptamers can be conjugated with molecules such as PEG[53] or cholesterol.[54] Multivalent aptamer constructs are also large enough to avoid renal clearance and additionally exhibit increased binding affinity.[55] Even though aptamers generally induce less side effects than antibodies due to their lower immunogenicity and toxicity[56], adverse reactions to aptamer therapy have been observed in clinical trials.[57] These might be caused by the polyanionic nature of the aptamers, which promotes non-specific binding to blood proteins and subsequent accumulation in non-target tissues.[58] These side effects can be further exacerbated by chemical modifications like an LNA backbone[59] or 2'-fluoropyrimidine bases.[60] PEGylated aptamers can also cause severe allergic reactions in patients with pre-existing PEG antibodies.[61]

1.1.4 DNAzymes

The first catalytically active NA was reported in 1982, which is a self-splicing RNA sequence in *Tetrahymena*[62], and over a decade later in 1994, the first catalytically active DNA (DNAzyme) was discovered through SELEX.[63] Since DNA exhibits higher chemical stability and nuclease resistance than RNA, and therefore is much easier and cheaper to synthesize and handle, DNAzymes have attracted the interest of many researchers. This has led to the development of new *in vitro* selection methods[64] and the discovery of a plethora of DNAzymes which catalyze various reactions, including DNA/RNA ligation, ester hydrolysis or thymine-dimer cleavage.[21, 65-66] An important subclass of DNAzymes are RNA-cleaving DNAzymes. The most prominent DNAzymes in this subclass are two Mg^{2+}-dependent DNAzymes named Dz8-17 (also known as 17E) and Dz10-23, which were identified by Santoro and Joyce in 1997.[67] These DNAzymes, which consist of two side chains and a catalytic core, catalyze RNA cleavage through a nucleophilic attack of the 2'-hydroxy group of the ribose unit towards the phosphate backbone. The side chains bind to the substrate through Watson-Crick base pairing and their sequence can be arbitrarily chosen, because they are not involved in the cleavage reaction. The side chains of the substrate can also consist of DNA, since only the nucleotide at the cleavage site requires a 2'-hydroxy group. The sequence of the catalytic core is mostly fixed and folds into a specific tertiary structure with the help of the M^{2+} cofactor. This geometry aligns the phosphate and 2'-hydroxy group of the substrate in a way that facilitates the nucleophilic attack.[68] Since the 8-17 and 10-23 DNAzyme sequences are very simple, they have been isolated in other independent *in vitro* selection experiments, a phenomenon that has been called the "tyranny of the small motif".[69] Due to their ubiquity, these DNAzymes have been studied extensively and have been used in a variety of applications.[70]

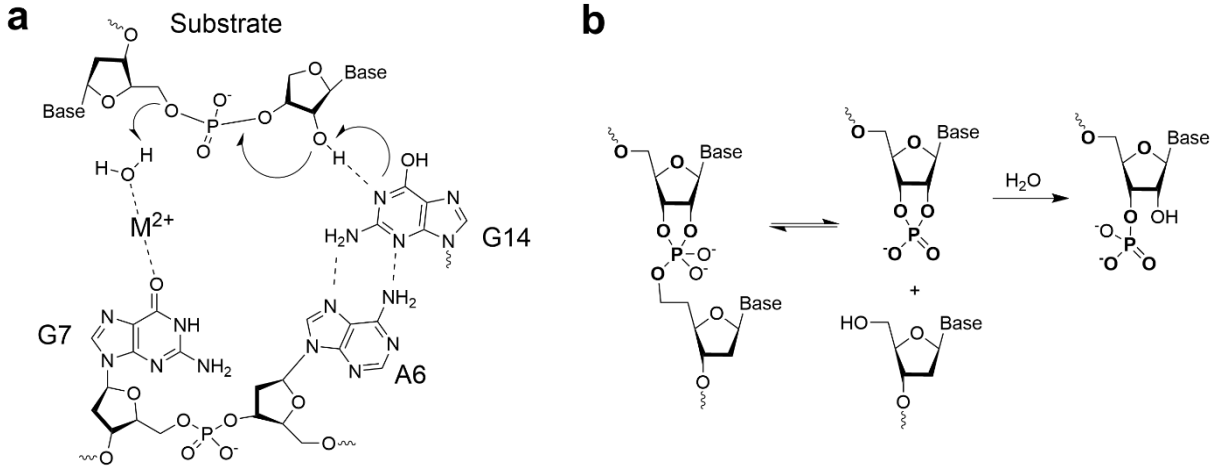

Figure 4. Reaction mechanism of 8-17-catalyzed RNA cleavage. (**a**) Orientation of nucleobases and cofactor at the catalytic site of the DNAzyme. (**b**) Nucleophilic attack of 2'-OH group at phosphate leads to formation of a cyclic intermediate, which is subsequently hydrolyzed.

The first big area of application for RNA-cleaving DNAzymes is sensing, the most important one being heavy metal ion sensing, since they are major environmental toxins. DNAzymes enable on-site detection of heavy metals in the environment and the monitoring of their *in vivo* distribution after ingestion. Since the original 8-17 and 10-23 DNAzymes bind M^{2+} cofactors quite promiscuously, versions of them have been engineered, that bind specific metals with high selectivity.[71-72] For metal sensing applications, the DNAzyme-substrate complex is typically pre-formed and upon addition of the metal cofactor, the substrate gets cleaved. One

of the oldest and most popular readout methods for DNAzyme sensing is the catalytic beacon, which consist of a fluorophore-quencher pair attached to the adjacent ends of the DNAzyme and the substrate strand.[73] Upon substrate cleavage, the fluorophore dissociates from the quencher and its fluorescence gets switched on. Other examples of detection methods are colorimetric readout[74], which is particularly useful for on-site applications, or electrochemical readout[75], which is less prone to background noise than optical methods. Besides metal ions, DNAzymes have also been used for the detection of proteins[76-77] or nucleic acids[78], by being coupled with various recognition domains.

Another field which utilizes DNAzymes is cancer gene therapy.[79] The substrate binding domains are freely programmable, therefore these DNAzymes can degrade any target mRNA and suppress tumor growth through different mechanisms: Firstly, the expression of oncogenes can be downregulated, for example the transcription factor c-Jun, which regulates cell proliferation, transformation and apoptosis in healthy cells, but is overexpressed in melanoma cells.[80] Cancer cells also commonly express membrane transport proteins, which can remove drugs from the cell, for example MDR1. By reducing the expression of these proteins, drug sensitivity can be restored.[81] Lastly, DNAzymes can be used to reduce the expression of endothelial growth factors (EGFs), thereby reducing angiogenesis, which plays an important part in tumor growth and the formation of metastases.[82]

RNA-cleaving DNAzymes have clearly demonstrated their potential for therapeutic and imaging applications, but their transfer to *in vivo* applications presents problems, mostly concerning stability and off-target effects. DNAzymes exhibit higher nuclease stability than their RNA counterparts, but it is still a limiting factor for *in vivo* applications of DNAzymes. To combat this, their stability has been enhanced through chemical modifications like xenobiotic nucleic acids (XNA)[83], 2'-O-methyl modifications[84] or phosphorothioate backbones.[85] Other problems that arise are poor cell uptake and low cofactor concentrations in the cell. By utilizing DNAzyme delivery systems, for example liposomes, polymers or inorganic nanoparticles[86], their cell uptake can be improved and additionally, their circulation time after systemic application can be increased through reduced renal clearance. These delivery systems can also be conjugated with targeting agents, e.g. aptamers, to further increase the local DNAzyme concentration at the target site. One of the biggest innovations for DNAzyme based sensing in cells have been caging-decaging strategies which enable spatiotemporal control over DNAzyme activity and therefore reduce false-positive signaling.[87] These strategies usually involve a chemical modification to the DNAzyme, which suppresses its catalytic activity and can be cleaved off through an external stimulus.[88-89] Such strategies have been realized using light[87, 90], heat[91-92], enzymes[93] or ROS[94] as external stimulus. **Chapter 2** presents a system for the US mediated activation of a DNAzyme. So far there is only one example utilizing US for the activation of an RNA-cleaving DNAzyme, which has been reported by Lu and coworkers in 2022.[95] In this system, the DNAzyme is deactivated through hybridization with a protector strand, which prevents the catalytic core from forming. Upon heating to 43 °C with the help of high intensity focused ultrasound (HIFU), the base pairing with the protector strand gets cleaved and DNAzyme activity is recovered. This system's utility has also been demonstrated *in vivo*, however potential problems might arise due to the prolonged hyperthermia (30 min) that is necessary for activation. Also, the specificity of heat as a stimulus is generally low. By switching to a mechanochemical activation mechanism, we hope to create a more sensitive system with a more specific stimulus, and therefore less off-target effects.

1.1.5 Rolling Circle Amplification

As outlined in the last paragraphs, *in vivo* applications of aptamers and DNAzymes are often limited due to rapid renal clearance and nuclease instability. These two problems can be addressed by utilizing rolling circle amplification (RCA) based systems. RCA is an isothermal amplification technique, which is conceptually similar to the PCR, except it uses a circular template.[96-97] The circular template is typically generated through the circular hybridization of a single stranded template with a primer followed by enzymatic ligation, typically with T4 DNA ligase. This process is often referred to as "padlock ligation". Afterwards, a phage derived DNA polymerase with a 5'-3' strand displacement function (Φ29, Bst or Vent *exo* polymerase) is used to generate polynucleotides with the repeating complementary sequence of the template. Due to the high activity and processivity of the phage derived DNA polymerases, very large molecular weights can be achieved for these polynucleotides. The template sequence can be freely chosen, so functional DNA sequences like aptamers and DNAzymes can be incorporated into the RCA strands. During the enzymatic DNA synthesis from dNTPs, pyrophosphate is formed as a side product, which forms insoluble $Mg_2P_2O_7$ with the magnesium ions from the polymerase buffer. This $Mg_2P_2O_7$ co-crystalizes with the DNA strands and forms DNA nanoflowers (DNFs). These are particles comprised of an inorganic $Mg_2P_2O_7$ core with the DNA adsorbed to the surface.[98-99]

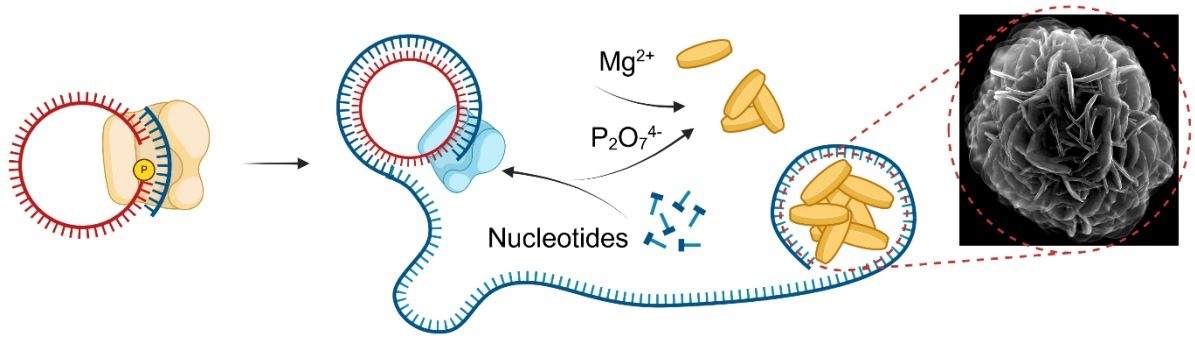

Figure 5. Padlock ligation, RCA and the subsequent formation of DNFs. Created in BioRender. Rath, W. (2025) https://BioRender.com/a26j677.

Since the DNA is present in this condensed state and has very few nicking sites, it is highly resistant against nuclease degradation.[100-101] Due to their high biostability and biocompatibility DNFs have been used for a variety of bioimaging and therapeutic applications.[101-102] In this thesis, two different novel applications for RCA are presented: Firstly, a DNF based system for the US triggered activation of a DNAzyme is shown in **chapter 2**. In this system, the DNAzyme is deactivated by hybridizing to a complementary RCA strand and its activity is recovered through ultrasonication. The reason to use a DNF based system for this task is the RCA strands' large molecular weight. This makes the DNA US-responsive and enables the DNAzyme to be released through a mechanochemical mechanism. The scientific background behind this US mediated release mechanism is discussed in **chapter 1.2**. DNF based systems have also been used to deliver DNAzymes for cancer gene therapy in the past.[103] DNFs are interesting in this context, since the $Mg_2P_2O_7$ nanoflowers dissolve under acidic conditions, and therefore provide additional Mg^{2+} ions for the DNAzyme.
The second RCA system in this thesis, which is presented in **chapter 3**, is an aptamer based system for the targeted delivery of anti-cancer drugs. DNF based DDSs can achieve long circulation times *in vivo*, since DNFs naturally exhibit higher nuclease stability than their oligomeric counterparts and their renal clearance is also suppressed, due to their large molecular weight. This also mitigates the need for conjugation with polymers like PEG, which

can cause adverse effects. Their very high DNA content helps to exploit the multivalency effect for increased binding affinity and to retain targeting ability in case of partial nuclease degradation. Due to these advantages, DNF based aptamer DDSs have already attracted some attention in the past.[104-105]

1.2 Polymer Mechanochemistry

The macroscopic mechanical properties of polymer materials have been studied for a long time. They often exhibit viscoelastic properties, meaning they exhibit behaviors of both solids (elastic) and liquids (viscous).[106] These macroscopic attributes are determined by molecular characteristics like molecular mass, chain entanglement and crosslinking density. The mechanical toughness of polymer materials can be characterized by metrics like tensile strength, failure strain or fracture toughness.[107] During these stress tests, force gets transferred into individual polymer chains, leading to chemical aging due to bond breakage and eventually mechanical failure.

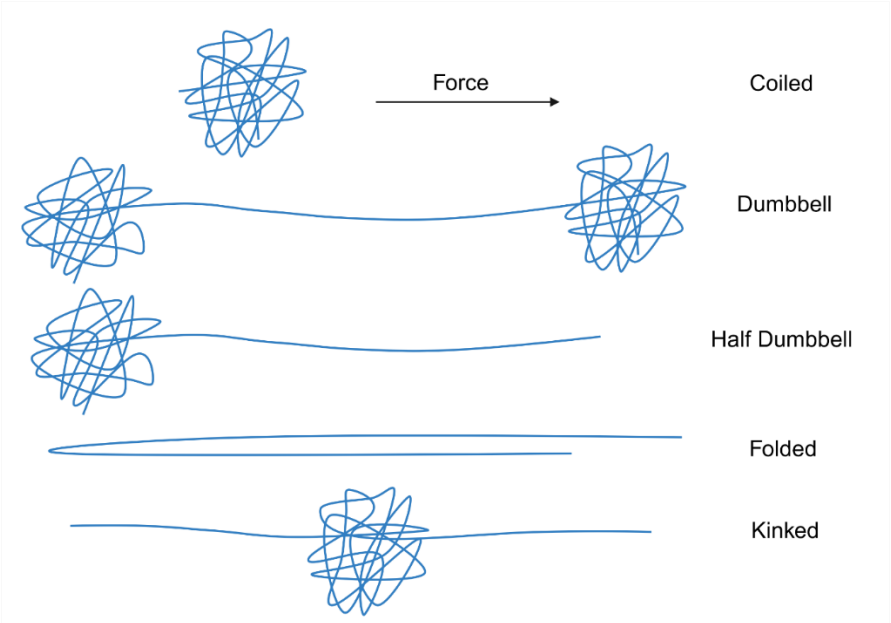

Figure 6. Conformations of polymer chains during stretching. Created in BioRender. Rath, W. (2025) https://BioRender.com/p39q383.

Aside from solid polymer materials, force induced bond scission can also occur in polymer chains in solutions. This was first observed by Staudinger in 1930 after exposing poly styrene (PS) to high shear flow.[108] A polymer coil passing through a flow field gets elongated once the hydrodynamic force exceeds the entropic elasticity of the polymer.[109] Bond scission occurs once the strain rate ε exceeds the critical strain rate ε_f, which is inversely proportional to the molecular weight of the polymer.[110-112] Mathematical calculations like the “yo-yo” model predict, that the strain rate is highest at the center of the polymer chain[110], and indeed this is where chain scission primarily occurs. Shearing experiments on fluorescently labeled DNA molecules have enabled the visualization of the stretching of individual polymer chains, which can adopt a large variety of stretched conformations including dumbbell, half dumbbell and folded geometries.[112] The dumbbell conformation closely resembles the “yo-yo” model, but it is still unclear which conformations promote midpoint scission, since this phenomenon was also observed for partially uncoiled polymers.[113-114]

1.2.1 Ultrasound and Cavitation

The term US describes longitudinal pressure waves between 20 kHz and 100 MHz. When US is applied to a liquid medium and the negative pressure of the soundwave exceeds the internal pressure of the medium, the liquid evaporates and so-called cavitation bubbles are formed.[115] Microbubbles can also be added directly to the medium to enhance bubble nucleation. Therefore microbubbles enhance cavitation and increase contrast for US imaging, making them an important tool in various therapeutic and imaging applications.[116] After nucleation, the cavitation bubble's size oscillates correlating with the acoustic pressure and slowly grows over many cycles. Once a critical size is reached, the bubbles collapse violently, resulting in localized increases in temperature and pressure up to 4500 K and several hundred bar. These collapses can also be accompanied by the emission of light (sonoluminescence). Cavitation events can induce chemical transformations in solution through a variety of effects, which can be separated into two categories: radical and mechanical effects.[6, 117] Radical effects, like the generation of ROS due to homolytic cleavage of water molecules, occur under the extreme conditions in collapsing cavitation bubbles or at the gas-liquid interface. The most important mechanical effects are shockwaves[118] and microjets[119], which are direct outcomes of cavitation bubble collapse, and are responsible for the induction of shear forces in solution. These mechanical effects can induce polymer chain scission if the hydrodynamic force is strong enough, similar to the elongational flow fields described above.[120-121] Other mechanical effects include acoustic streaming, which is induced by the US wave itself[122], or microstreaming caused by oscillating cavitation bubbles.[123] These effects are weaker than shockwaves and microjets and cannot induce chemical transformations, but they enhance the mass transport in solution.

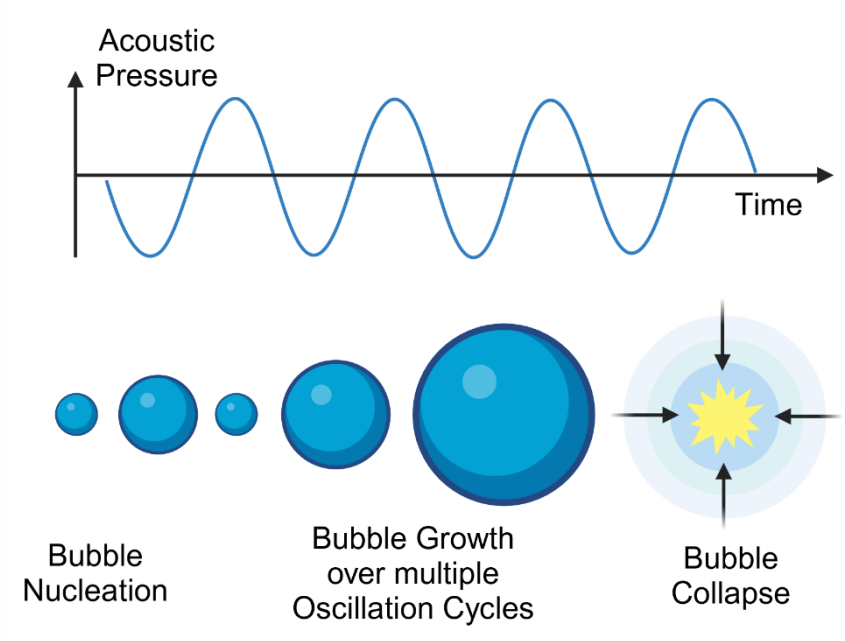

Figure 7. Cavitation bubble nucleation, growth and collapse in response to the US pressure wave. Created in BioRender. Rath, W. (2025) https://BioRender.com/o76e095.

US induced bond scission typically occurs homolytically, which has been confirmed by radical trap experiments[124] and isotope labeling.[125] It was discovered early, that a large molecular weight is a very important parameter to ensure a high rate of US induced chain scission. For example, during the US induced scission of PS in decalin a minimal molecular weight of 30 kDa was found.[126] While molecular weight is an important factor, a lot of contextual parameters also have been uncovered over the years. For example, recent studies have shown, that contour length and not molecular weight is the crucial parameter influencing scission rate.[127-128] For this reason, polymer architecture plays a major role in determining the scission behavior.[129] Polymer-solvent interactions also play a crucial role, since swollen polymer coils undergo a coil-stretch transition more easily than

collapsed coils, and are therefore degraded faster.[112]
While bond scission in elongational flow fields is largely independent of solvent viscosity[130] and temperature[131], US induced bond scission is dependent on a variety of solvent properties, which influence the cavitation process. The most important solvent parameter is vapor pressure, which is inversely proportional to the chain scission rate.[132-133] Since solvents with higher vapor pressure are more volatile, more vapor is generated upon nucleation of a cavitation bubble. This vapor is believed to have a cushioning effect on the collapse of the bubble, therefore reducing the generated shear force. Vapor pressure is also proportional to the solvent temperature, therefore increases in temperature typically lead to a decrease in scission rate.[134-135] The viscosity of the solution is inversely proportional to the bond scission rate, since the collapse of cavitation bubbles in solvents with high viscosity generate lower shear forces. Additionally, viscous solvents exhibit an increased cavitation threshold. High polymer concentrations can also increase the viscosity of the solution and therefore lower the scission rate.[132, 136-137]

1.2.2 Mechanophores

Mechanochemical bond scission can fundamentally be described as a thermally activated process[138], whose rate is predicted by the Arrhenius equation. The mechanical force however lowers the activation energy required for bond scission, since increasing the bond distance between two atoms increases the bond's potential energy, as described by the Morse potential. The "thermally activated barrier to scission" (TABS) model can be derived from these two equations.[139] This means, that the rate of mechanochemical bond scission is directly correlated with the bond dissociation energy. Therefore, weak bonds can be strategically incorporated into polymers to induce bond scission at defined points of the chain, so called mechanophores. An early example of this has been shown by Radic and coworkers[140], who incorporated a peroxide bond into poly vinylpyrrolidone, which is significantly more labile than a C-C bond (146 kJ/mol vs. 348 kJ/mol[141]). In the 2000s the field of mechanophores was vastly expanded by Moore *et al.*, who designed a plethora of new mechanophores, including Azo-bonds[125], benzocyclobutene[142] or spiropyranes.[143]

1.2.3 Soft Mechanochemistry

Mechanical force has also been shown to affect non covalent interactions between polymer chains, including hydrogen bonding[144], π-stacking[145] or metal coordination.[146] This has led to the design of mechanophores which rely purely on non-covalent interactions like hydrogen bonding and closely resemble natural structures like DNA base-pairing[147] or beta sheets.[148] Other examples of supramolecular mechanophores are based on excimers, which separate upon force application, and in turn exhibit a blue shift in fluorescence.[149] Mechanoresponsive supramolecular materials can be applied for US mediated drug delivery[150] or force sensing.[151] Besides disrupting supramolecular bonds, mechanical force can also induce conformational changes in covalent bonds[152], which is the mechanism upon which many mechanosensitive biological systems rely.[153] All these non-covalent chemical transformations are typically reversible and require low mechanical force, therefore they are referred to as soft-mechanochemistry.[7]

1.2.4 Chemical Ultrasound vs. Medical Ultrasound

Besides its utility in mechanochemistry, US is an ubiquitous clinical tool which has a variety of diagnostic[154] and therapeutic[155] applications. Therefore, it seems like a natural conclusion to utilize mechanochemical concepts for the development of new clinical applications. Indeed US has proven to be viable stimulus to control the release of drugs (sonopharmacology)[150, 156-158] or the expression of genes (sonogenetics).[159] US is an elegant trigger for biological applications, since it offers accurate spatiotemporal resolution and higher tissue penetration than other stimuli like light, therefore enabling non-invasive treatment. A big barrier for the mass adoption of these novel US applications in biological systems are the safety risks associated with prolonged exposure to US. These risks result from the thermal and mechanical effects of US.[160] In a few applications, these effects can be useful, for example during tumor treatment through hyperthermia[161] or thrombolysis through cavitation effects[162], but they necessitate strict safety guidelines to avoid injuries like burns or bleeding.[163] An important parameter to judge the safety of US is the mechanical index (MI), which quantifies the amount of cavitation generated by US. It is calculated with the following equation:

$$MI = \frac{P}{\sqrt{f}}$$

P: Acoustic pressure [MPa]

f: US frequency [MHz]

Below an MI of 0.5 no cavitation bubbles are formed and the maximum MI approved by the FDA for diagnostic imaging is 1.9.[164] Since the MI is inversely proportional to the US frequency, lower frequencies, e.g. 20 kHz, are mostly reserved for mechanical shearing applications. There are rare examples of 20 kHz US being used for clinical applications like transdermal drug delivery[165], which benefits from strong cavitation to disrupt the skin barrier (sonophoresis[166]), but most medical applications like imaging are performed at higher frequencies above 1 MHz and low intensities.

1.2.5 Towards Biocompatible Mechanochemistry

Since the use of 20 kHz US in biological systems is so limited, it has been a challenge to apply mechanochemical principles for the design of biomedical systems. One potential solution for this problem is to use high intensity focused US (HIFU) instead of 20 kHz US, since it typically operates at higher frequencies (500 kHz – 5 MHz) and therefore exhibits a lower MI. The activation of a naphthopyran-, dioxetan- and an azo-mechanophore through HIFU have already been demonstrated by Moore and coworkers.[167-168] Recently, the Herrmann lab has also successfully activated disulfide mechanophores through HIFU.[169] Additionally, Robb and coworkers have shown, that the activation of 2-furylcarbinol mechanophore with HIFU can be enabled by the addition of microbubbles.[170] All these examples have utilized HIFU to induce covalent bond breakage in mechanophores, but to achieve a further reduction in activation barrier, mechanophores can be designed with the principles of soft mechanochemistry in mind. Therefore, the Herrmann group explored the potential of biomacromolecules like DNA for mechanochemical applications, since their functions usually emerge from their noncovalently assembled secondary and tertiary structures.

Many of the mechanosensitive DNA systems we have designed are based on DNFs generated through RCA (see **chapter 1.1.5**). Since RCA strands have a very large contour length, they are susceptible towards US. Since the RCA template sequence can be freely customized, a

variety of functional DNA motifs can be incorporated into the DNFs, including aptamers, DNAzymes and restriction sites.[171] Based on this, we have been able to design different force responsive DNF systems to control the activity of the enzyme thrombin[172] or the antibiotics neomycin B and paromomycin.[173] Both examples utilize DNFs bearing the aptamer to either thrombin or the antibiotic (polyaptamer), which deactivates the catalytic or antimicrobial activity of the ligand upon binding. Through the application of US, the hydrogen bonds stabilizing the aptamer secondary structure, as well as the covalent bonds at the DNA phosphate backbone get cleaved[174], resulting in the release of the ligand. Both these systems can be activated with 20 kHz US, and the thrombin-polyaptamer system is responsive towards 5 MHz HIFU as well. Very recently we have developed the first mechanochemical system that can be activated with diagnostic US (4-12 MHz, MI=0.9).[175] This system again utilizes a DNF based carrier system, onto which therapeutic oligonucleotides are loaded through Watson-Crick base pairing. We have successfully used this system to release CpG oligodeoxynucleotides (ODNs) *in vivo* with the help of diagnostic US, in order to achieve targeted immunostimulation through the TLR-9 pathway. These three examples illustrate that DNFs are a versatile platform for the design of force responsive release systems, which have the potential to bridge the gap between chemical and medical US applications due to their low activation barrier. In **chapter 2** of this thesis, a DNF based system for the US triggered activation of an RNA cleaving DNAzyme is presented.

1.3 Cancer Drug Delivery

1.3.1 Historic Development of Chemotherapy

Chemotherapy is one of the most common cancer treatments besides surgery and radiation therapy. It was pioneered after World War II by Louis Goodman and Alfred Gilman, who observed significant anti-cancer effects after administering nitrogen mustard to lymphoma patients.[176-177] These compounds have originally been designed as chemical warfare agents, whose toxicity is caused by the formation of interstrand cross-links (ICL) between DNA molecules.[178] Other early chemotherapeutics also work by disrupting DNA replication, such as 5-fluoro-uracil[179], mitomycin C[180] or cisplatin.[181] Since cancer cells divide faster than healthy cells, these compounds disproportionally affect cancer cells, but healthy tissues are still damaged, which can lead to strong side-effects. In order to reduce these side effects, more specific treatments had to be developed. Paul Ehrlich, who also was a pioneer of chemotherapy, recognized this need for targeted therapy early in his career and coined the term “magic bullet” to describe these treatments.[182] In order to achieve this, chemotherapeutics have been developed in the 1970s and 1980s, which interact with the specific cellular signaling pathways that are dysregulated in cancer cells. These signaling abnormalities include an upregulation of angiogenesis and growth signals as well as suppression of apoptosis.[183] An important class of drugs that interfere with these specific pathways are tyrosine kinase inhibitors, which block the ATP binding site at the intracellular kinase domain of various receptors like the EGF receptor or the VEGF receptor, therefore inhibiting their downstream signaling pathways.[184] More recent research has focused on the development of drugs that target metabolic pathways[185], ion channels[186] or the epigenome.[187] Despite these advances in drug development that enable pharmacological targeting of cancer cells, the outcomes during therapy have been sobering, since the uptake of drugs into the target cells is typically very low.

1.3.2 Tumor Microenvironment

In order to explain the process of drug delivery into the target cells, it is important to understand the patterns of pathogenic angiogenesis in tumors.[188] Angiogenesis in tumors is mediated through different growth factors, most importantly VEGF.[189] The expression of these growth factors is upregulated in response to metabolic stresses like lack of oxygen and low intracellular pH, mechanical stress through the pressure of proliferating cells or genetic mutations. This unusual growth factor profile leads to the formation of irregular, highly branched vasculature[190], which is not fully surrounded by perivascular cells (e.g. pericytes) and therefore lacks vasoactive control, leading to permanent dilation.[191] This lack of perivascular support alongside wider interendothelial cell junctions and the lack of a basement membrane promotes increased leakiness of the tumor vasculature compared to the surrounding tissue.[192] VEGF also promotes fenestration of newly formed vasculature, further increasing the permeability of the tumor vessels. [193] Another feature of tumor tissue is its distinct lack of lymphatic drainage, especially at the tumor center, which is likely caused by the mechanical stress that gets exerted onto the newly forming lymphatic channels by the rapidly proliferating cancer cells.[194] This lack of lymphatic drainage combined with the increased permeability of the vasculature leads to an increase in interstitial pressure inside the tumor.[195]

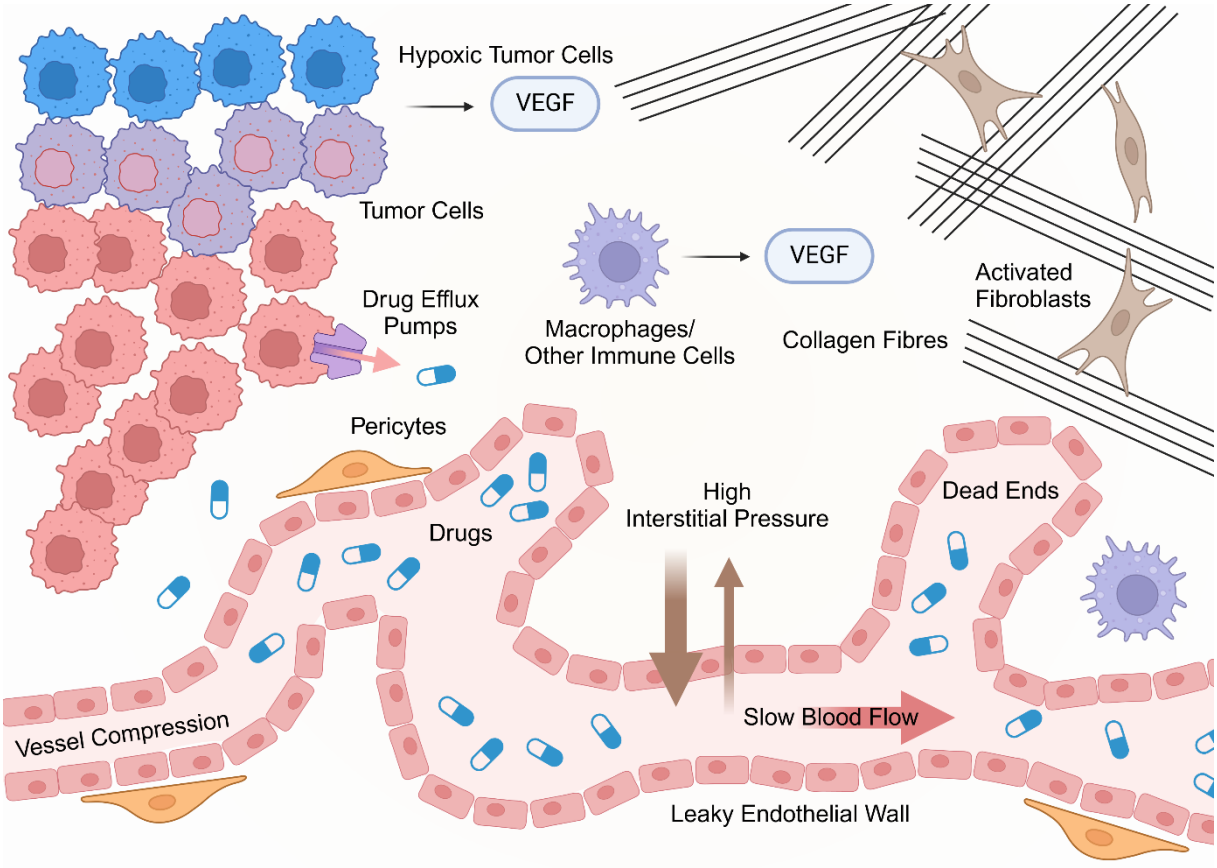

Figure 8. Different features of the tumor microenvironment, which hinder the delivery of drugs into the tumor cells. Created in BioRender. Rath, W. (2025) https://BioRender.com/z79d908.

Since tumor vessels exhibit irregular branching patterns and are permanently dilated, the blood flow in these vessels tends to be stagnant and undirected. This, in addition to the high interstitial pressure, leads to slow and inhomogeneous blood circulation. Systemic therapies rely on passive transendothelial drug delivery, which is purely based on a concentration gradient between blood and tumor. This typically results in a very low percentage of the given

drug actually reaching the tumor site (≤ 1%), thus necessitating very high drug doses, which in turn lead to drug toxicity.[196] Some attempts have been made to increase therapeutic efficacy of drugs by improving the blood flow into the tumor, for example through the co-administration of VEGF blockers.[197] These anti-angiogenic therapies have yielded mixed clinical results so far[198], since many tumor types can establish their blood supply through VEGF-independent processes, for example vessel-co-option.[199-200]

1.3.3 Drug Resistance

Besides the low delivery efficiency of drugs into tumors, cancer cells can also develop multi drug resistance (MDR) in response to the exposure to chemotherapeutic drugs. The processes behind the development of MDR vary between drugs and cancer types, but possible mechanisms include increased repair of DNA damage, suppression of apoptosis, upregulation of alternative signaling pathways and alterations in drug metabolism and drug transport.[201] The best known drug transport protein is P-glycoprotein (P-gp)[202], which recognizes hundreds of hydrophobic molecules that accumulate in the lipid bilayer of the cell membrane and expels them. Due to its substrate promiscuity, P-gp plays an important role in the development of resistance to a variety of drugs. One of the drugs whose resistance is mediated through P-gp is Dox, which is also used in the system presented in **chapter 3**. Dox is used for the treatment of various cancers including breast cancer[203], lung cancer[204], bladder cancer[205] or glioblastoma.[206] It is an anthracycline drug, which interferes with DNA replication by inhibiting Topoisomerase II, intercalating into DNA double helixes and disrupting DNA-histone binding.[207] Side effects include major cardiotoxicity, gonadotoxicity or even the formation of therapy-related malignant neoplasms, therefore it is not recommended to increase the dose, once Dox resistance develops in a patient. In order to prevent the formation of Dox resistance, the cellular mechanisms that stimulate the expression P-gp have been extensively studied. For example, P-gp expression can be downregulated by inhibiting the PI3K/AKT/mTOR signaling pathway[208] or by reducing NRF2 signaling.[209]

1.3.4 Glioblastoma and the Blood Brain Barrier

Glioblastoma is a highly aggressive and treatment-resistant form of brain tumor.[210] The standard treatment is comprised of surgical removal followed by chemotherapy with temozolomide, but the current 5 year survival rate is < 10 %. Glioblastoma's treatment resistance seems to arise from its uniquely complex tumor microenvironment and its propensity to mutate in response to external stress.[211] One of the most prevalent mutations is found in isocitrate dehydrogenase (IDH). IDH mutated glioblastomas are associated with better disease outcomes, but also recur more often with malignant transformations.[212] An additional reason for glioblastoma's treatment resistance is the blood-brain barrier (BBB), which greatly limits the passage of drugs into the brain.[213] The BBB is a non-fenestrated barrier that consists of specialized endothelial cells, which are connected through transmembrane proteins to form tight junctions. These endothelial cells are supported by pericytes and astrocytes.[214] The BBB only lets small hydrophilic molecules (<500 Da) and hydrophobic molecules like O_2 or CO_2 diffuse through, while larger molecules like glucose or insulin get transported across by pinocytosis, receptor- or carrier-mediated transcytosis and solute-carrier-protein mechanisms.[215] In addition, P-gp has also been found on the surface of endothelial cells of the BBB, which further prevents drugs like Dox from entering the brain.[216] In many glioblastoma patients the BBB is disrupted, since hypoxic glioblastoma cells release VEGF,

which promotes the formation endothelial cells with downregulated expression of the transmembrane proteins that form tight junctions.[217] This helps to increase the permeability of the BBB, although in a very heterogeneous fashion, which is why additional disruption is needed to overcome the BBB for drug delivery. One of the earliest methods to open the BBB has been through osmotic shrinkage of the BBB endothelial cells.[218] Other strategies rely on the invasive administration of wafers or infusates.[219] Recent research focusses on the transient opening of the BBB through focused US.[220]

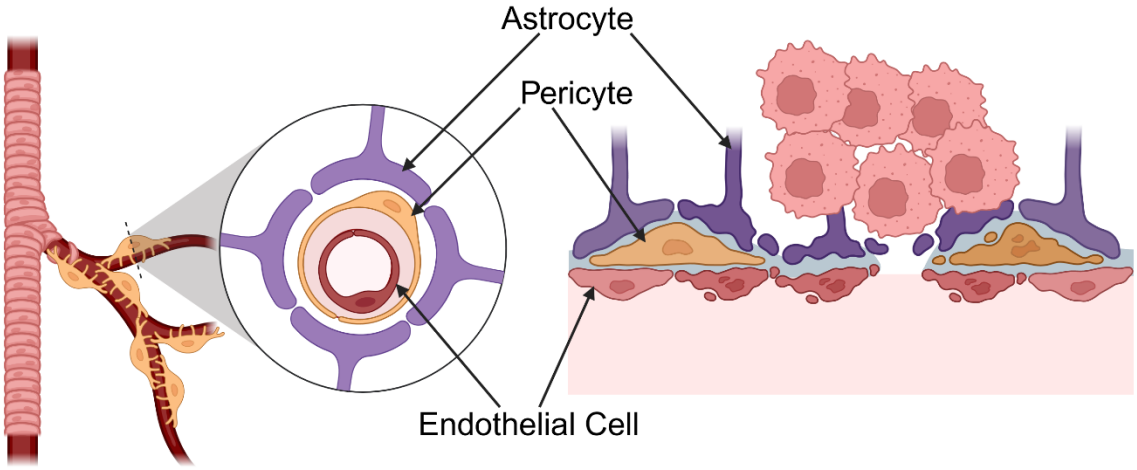

Figure 9. Architecture of the BBB and its disruption through glioblastoma. Created in BioRender. Rath, W. (2025) https://BioRender.com/b49x088.

1.3.5 Targeted Drug Delivery

Due to low drug accumulation in the target cells and the development of MDR, it has become clear that pure pharmacological targeting is not sufficient to realize Paul Ehrlich's vision of the "magic bullet" that selectively kills cancer cells. In order to further boost therapeutic efficacy and to reduce drug toxicity, targeted DDSs have been developed.[221] These systems rely on carrier materials to transport drugs to the tumor site and can roughly be categorized into two categories: passive targeting and active targeting. Passive targeting is based on the accumulation of nanoparticles (d ≤ 200 nm) at the tumor site, due to the increased leakiness of the vasculature and poor lymphatic drainage. This phenomenon is called enhanced permeability and retention (EPR) effect. Encapsulation of drugs into nanoparticles also increases the blood circulation time, since they are above the size threshold for renal clearance (20-30 nm or 60 kDa).[222-223] Many different materials have been used for particle based drug delivery, including gold[224], silica[225], liposomes[226] and polymers.[227] Particle size is arguably the most important parameter for the design of these systems, since it fundamentally affects the biodistribution. Particles with a size below 30 nm are rapidly cleared through renal excretion, 30-150 nm particles preferentially accumulate in the bone marrow, the heart, the kidney and the stomach, while 150-300 nm are found mainly in the liver and the spleen. The optimal size for tumor targeting seems to lie between 70 and 200 nm.[228] This medium size seems to balance out plasma half-life, vascular permeability and tumor clearance.[229] Other parameters that impact the biodistribution of particles include surface charge[230] and shape.[231] Despite all advances in the field of passive tumor drug delivery, delivery efficiency of nanoparticles is still quite low, therefore necessitating the use of active targeting strategies. These strategies utilize nanocarriers that are conjugated with antibodies, aptamers, peptides or carbohydrates, which recognize cell surface proteins that are overexpressed in cancer cells.

Common targets include the EGF receptor[232] or the tumor necrosis factor (TNF) receptor 2.[233] Historically, antibodies have been the most popular targeting agents, but since their discovery in the 1990s, aptamers have seen widespread use.[234] The general advantages and limitations of aptamer conjugated DDSs have already been discussed in **chapter 1.1.3**. The first examples of aptamer-based cancer drug delivery have been presented in 2006 by two independent research groups. Both used an anti-prostate specific membrane antigen (PSMA) aptamer to deliver siRNA into prostate cancer cells.[36, 38] Since then, various cancer targeting DNA aptamers have been developed, for example the 5TR1, 5TRG2 or MA3 aptamers, which all target the Mucin 1 (MUC1) protein[235], or the Sgc8-c aptamer, which targets the receptor tyrosine kinase PTK7.[236]

1.3.6 AS1411 Aptamer

The DNF based DDS presented in **chapter 3** utilizes the AS1411 aptamer, which specifically binds to nucleolin, a protein that is overexpressed on the surface of various cancer cells.[237] AS1411 (also known as AGRO100) is a G-rich DNA 26-mer that forms uni- and bimolecular G-quadruplex structures with a predominantly parallel conformation.[238] Studies have demonstrated the intrinsic therapeutic effects of AS1411[239-240], but it is mainly used as a targeting agent. There are examples of AS1411 drug conjugates, for examples with Dox[241] or melittin[242], and numerous examples of AS1411 conjugated nanocarrier systems, including chitosan particles[243], PLGA particles[244], silica particles[245], liposomes[246] or DNA tetrahedrons.[247] In 2019, Li *et al.* have demonstrated that Dox can be loaded onto the AS1411 aptamer solely through non-covalent interactions, instead of forming a covalent aptamer-Dox conjugate.[248] This is achieved through intercalation of Dox into the aptamer's G-quadruplex structure. In the same study, the authors have observed increased accumulation of Dox in the nucleus and higher cytotoxicity after the administration of AS1411-Dox complexes, compared to free Dox. This effect can be explained by the endocytotic uptake of the AS1411-Dox complex, which circumvents the P-gp mediated removal of Dox from the cell. Nucleolin is also involved in nucleocytoplasmic transport processes[249], which explains the increased accumulation of the AS1411-Dox complex in the nucleus.

1.3.7 Glioblastoma Targeting

Since the success rate of systemic glioblastoma treatment is so low, current research is focusing on targeted strategies to combat glioblastoma. On the one hand, new drugs are being developed for the pharmacological targeting of specific genotypes of glioblastoma, for example the IDH mutated variant.[212] Another important goal is to overcome the complex tumor microenvironment of glioblastoma. For this purpose, aptamer-based systems have been developed for a variety of molecular targets, and one aptamer has entered phase 1/2 clinical trials so far.[250] Among the various aptamers, AS1411 has also been used to construct targeted DDSs for the treatment of glioblastoma.[251-255]. Additionally, the transport of drugs across the BBB has to be further improved. Aside from the methods to transiently increase permeability of the BBB that are described above, physiological transport processes like receptor-mediated transcytosis can be exploited. A common pathway for this is the transferrin receptor, which can be targeted with antibodies[256] or peptides[257], and more recently aptamers have been developed for this purpose.[258] These aptamers have been used to construct dual-targeting systems in combination with a cancer targeting aptamers like AS1411.[259-260] In this thesis, an AS1411 based DNF system is used. The general advantages of using DNFs for drug delivery

purposes have already been discussed in **chapter 1.1.5**. Very recently; DNFs specifically bearing the AS1411 aptamer sequence have been shown to be effective DDSs.[261-262] This thesis builds upon this concept by introducing a chelator for radiolabeling through Click-chemistry (see **chapter 1.5**).

1.3.8 Chicken Embryo Model

During pre-clinical studies, animal models provide valuable information that *in vitro* models cannot deliver, including disease progression, off-target effects and toxicity. Since the postulation of the 3Rs principle (reduction, replacement and refinement) by Russel and Burch in 1959, there has been an increasing drive to reduce animal experiments.[263] To achieve this, more complex *in vitro* models have been developed, like 3D cell culture models[264] or microfluidic "organ-on-a-chip" models.[265] These microfluidic models are also specifically available for glioblastoma[266-267] and the BBB.[268] Even though these *in vitro* models are becoming more advanced, they still cannot provide information about off-target effects, pharmacokinetics and toxicity. The chicken (*Gallus Gallus*) embryo is a more complex model which still meets the 3R criteria to reduce animal use.[269] Chicken embryos are considered to be a more ethical animal model, since they only experience pain in their later parts of development (day 15+).[270] For this reason, chicken embryos are exempt from many regulations concerning the protection of lab animals, for example the EU guideline 2010/63/EU. Additionally, chicken embryos grow much faster than mammals, making the model overall easier to handle, faster and less costly. During its development, the embryo is surrounded by the chorioallantoic membrane (CAM), which is a highly vascularized structure that is responsible for the exchange of O_2 and CO_2 between the embryo and the environment. Since the CAM undergoes rapid angiogenesis during its development, it has been used as model environment to study anti-angiogenic drugs[271] and wound healing.[272] It is also an ideal environment for tumor xenografts, since it mimics the mammalian tumor stoma.[273] Tumor xenografts in the CAM grow much faster compared to mammal models, since the chicks adaptive immune system is only fully functional after hatching.[274] Since the CAM is readily accessible through a fenestration in the eggshell, these tumor models are easy to handle and treatment outcomes can be immediately observed. For these reasons, CAM xenograft models are a popular tool for the assessment of tumor angiogenesis and metastasis potential, as well as the efficacy of various treatment and imaging modalities.[273] The CAM xenograft model has been extensively used to evaluate the efficacy of various nanoparticle-based DDSs.[275-276] Chicken embryos are a good model for the distribution of particle-based DDSs, since macrophage-like cells are present in the liver of the embryo and are capable of phagocytosing particles after day 12, similar to mammal models.[274] They also accurately model unwanted interactions with plasma proteins, extravasation and interactions with interstitial fluid in the tumor.[277] Some studies have directly compared the efficacy of nanoparticle-based DDSs in CAM xenograft and mouse xenograft models, and observed very similar results.[278-279]

1.4 DNA Functionalization

1.4.1 Bottom-up Synthesis of Nucleic Acids

The main two synthesis methods for NAs are either chemical synthesis or enzymatic polymerization, which respectively utilize phosphoramidites or nucleoside triphosphates as building blocks. The bottom-up synthesis of these building blocks has opened up the possibility for extensive chemical modifications of NAs. Nucleotide synthesis starts off by choosing a nucleobase. Besides the natural nucleobases, a variety of modified nucleobases can be chosen, for example halogenated nucleobases.[280] These can easily be further functionalized, for example through Suzuki coupling[281] or Sonogashira coupling[282] to introduce Click-functionalities like azides or alkynes. Methylated nucleobases, which play important roles *in vivo*, can also be incorporated.[283]

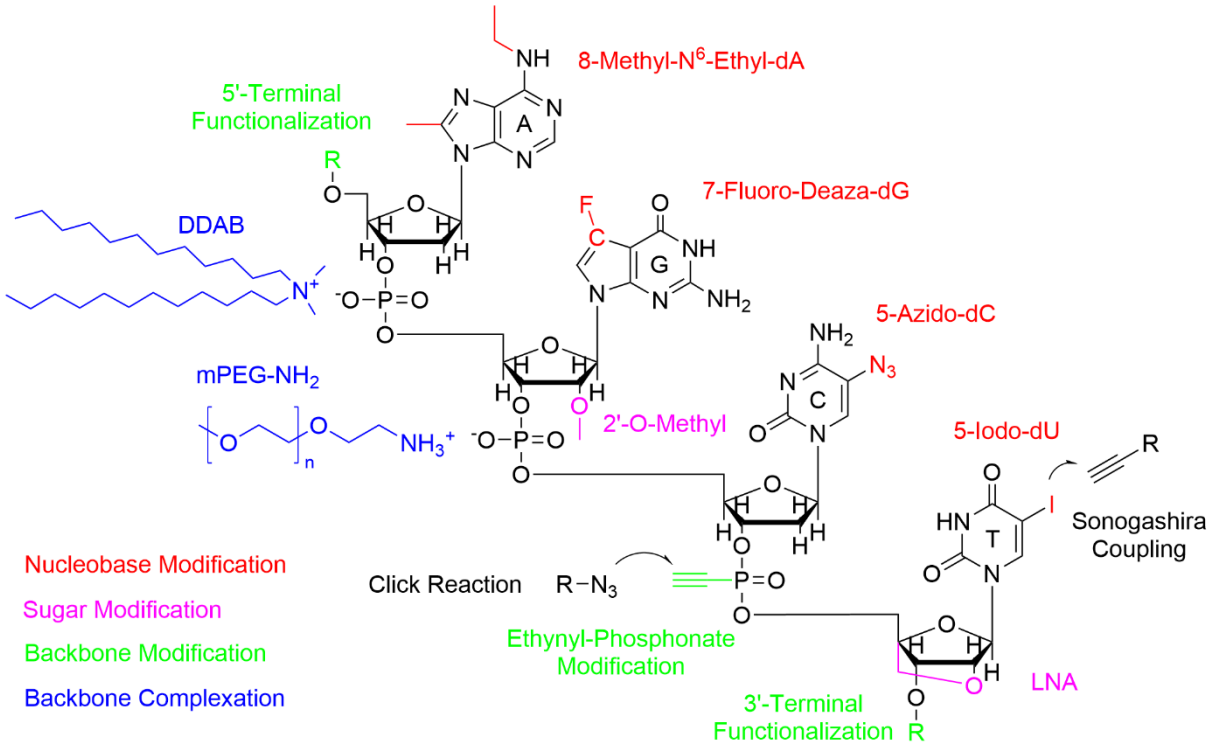

Figure 10. Examples of various chemical modifications of DNA.

In the next step, the sugar unit is introduced, which can also be heavily modified. For example 2'-O-alkylated sugars or LNA modifications can be incorporated during this step.[284] Finally, the 3'-OH group of the sugar is coupled with either a phosphoramidite moiety to perform chemical NA synthesis or with a triphosphate unit for enzymatic NA synthesis. When comparing the two synthesis approaches, the phosphoramidite method allows for the synthesis of large amounts of NAs, but it is limited to short oligonucleotides.[285] The handling of phosphoramidites is especially complicated, since they are prone to oxidation and degrade quickly in the presence of small amounts of water.[286] Enzymatic synthesis enables the formation of longer NA strands, but is only suitable for small amounts. Additionally, the polymerase enzymes might not be compatible with fully synthetic nucleotides. Overall, the bottom-up modification of NAs through fully synthetic nucleotides is an invaluable tool to expand the functionality of NAs, but it is very labor intensive and poses unique synthetic challenges. Therefore, it makes sense to only introduce selected functional groups like azides, alkynes, amines or thiols through synthetic nucleotides, which allow the post-synthetic

modification of NAs with more complicated label molecules. The position in which these chemical handles can be introduced into oligonucleotides is dependent on the synthesis method. Phosphoramidite chemistry enables the modifications to be inserted at very specific spots in the sequence. For example, it is very easy to terminally functionalize NAs at the 5'- or 3'-end through commercially available phosphoramidites.[287] This is for example utilized during the synthesis of molecular beacons (compare **chapter 1.1.4**).[288] Chemical synthesis also accommodates a wide variety of internal nucleobase modifications[289], 2'-OH modifications on the sugar unit[290-291] and backbone modifications.[292] Enzymatic synthesis generally offers less flexibility for the attachment of chemical handles. Modifications are also less site-specific, since the modified nucleoside triphosphates are statistically incorporated into the chains. Nucleobase modifications are usually attached at the 5-position for pyrimidines and at 7-position for purines, since they are best tolerated by polymerase enzymes.[293] Some polymerases, especially DNA polymerases, also cannot process nucleotides with 2'-OH modified sugars due to steric hindrance.[294] To widen the scope for enzymatic polymerization of modified NAs, the polymerase compatibility of many nucleotides has been evaluated[295] and mutation studies have been conducted on polymerase enzymes to expand their nucleotide tolerance.[296] Backbone modifications can also be incorporated during enzymatic NA synthesis through the use of α-phosphate-modified triphosphates.[297]

1.4.2 Post-synthetic Modification

Post synthetic labeling reactions need to achieve high selectivity and yield under mild conditions, ideally in aqueous solution. The oldest biolabeling approaches involve the coupling of an amine function with thiocyanates, activated esters or acid chlorides.[298] Since these reactants quickly degrade in the presence of water, various alternatives have been developed. For example, thiol groups can be used for the coupling with maleimides[299], disulfides[300] or a bromoacetyl group.[301] Alternatively, maleimide functions can also be utilized in the Diels-Alder [4+2] cycloaddition.[302] Another highly selective cycloaddition is the Huisgen [2+3] cycloaddition between an azide and an alkyne. This reaction is often referred to as "Click reaction", and arguably is the most important biolabeling reaction.[303] The first iteration of the Click reaction has been catalyzed by Cu(I), but in order to avoid copper's cytotoxicity, metal free versions of this reaction have been developed. These metal free Click reactions typically employ cyclic alkynes, for example dibenzocyclooctyne (DBCO), which exhibit a lot of ring strain due to the linear alkyne bond. An alternative use for an azide moiety is the Staudinger ligation, which allows the coupling of azides with triarylphosphines.[304]

1.4.3 Backbone Complexation

Due to their polyanionic nature, post-synthetic NA chemistry is limited to aqueous solution only, with a limited possibility to add co-solvents. This can hinder the post-synthetic modification of NAs with hydrophobic moieties or water-labile compounds, e.g. NHS esters. There are however strategies to transfer NAs to organic solvents through complexation with cationic lipids, which form a contact ion pair with the anionic phosphate backbone of the NA. This results in a charge neutral complex in which the hydrophobic tails of the lipids are attached to the NA in a brush-like fashion. This technique was pioneered by Ijiro and Okahata in 1992[305], and has since been a popular tool to enable the use of NAs in organic media. At the Herrmann group, we have demonstrated this approach's usefulness numerous times. For example, in 2014 we have used didoceyldimethylammonium bromide (DDAB) for the complexation of

ssDNA to enable its subsequent functionalization in THF and $CHCl_3$.[306] This way we have been able to couple a 5'-amino functionalized DNA with NHS esters or acid chlorides of hydrophobic compounds like pyrene or triphenylphosphine. Additionally, we have been able to perform post-synthetic Sonogashira coupling between a 5-iodouracil base and 1-ethynylpyrene by transferring the DNA into the organic phase this way. One drawback of this method is the very narrow range of surfactants that are suitable for the complexation of DNA, which need to be hydrophilic enough to be soluble in water and hydrophobic enough to precipitate the DNA complex from aqueous solution. To address this problem and widen the scope of possible ligands for the backbone complexation of DNA, we developed a two-step complexation method in 2015.[307] This process starts with the precipitation of DNA through the addition of 4-(hexyloxy)anilinium hydrochloride (ANI-HCl), which can then be exchanged with other amphiphilic amines in organic solvents. This ligand exchange is unlikely to be purely diffusion based, since it is performed in solvents with low dielectric constant, which heavily favor the formation of a contact ion pair between DNA and ANI. Therefore, it has been hypothesized that the ligand exchange is driven by the transfer of a proton from the ANI onto the more basic aliphatic amine. Since its inception, this two-step complexation method has proven a useful tool to obtain complex DNA-based supramolecular assemblies.[308-309]

1.5 Chelator Labels

Chapter 3 presents a DNF based DDS, which is post-synthetically Click-functionalized with the chelator NOTA. This chelator can bind the radionuclides ^{68}Ga and ^{177}Lu in order to enable positron emission tomography (PET) imaging and endogenous radiotherapy respectively. PET is a powerful diagnostic method, which is based on the detection of the gamma radiation that gets emitted during the annihilation reaction between a positron and an electron. Through the application of positron emitting tracers which selectively accumulate in cancer cells, PET can be utilized for the identification of tumors and metastases. A traditional tracer molecule is ^{18}fluoro-2-deoxyglucose (FDG), which accumulates in tumor cells due to their increased metabolic rate and makes them visible for PET due to the positron emission of ^{18}F. Unfortunately, this method is quite unreliable, since FDG also gets taken up by healthy tissues or inflammatory cells like macrophages.[310] To enable the specific uptake of positron emitters into cancer cells, targeting ligands like antibodies, peptides or aptamers can be used. Aptamers are becoming increasingly popular in this field, due to their advantages that have been discussed in **chapter 1.1.3**. In the past decade, ^{68}Ga has become a popular positron emitter for PET imaging, since it is conveniently available through the decay of ^{68}Ge and does not require a cyclotron.[311] For this reason, ^{68}Ga is also used in this work. Other suitable isotopes for PET imaging are ^{99m}Tc, ^{111}In or ^{64}Cu.[312] In order to label targeting agents like aptamers with these radioactive isotopes, they are usually complexed with a chelate ligand, which can then be conjugated to the targeting moiety. Various cyclic and non-cyclic chelators are available[313], but one of the earliest chelators for ^{68}Ga which is still relevant today, is 1,4,7,10-tetraazacyclododecane-1,4,7,10-tetraacetic acid (DOTA).[314]

DOTA coordinates $^{68}Ga^{3+}$ through its 4 nitrogen atoms and 2 of its 4 carboxy groups, leaving 2 carboxy functions to be utilized for conjugation reactions.[315] Typical conjugation methods include coupling amine compounds with DOTA NHS ester[316-318] or other activated esters.[319] These methods have also been used to couple DOTA with Click moieties for subsequent biolabeling[320-321], which resembles the approach that is implemented in **chapter 3**. With time, 2,2′,2"-(1,4,7-triazacyclononane-1,4,7-triyl)triacetic acid (NOTA) has overtaken DOTA as the most popular ^{68}Ga chelator. Chemically, these two compounds are very similar, therefore they

can be conjugated through similar methods and complex $^{68}Ga^{3+}$ through the same functional groups. Even though NOTA has fewer binding sites, it exhibits higher binding affinity for $^{68}Ga^{3+}$ than DOTA, because the smaller ring structure offers a better fit for $^{68}Ga^{3+}$.[322] For larger metals like lanthanoids, the smaller amount of coordination sites can lead to low binding affinity. Therefore NOTA derivates have been developed, which are not conjugated through the acetic acid groups, for example 1,4,7-triazacyclononane-1-glutaric acid-4,7-acetic acid (NOGADA) or NOTA-p-Bn-SCN.[323]

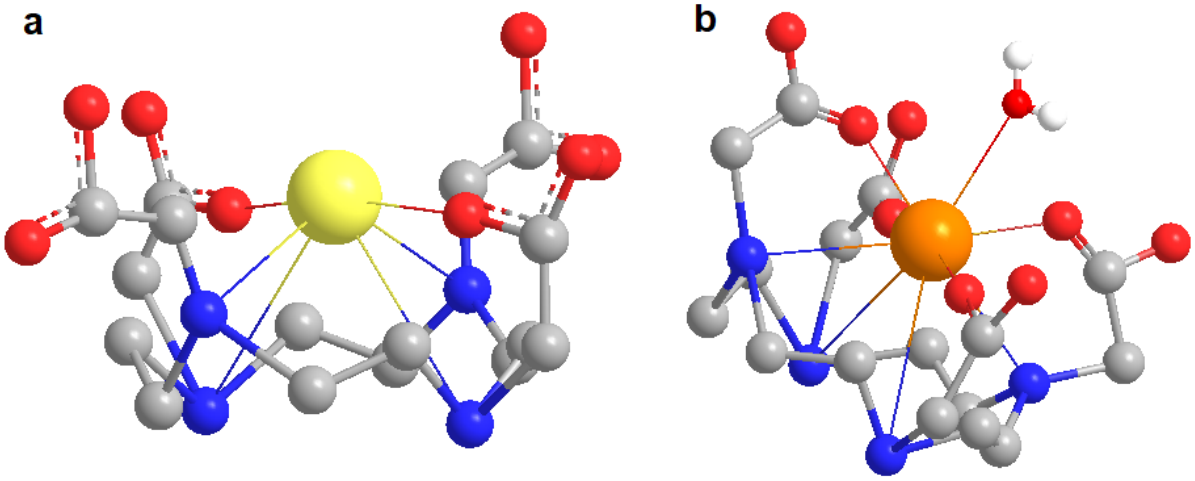

Figure 11. Complexes of DOTA with (**a**) Ga^{3+} ion or (**b**) Lu^{3+} ion.

Due to its ability to penetrate tissues, gamma radiation is very useful for diagnostic applications. For endogenous radiotherapy, alpha and beta radiation are needed, since they actually get absorbed by tissues where they cause ROS mediated DNA damage.[324] Common alpha emitters are ^{225}Ac, ^{212}Pb and ^{211}At[325], and typical beta emitters are ^{90}Y, ^{188}Re or ^{177}Lu[326], the latter is also being used in **chapter 3**. The premier chelate ligand for ^{177}Lu is DOTA, which complexes it with all of its 8 binding sites.[327] Despite its smaller ring size, NOTA can still bind ^{177}Lu, although the stability of the complex is lower compared to DOTA, especially if one of the carboxy groups is used for conjugation reactions. While complex stability is an important consideration, other factors can impact the choice of chelator molecule, for example complexation kinetics and the required temperature.[328] These parameters are typically proportional to the number of coordination sites, which is the reason why DOTA radiolabeling is slow and requires high temperatures. This can cause problems when using radionuclides with a short half-life time, e.g. ^{68}Ga, or heat sensitive ligands, e.g. antibodies.

The high chemical and thermal stability of aptamers compared to antibodies makes them ideal targeting ligands to be radiolabeled. The first radiolabeled aptamer has been the TTA1 aptamer, which has been conjugated with the chelator mercapto-acetyl diglycine (MAG_2) and radiolabeled with ^{99m}Tc.[329] The AS1411 aptamer has also been radiolabeled in various studies, for example with ^{99m}Tc for the PET imaging of prostate cancer[330] and glioblastoma[331] or with ^{64}Cu for the imaging of lung cancer[332] and glioblastoma.[333] Besides the aptamer, the choice of chelator also has a great effect on the pharmacokinetics.[332] Due to their low molecular weight, radiolabeled aptamers still get easily cleared from the bloodstream through renal and hepatic clearance. To mitigate this, radiochelators can be attached to the surface of nanoparticles, which additionally can be decorated with targeting moieties.[334] This approach gets also implemented in **chapter 3**, where a DNF based DDS bearing the AS1411 aptamer is presented, which is radiolabeled through Click chemistry. To achieve this goal, azide functionalized RCA products are synthesized through the addition of N^6-(6-azido)hexyl-dATP

to the RCA reaction mixture. In 2021, Brown and coworkers have already demonstrated the synthesis of modified RCA products and their subsequent Click functionalization.[335] In that study, various 5-modified dUTPs have been used for the introduction of the Click handles into the RCA strands, which have previously been known to be compatible with Φ29 polymerase.[336] In this work, the successful formation of RCA products using an N^6-modified dATP is demonstrated for the first time. These azide-modified RCA products are then decorated with DBCO-NOTA to enable PET imaging with ^{68}Ga and endogenous radiotherapy with ^{177}Lu.

1.6 Hyperpolarization

1.6.1 Nuclear magnetic resonance basics

Nuclear magnetic resonance (NMR) spectroscopy is a powerful tool for the structure elucidation of organic molecules and magnetic resonance imaging (MRI) is a widespread clinical imaging method. Both are based on the physical principle of magnetic resonance, which is explained below.[337] Protons and neutrons are fundamentally characterized by a magnetic spin quantum number m_s. This number can assume the values ½ or -½, which are commonly referred to as “spin up” and “spin down”. Protons and neutrons combine to form the atomic nuclei, which possess a total nuclear spin I. In the case that all protons and neutrons are paired, I assumes a value of 0, and if the number of protons and neutrons is odd, I is a multiple of ½. The number of possible spin states is $2I+1$ and only nuclei with $I > 0$ can be observed by NMR spectroscopy. The most important example is ^{1}H, which has I = ½ and therefore two possible spin states. In the absence of an external magnetic field B_0, these spin states are degenerate, but when the nuclei are exposed to an external magnetic field B_0, the spins orient themselves parallel (α) or antiparallel (β) to B_0 and the energy levels of these states are split up due to the Zeeman effect.

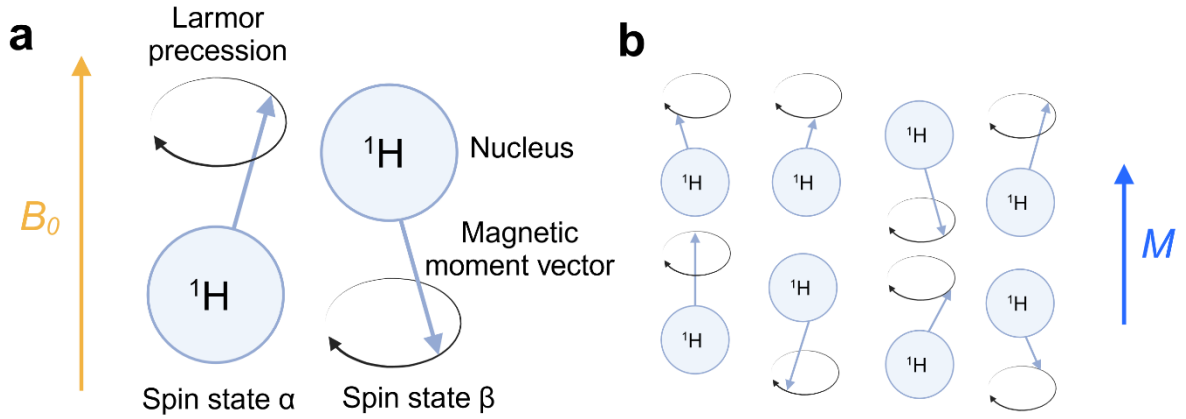

Figure 12. Nuclear magnetization of ^{1}H nuclei resulting from exposure to external magnetic field B_0. (**a**) Spin state α is parallel to B_0, spin state β is antiparallel. The magnetic moment vector M of the nucleus precesses around B_0. (**b**) The α spin state is more populated and the precession of M is phase incoherent. This results in a net magnetization parallel to B_0. Created in BioRender. Rath, W. (2025) https://BioRender.com/i83h987.

The α state is energetically favored, therefore it is more populated, which results in a net nuclear magnetization M in the direction of B_0. Additionally, the magnetic moment vectors of

the nuclei precess around the direction on B_0 at the angular frequency ω (Larmor frequency), which is dependent on the gyromagnetic ratio γ of the nucleus and the strength of B_0. In thermal equilibrium, these precessions are out of phase, therefore the net magnetization M is parallel to B_0, but they can be moved out of equilibrium through nuclear resonance. This occurs when a second magnetic field B_1, which is perpendicular to B_0 and oscillates at ω, is introduced. This causes the precessions of the magnetic moments to be phase coherent, making M rotate around the axis of B_1.

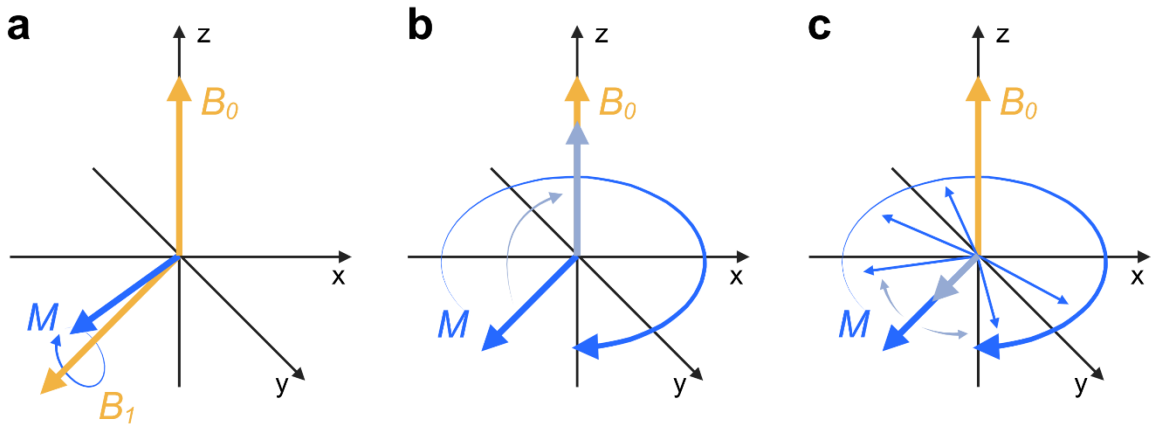

Figure 13. Nuclear resonance and relaxation. (**a**) When B_1 is applied, nuclear resonance occurs and M precesses around B_1. After B_1 is removed, M undergoes longitudinal relaxation (**b**) and transversal relaxation (**c**). Created in BioRender. Rath, W. (2025) https://BioRender.com/x51i344.

After B_1 is removed, M undergoes relaxation into its equilibrium state. During the relaxation process, M rotates around the z-axis of B_0. This rotating magnetization can then induce a signal in an RF coil, enabling signal readout. T_1 is the longitudinal relaxation time that describes the time M takes to return to its original orientation around the z-axis. T_2 is the transversal relaxation time that indicates the return to phase incoherence of the magnetic moment vectors, resulting in a decrease in net magnetization. This decay in magnetization leads to a decreasing signal in the receiver coil, which is referred to as free induction decay (FID). By modulating the frequency of B_1, nuclear resonance can be induced in different nuclei. While the resonance frequency should be identical for the same nuclei in a given magnetic field, it is greatly influenced by the chemical environment in the molecule. A nucleus in an electron dense environment experiences a smaller local magnetic field, a phenomenon called shielding. These changes in resonance frequency are called chemical shift and are a key element for structure elucidation with the help of NMR spectroscopy. Chemical shifts are usually given in parts per million (ppm) in comparison to a reference compound. Besides the shielding effect, nuclear spins are also influenced by nearby nuclei that are covalently bound to it. This effect is called J-coupling and arises from nuclei polarizing the spin of binding electrons, which in turn affect the neighboring nuclei. J-coupling causes signal multiplicity, which informs the observers about the number of neighboring nuclei and therefore is another important factor to infer the molecular structure of the sample.

1.6.2 MRI contrast agents

Most MRI applications utilize ^{1}H-NMR signals to construct accurate images of soft biological tissues. These images are taken in a slice-wise manner. In order to only excite ^{1}H nuclei of a specific slice, a magnetic field strength gradient is applied to B_0 (z-axis), resulting in slight changes in resonance frequency along the gradient.[338-339] Inside of this slice, specific voxels can be excited by applying additional gradients in x- and y-direction. From the signal intensity that is recorded for each voxel, a 2D image can be reconstructed. This signal intensity is mostly determined by the spin density as well as the T_1 and T_2 relaxation times of the ^{1}H nuclei, which can vary whether they are connected to water molecules or to macromolecules like proteins or lipids. ^{1}H nuclei in fats typically exhibit shorter relaxation times compared to water, making them appear brighter during MRI scans. This enables the differentiation of tissues due to their variations in water and fat content.[340] T_1 and T_2 times of ^{1}H nuclei are also dependent on tissue microstructure, which can differ between healthy and pathogenic tissue.[341] The contrast that can be achieved between different tissues is heavily dependent on the field strength of B_0. Routine medical applications nowadays utilize 3 T fields, but field strengths up to 21 T are being researched.[342] To achieve magnetic fields of this strength, superconducting coils with liquid helium cooling (4 K) are necessary, which greatly increases the technical complexity and the operating costs of these imagers. As an alternative to strong magnetic fields, contrast agents can be used to increase the image quality of MRI.[343] Most contrast agents are based on Gadolinium(III), which is complexed by chelate ligands, for example DOTA (see **chapter 1.5**).[344] Gd(III) is a paramagnetic contrast agent, which exhibits high magnetic susceptibility due to its 7 unpaired electrons. This makes Gd (III) based contrast agents especially useful for high-field MRI applications. Other examples of paramagnetic contrast agents are high-spin Mn(II) or Fe(III) complexes. These contrast agents reduce the T_1 and T_2 times of nearby water protons, which in turn increases their brightness during the MRI scan. Gd(III) based contrast agents are routinely used and are generally considered safe, but over the last decade some safety concerns have been raised, regarding the development of nephrogenic systemic fibrosis[345] and the accumulation of Gd(III) in the brain.[346] Therefore alternative contrast agents have to be developed, for example through the use of para-hydrogen induced polarization (PHIP). During PHIP, the magnetization of the substrate is artificially enhanced through the use of para-hydrogen, and is therefore independent of the strength of B_0. This makes PHIP contrast agents especially useful in combination with portable MRI machines, which have to operate at lower magnetic field strength.

1.6.3 Para-hydrogen

Molecular hydrogen (H_2) has a total nuclear spin I of either 0 or 1, which results in four possible spin states: three triplet states with I = 1 and the magnetic spin quantum number m_s = -1, 0 ,1 (ortho-hydrogen), and one singlet state with I = 0 and m_s = 0 (para-hydrogen). The singlet state has slightly lower energy, but at room temperature all spin states are equally populated, resulting in a para-hydrogen content of 25 %. At low temperatures however, ortho-hydrogen slowly converts to para-hydrogen in an exothermic reaction. This poses a challenge during the storage of liquefied hydrogen, since the internal heat liberation of ortho-para conversion leads to the boil-off of hydrogen. Through the addition of a catalyst, the ortho-para conversion can be accelerated to reach the equilibrium state (99.9 % para-H_2 at 21 K) before storage.[347] Typical catalysts for the ortho-para conversion are iron oxide[348] or other metal oxides.[349] Para-H_2 can be stored much longer, which is crucial for its use as spacecraft fuel.[350] High enrichment of para-H_2 is not only desirable for its storage, but is also necessary for PHIP applications.

1.6.4 PHIP

The equilibrium net nuclear magnetizations resulting from the Zeeman effect are less than 10^4 the value that could theoretically be achieved if all spins were parallel to B_0. This fundamentally restricts the signal intensity, and therefore the limit of detection during NMR spectroscopy and MRI imaging. One way of achieving higher non-equilibrium magnetizations is an addition reaction of para-H_2 onto an unsaturated carbon compound. This concept was hypothesized in 1986[351] and experimentally verified in 1987[352] by Weitekamp *et al.*, who termed this concept PASADENA (parahydrogen and synthesis allow dramatically enhanced nuclear alignment). Since then, many variations of this technique have been developed, which are collectively referred to as PHIP.

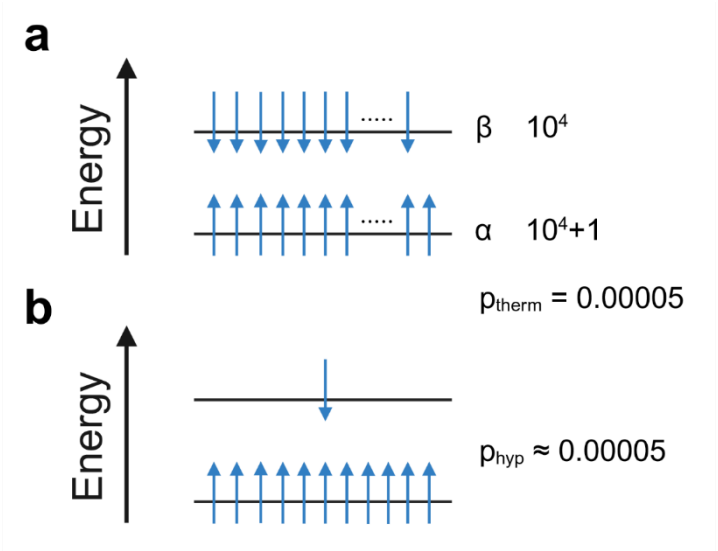

Figure 14. Net nuclear magnetization *M* under (**a**) thermal equilibrium conditions purely due to Zeeman effect or (**b**) PHIP conditions. Created in BioRender. Rath, W. (2025) https://BioRender.com/i75e551.

A simple way to explain the principle of the PASADENA effect is a population model of an AX spin system (see **Figure 15**).[353] In a normal AX spin system, all four states αα, αβ, βα and ββ are almost equally populated. The observed spectral lines correspond to the transitions between these states, resulting in two doublets. Once para-H_2 is introduced into this AX spin system, the αβ and βα states become selectively more populated. This leads to the observation of two antiphase doublets with significantly enhanced signal strength due to the large population differences. It is crucial that the symmetry of the para-H_2 molecule is broken during hydrogenation, so the transition of the spin states from para-H_2 to the AX system is not symmetry-forbidden.

After hydrogenation, this effect lasts until T_1 relaxation is completed, which for most ^{1}H nuclei take a few seconds. Therefore, fast hydrogenation kinetics are important to obtain significant polarization before the system returns to equilibrium. To achieve this, a suitable catalyst has to be chosen, for example [Rh(1,5-cyclooctadiene)(1,2-bis(diphenylphophino)ethane)].[354] The hydrogenation mechanism of this specific complex also ensures that protons are added in a pairwise manner and their spin correlation is maintained, which are important factors for the efficient transfer of hyperpolarization onto the target molecule.[355] The hyperpolarization from hydrogenative PHIP can also be transferred from the para-H_2 protons onto neighboring (hetero)nuclei through J-coupling.[356-357] This is commonly used to enhance the signal intensity during ^{13}C NMR, which is typically low due to the low isotope prevalence of ^{13}C and low gyromagnetic ratio. Similarly, J-coupling can also be exploited to achieve PHIP without directly transferring para-H_2 onto the target molecule. The first non-hydrogenative PHIP method was discovered in 2009 by Williamson *et al.* who coined it SABRE (signal amplification by reversible exchange). During this process, para-H_2 and the substrate reversibly bind to a polarization transfer complex (PTC), for example [Ir(H)$_2$(1,3-bis(2,4,6-trimethylphenyl)imidazolium)(py)$_3$].[358] The J-coupling between the hydride and the substrate through the equatorial plane of the PTC is then strong enough to induce spin-order transfer

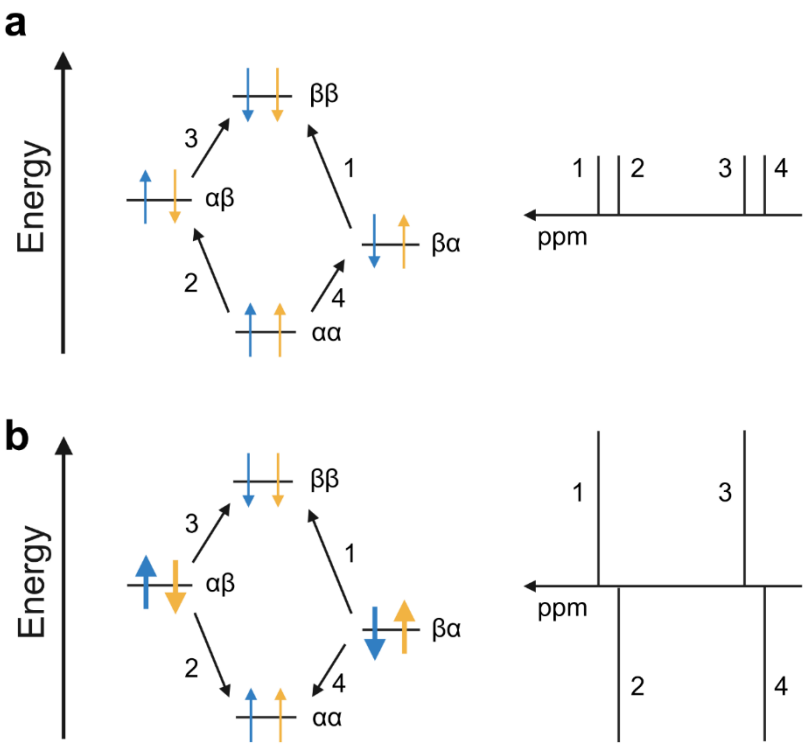

Figure 15. Spin state transitions in an AX spin system and their corresponding spectral lines under (**a**) thermal equilibrium conditions and (**b**) PHIP conditions. Created in BioRender. Rath, W. (2025) https://BioRender.com/n62h032.

onto the substrate. Similar to hydrogenative PHIP, it is important that the symmetry of the hydride spins is broken, which is often achieved through the use of an asymmetric substrate. Since SABRE methods do not alter the substrate permanently, they enable the continuous hyperpolarization of the substrate.[359] SABRE also allows for a wider range of substrate molecules, for example drugs[360-361], since they don't require an unsaturated carbon bond. This is compelling, since hyperpolarization of biologically relevant substrates like drugs or metabolites has attracted more and more attention over the last two decades, since they are a potentially useful tool for bioimaging applications with MRI.

1.6.5 Biocompatible PHIP

Applications of PHIP techniques *in vivo* present some unique challenges. First off, the substrate has to be rapidly separated from the solvent and the catalyst before being administered, for example through precipitation.[362] To avoid organic solvents, water-soluble catalysts for hydrogenative PHIP[363] and SABRE[364-365] have also been developed. Additionally, methods for the efficient removal of the catalyst have been explored, for example through capturing and centrifugation with 3-mercaptopropyl functionalized SiO_2 nanoparticles.[366] Alternatively, heterogeneous catalysts for hydrogenative PHIP[367-369] and SABRE[370-371] have been tested, also in aqueous media. These are promising tools to solve the problem of catalyst removal, but so far, their hyperpolarization efficiency is quite low. Finally, the lifetime T_1 of the hyperpolarized state is a limiting factor. Higher T_1 times are associated with generally stronger hyperpolarization and ensure that the substrates stay polarized until they arrive at the target site. So far, *in vivo* hyperpolarization markers have relied on heteronuclei like ^{13}C[372-373] or ^{15}N[374], which offer reasonably long T_1 times (> 10 s). In order to achieve even longer T_1 times, symmetric molecules that form long-lived spin states like diazirines (^{15}N-^{15}N) can be used for hyperpolarization (T_1 ~ 30 s).[375] Other potential heteronuclei include ^{29}Si (T_1 ~ 1 min)[376] or ^{31}P[377], which has a T_1 time of only 6 s, but still achieves high sensitivity through its high gyromagnetic ratio and 100 % natural abundance.

1.6.6 Targeted MRI

Similar to the targeted imaging applications using radiolabels and PET, which have been discussed in **chapter 1.5**, PHIP can potentially be exploited for targeted imaging applications using MRI. Rudimentary targeting can be achieved with hyperpolarized metabolic agents, which accumulate in cancer cells due to their increased metabolic rate. Analogous to tumor PET imaging with ^{18}F-FDG, various metabolic agents have been hyperpolarized, for example pyruvate[378], succinate[379] or phospholactate[380], which all have been used for *in vivo* imaging already. Since metabolic targeting suffers from low specificity, achieving hyperpolarization of active targeting ligands like peptides or aptamers are high priority goals for the future of the field. Multiple studies have demonstrated hyperpolarization of peptides through hydrogenative PHIP[381-382] or SABRE[383-384], but these methods are far away from *in vivo* applications. Here, we are pioneering the hyperpolarization of DNA. In 2023, Brenske *et al.* demonstrated hydrogenative PHIP of the AS1411 cancer targeting aptamer (see **chapter 1.3.6**).[282] This marks the first time a DNA molecule has been hyperpolarized, since up to that point only SABRE hyperpolarization of adenosine had been shown.[359] In this study, the DNA was labeled with an alkyne function to enable hydrogenative PHIP. To achieve this, different alkyne compounds were conjugated to 5-iodo-deoxyuracil or 8-iodo-deoxyadenosine through Sonogashira coupling (see **chapter 1.4.1**). The signal enhancement for these modified nucleotides was assessed and the best was achieved with 5-ethynyl-deoxyuracil and 5-(3-propargyloxyl-propynyl)-deoxyuridine. Through the use of magnetic field cycling techniques, polarization transfer from the proton onto the alkene or alkane ^{13}C nuclei was possible in order to increase T_1. Polarization transfer onto the quaternary ^{13}C or ^{15}N nuclei of the nucleobase was not possible, due to the necessity of a spacer unit between the PHIP tag and the nucleobase. These modified nucleotides were then incorporated into the aptamer sequence at the 3'-end through phosphoramidite chemistry. The catalytic hydration reaction of the aptamer was performed in methanol, so the DNA backbone was complexed with NH_2-mPEG (see **chapter 1.4.3**) to enable its solubility. The PHIP experiments on the aptamer molecules bearing the 5-ethynyl tag were unsuccessful, likely due to steric effects hindering the binding to the catalyst, and only DNA bearing the 3-propargyloxyl-propynyl tag could be hydrogenated. During these measurements, a 187-fold signal enhancement could be achieved.

This study represents a big milestone towards the development of targeted MRI imaging agents, but the system still faces some problems that are in part addressed in this work. First, bottom up synthesis of PHIP labelled DNA through phosphoramidite chemistry with modified nucleotides requires a lot of effort. In order to reduce this effort, the DNA can be post-synthetically labeled through Click-chemistry (see **chapter 1.4.2**). Also, the T_1 times that were achieved in this study are not long enough for *in vivo* targeting, so PHIP tags need to be designed in a way that enables polarization transfer onto heteroatoms with longer T_1 time. Lastly, the reaction needs to be transferred into aqueous medium, or a method needs to be developed to separate the hyperpolarized DNA from the catalyst and the NH_2-mPEG. This last point is outside the scope of this work, but possibilities to solve the first two issues are discussed in **chapter 4**.

2. Mechanochemical Activation of DNAzyme by Ultrasound

2.1 Aim and Motivation

RNA cleaving DNAzymes are a versatile tool for imaging and therapeutic applications. They enable gene therapy of cancers, due to their ability to degrade mRNA with high sequence specificity. Different tumor related genes can be silenced this way, including the primary oncogenes, drug resistance genes and angiogenesis genes. RNA cleaving DNAzymes are also a popular tool for the detection of metal ions. For this purpose, the DNAzyme-substrate complex is usually pre-formed, and the substrate gets cleaved in presence of the analyte, which acts as the co-factor for the DNAzyme. A common readout method is based on a substrate that is labeled with a fluorescent dye and a quencher, which generates a switch-on fluorescence signal upon being cleaved (catalytic beacon). This sensing strategy is prone to false positive signaling during *in vivo* sensing applications, since the co-factor is present in the biological environment. To prevent this, various strategies have been developed to enable spatio-temporal control over DNAzyme activity. These typically involve the chemical modification of the DNAzyme with a functional group that inhibits its activity and can be cleaved off through an external stimulus like light, heat, enzymes or ROS. This chapter introduces a method to enable spatio-temporal control over DNAzyme activity through US induced mechanical force. US is a superb stimulus for biological systems, due to its non-invasive nature, high penetration depth and accurate spatial and temporal resolution. In spite of this, US has rarely been used in the context of controlling DNAzyme activity. Lu and coworkers developed a system which exploits HIFU induced heating to release a DNAzyme that has been previously deactivated through base pairing with an inhibitor strand.[95] The system introduced here takes advantage of the mechanical effects of US instead of the thermal effects. The use of mechanochemical concepts *in vivo* is an underexplored topic. In traditional mechanochemical systems, covalent bond scission is induced through high intensity, cavitational US, which is incompatible with biological systems. In order to lower the activation barrier of mechanochemical systems, they can be designed with non-covalent sacrificial bonds, for example based on DNA. RCA can be used to generate DNA strands with sufficient molar mass to be US responsive (**Figure 16a+b**). The system presented here utilizes an RCA strand, onto which the DNAzyme is hybridized (**Figure 16b**). With the help of $Mg_2P_2O_7$, the loaded RCA strands then condense into DNFs to deactivate the DNAzyme. When exposed to US, shear forces act on the RCA strand, which leads to the cleavage of the RCA backbone as well as the Watson-Crick base pairing between the RCA strand and the DNAzyme (**Figure 16c**). The free DNAzyme can then bind to a catalytic beacon and catalyze its cleavage, which is observable through an increase in fluorescence (**Figure 16d**).

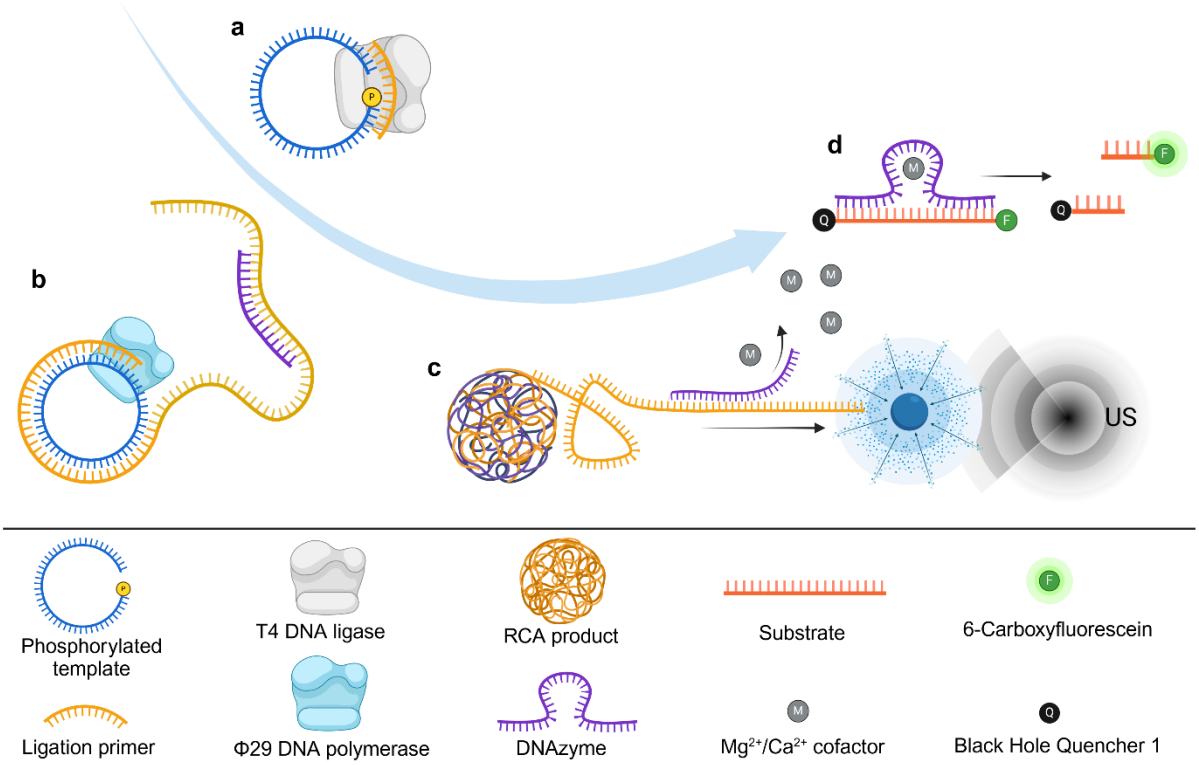

Figure 16. Strategy for controlling DNAzyme activity through US. (**a**) Padlock ligation of RCA template. (**b**) RCA reaction and hybridization of DNAzyme to RCA strand. (**c**) US induced cavitation generates shear forces on RCA strand to release DNAzyme. (**d**) DNAzyme cleaves fluorophore-quencher-labeled substrate, which turns on fluorescence. Created in BioRender. Rath, W. (2025) https://BioRender.com/s99o814.

2.2 Results

2.2.1 DNA Sequence Design and RCA Optimization

The 8-17 DNAzyme (also known as 17E) was used in this study (see **chapter 1.1.4**). The 17E sequence was taken from the literature[385] and slightly altered. First, the side chains were shortened by 5 nucleotides on each side in an effort to promote the release of the DNAzyme from the RCA strand due to the reduced number of base pairing interactions. The sequence of the side chains was also slightly altered to prevent the formation of undesired secondary structures, which were predicted with the help of NUPACK. This modified DNAzyme sequence was used as the basis for the template design, meaning the resulting RCA products contained the reverse complementary sequence. Varying amounts of mismatches with the DNAzyme were introduced into the template to further reduce the binding strength of the DNAzyme to the RCA strand. These mismatches also caused the substrate binding to be energetically favored compared to rebinding of the DNAzyme to the RCA strand. To finish the template design, two primer binding sites as well as poly-A spacers between DNAzyme and primer binding site were added. The final DNA sequences can be found in **Table 1** (*cf* Experimental section).

Next, the padlock ligation of the linear RCA template was performed. The optimal ratio between template and primer strand varies, depending on the template size and primer sequence. Therefore, both strands were mixed in different ratios and annealed by heating to 95 °C for 5 min and slowly cooling down to 16 °C. Afterwards T4 DNA ligase was added, and the mixture was incubated at 16 °C overnight. The circularized templates before and after the addition of T4 ligase were analyzed by agarose gel-electrophoresis (GE) (**Figure 17a**).

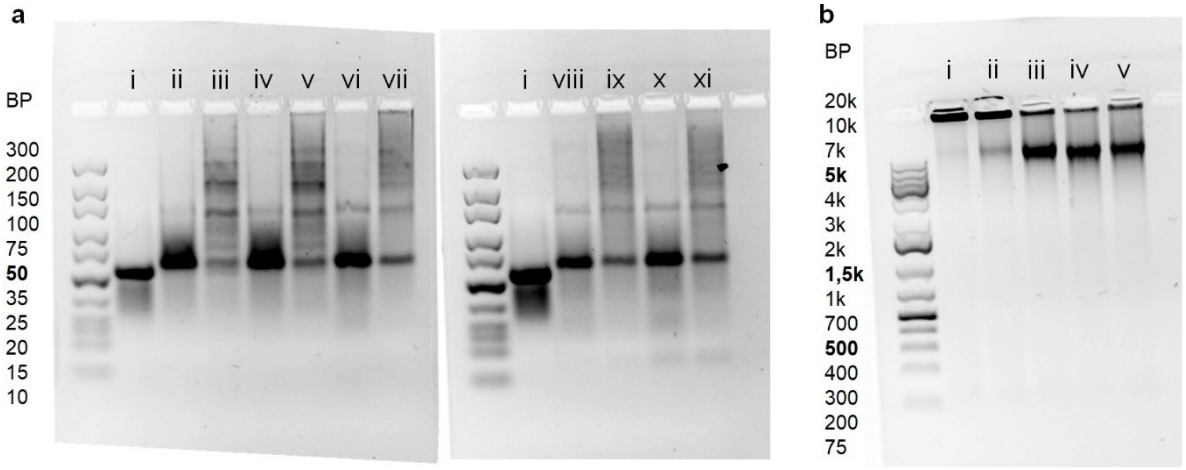

Figure 17. Agarose GE of padlock ligation and RCA reaction. (**a**) Circularized RCA templates with different template:primer ratios before and after addition of T4 ligase, 4 % agarose, ladder: GeneRuler ULR. Lane i: linear template; ii 2:1 ratio, no ligase; iii: 2:1 ratio, after ligation; iv 1.5:1 ratio, no ligase; v: 1.5:1 ratio, after ligation; vi 1:1 ratio, no ligase; vii: 1:1 ratio, after ligation; viii 1:1.5 ratio, no ligase; ix: 1:1.5 ratio, after ligation; x 1:2 ratio, no ligase; xi: 1:2 ratio, after ligation. (**b**) RCA reaction with different template:primer ratios, 0.8 % agarose, ladder: GeneRuler 1kb plus. Lane i: 2:1 ratio, lane ii: 1.5:1 ratio, lane iii: 1:1 ratio, lane iv: 1:1.5 ratio, lane v: 1:2 ratio.

After annealing the linear template and the primer, one main band with slightly lower electrophoretic mobility than the linear template was observed (compare lane i and ii), which confirmed the successful circular hybridization. After the ligation step, multiple bands with significantly lower mobility than the nicked circularized template were observed (compare lane ii and iii). The first band over the nicked circular template represented the ligated circular template, which was less flexible than the nicked circular template and therefore migrated through the gel more slowly. The distinct bands above the ligated circular template indicated the formation of higher aggregates like tetramers or hexamers. Additionally, a background smearing could be observed on all lanes, which hinted at the formation of larger linear aggregates. After successful ligation, the different circular templates were used to perform the RCA reaction, which was also analyzed by agarose GE (**Figure 17b**). In all cases, the RCA products were too large to migrate into the gel and no separation was observed, as is typical for RCA products. In lanes ii-v, the formation of a side product with an approximate size of 20 000 base pairs was observed. This has been reported before in the literature[386], and is most likely caused by attachment of the Φ29 polymerase to the product strand, resulting in the formation of a double-stranded side product. Since this process sequesters Φ29 polymerase and deactivates the reaction, all following experiments were performed with a template:primer ratio of 2:1 to avoid the formation of this side product.

2.2.2 Controlling DNAzyme Kinetics by RCA

To monitor DNAzyme activity, a catalytic beacon labeled with 6-carboxyfluorescein (6-FAM) and Black Hole Quencher 1 (BHQ-1) was used as a substrate (**Table 1**, *cf* Experimental Section). First, the kinetics of the free DNAzyme were tested (**Figure 18a**). For this purpose, varying amounts of DNAzyme were added to a 2 µM solution of the substrate without performing an additional folding protocol for the DNAzyme. At a 1:1 ratio of DNAzyme and substrate, full conversion was reached after about one min, resulting in an approximate 10-fold increase in fluorescence. After reducing the DNAzyme concentration to 1 µM (1:2 ratio), full conversion was reached after 10 min, or in the case of 0.4 µM (1:5 ratio) after 30 min. When further reducing DNAzyme concentration to 0.2 µM (1:10 ratio), fluorescence plateaued before reaching full conversion due to deactivation of the DNAzyme. This indicated that the maximum number of catalytic cycles for this DNAzyme lay between 5 and 10. Additionally, an extended fluorescence kinetic was recorded after reaching full conversion, which revealed an approximate 20 % drop in fluorescence intensity due to photobleaching after 1000 min (**Figure 18b**).

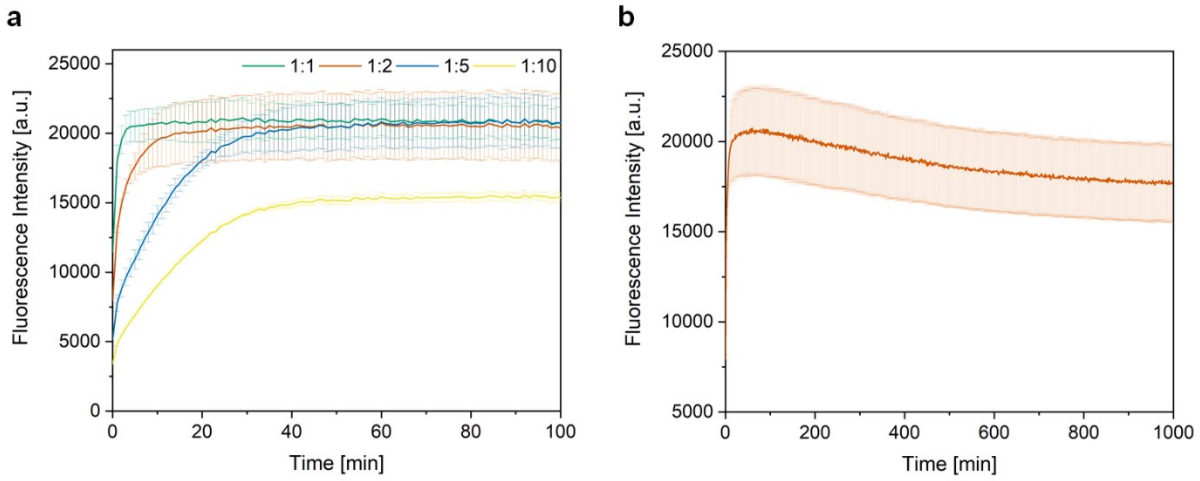

Figure 18. Free DNAzyme kinetics, 2 µM substrate, all data presented as mean ± SD, N = 3 experiments. (**a**) Substrate cleavage kinetics at different DNAzyme:substrate ratios. (**b**) Photobleaching of cleaved substrate during long-time fluorescence measurement.

Next, the DNAzyme was hybridized with the DNFs to investigate the influence of this process on the DNAzyme kinetics. Interestingly, almost no effect was observed after adding the DNAzyme to the DNFs post-synthetically and performing an annealing protocol (**Figure 19a**). The most likely explanation for this was that the RCA strand was inaccessible for hybridization, since it was adsorbed to the $Mg_2P_2O_7$ core of the DNFs. In this state, the DNA was highly condensed and could not be denatured sufficiently through the typical denaturing step of heating to 95 °C for 5 min. To prevent this problem, the DNAzyme was added directly to the RCA reaction mixture, so it can hybridize *in situ* with the newly synthesized RCA strand before being condensed into DNFs. This method yielded a significant decrease in catalytic activity (**Figure 4a**) therefore it was used for all future experiments.

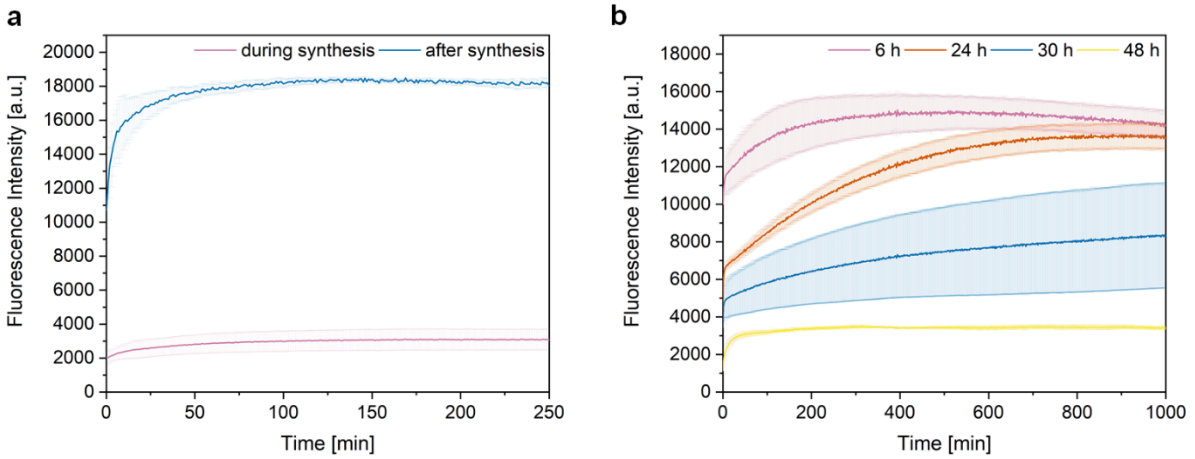

Figure 19. DNAzyme deactivation through loading onto DNFs, 2 µM substrate, 8 µM DNAzyme, all data presented as mean ± SD, N = 3 experiments. (**a**) Fluorescence kinetics after loading DNAzyme onto DNFs during or after synthesis. (**b**) Influence of RCA reaction time on DNAzyme deactivation.

To optimize the deactivation process, the influence of RCA reaction time, number of mismatches on the template and DNAzyme concentration were systematically investigated. The influence of the RCA reaction time at a constant DNAzyme concentration of 8 µM and a template with two mismatches is shown in **Figure 19b**. After 6 h reaction time only a minimal effect could be observed and reliable deactivation was achieved after 48 h, which was used for all following experiments. This is much longer than the time required for the actual RCA reaction, which should be finished after 10 h (using 900 pmol dNTPs and 30 U Φ29 polymerase), according to the manufacturer of the RCA kit. This hints at the possibility, that the slower condensation process of DNA into DNFs with the help of $Mg_2P_2O_7$ plays a big role in the deactivation process in addition to base pairing. During the RCA process, the viscosity of the solution also increased, which slowed down RCA kinetics and might explain the long reaction time required for deactivation. The high viscosity could also play a role in the deactivation process by hindering substrate diffusion.

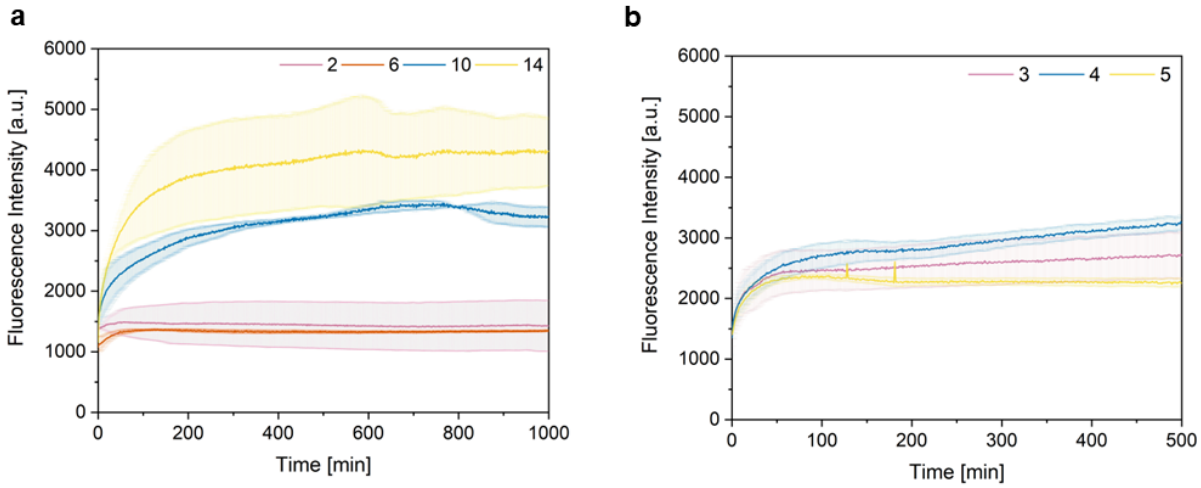

Figure 20. Influence of mismatches on DNAzyme deactivation, 2 µM substrate, 8 µM DNAzyme, all data presented as mean ± SD, N = 3 experiments. (**a**) 2, 6, 10 or 14 mismatches. (**b**) 3, 4 or 5 mismatches.

Next, the influence of the mismatches between the RCA strand and the DNAzyme was investigated (**Figure 20**). Reliable deactivation was possible with up to 6 mismatches, but with 10 or 14 mismatches a 2-3-fold increase in fluorescence was observed. This proves that besides the DNF condensation process, Watson-Crick base-pairing between RCA strand and the DNAzyme plays a significant role during the deactivation process. In the case of 10 or 14 mismatches, the DNAzyme probably got released through spontaneous strand displacement, since binding of the DNAzyme to the substrate is energetically favored compared to the RCA strand. Also, since the mismatches were placed at the ends of the DNAzyme strand, the substrate strand had a place to attach and start the strand displacement process. Since reliable deactivation could be achieved with 2 and 6 mismatches, this amount was used for the following experiments.

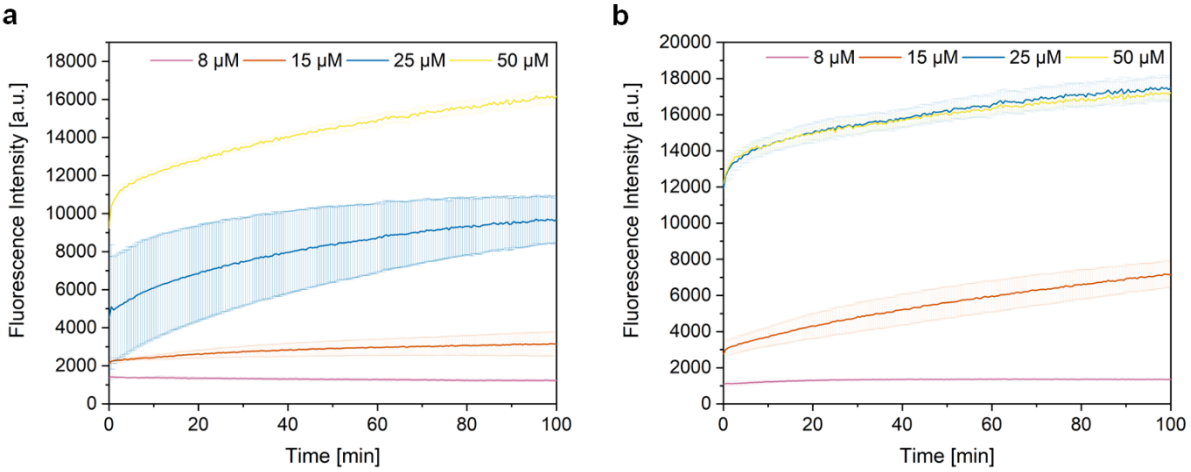

Figure 21. DNAzyme deactivation after loading increasing amounts of DNAzyme, 2 µM substrate, all data presented as mean ± SD, N = 3 experiments. (**a**) 2 mismatches. (**b**) 6 mismatches.

Finally, the deactivation process was tested for increasing amounts of DNAzyme with templates containing 2 mismatches (**Figure 21a**) and 6 mismatches (**Figure 21b**). In the case of 2 mismatches, almost full deactivation was observed after increasing DNAzyme concentration from 8 µM to 15 µM, but after further increasing the concentration to 25 µM significant DNAzyme leakage was observed. The template with 6 mismatches exhibited worse deactivation performance and leakage was already observed at an DNAzyme concentration of 15 µM. To ensure consistent full deactivation, a DNAzyme concentration of 8 µM was used for all following experiments. After the deactivation protocol was optimized, the DNAzyme-loaded DNFs were characterized through scanning electron microscopy (SEM) (**Figure 22**). The SEM images revealed particles with an average diameter of 4.72 ± 2.40 µm and a sponge-like morphology which is typical for DNFs. **Figure 22b** also shows a film covering the surface of the particles, which likely consisted of excess DNA adsorbed to the surface of the $Mg_2P_2O_7$ particles. This film probably also promoted the aggregation of the particles (**Figure 22c**).

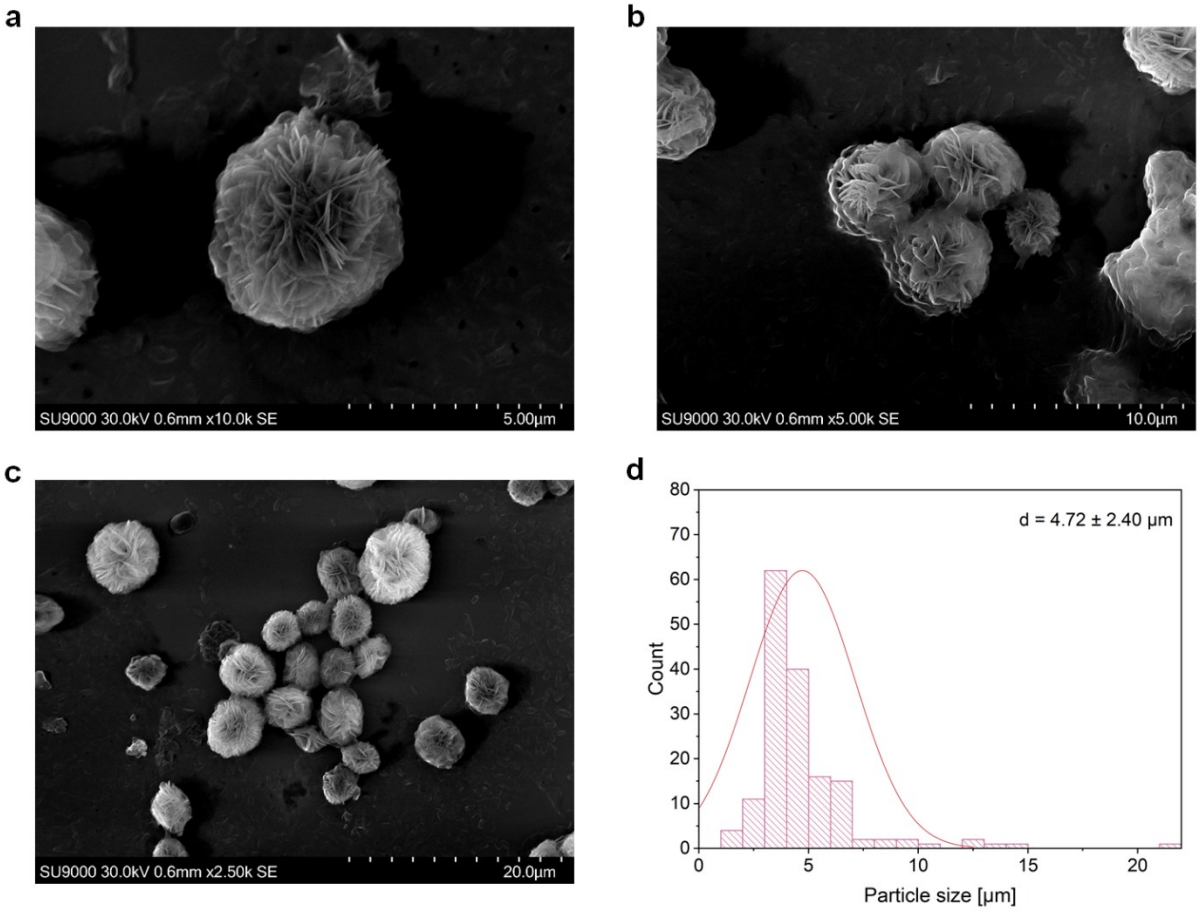

Figure 22. Representative SEM images of loaded DNFs before sonication. (**a**) 10 000 x magnification. (**b**) 5 000 x magnification. (**c**) 2 500 x magnification. (**d**) Particle size histogram, diameter presented as mean ± SD, N = 160 particles.

2.2.3 Mechanochemical Release of DNAzyme by Ultrasound

After establishing a solid protocol for the deactivation of the DNAzyme, its release through cavitational US and subsequent recovery of catalytic activity was investigated. For this purpose, the loaded DNFs and the substrate (2 µM) were added to the DNAzyme buffer and the mixture was sonicated with a 20 kHz immersion sonicator to form the active DNAzyme-substrate complex *in situ*. Different sonication times between 2 and 20 min were tested, during which the mixture was cooled with ice, resulting in a maximum observed temperature of 6 °C directly after sonication (**Figure 23a**). Afterwards, the DNFs were analyzed by agarose GE (**Figure 23b**). The gel revealed a sonication time dependent decrease in DNA chain length, which was caused by cavitation induced bond scission of the DNA backbone. With increased sonication time, the size distribution got narrower and its maximum approached a cut-off size of approximately 200 base pairs, which we also observed in our previous work.[173] At this length, the DNA was no longer US responsive. The exact length of the DNA fragments was determined by quantifying the intensity of the bands using the ImageJ gel analysis tool and plotting it against the number of pixels in elution direction (**Figure 23c**). The local maxima of the ladder bands were then used to correlate the number of pixels with the DNA chain length in base pairs, which exhibited a linear relationship in the bottom part of the gel. (**Figure 23d**) The minimum chain length found this way after 20 min sonication was 225 base pairs.

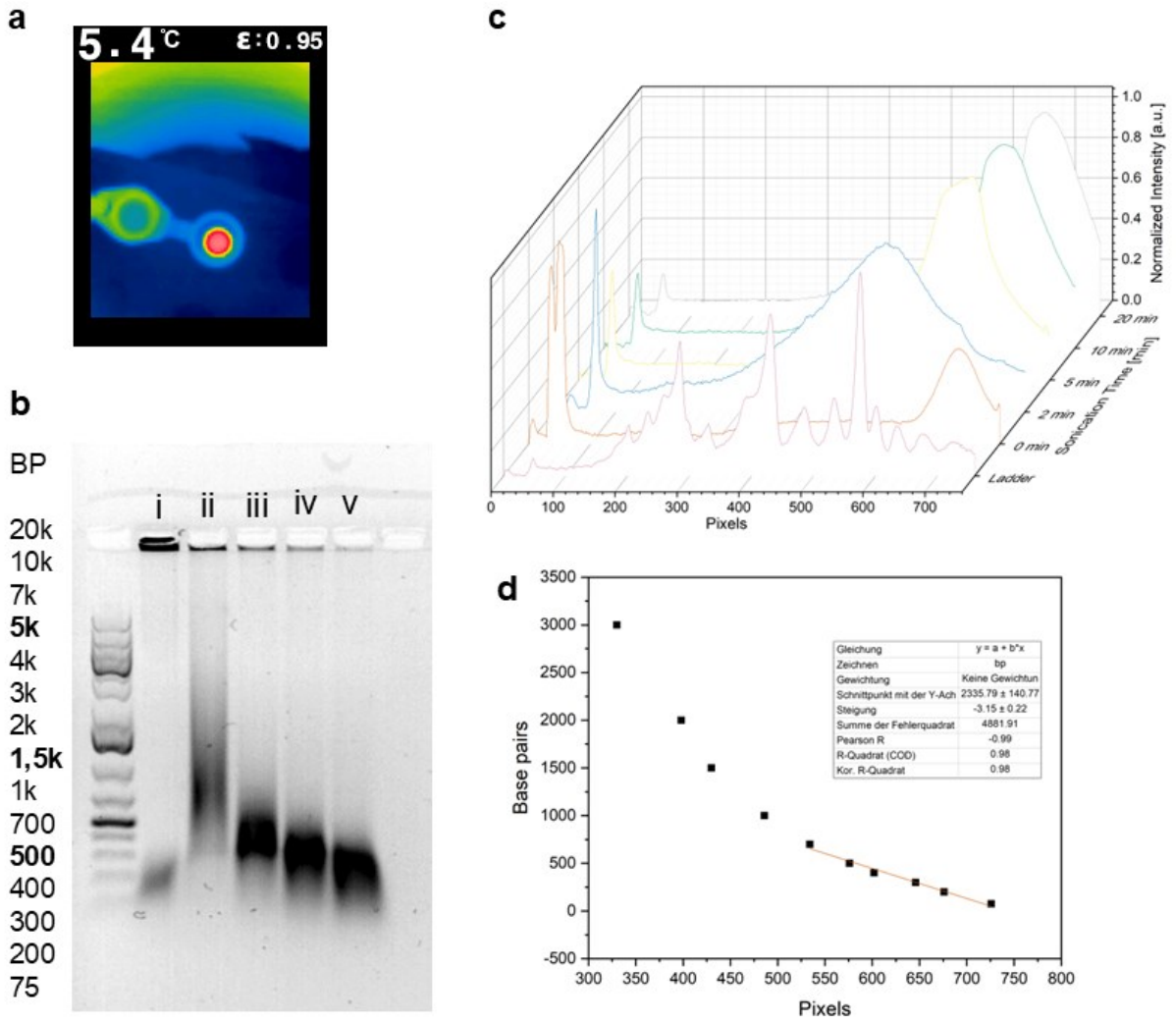

Figure 23. Influence of 20 kHz sonication on DNFs. (**a**) Thermal image of reaction mixture directly after sonication. (**b**) Agarose GE of DNFs after sonication, 0.8 % agarose, ladder: GeneRuler 1kb plus, lane i: 0 min sonication, ii: 2 min, iii: 5 min, iv: 10 min, v: 20 min. (**c**) Normalized intensity of GE bands plotted against pixels in elution direction (y-axis). (**d**) Calibration curve correlating pixels in elution direction to DNA chain length, local maxima after sonication were found at 647 bp (2 min), 338 bp (5 min), 301 bp (10 min) and 225 bp (20 min).

The influence of sonication on the DNFs was also investigated by SEM (**Figure 24**). The images showed a decrease in average particle diameter to 2.63 ± 0.70 µM (**Figure 24d**) and a change in morphology from spherical to oval (**Figure 24a+b**) or irregular shapes (**Figure 24c**). Additionally, no aggregation of particles was observed, opposed to the pre-sonication images (**Figure 22**). This is consistent with the GE results, since aggregation was previously attributed to the presence of large DNA strands adsorbed to the surface of the $Mg_2P_2O_7$ particles.

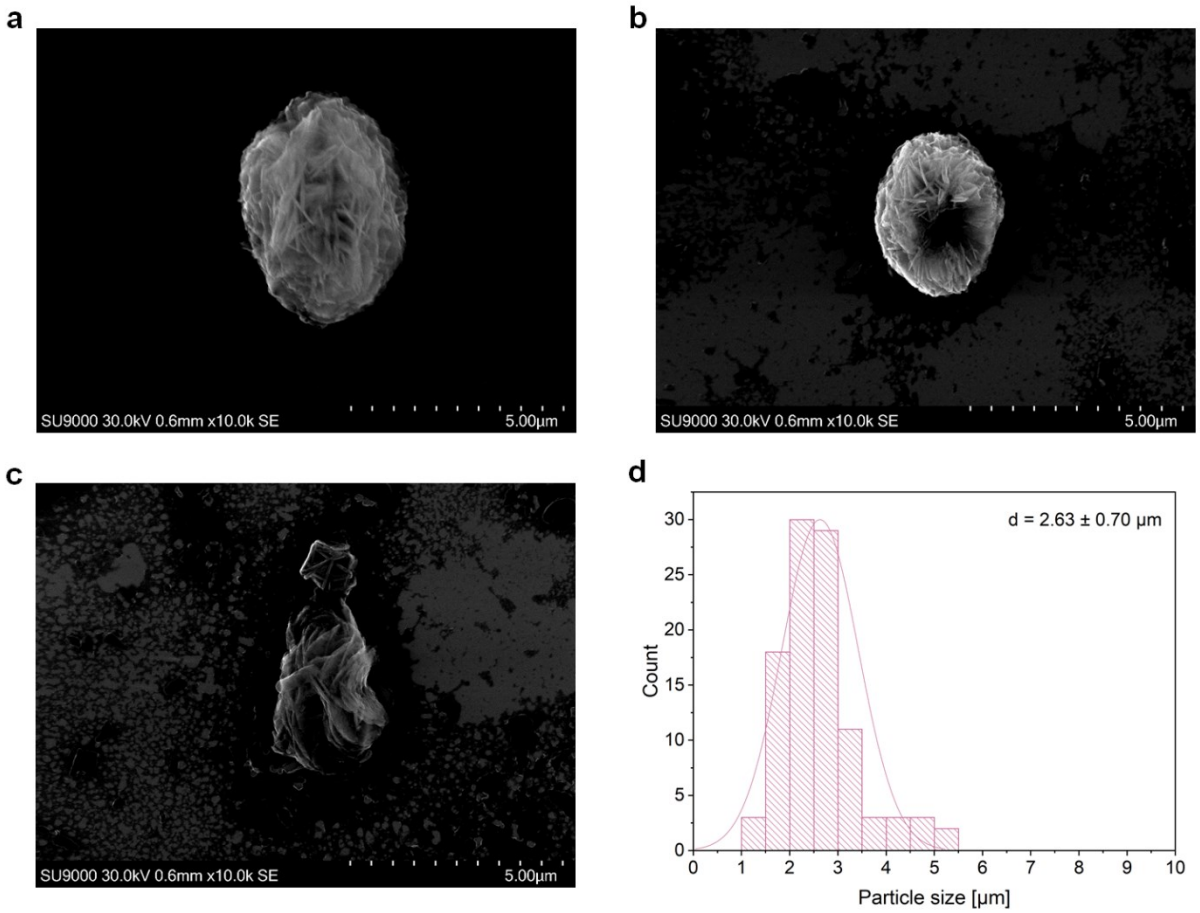

Figure 24. Representative SEM images of loaded DNFs after 20 kHz sonication. (**a-c**) 10 000 x magnification. (**d**) Particle size histogram, diameter presented as mean ± SD, N = 100 particles.

After confirming the degradation of DNFs through US, the release of the DNAzyme and subsequent recovery of its catalytic activity was tested through fluorescence measurements. **Figure 25a** shows the fluorescence kinetics after sonication of loaded DNFs bearing 2 mismatches for 2 to 20 min in the presence of the substrate (2 µM). The first striking observation was that no gradual increase in fluorescence could be observed over time, as would be expected if the active DNAzyme was present in the mixture. Instead of an increase in fluorescence, a slight drop-off in fluorescence was observed, likely due to photobleaching (compare **Figure 18b**). The negative control sample without DNAzyme also demonstrated that the substrate was indeed cleaved catalytically and not through cavitation effects. This means that the DNAzyme must have been present during sonication but got deactivated afterwards. A possible mechanism that explains this behavior is the rebinding of the DNAzyme to the RCA strand. During the sonication process, the DNAzyme could have been continuously re-released, but once the RCA fragments reached the cut-off size and were no longer US responsive, the DNAzyme would have gotten permanently deactivated. Due to the abundance of RCA fragments, rebinding to them would have been kinetically favored over substrate binding, even though the mismatches caused the substrate binding to be energetically favored.

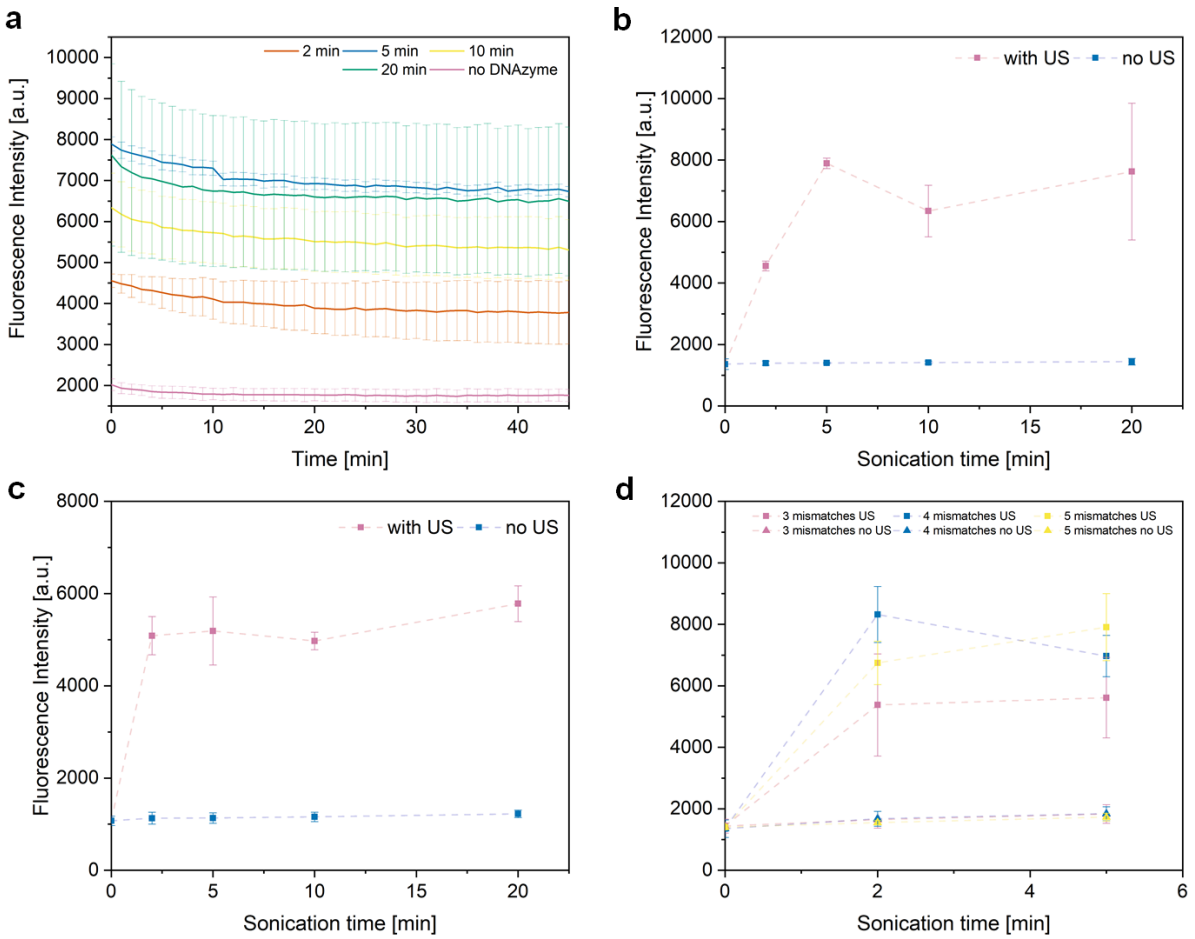

Figure 25. DNAzyme activation through 20 kHz sonication, 2 µM substrate, 8 µM DNAzyme, all data presented as mean ± SD, N = 3 experiments. (**a**) Fluorescence kinetics after increasing sonication time. (**b**) Maximum observed fluorescence after increasing sonication time, 2 mismatches. (**c**) Maximum observed fluorescence after increasing sonication time, 6 mismatches. (**d**) Maximum observed fluorescence after increasing sonication time, 3, 4, 5 mismatches.

Figure 25b-d shows the maximum fluorescence intensity that was reached after sonicating the loaded DNFs with 2-6 mismatches in the presence of the substrate (2 µM) for 2 to 20 min. The sample with 2 mismatches reached its maximum intensity after 5 min sonication, while the samples with 3,4,5 or 6 mismatches reached their maximum intensity after 2 min already. This demonstrates that an increasing number of mismatches accelerates the release process without having a significant influence on the maximum conversion that can be reached, which was 30-40 % in all cases. This ceiling of the maximum conversion could be explained by the fact that the RCA strands are already heavily fragmented after only 5 min sonication (compare **Figure 8b**), and therefore rebinding of the DNAzyme is heavily favored over substrate binding.

In order to support the rebinding hypothesis, the DNAzyme was also activated through a thermal release process. During this process the RCA strands are not fractured and are still present as highly condensed DNFs. Therefore, rebinding is less favored compared to the sonication method. The fluorescence kinetics after heating the loaded DNFs in the presence of the substrate (2 µM) are shown in **Figure 26**. Qualitatively, a constant increase in fluorescence intensity was observed after heating, suggesting the DNAzyme was still present in solution and did not rebind to the DNFs. The difference between DNFs with 2 and 6

mismatches was also more pronounced compared to US activation. With 6 mismatches, a total conversion of approx. 85 % was already achieved after heating to 50 °C (**Figure 26a**), while with two mismatches only approx. 30 % were achieved after heating to 100 °C (**Figure 26b**). Since the kinetic profile differs so strongly between US- and heat-triggered release, it is likely that the release during sonication is mediated through cavitation forces and not the thermal effects of US. The US release was characterized by constant fluorescence intensity after sonication and limited maximum conversion. This was consistent with constant rebinding to the RCA strand and a mechanochemical release mechanism, which stops being effective after reaching the cut-off length. If the US-triggered release were mediated through thermal effects, a longer sonication time would likely be directly correlated with higher fluorescence intensity, since a constant re-release would be possible regardless of chain length.

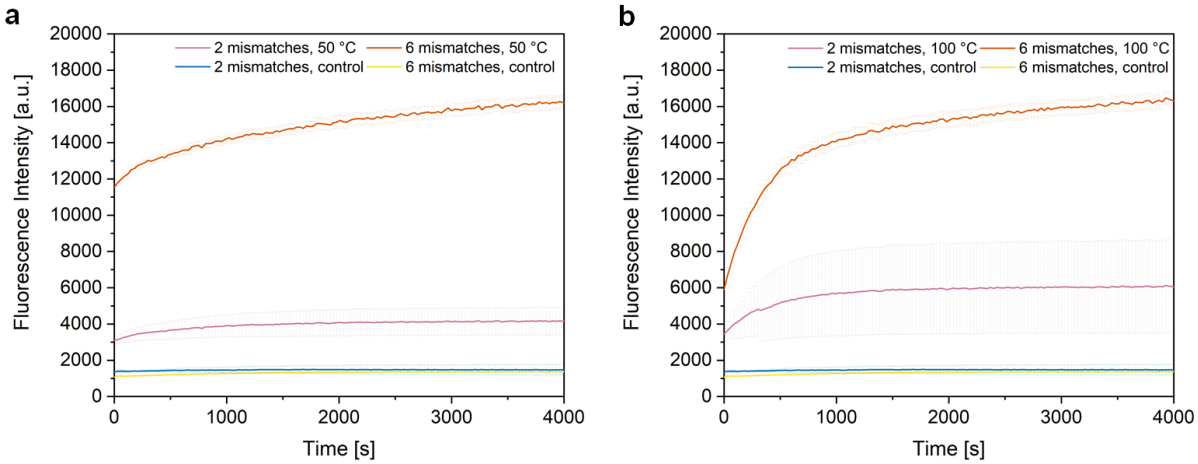

Figure 26. DNAzyme activation through heating, 2 µM substrate, 8 µM DNAzyme, all data presented as mean ± SD, N = 3 experiments. (**a**) 50 °C. (**b**) 100 °C.

After successfully demonstrating DNAzyme release with 20 kHz US, the activation process was also tested with HIFU, which has a lower MI due to its higher frequency (see **chapter 1.2.4**). For this purpose, the samples were exposed to HIFU with a frequency of 0.66 MHz and a focal pressure of 1940 kPa for 10 min (**Figure 27**). These parameters resulted in an MI of 2.38, compared to the 20 kHz US with an MI of 20.46 (*cf* Experimental section). The fluorescence kinetics after HIFU sonication are shown in **Figure 27a**, which exhibit no increase in fluorescence intensity similar to the 20 kHz experiments. This suggests that, even at the lower MI, the DNAzyme release during HIFU sonication is mediated through the mechanochemical pathway rather than the thermal effects. The mismatches also played a larger role compared to the 20 kHz sonication, since with 2 mismatches no activation was observed, while at 6 mismatches a total conversion of approx. 10 % was achieved.

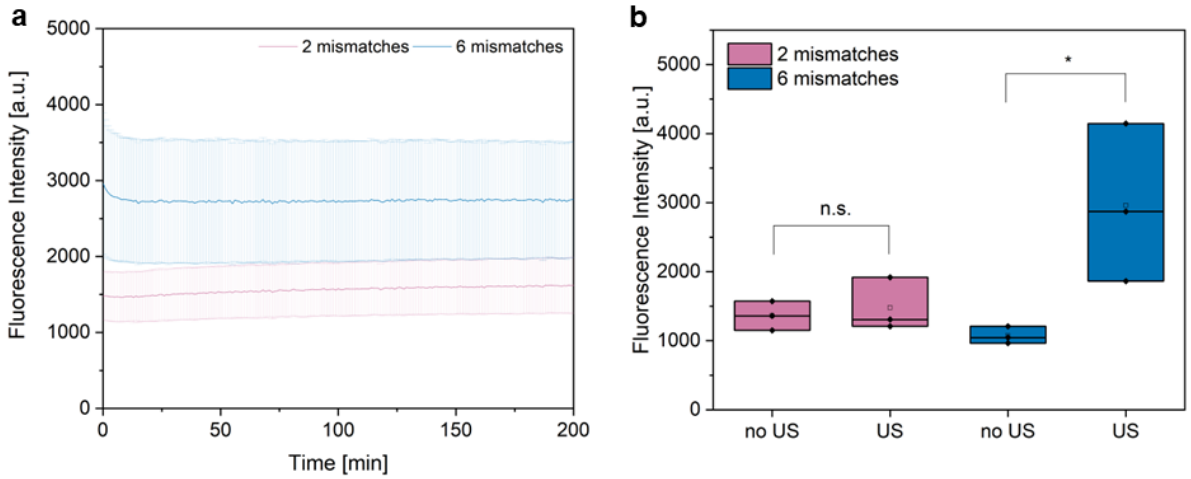

Figure 27. DNAzyme activation after 10 min 0.66 MHz sonication, 2 µM substrate, 8 µM DNAzyme, all data presented as mean ± SD, N = 3 experiments, p = 0.047, calculated through an unpaired two sample t-test, *p ≤ 0.05. (**a**) DNAzyme kinetics after HIFU sonication. (**b**) Maximum fluorescence intensity after HIFU sonication.

2.3 Discussion and Outlook

This chapter presents a novel approach of controlling the activity of a DNAzyme by loading it onto DNFs and releasing it through the mechanochemical effects of US. The deactivation through loading the DNAzyme onto DNFs has proven to be very reliable, even though it is solely based on non-covalent interactions. The release of the DNAzyme could also be reliably achieved with 20 kHz US and was also possible with HIFU. The biggest achievement of this study is the insight into the release mechanism, which was mediated through a cavitation-induced mechanochemical pathway. This release mechanism is clearly distinct from the similar system demonstrated by Lu and coworkers[95], which relied on the thermal effects of HIFU to release a DNAzyme. Beyond acting as a model system for the release mechanism, DNAzyme loaded DNFs have potential to be adapted for *in vivo* applications, since they are non-toxic and are capable of being activated with HIFU. In this study, HIFU with an MI of 2.38 was used, which is still slightly above the threshold of 1.9 to be considered safe for applications in biological systems. To further decrease the activation barrier and enable DNAzyme release with even weaker US, the number of mismatches on the RCA strand can be further tuned, for example by testing the range of 7 to 9 mismatches. By evenly distributing the mismatches across the whole sequence, instead of placing them all at the ends, spontaneous strand displacement can possibly be suppressed even further, enabling the use of even more mismatches or higher DNAzyme concentrations. Once the activation barrier is tuned to accommodate biocompatible US, this DNF based system could be utilized for controlled *in vivo* bioimaging or gene silencing. These applications would benefit from this mechanochemically release mechanism, since it enables short sonication times and does not require prolonged hyperthermia. *In vivo* applications are also typically hindered by low cellular uptake of the DNAzyme. As demonstrated in **chapter 3**, this DNF based system could help to solve this problem by encoding an aptamer sequence onto the RCA template to facilitate receptor mediated cell uptake. DNF based DNAzyme delivery systems are also appealing, since they additionally deliver the Mg^{2+} cofactor, which is typically not abundant enough in cells. To increase the lifetime of the DNAzyme for *in vivo* applications, using chemical sugar- or backbone-modifications should be considered.

2.4 Experimental

General Materials

All oligonucleotides were purchased from Biomers. The sequences are listed in **Table 1**, with the mismatches on the RCA template marked in bold. T4 DNA ligase and 10X ligation buffer were purchased from Thermo Fisher. Φ29 polymerase and 10X polymerase buffer were purchased from Biosearch Technologies. Tris and boric acid were purchased from Thermo Fisher. EDTA disodium dihydrate was purchased from Sigma. ROTI GelStain Red was purchased from Carl Roth. All experiments were performed with ultrapure water (18.2 MΩ cm) from a PURELAB Chorus 1 system by Elga.

Table 1. DNA sequences **chapter 2**.

Name)	Sequence (5'→3')
17E DNAzyme	GCC ATC TTC TCC GAG CCG GTC GAA ATA CTG ACT
17E Substrate	6-Fam – AGT CAG TAT rAGG AAG ATG GC – BHQ-1
RCA Template 1	P - CCC TCT CTC CTC AAA AAA AAA AAA **T**CC ATC TTC TCC GAG CCG GTC GAA ATA CTG AC**A** AAA AAA AAA AAA CTC CTC CTG ACT
RCA Template 2	P - CCC TCT CTC CTC AAA AAA AAA AAA **TG**C ATC TTC TCC GAG CCG GTC GAA ATA CTG AC**A** AAA AAA AAA AAA CTC CTC CTG ACT
RCA Template 3	P - CCC TCT CTC CTC AAA AAA AAA AAA **TG**C ATC TTC TCC GAG CCG GTC GAA ATA CTG A**TA** AAA AAA AAA AAA CTC CTC CTG ACT
RCA Template 4	P - CCC TCT CTC CTC AAA AAA AAA AAA **TGG** ATC TTC TCC GAG CCG GTC GAA ATA CTG A**TA** AAA AAA AAA AAA CTC CTC CTG ACT
RCA Template 5	P - CCC TCT CTC CTC AAA AAA AAA AAA **TGG** ATC TTC TCC GAG CCG GTC GAA ATA CTG **GTA** AAA AAA AAA AAA CTC CTC CTG ACT
RCA Template 6	P - CCC TCT CTC CTC AAA AAA AAA AAA **TGG CG**C TTC TCC GAG CCG GTC GAA ATA C**AC GTA** AAA AAA AAA AAA CTC CTC CTG ACT
RCA Template 7	P - CCC TCT CTC CTC AAA AAA AAA AAA **TGG CGA A**TC TCC GAG CCG GTC GAA AT**G TAC GTA** AAA AAA AAA AAA CTC CTC CTG ACT
RCA Primer	GAG GAG AGA GGG AGT CAG GAG GAG

Padlock Ligation

The ligation was performed with a total reaction volume of 60 µL in 1X ligase buffer, containing 40 mM Tris-HCl, 10 mM $MgCl_2$, 10 mM DTT, and 0.5 mM ATP at pH 7.8. A template concentration of 40 µM and a primer concentration of 20 µM were used. The two strands were annealed by heating to 95 °C for 5 min, then cooling down by 1 °C every 2.5 min to 16 °C (standard annealing protocol). Afterwards, 10 U of T4 ligase were added and the mixture was incubated at 16 °C overnight. The ligation product was used without further purification. GE was performed in TBE buffer (89 mM Tris, 89 mM boric acid, 2 mM EDTA, pH = 8,0) and

staining was performed with ROTI GelStain Red. Gel images were inverted using ImageJ and the contrast was enhanced to 2 % saturated pixels.

RCA

RCA was performed at a total reaction volume of 60 µL in 1X polymerase buffer, containing 50 mM Tris-HCl, 10 mM $(NH_4)_2SO_4$, 4 mM DTT, and 10 mM $MgCl_2$ at pH 7.5. 10 µL of the ligation mixture were used. A total dNTP concentration of 15 mM was used, and the mixture of nucleotides was adjusted to the template sequence. The DNAzyme was added at a concentration of 26.7 µM, so the final concentration of 8 µM was reached at a volume of 200 µL. Finally, 30 U of Φ29 polymerase were added and the mixture was incubated at 30 °C for 48 h. GE was performed as described above.

DNAzyme Activity Assays

All fluorescence measurements were performed with a SpectraMax M3 microplate reader by Molecular Devices. The wavelength settings were λ_{exc} = 495 nm and λ_{em} = 525 nm and the PMT gain was set to medium with 6 flashes per read. The DNAzyme activity assays were performed in a buffer containing 50 mM Tris, 6.25 mM $CaCl_2$, and 2.75 mM $MgCl_2$ at pH 7.9 with a total volume of 200 µL and a substrate concentration of 2 µM.

Release Experiments

Sonication experiments were performed under the same conditions as the activity assays, except the total volume was scaled up to 500 µL and the RCA reaction volume was scaled up to 150 µL. Sonication was performed with a Qsonica Q125 sonicator with a 3 mm probe (A12627PRB20). The frequency was 20 kHz with a pulse setting of 2 s on, 1 s off and the amplitude was set to 60%, resulting in a power density of 5.66 W cm^{-2} (2.89 MPa). The mixture was cooled with an ice bath, and the temperature was monitored with a FLIR TG165 thermal camera. After sonication, GE was performed as described above and the band intensity was determined using the gel analysis tool in ImageJ. The plots were normalized to their individual maximum. For the thermal release experiments, 200 µL solution was heated for 10 min to 50 °C or 100 °C, respectively. HIFU experiments were performed with a 0.66 MHz HIFU transducer by Precision Acoustics submerged in a water tank. The transducer was connected to a 33500B waveform generator by Keysight and an AG1021 amplifier by T&C Power Conversion. Furthermore, the HIFU setup was equipped with a DSOX3024T oscilloscope and a needle hydrophone by Precision Acoustics. 200 µL samples were prepared as described above in a Lumox 96 well plate with foil bottom by SARSTEDT and sealed with a 4titude moisture barrier seal. The bottom of the well plate was immersed in the water tank and sonicated for 10 min with a power density of 126.3 W·cm^{-2} (1.94 MPa) at the focal point.

Scaning Electron Microscopy

Samples (1-5µL) were applied to a silicon wafer and dried at room temperature over night. The wafer was attached to the sample holder using carbon tape and the sample was coated with ~3 nm carbon using a Leica EM ACE600 sputter coater. Measurements were performed on a Hitachi SU9000 electron microscope using a secondary electron detector. An acceleration voltage of 30 keV at 10 µA was used. Particle diameters were measured using ImageJ.

Statistical Analysis

All data in Figures 18, 19, 20, 21, 25, 26 and 27 were presented as mean ± SD, n = 3. Statistical significance in Figure 27 was determined using an unpaired two sample t-test (P = 0.047), where significance was defined as $P \leq 0.05$. Statistical analysis was performed using OriginPro 2018b.

3. Click-functionalized DNFs for Targeted Cancer Theranostics

3.1 Aim and Motivation

This chapter presents the development of a novel DNF based theranostic platform for the treatment of glioblastoma through synergistic chemo- and radiotherapy. Glioblastoma is one of the most aggressive cancer types with a high recurrence rate. In order to boost the efficacy of chemotherapeutics for the treatment of glioblastoma, targeted DDSs have to be used. In this case, the AS1411 aptamer is used as a targeting moiety, which binds to nucleolin, a protein that is overexpressed on the surface of various cancer types, including glioblastoma. Due to its G-quadruplex structure, the AS1411 aptamer can also be loaded with the anticancer drug Dox through intercalation. Aptamer based systems often are limited by rapid renal clearance and nuclease degradation. By using an aptamer bearing RCA polymer instead of an oligomeric aptamer, renal clearance can be avoided through the increase in molecular weight above the glomerular filter threshold, and nuclease degradation is reduced since the RCA strand exhibits fewer nicking sites and is highly condensed.

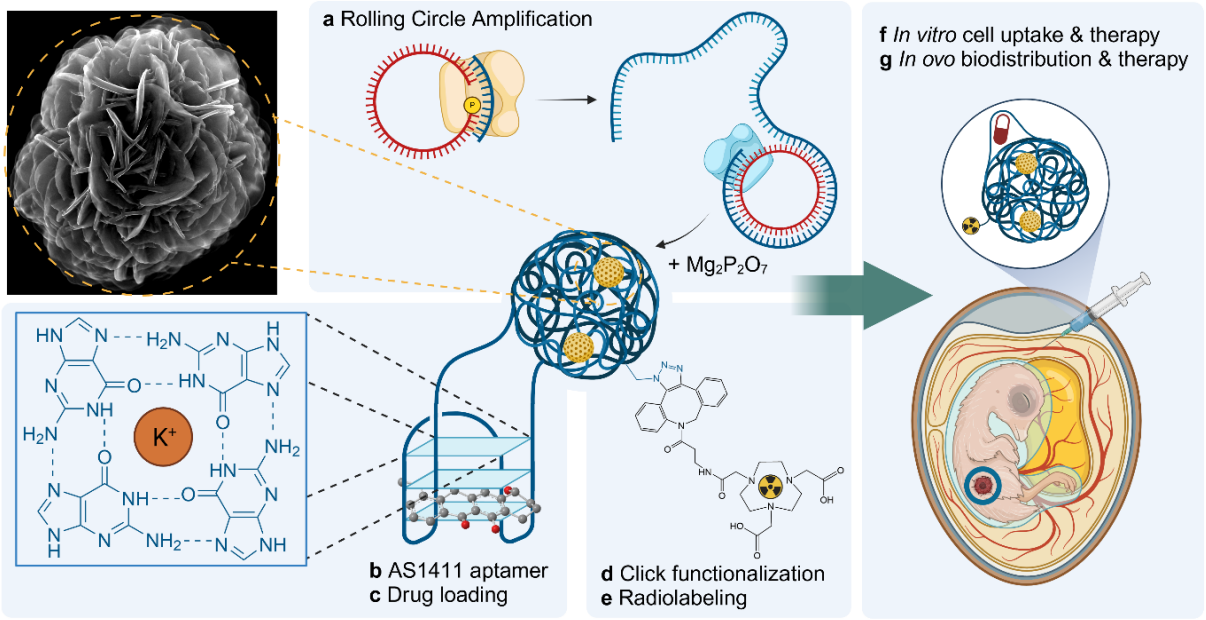

Figure 28. Synthesis strategy for Dox loaded, radiolabeled ^{Apt}DNFs and pre-clinical studies using *in vitro* cell culture and a CAM xenograft tumor model. (**a**) DNF synthesis through RCA. (**b**) Encoding of AS1411 aptamer sequence onto RCA template. (**c**) Loading of Dox through intercalation into AS1411's G-quadruplex structure. (**d**) Click-functionalization of ^{Apt}DNFs with DBCO-NOTA. (**e**) Radiolabeling of NOTA with ^{68}Ga for PET imaging or ^{177}Lu for endogenous radiotherapy. (**f**) *In vitro* uptake and toxicity studies using glioblastoma cells. (**g**) Biodistribution, tumor accumulation and therapy studies in glioblastoma CAM xenograft tumor model. Created in BioRender. Rath, W. (2025) https://BioRender.com/g57y464.

The RCA reaction is also compatible with azide-modified nucleotides, which allows the post-synthetic Click functionalization of the RCA products. In this work, the RCA strand is Click labeled with the chelator NOTA, which can bind the radionuclides ^{68}Ga or ^{177}Lu. This modified RCA strands acts as a flexible theranostic platform for either targeted PET imaging with ^{68}Ga

or the simultaneous targeted delivery of Dox and ^{177}Lu for combined chemo- and radiotherapy. This system's potential for the treatment of glioblastoma is then assessed, first by testing its *in vitro* serum stability and its *in vitro* cell uptake. Its *in ovo* biodistribution is investigated through PET imaging in a healthy chicken embryo and one bearing a CAM xenograft tumor. Then its therapeutic impact after being loaded with ^{177}Lu and Dox is tested in an *in vitro* cell culture model.

3.2 Results

3.2.1 Synthesis of Azide-modified ^{Apt}DNFs

First, the RCA reaction to synthesize AS1411 aptamer bearing nanoflowers (^{Apt}DNFs) was optimized. As already mentioned in **chapter 2.2.1**, the optimal conditions for the padlock ligation to form the circular RCA template vary, depending on the size of the template strand and the primer sequence. The 5' phosphorylated template strand bearing the reverse complementary AS1411 aptamer sequence and the primer strand (**Table 2**, *cf* Experimental section) were mixed in different ratios, heated briefly to 95 °C and slowly cooled down to 16 °C. T4 DNA ligase was added, the mixture was incubated overnight and the ligation products were analyzed through agarose GE (**Figure 29a**).

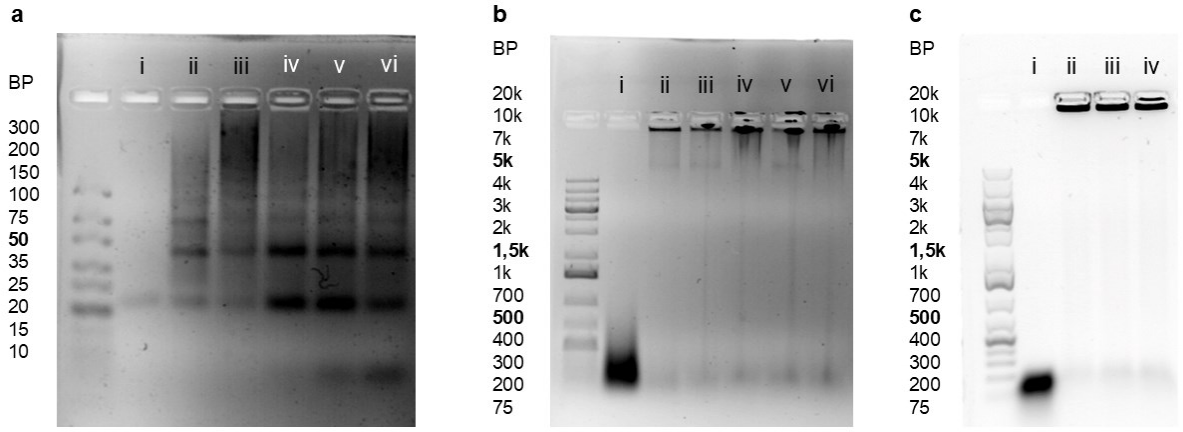

Figure 29. Synthesis of azide-bearing ^{Apt}DNFs, analyzed by agarose GE. (**a**) Padlock ligation of linear RCA template with different template:primer ratios, 4 % agarose, ladder: GeneRuler ULR. Lane i: linear template, lane ii: 2:1 ratio, lane iii: 1.5:1 ratio, lane iv: 1:1 ratio, lane v: 1:1.5 ratio, lane vi: 1:2 ratio. (**b**) RCA products synthesized with different template:primer ratios, 0.8 % agarose, ladder: GeneRuler 1kb plus. Lane i: circularized template, lane ii: 2:1 ratio, lane iii: 1.5:1 ratio, lane iv: 1:1 ratio, lane v: 1:1.5 ratio, lane vi: 1:2 ratio. (**c**) RCA products synthesized with 1:1 template primer ratio and different amounts of dATP replaced by N^6-(6-azido)hexyl-dATP, 0.8 % agarose, ladder: GeneRuler 1kb plus. Lane i: circularized template, lane ii: 25 % dATP replaced, lane iii: 50 % dATP replaced, lane iv: 100 % dATP replaced.

For all template:primer ratios (lanes ii-vi), two main bands can be observed. The lowest band represents the circular hybrid between the template and the primer, which exhibits very similar electrophoretic mobility (approx.60 BP) to the linear template (lane i). Upon ligation, the template adopts a rigid circular conformation, which occupies a much larger volume than the nicked template, leading to drastically reduced electrophoretic mobility (approx. 120 BP). The formation of higher order aggregates like tetramers or hexamers can also be observed. All these results are very similar to those from **chapter 2.2.1**. The RCA reaction was performed with the different circularized templates, and the results were evaluated by agarose GE (**Figure 29b**). Most of the RCA product is too large to migrate into the gel and the formation of a side

product around 40 000 BP can be observed[386] (compare **chapter 2.2.1**). In this case, the least amount of side product was formed with a template:primer ratio of 1:1, which was used for all following experiments.

Next, N^6-(6-azido)hexyl-dATP was added to the RCA mixture to generate azide modified ^{Apt}DNFs. To test whether this nucleotide was compatible with Φ29 DNA polymerase, 25-100 % of regular dATP in the RCA mixture was replaced with N^6-(6-azido)hexyl-dATP, and agarose GE of the different RCA products was performed (**Figure 29c**). The reaction seems to be unaffected even at 100 % replacement rate (lane iv), indicating full compatibility of the polymerase with the modified nucleotide, but all following experiments were performed with 50 % N^6-(6-azido)hexyl-dATP. The same protocol was also used to generate azide labeled ^{Ctrl}DNFs, which contained a random DNA sequence instead of the AS1411 aptamer (**Table 2**, *cf* Experimental section). The incorporation of N^6-(6-azido)hexyl-dATP into the RCA polymer was also confirmed through NMR spectroscopy. For this, the native and azide-modified RCA products were purified with a centrifugal concentrator to remove excess salt and unreacted nucleotides before recording a ^{1}H-^{13}C-HSQC spectra in D_2O (**Figure 30**). The spectrum of the modified ^{Apt}DNFs compared to the native ^{Apt}DNFs displays some additional signals in the aliphatic region (^{1}H: 1.6-1.1 ppm, ^{13}C: 25-30 ppm; ^{1}H: 3.2 ppm, ^{13}C: 50 ppm), which can be assigned to the hexyl moiety of the modified nucleotide.

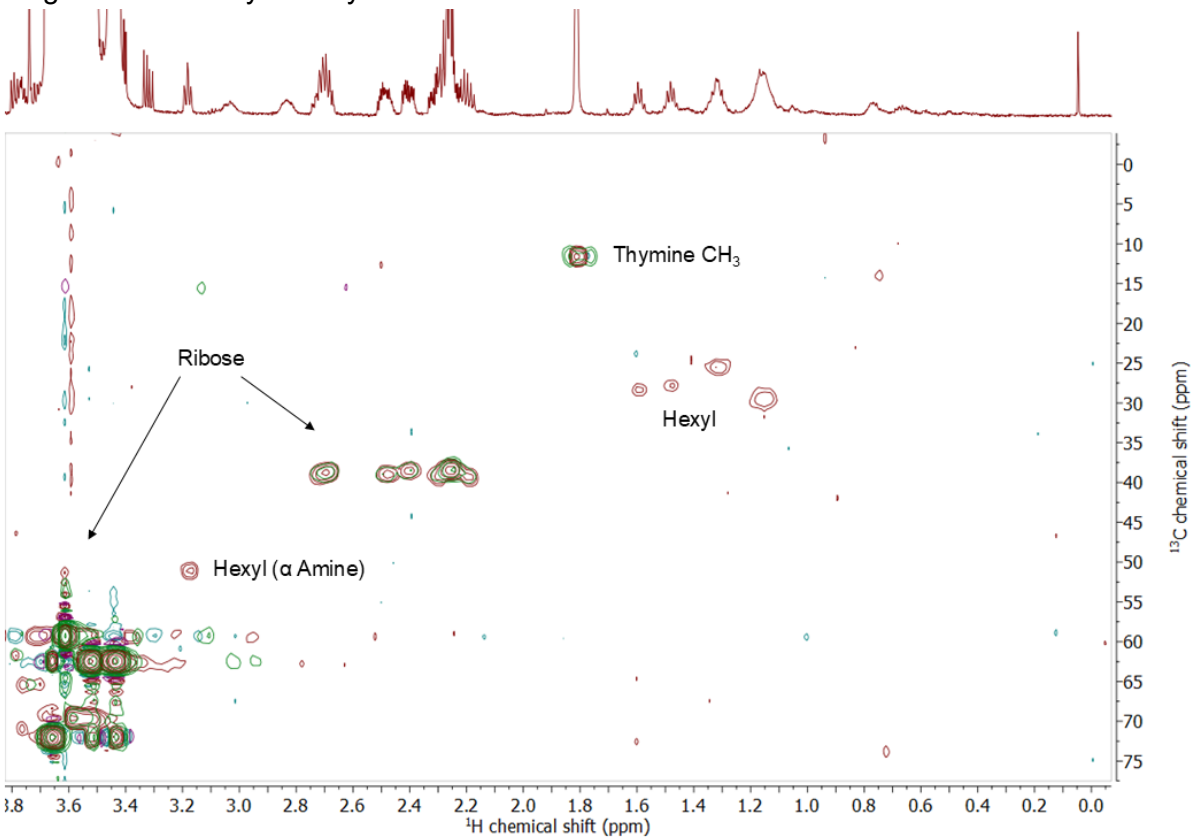

Figure 30. Superimposed ^{1}H-^{13}C-HSQC spectra (600 MHz) of native ^{Apt}DNFs (green) and N^6-(6-azido)hexyl-modified ^{Apt}DNFs (red) in D_2O with peak assignments.

The azide-modified ^{Apt}DNFs were then characterized using SEM (**Figure 31**). The images show particles with a mean diameter of 4.12±1.20 µm and a sponge like morphology, which is typical for the $Mg_2P_2O_7$ scaffold of DNFs. In **Figure 31c** a film covering the particles can be observed, which is likely comprised of excess DNA adsorbed to the surface of the $Mg_2P_2O_7$ scaffold.

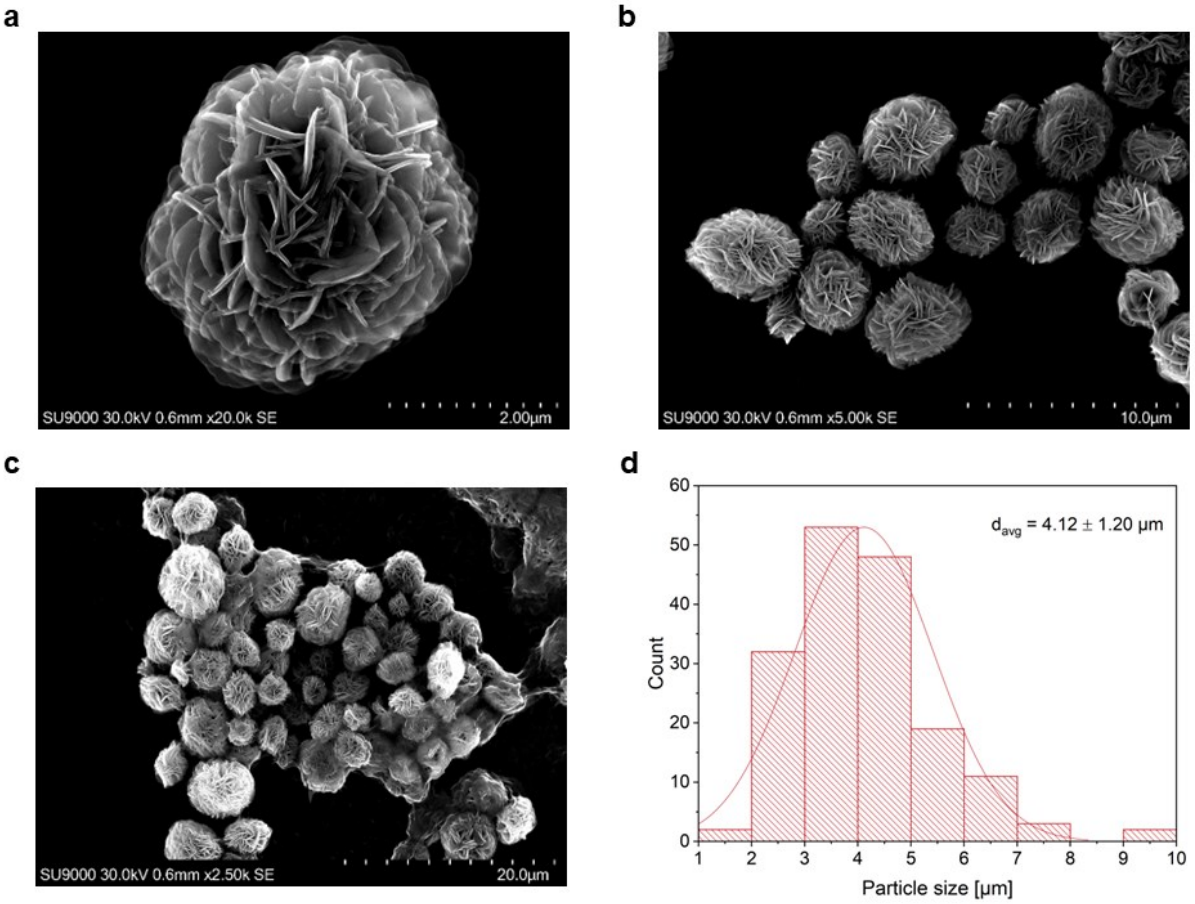

Figure 31. Representative SEM images of azide-bearing ^{Apt}DNFs. (**a**) 20 000 x magnification. (**b**) 5 000 x magnification. (**c**) 2 500 x magnification. (**d**) Particle size histogram and mean diameter ± SD from the mean, N = 150 particles.

3.2.2 Click-Functionalization of ^{Apt}DNFs

3.2.2.1 Optimizing Conditions

After successfully incorporating an azide function into the ^{Apt}DNFs, the conditions for their Click labeling were optimized. For this task, DBCO-PEG$_4$-5/6-FAM was used as Click label. In an effort to increase the accessibility of the azide groups, the reaction was performed at increased temperature and pH to denature the DNA. The conversion of the Click reaction under these conditions was quantified by FAM fluorescence (**Figure 32**). After Click labeling, the ^{Apt}DNFs were precipitated through the addition of NaCl solution and iso-propanol, washed to remove excess DBCO-PEG$_4$-5/6-FAM, lyophilized and redissolved to generate solutions with identical DNA concentration. This was confirmed by measuring the UV absorbance at 260 nm (**Figure 32a**), which was indeed almost identical for most samples, except for the one reacted at 95 °C and pH 12. In this sample, clouding of the solution and therefore an overall increase in optical density at all wavelengths could be observed, likely due to degradation of the ^{Apt}DNFs. Afterwards, the fluorescence intensities were compared (**Figure 32b**) to determine the sample with the highest labeling efficiency, which was achieved at pH 12 and 25 °C. Under these conditions, ^{Apt}DNFs were labeled with AlexaFluor 488 (AF488)-DBCO for immunocytochemistry, as well as DOTA and NOTA for radiolabeling.

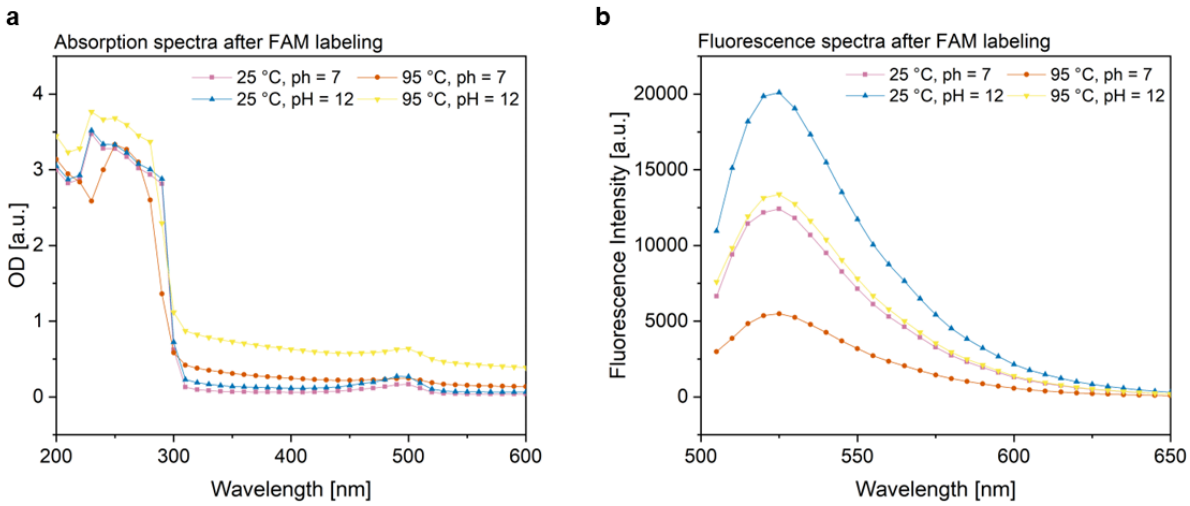

Figure 32. Quantification of ^{Apt}DNF Click-labeling efficiency at different pH and temperature. (**a**) UV-Vis absorbance spectra confirming equal DNA concentration. (**b**) Fluorescence spectra (λ_{Ex} = 485 nm) quantifying the amount of 5/6-FAM bound to the ^{Apt}DNFs.

3.2.2.2 Chelator Functionalization

After optimizing the conditions for the Click reaction, the ^{Apt}DNFs were functionalized with the radiochelator DOTA-DBCO. After the labeling reaction, the ^{Apt}DNFs were purified with a centrifugal concentrator to remove excess DOTA-DBCO, lyophilized and an ^{1}H-NMR spectrum in D_2O was recorded to confirm the successful coupling. **Figure 33** shows the superimposed ^{1}H-NMR spectra of the native and the DOTA-DBCO functionalized ^{Apt}DNFs.

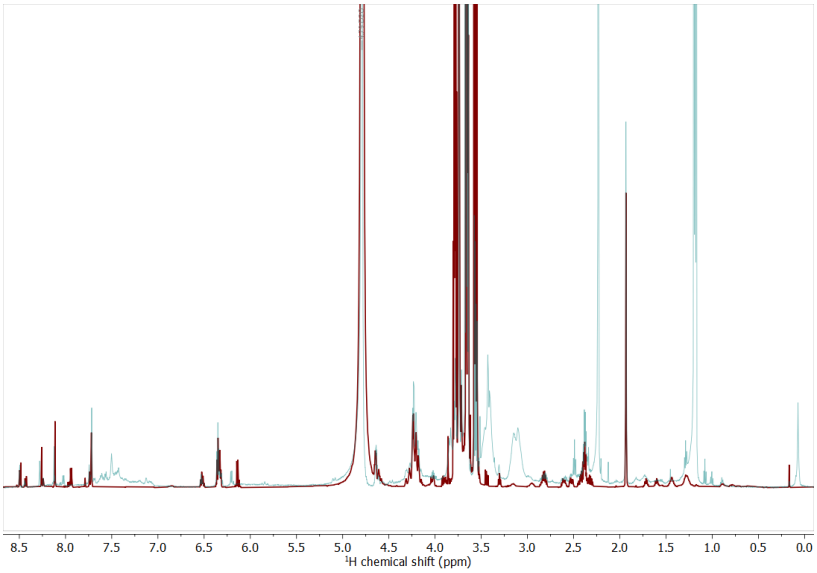

Figure 33. Superimposed ^{1}H-NMR spectra (400 MHz) of N^6-(6-azido)hexyl-modified ^{Apt}DNFs (red) and DOTA-functionalized N^6-(6-azido)hexyl-modified ^{Apt}DNFs (blue) in D_2O.

The post-functionalization spectrum clearly shows additional signals in the aromatic range (7.5-7 ppm), which correspond to the DBCO function, and in the aliphatic range, which originate from the chelator ring (3.5-2 ppm). After confirming successful labeling, the DOTA- ^{Apt}DNFs were handed over to Sabri Sahnoun (Nuclear Medicine, University Hospital Aachen), who performed ^{68}Ga radiolabeling experiments. The success of the radiolabeling was evaluated with radio thin-layer chromatography (radio-TLC), which allows the intensity of TLC spots to be quantified through γ-counter (**Figure 34**). During these TLC experiments the DOTA- ^{Apt}DNFs were not eluted and stayed at the baseline, while free $^{68}Ga^{3+}$ barely interacted with the stationary phase and was eluted quickly. The first radiolabeling attempt was performed at room temperature and pH 4.5

(**Figure 34a**), which resulted in almost no binding of $^{68}Ga^{3+}$ to the DOTA- ^{Apt}DNFs. In an effort to increase the labeling efficiency, the temperature was raised to 85 °C (**Figure 34b**). This resulted in $^{68}Ga^{3+}$ being bound to DOTA, and no free $^{68}Ga^{3+}$ could be observed on the TLC plate.

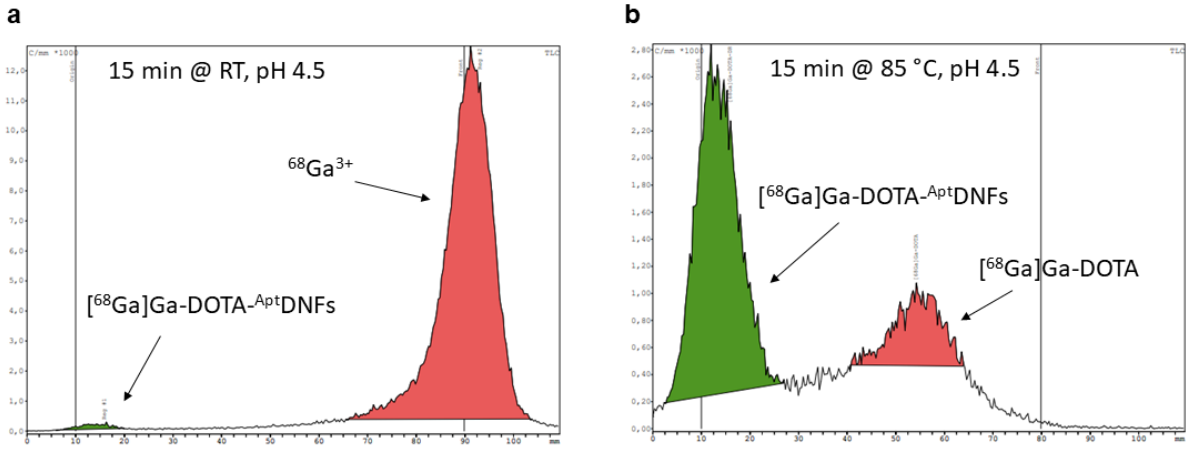

Figure 34. Radiolabeling of DOTA-^{Apt}DNFs with ^{68}Ga. (**a**) Radio-TLC after radiolabeling at RT and pH 4.5, showing very little ^{68}Ga bound to the ^{Apt}DNFs. (**b**) Radio-TLC after radiolabeling at 85 °C and pH 4.5, indicating ^{68}Ga was fully bound to DOTA but a significant amount of DOTA was removed from the ^{68}Ga bound to the ^{Apt}DNFs through depurination.

The largest part of $^{68}Ga^{3+}$ was bound to the DOTA- ^{Apt}DNFs, as shown by the intense baseline spot, but a significant amount of $^{68}Ga^{3+}$ was bound to a different species that was eluted halfway up the plate. This is most likely a ^{68}Ga-DOTA-adenine species, that got cleaved off from the RCA polymer through depurination, which typically occurs at high temperature and low pH.[387] In order to prevent depurination during the radiolabeling process, the chelator was changed from DOTA to NOTA, which can bind $^{68}Ga^{3+}$ under milder conditions. NOTA-DBCO was synthesized through amine-NHS coupling from NOTA-NHS and DBCO-amine. After purification by HPLC, formation of the correct product was confirmed through ^{1}H-NMR spectroscopy (**Figure 35**) and ESI-MS (**Figure 36**). The Click labeling with NOTA-DBCO was performed like described above and the NOTA-^{Apt}DNFs were purified with a centrifugal concentrator. Afterwards the ^{68}Ga radiolabeling was performed at room temperature and pH 4.5 and the radio-TLC experiment was repeated (**Figure 37**). This time, almost quantitative binding of $^{68}Ga^{3+}$ to the NOTA-^{Apt}DNFs was observed. Additionally, this procedure resulted in almost no depurination, therefore all further experiments were performed with NOTA labeled ^{Apt}DNFs.

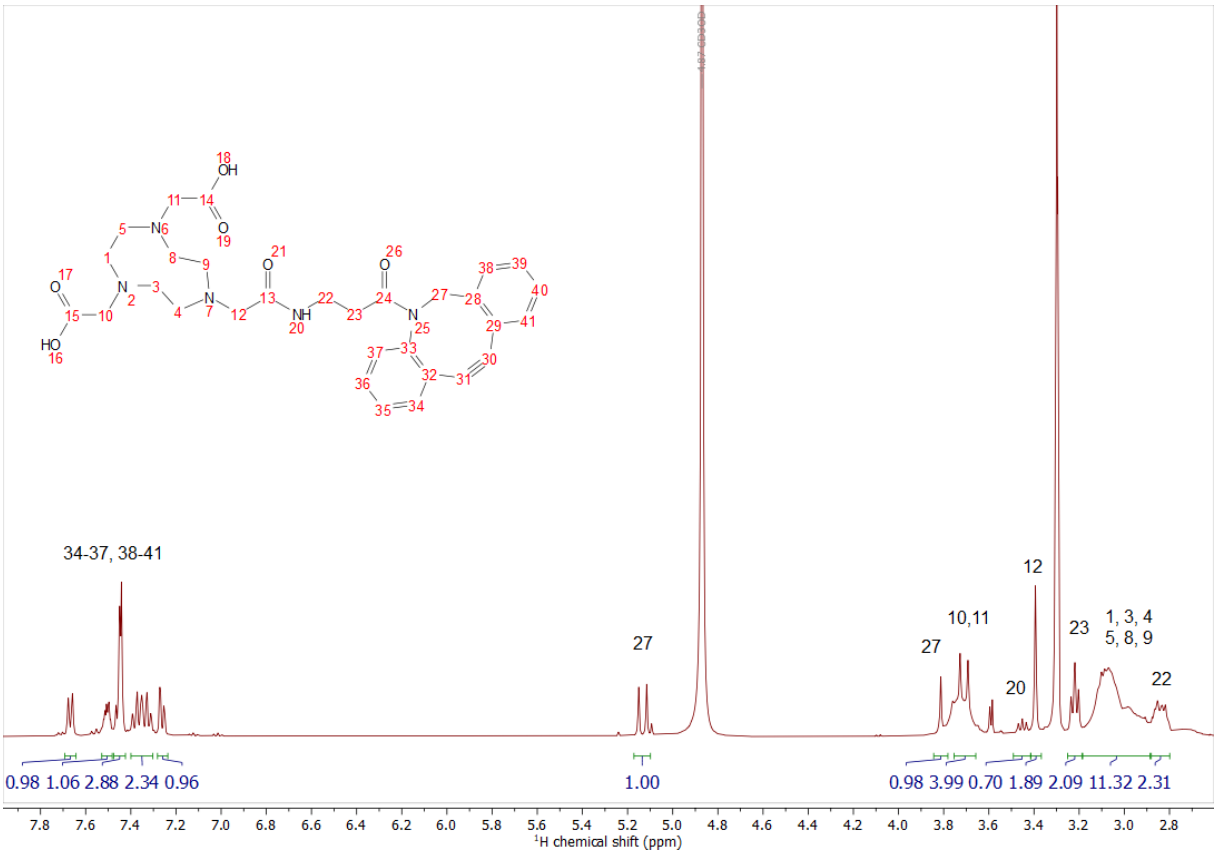

Figure 35. ^{1}H-NMR spectrum (400 MHz) of NOTA-DBCO in methanol-d_4 with peak-assignments.

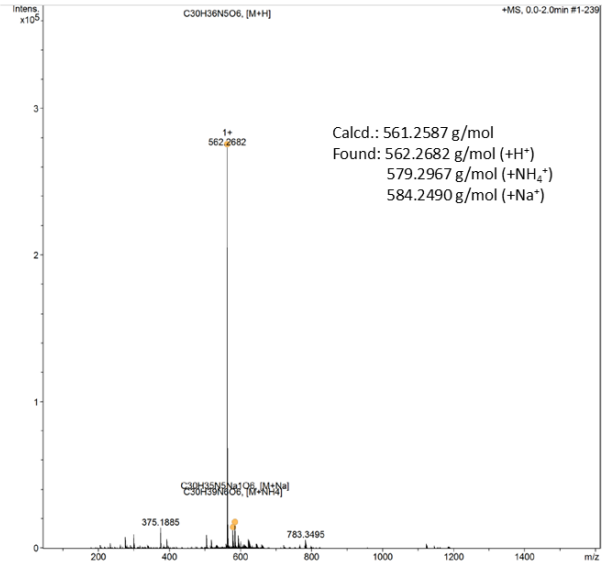

Figure 36. ESI-MS spectrum of NOTA-DBCO.

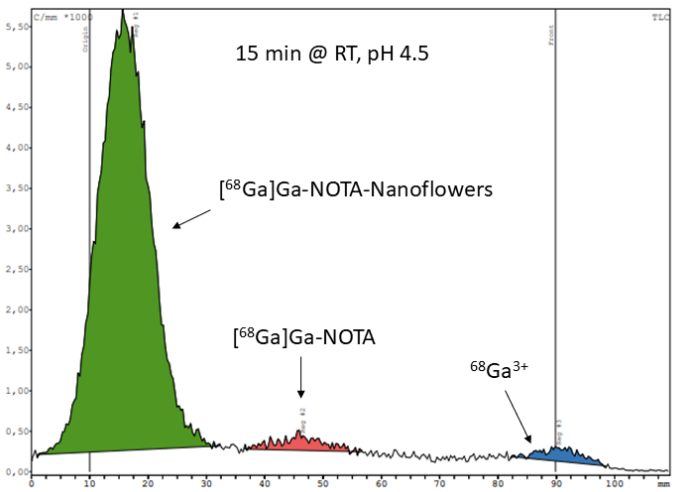

Figure 37. Radio-TLC after radiolabeling of NOTA-^{Apt}DNFs at RT and pH 4.5, indicating a majority of ^{68}Ga was bound to the ^{Apt}DNFs with marginal amounts of free ^{68}Ga and depurination fragments.

3.2.3 Dox Loading

Next, the Dox loading of ^{Apt}DNFs was optimized, which can easily be observed through the quenching of Dox's autofluorescence once it intercalates into AS1411's G-quadruplex structure. To perform the loading, varying amounts of ^{Apt}DNFs were incubated in a K^+-rich buffer containing 10 µM Dox-HCl at room temperature for 30 min. Afterwards, fluorescent spectra (λ_{Ex} = 488 nm) were recorded (**Figure 38a**). At an ^{Apt}DNF concentration of 0.5 mg/mL, full quenching was observed, indicating complete loading of Dox. The same loading protocol was used for all further experiments. The stability of Dox binding was also tested at pH 7.4 and 5 (**Figure 38b**). Over a time of 20 h, no Dox release was observed at both pH values. The high stability of the Dox binding suggests that AS1411 ^{Apt}DNFs are a suitable carrier material that can deliver Dox to glioblastoma cells without leaking.

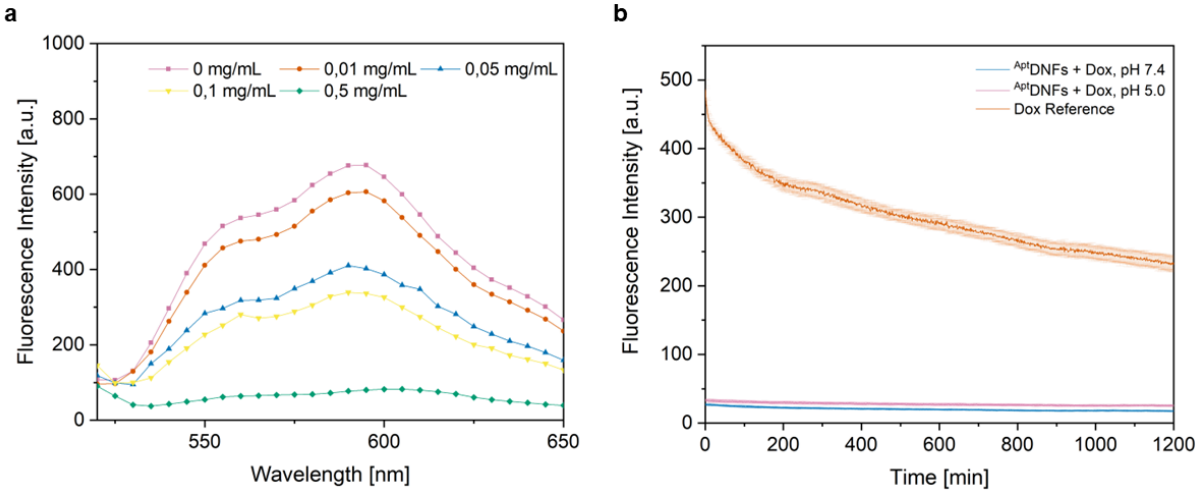

Figure 38. Dox loading of ^{Apt}DNFs. (**a**) Fluorescence spectra (λ_{Ex} = 488 nm) of 10 µM Dox after incubation for 30 min at RT with different concentrations of ^{Apt}DNFs. (**b**) Fluorescence kinetics (λ_{Em} = 595 nm) of Dox loaded ^{Apt}DNFs at pH 7.4 and pH 5.0.

After successfully synthesizing NOTA-^{Apt}DNFs and demonstrating they can be loaded with Dox and ^{68}Ga, their utility for the treatment of glioblastoma was evaluated. These translational experiments were performed by Sabri Sahnoun (Nuclear Medicine, University Hospital Aachen). This thesis only highlights the most important results from these experiments. A more comprehensive report will be found in a future publication.

3.2.4 Radiochemical Purity and Stability

First, the radiolabeling of NOTA-^{Apt}DNFs was investigated in more detail (**Figure 39**). To determine the radiochemical yield (RCY) (**Figure 39a,b**), increasing amounts of NOTA-^{Apt}DNFs were incubated with $^{68}Ga^{3+}$ or $^{177}Lu^{3+}$ (1 GBq), washed and afterwards radio-TLC was performed. RCY was calculated by comparing the integrals of the free ^{68}Ga/^{177}Lu spot with the integrals of all labeled species. At a NOTA-^{Apt}DNF concentration of 250 µg/mL, RCY of approximately 95 % was achieved. The representative radio-TLCs (**Figure 39c,d**) also show that NOTA-^{Apt}DNFs were the only radiolabeled species, and no fragments were present. This demonstrates that very high radiochemical purity (> 95 %) can be achieved through this method without additional purification steps. Finally, the decay-corrected long-term stability of radiolabeling in PBS buffer and in human serum at 37 °C was assessed by performing radio-TLCs in a time dependent manner (**Figure 39e,f**). The RCY for ^{68}Ga-^{Apt}DNFs ($t_{1/2}$ = 68 min) dropped to approximately 90 % after 3 h, and RCY for ^{177}Lu-^{Apt}DNFs ($t_{1/2}$ = 6.7 d) dropped to

approximately 80 % after 24 h. This reduction in RCY was likely caused by radiolysis[388], and was therefore expected, especially for ^{177}Lu. After these experiments the radiolabeling was deemed to be stable enough, since the accumulation timespan during most clinical applications is in the range of 1 h.

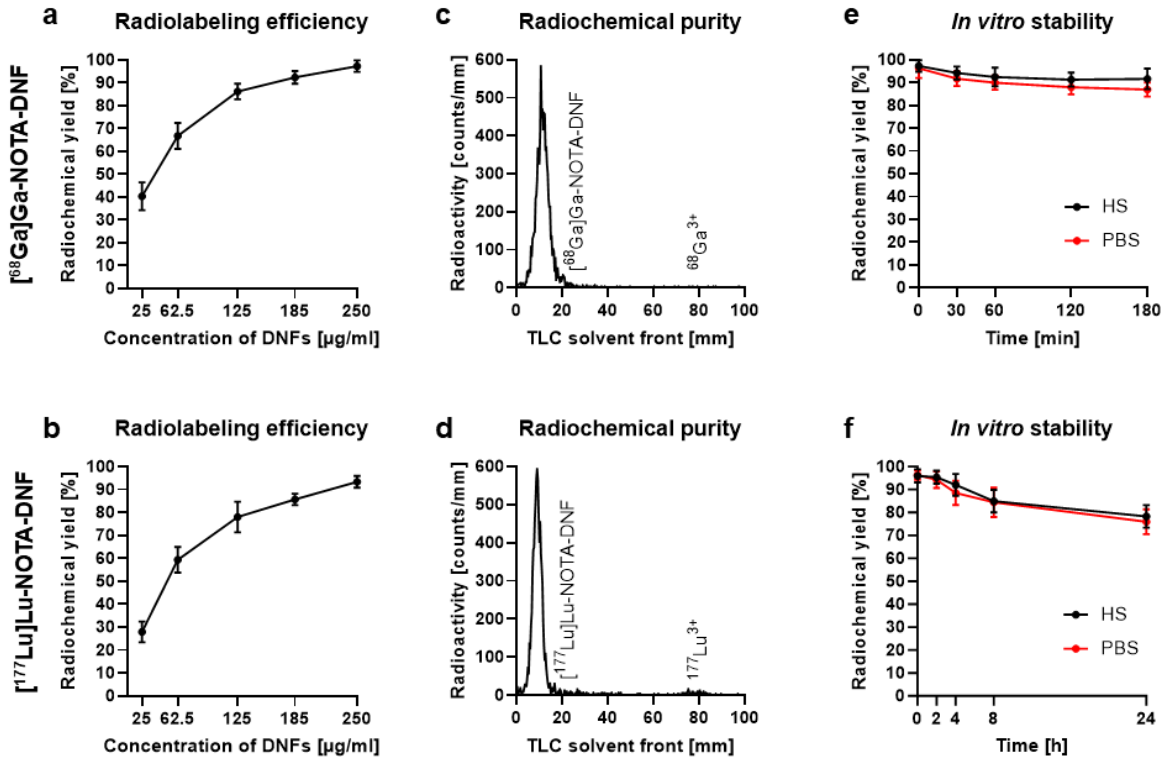

Figure 39. RCY and radiochemical purity of NOTA-^{Apt}DNFs radiolabeled with ^{68}Ga and ^{177}Lu as determined by radio-TLC. (**a,b**) RCY after incubation of ^{68}Ga (**a**) and ^{177}Lu (**b**) (1 GBq) with different amounts of NOTA-^{Apt}DNFs at RT and pH 4.5. (**c,d**) Representative radio-TLC of NOTA-^{Apt}DNFs radiolabeled with ^{68}Ga (**c**) and ^{177}Lu (**d**) demonstrating their high radiochemical purity. (**e,f**) Time dependent RCY of NOTA-^{Apt}DNFs radiolabeled with ^{68}Ga (**e**) and ^{177}Lu (**f**) in PBS buffer and human serum as determined by radio-TLC. Data presented as mean ± SD, N = 9.

3.2.5 *In vitro* Cell Uptake

3.2.5.1 Quantification of Cell Uptake

To start, the impact of the aptamer sequence on the uptake of ^{68}Ga-DNFs into glioblastoma cells was evaluated using γ-counter. ^{68}Ga-^{Apt}DNFs and ^{68}Ga-^{Ctrl}DNFs with a random DNA sequence were incubated with U87-IDH^{wt} and U87-IDH^{mut} glioblastoma cell lines. Cell samples were taken after 1 and 4 h, excess ^{68}Ga-DNFs were washed off with PBS buffer, and cell uptake was quantified via γ-counter (**Figure 40**). For the U87-IDH^{wt} cell line, approximately 5 % of ^{68}Ga-^{Apt}DNFs were taken up after 1 h and approximately 8 % were taken up after 4 h (**Figure 40a**). This represents an 8-10-fold increase over the ^{68}Ga-^{Ctrl}DNFs, whose uptake reached only around 0.5 % after 1 h and 1 % after 4 h. The U87-IDH^{mut} cell line exhibited very similar uptake behavior (**Figure 40b**). Statistical analysis confirmed that no significant difference in uptake rate could be observed between U87-IDH^{wt} and U87-IDH^{mut} cell lines (**Figure 40c**).

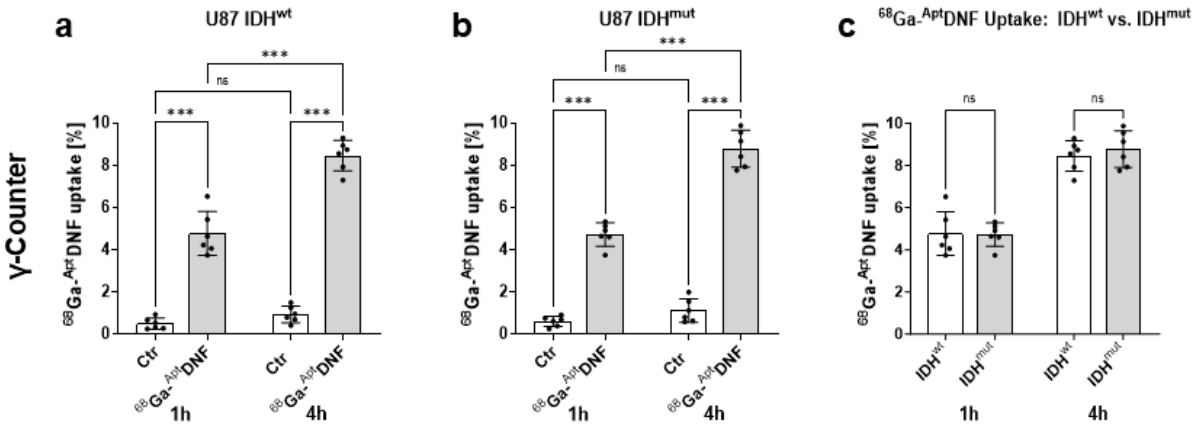

Figure 40. Time dependent *in vitro* cell uptake of ^{68}Ga-^{Apt}DNFs into U87 glioblastoma cells quantified by γ-counter. (**a**) ^{68}Ga-^{Apt}DNFs uptake into U87 IDH^{wt} glioblastoma cells compared to ^{68}Ga-^{Ctr}DNFs after 1 and 4 h. (**b**) ^{68}Ga-^{Apt}DNFs uptake into U87 IDH^{mut} glioblastoma cells compared to ^{68}Ga-^{Ctr}DNFs after 1 and 4 h. (**c**) Comparison of uptake rate of ^{68}Ga-^{Apt}DNFs into U87 IDH^{wt} and U87 IDH^{mut} glioblastoma cells after 1 and 4 h. Data presented as mean ± SD, N = 18. Statistical analysis was performed with two-way ANOVA followed by multiple comparison tests and *post-hoc* Turkey test, ***p < 0.001.

3.2.5.2 Immunocytochemistry

The intracellular localization of ^{Apt}DNFs after uptake was also investigated through immunocytochemistry. For this purpose, ^{Apt}DNFs were labeled with AF488. U87-IDH^{wt} cells were incubated with AF488-^{Apt}DNFs, samples were taken after 15 min, 30 min, 60 min, 120 min, and 240 min and excess AF488-^{Apt}DNFs were washed off with PBS. Afterwards, the cells were stained with phalloidin to visualize the actin cytoskeleton and with 4'-6-diamidin-2-phenylindol (DAPI) to visualize the DNA in the nucleus. **Figure 41** shows the fluorescence microscopy images that were taken after staining. As expected, the intensity of the AF488 signal increased with higher incubation time, while the phalloidin and DAPI signal remained stable. In the merged images the AF488 also overlaps with the phalloidin and the DAPI signal, suggesting the AF488-^{Apt}DNFs not only got internalized, but specifically accumulated at the nucleus.

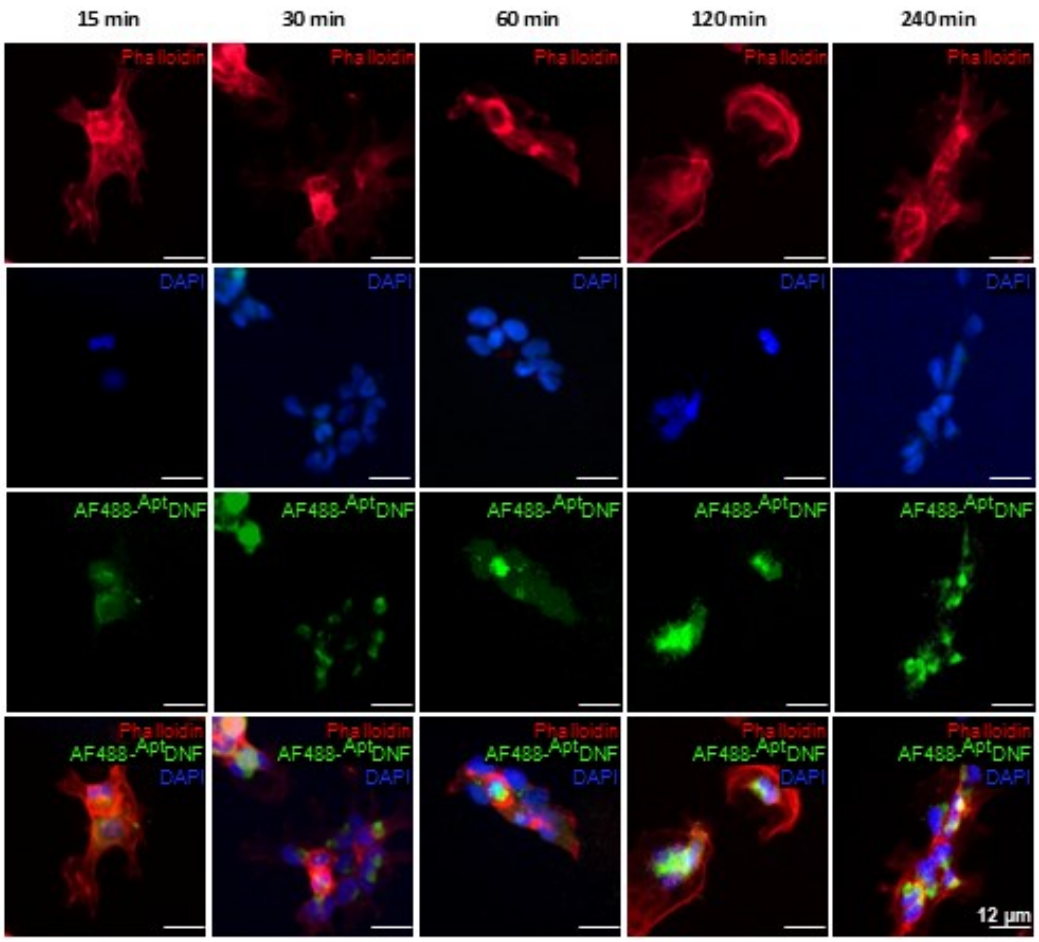

Figure 41. Immunocytochemical co-staining of U87 IDH^{wt} glioblastoma cells with DAPI (blue) and phalloidin (red) after incubation with AF488-^{Apt}DNFs for different times.

3.2.6 *In ovo* Biodistribution

3.2.6.1 Non-Tumor Bearing

Next, the biodistribution of NOTA-^{Apt}DNFs was investigated with an *in ovo* chicken embryo model. At first, the biodistribution in a healthy chicken embryo was tested. For this, NOTA-^{Apt}DNFs were labeled with ^{68}Ga and administered to the embryo through peripheral intravenous injection at day 20 after fertilization. 30 and 60 mins after injection, the distribution of ^{68}Ga-^{Apt}DNFs in the embryo was visualized through combined PET and computer tomography (PET-CT) (**Figure 42a**). The PET-CT images after 30 mins circulation time showed that the ^{68}Ga-^{Apt}DNFs were distributed all over the body of the embryo with one hotspot in the torso. After 60 mins circulation time the signal intensity of this hotspot further increased, while dropping off for the rest of the body. This hotspot indicated the time-dependent enrichment of ^{68}Ga-^{Apt}DNFs in the heart and the hepatic systems, which are the most perfused organs. After the PET-CT scans, the embryo was sacrificed, the organs were resected and the carcass (body) and the blood were collected. Afterwards, the accumulation of ^{68}Ga-^{Apt}DNFs in the individual organs was quantified by γ-counter (**Figure 42b**). The γ-counter showed that after 30 mins the majority of ^{68}Ga-^{Apt}DNFs were still localized in the blood and body, which explains their high presence in the heart and liver. The organs accumulated only small amounts (< 10 %) of ^{68}Ga-^{Apt}DNFs and no statistically significant difference in uptake was found between the organs after 30 mins. After 60 mins of circulation time (**Figure 42c**), the γ-counter showed that the amount of ^{68}Ga-

^{Apt}DNFs in the blood and the body decreased compared to 30 mins circulation time, while the amount of ^{68}Ga-^{Apt}DNFs in the organs increased. The most notable accumulation was observed in the liver and surprisingly in the brain. The time dependent increase in brain accumulation was also found to be statistically significant (**Figure 42d**). This demonstrated that the ^{Apt}DNFs had the ability to penetrate the BBB in healthy chicken embryos.

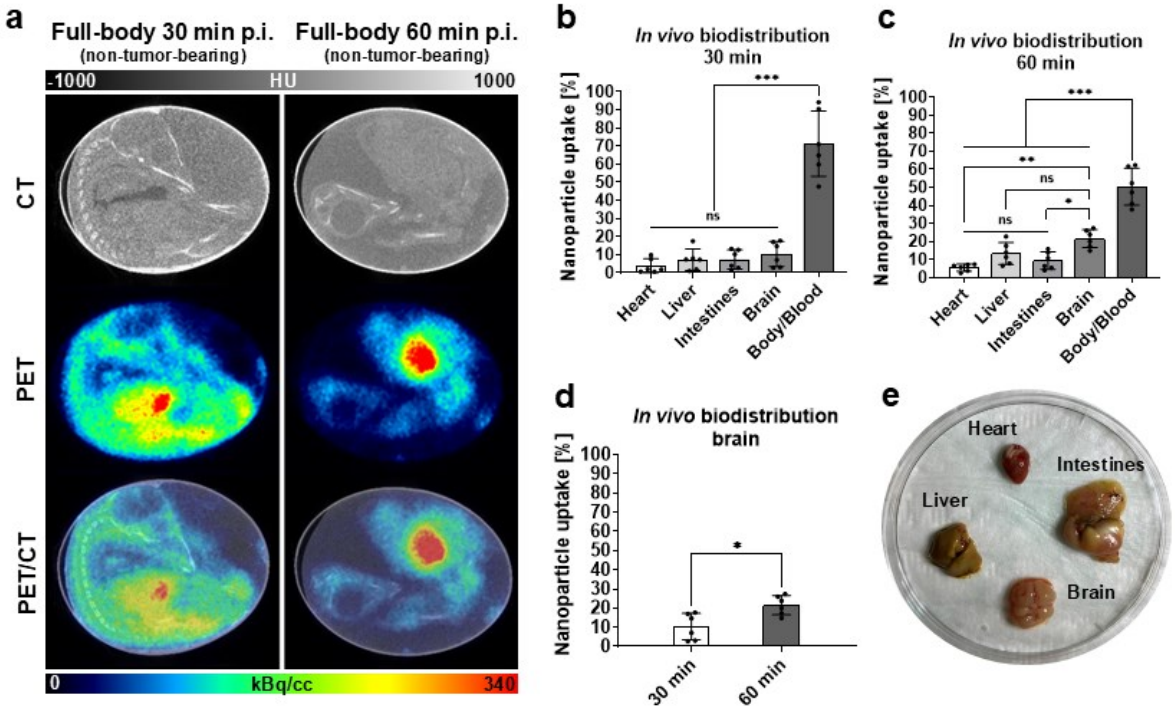

Figure 42. Biodistribution of ^{68}Ga-^{Apt}DNFs in non-tumor-bearing chicken embryo after 30 and 60 mins circulation time. (**a**) PET-CT images visualizing the biodistribution of ^{68}Ga-^{Apt}DNFs in the healthy chicken embryo after 30 mins (left) and 60 mins (right). (**b**) Post-mortem quantification of ^{68}Ga-^{Apt}DNF accumulation in the individual organs after 30 mins circulation time, determined through γ-counter (decay corrected). (**c**) Post-mortem quantification of ^{68}Ga-^{Apt}DNF accumulation in the individual organs after 60 mins circulation time, determined through γ-counter (decay corrected). (**d**) Post-mortem quantification of time dependent accumulation of ^{68}Ga-^{Apt}DNFs in the brain after 30 and 60 mins circulation time, determined through γ-counter (decay corrected). (**e**) Representative images of resected organs.

3.2.6.2 Tumor Bearing

The same *in ovo* biodistribution experiments were repeated with chicken embryos bearing a CAM xenograft glioblastoma (**Figure 43**). The tumor cells were transplanted on day 15 after fertilization, and the embryo was intravenously injected with the ^{68}Ga-^{Apt}DNFs on day 20. The PET-CT images again show a full body distribution of ^{68}Ga-^{Apt}DNFs with a hotspot at the heavily perfused organs in the torso (**Figure 43a**). After 60 min circulation time, the PET-CT images also reveal accumulation of ^{68}Ga-^{Apt}DNFs at the tumor site. After the PET-CT scan, the embryo was again sacrificed, the tumor was resected and its accumulation of ^{68}Ga-^{Apt}DNFs was compared to the rest of the body by γ-counter. Here, a circulation-time dependent increase in ^{68}Ga-^{Apt}DNFs accumulation in the tumor could be observed. Approximately 5 % of ^{68}Ga-^{Apt}DNFs were taken up by the tumor after 30 mins circulation time (**Figure 43b**) and approximately 15 % after 60 mins circulation time (**Figure 43c**). This increase was also confirmed to be statistically significant (**Figure 43d**).

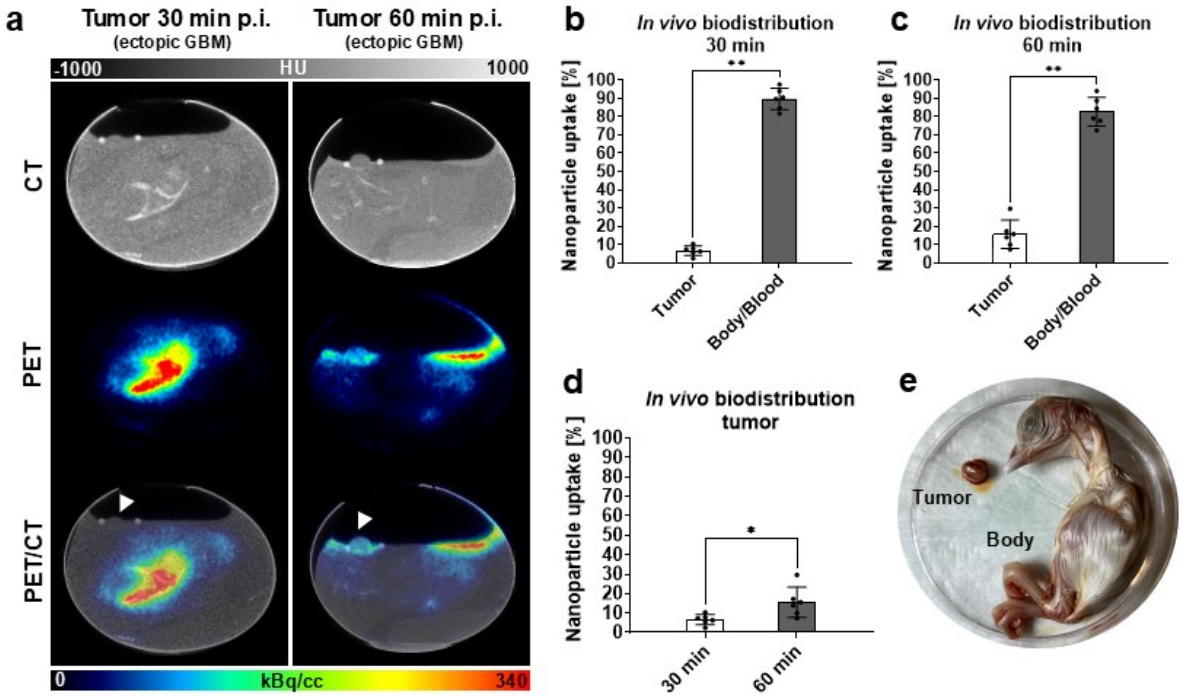

Figure 43. Biodistribution of ^{68}Ga-^{Apt}DNFs in chicken embryo bearing a CAM xenograft glioblastoma after 30 and 60 mins circulation time. (**a**) PET-CT images visualizing the biodistribution of ^{68}Ga-^{Apt}DNFs after 30 mins (left) and 60 mins (right), white arrows highlighting xenograft tumor. (**b**) Post-mortem quantification of ^{68}Ga-^{Apt}DNF accumulation in the tumor after 30 mins circulation time, determined through γ-counter. (**c**) Post-mortem quantification of ^{68}Ga-^{Apt}DNF accumulation in the tumor after 60 mins circulation time, determined through γ-counter. (**d**) Post-mortem quantification of time dependent accumulation of ^{68}Ga-^{Apt}DNFs in the tumor after 30 and 60 mins circulation time, determined through γ-counter (decay corrected). (**e**) Representative images of resected tumor and remaining carcass.

3.2.7 *In vitro* Cell Toxicity

After the ^{Apt}DNFs demonstrated favorable biodistribution and sufficient accumulation at the tumor site, their potential for glioblastoma therapy was assessed with *in vitro* cell culture experiments. For this purpose, NOTA-^{Apt}DNFs were radiolabeled with ^{177}Lu, loaded with Dox and added into the medium for U87 IDH^{wt} and U87 IDH^{mut} cell culture. Control cell cultures were incubated together with unloaded ^{Apt}DNFs, free Dox and ^{Apt}DNF[Dox]. Samples were taken after 48 h, 72 h and 96 h, afterwards cell damage was assessed through lactate dehydrogenase (LDH) release assay (**Figure 17**) and resazurin assay (**Figure 18**). Both these assays detect NADH, which is a product of many cellular processes, for example the oxidation of lactate to pyruvate through LDH. Once the cells get damaged and LDH is released into the medium, the presence of NADH can be detected through the addition of tetrazolium salts which get reduced into colored formazan compounds.[389] Resazurin is a redox dye that can migrate into living cells, where it is reduced into the strongly fluorescent resorufin.[390]

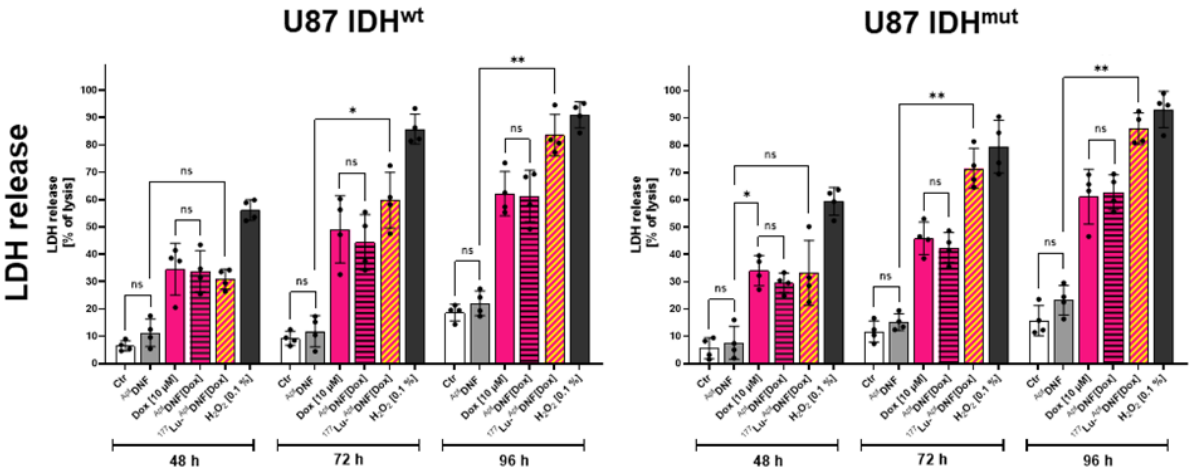

Figure 44. LDH release assay of U87 IDH^{wt} (left) and U87 IDH^{mut} (right) glioblastoma cells after different incubation times with unloaded ^{Apt}DNFs (grey), 10 µM free Dox (pink), ^{Apt}DNF[Dox] (pink-black), ^{177}Lu-^{Apt}DNF[Dox] (yellow-red) or 0.1 % H_2O_2 (black), compared to LDH release after lysis.

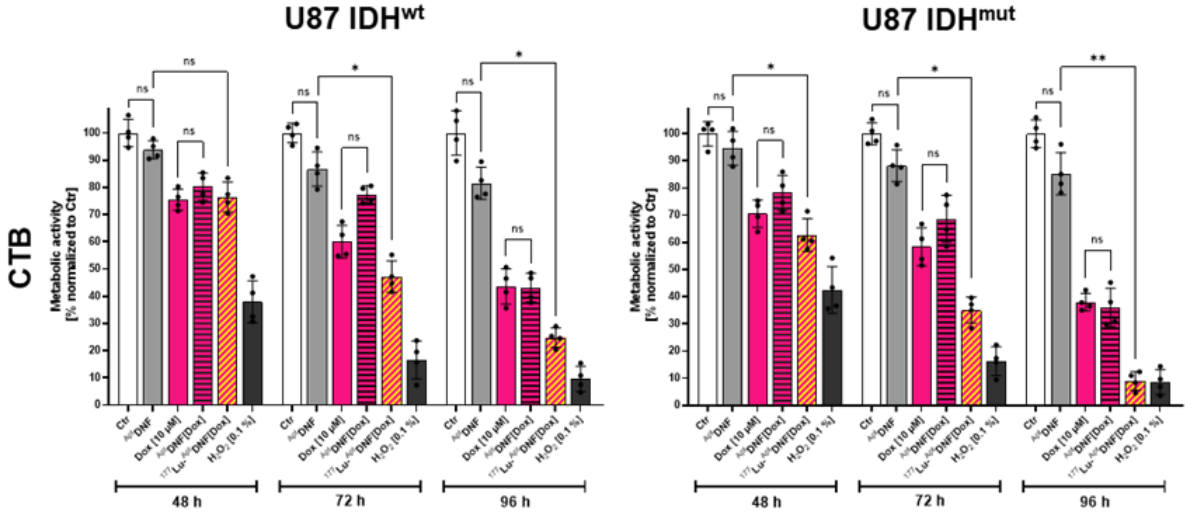

Figure 45. Metabolic activity of U87 IDH^{wt} (left) and U87 IDH^{mut} (right) glioblastoma cells determined through cell titer blue (resazurin) assay after different incubation times with unloaded ^{Apt}DNFs (grey), 10 µM free Dox (pink), ^{Apt}DNF[Dox] (pink-black), ^{177}Lu-^{Apt}DNF[Dox] (yellow-red) or 0.1 % H_2O_2 (black), normalized to negative control (white).

Due to their large similarity, the results from the LDH release assay (**Figure 44**) and the resazurin assay (**Figure 45**) mirror each other. Overall, cell viability dropped over time for untreated and treated cultures, but the difference between the treated and untreated group grew over time, since the cytotoxic compounds had more time to affect the cells. No statistically significant difference in cell viability was observed between the negative control group and the unloaded ^{Apt}DNFs, demonstrating the low cytotoxicity of ^{Apt}DNFs. After 48 h, no significant difference was observed between the cells treated with free Dox, ^{Apt}DNF[Dox] and ^{177}Lu-^{Apt}DNF[Dox], suggesting that all cytotoxic effects at this point were caused by Dox, and that the ^{Apt}DNFs did not increase Dox uptake. After 72 h and 96 h however, ^{177}Lu-^{Apt}DNF[Dox] caused a significantly larger amount of cell death due to the slow accumulation of additional DNA damage from ^{177}Lu beta-radiation. These observations were made for both U87 IDH^{wt} and U87 IDH^{mut} cell lines.

3.3 Discussion and Outlook

In this chapter, azide bearing DNFs were successfully Click labeled with NOTA to generate a versatile theranostic platform for targeted cancer imaging and synergistic radio- and chemotherapy. The sequence programmability is one of the outstanding features of RCA-based systems, which in this case was used to incorporate the AS1411 aptamer sequence to achieve a targeting effect towards glioblastoma cells. In the future, other aptamers could easily be incorporated to target different cancer types or to facilitate BBB permeability through receptor-mediated transcytosis (see **chapter 1.3.7**). Other functional sequences like RNA-cleaving DNAzymes could also be encoded into DNFs for potential gene-silencing applications. The azide functionalization of the DNFs was achieved through the addition of N^6-(6-azido)hexyl-dATP into the RCA mixture. Φ29 polymerase seems to be fully compatible with this nucleotide, which is the first time this has been demonstrated. Since N^6-(6-azido)hexyl-dATP is commercially available, this represents a convenient way of obtaining azide-bearing DNFs. In the future, other modified nucleotides could also be added to the RCA mixture, for example 5-fluorouridine-5'-triphisphate, in order to add an additional therapeutic payload to the system.

The reaction conditions for Click labeling were optimized, and afterwards the azide-bearing DNFs were functionalized with AF488-DBCO for fluorescent microscopy and with the chelators DOTA-DBCO and NOTA-DBCO for the binding of radionuclides. This labeling procedure is simple to execute and could be potentially adapted for other DBCO compounds. For example, DNFs could be functionalized with folate or cholesterol to improve cell uptake[391] or with ferrocene derivates to enable electrochemical detection.[392] Many Click labels are commercially available, including the AF488-DBCO and DOTA-DBCO that were used in this study. NOTA-DBCO had to be synthesized through amine-NHS-ester coupling, but since many NHS esters are readily available, a variety of Click labels can be accessed with relatively low synthetic effort. Overall, this synthesis strategy for labeled DNFs constitutes a straightforward approach, that can easily be adapted through changes in RCA template sequence, nucleotide mixture and Click label.

The loading of DNFs with Dox through its intercalation into AS1411's G-quadruplex structure was also demonstrated. This approach of loading DNFs with a chemotherapeutic drug is quite elegant, since it makes double use of the targeting function and does not require an additional loading moiety. The intrinsic fluorescence of Dox also provides a convenient, label-free readout method to confirm the loading. The long-term stability of Dox binding was also evaluated. No Dox release was observed at pH 7.4, which ensures that Dox is not released into the blood stream after administration and reliably reaches the tumor site. Dox binding was stable even under tumor environmental conditions (pH 5). This suggests that Dox binding to AS1411 is stable even after cell uptake, which potentially enhances accumulation in the nucleus and in turn cytotoxicity (compare **chapter 1.3.6**). In the future, other chemotherapeutic drugs with intercalating properties could also be loaded onto AS1411-DNFs.[393] Dox conjugates with non-intercalating chemotherapeutic drugs, for example temozolomide, have also been reported.[394] These novel drug conjugates have great potential for the treatment of glioblastoma, and could possibly be loaded onto the AS1411-DNFs.

Next, radiolabeling of DOTA-DNFs and NOTA-DNFs was evaluated. The necessary conditions for the radiolabeling of DOTA were too harsh for DNA and led to depurination, which is why NOTA was used for the rest of the study. NOTA can be labeled under milder conditions, but also forms less stable complexes, especially with larger metals like ^{177}Lu. Nevertheless, radiochemical purities above 95 % could be achieved, which is sufficient for the application to patients. The radiolabeling was also sufficiently stable in serum, demonstrating the usefulness of NOTA-DNFs for *in vivo* applications. In the future, NOTA functionalized DNFs could also be labeled with other trivalent metal cations, for example with Gd^{3+} to enable their use as targeted MRI contrast agents.[395]

Radiolabeling of NOTA-DNFs with ^{68}Ga provided a convenient way of quantifying their uptake into U87 IDH^{wt} and U87 IDH^{mut} cells. DNFs bearing the AS1411 aptamer sequence exhibited an 8-10 fold higher uptake compared to randomized control DNFs. This is a very impressive result, since traditional particle based systems only achieve a 2-3 fold increase in cell uptake when functionalized with AS1411.[251-253] The excellent targeting ability ^{Apt}DNFs could be explained through its high aptamer content, which allows for multivalent binding and provides redundancy in case of nuclease degradation. Additionally, the unspecific uptake of control DNFs is hindered by their high negative charge. No significant difference in ^{Apt}DNF uptake was observed between U87 IDH^{wt} and U87 IDH^{mut} cells, suggesting both cell lines carry similar amounts of nucleolin on their surface. IDH mutation is typically associated with changes in metabolism and the epigenome.[396] These epigenetic changes can alter the expression of several genes, but in this case, the expression of nucleolin seems to be unaffected. IDH mutation also promotes changes in the tumor microenvironment[396], therefore it is still possible that differences in uptake between U87 IDH^{wt} and U87 IDH^{mut} tumors might be observed during future *in vivo* studies. Immunocytochemistry revealed that ^{Apt}DNFs accumulated at the nucleus. This was expected, since AS1411's target, nucleolin, is involved in nucleocytoplasmic transport processes (see **chapter 1.3.6**). This again strengthens the hypothesis that the AS1411-^{Apt}DNFs could help to increase Dox's accumulation in the nucleus and therefore its cytotoxicity.

The biodistribution of ^{68}Ga-^{Apt}DNFs was tested with an *in ovo* model bearing a CAM grafted glioblastoma tumor, which revealed significant accumulation of ^{Apt}DNFs in the liver (12 %), the tumor (15 %) and the brain (20 %) after 1 h. Accumulation in the liver was expected, since it is heavily perfused. After administering AS1411-conjugated nanoparticles to mice, similar accumulation in the liver could also be observed after 6 h.[252] Compared to this murine model, the *in ovo* model exhibited much higher enrichment in the blood, since the embryo does not excrete the DNFs through the hepatobiliary pathway. The high tumor accumulation of 15 % was achieved after only 1 h during the *in ovo* experiments. This process seems to be fast enough to be translatable into a murine model, in which the tumor accumulation is competing with the excretion rate. CAM graft models are also known to accurately replicate the vascular environment of the tumor. This implies that similar or slightly lower tumor accumulation of ^{Apt}DNFs is also possible in a murine model, especially for ectopic tumors. Whether the ^{Apt}DNFs are also effective for treating intracerebral GBM in a murine model remains unclear. *In ovo*, the uptake of ^{Apt}DNFs into the brain was exceptionally high, even though the chicken embryos possess a fully developed BBB from day 15.[397] AS1411's ability to facilitate the transport of particle based DDSs across the BBB in mice is controversially discussed in the literature. Some papers report no increase in brain accumulation for AS1411-functionalized particles in mice.[254-255] Although, in these cases AS1411 caused the particles that crossed the BBB to accumulate at the actual tumor site. Other studies claim that AS1411 actually helped to

increase the amount of DDS transported across the BBB in mice.[251-252] The most reliable way to enable transport across the BBB still seems to be a separate targeting function[254, 398-400], which in the future could also be incorporated into the ^{Apt}DNFs, by simply encoding a BBB specific aptamer[258, 401-402] onto the RCA template.

The *in vitro* cytotoxicity assays showed that the unloaded ^{Apt}DNFs exhibit barely any toxicity, thus demonstrating their safety for *in vivo* applications. Also, no difference between Dox loaded ^{Apt}DNFs and free Dox was observed. This could be explained by the high Dox concentrations used in these experiments, which might exceed the cell's ability to effectively remove free Dox through P-gp. If these experiments were repeated with lower Dox concentration in the future, the cells might be able to develop resistance to the free Dox and Dox-^{Apt}DNFs might yield comparatively better results. However, a very clear difference in toxicity was observed between Dox-^{Apt}DNFs and ^{177}Lu-Dox-^{Apt}DNFs, especially over longer timespans. The delayed toxicity can be explained by the slow accumulation of additional DNA damage through ^{177}Lu's beta-radiation. The fact that ^{177}Lu-Dox-^{Apt}DNFs performed almost as well as the positive control group treated with H_2O_2, emphasizes their efficacy for GBM treatment.

3.4 Experimental

General Materials

Oligonucleotides were purchased from Biomers. The sequences are listed in **Table 2**. T4 DNA ligase and 10X ligation buffer was purchased from Thermo Fisher. Φ29 polymerase and 10X polymerase buffer were purchased from Biosearch Technologies. Regular dNTPs were purchased from GeneOn Bioscience. N^6-(6-Azido)hexyl-dATP, Alexa Fluor 488-DBCO and DBCO-PEG_4-5/6-FAM were purchased from Jena Bioscience. DOTA-DBCO was purchased from Macrocyclics. Dibenzocyclooctyne-amine was purchased from Thermo Scientific. NOTA-NHS ester was purchased from CheMatech. All experiments were performed with ultrapure water (18.2 MΩ cm) from a PURELAB Chorus 1 system by Elga. All regular solvents were purchased from Fisher Scientific. Methanol-d_4 and D_2O were purchased from Deutero.

Instrumentation

HPLC was performed with a Shimadzu system equipped with a degasser, 2 isocratic HPLC pumps (LC-20AT), autosampler (SIL-20A HT), oven (CTO 20A), refractive index indicator (RID 10A) and diode-array detector (SPD-M20A). Analysis was performed with the Shimadzu LabSolutions software (version 5.92). ESI-MS was performed with a Bruker micrOTOF-Q II.

Table 2. DNA sequences.

Name)	Sequence (5'→3')
RCA AS1411 Template	Phosphate – CCC TCT CTC CTC TAT TAT **AAC CAC CAC CAC CAC AAC CAC CAC CAC C** TAT TTT CTC CTC CTG ACT
RCA Control Template	Phosphate – CCC TCT CTC CTC TAT TAT **GCG ATA AGT CCC TAA CTG ACT ATG GCC T** TAT TTT CTC CTC CTG ACT
RCA Primer	GAG GAG AGA GGG AGT CAG GAG GAG

Padlock Ligation

The ligation was performed with a total reaction volume of 60 µL in 1X ligase buffer containing 40 mM Tris-HCl, 10 mM $MgCl_2$, 10 mM DTT, and 0.5 mM ATP at pH 7.8. A template concentration of 40 µM and a primer concentration of 20 µM were used. The two strands were annealed by heating to 95 °C for 5 min, then cooling down by 1 °C every 2.5 min to 16 °C (standard annealing protocol). Afterwards, 10 U of T4 ligase were added and the mixture was incubated at 16 °C overnight. The ligation product was used without further purification.

RCA

RCA was performed at a total reaction volume of 120 µL in 1X polymerase buffer, containing 50 mM Tris-HCl, 10 mM $(NH_4)_2SO_4$, 4 mM DTT, and 10 mM $MgCl_2$ at pH 7.5. 10 µL of the ligation mixture were used. A total dNTP concentration of 15 mM was used, and the mixture of nucleotides was adjusted to the template sequence. For the synthesis of azide-modified RCA products, 50 % of dATP was substituted with N^6-(6-Azido)hexyl-dATP. After mixing, 40 U of Φ29 polymerase were added and the mixture was incubated at 30 °C for 48 h. Afterwards the polymerase was deactivated by heating to 65 °C for 10 min. GE was performed in TBE buffer (89 mM Tris, 89 mM boric acid, 2 mM EDTA) and staining was performed with ROTI GelStain Red. Gel images were inverted using ImageJ and the contrast was enhanced to 2 % saturated pixels. ^1H-^{13}C-HSQC spectra of native and N^6-(6-azido)hexyl-modified RCA products in D_2O were recorded with a BRUKER Avance Neo 600 NMR spectrometer.

Click Reaction with 5/6-FAM

The click reaction was performed in a total reaction volume of 350 µL. The RCA product was used without further purification and was diluted with 228 µL of a buffer containing 10 mM Tris-HCl and 0.1 mM $MgCl_2$ at pH 7.4 or 12.2. 2 µL of a stock solution of DBCO-PEG_4-5/6-FAM in DMSO (1 mg/mL) was added to achieve final concentration of 6.5 µM. The mixture was incubated for 24 h at RT or 95 °C. Afterwards the RCA products were precipitated by adding 50 µL of 3M NaCl and 900 µL of iso-propanol to the mixture and cooling to -80 °C for 1 h. The mixture was centrifuged at 15 000 rpm for 30 min and washed with a mixture of 70 % iso-propanol and 30 % water. The RCA product was lyophilized and redissolved at a concentration of 5 µg/mL. Absorbance and fluorescence spectra were recorded with a SpectraMax M3 microplate reader by Molecular Devices. The excitation wavelength was 485 nm and the PMT gain was set to medium with 6 flashes per read.

NOTA-DBCO Synthesis

The synthesis was performed analogous to the reported procedure.[403] 10.3 mg DBCO amine (36.2 µmol, 1 eq.) and 56 µL triethyl amine (400 µmol, 11.05 eq.) were added to a Schlenk flask with 2 mL dry DMF and stirred for 10 min at RT. Then 36.3 mg of NOTA-NHS ester (55.4 µmol, 1.53 eq.) were added and the mixture was stirred over night. 1 mL of water was added to hydrolyze the excess NHS ester. The solvents were removed *in vacuo* and the residue was dissolved in methanol. The product was purified using the HPLC system described above, equipped with a Phenomenex Gemini Nx-C18 column (10 x 250 mm, 5 µm particle size). The eluents A (H_2O/MeCN, 95/5 V/V) and B (H_2O/MeCN, 5/95 V/V) were used at a flow rate of 4 mL/min and the following gradient: 0-5 min: 30 % B, 5-35 min: 30-80 % B. Under these conditions, NOTA-DBCO was eluted at approximately 7 minutes. After lyophilisation, 5.5 mg of NOTA-DBCO were obtained as a white solid (27 % yield). ESI- MS: m/z = 562.2682 $[M+H]^+$, 579.2925 $[M+NH_4]^+$ and 584.2479 $[M+Na]^+$. ^1H-NMR (400 MHz, CD_3OD): δ = 7.66 (d, J = 7.2 Hz, 1H), 7.50 (m, 1 H), 7.44 (m, 3 H), 7.35 (m, 2 H), 7.26 (d, J = 7.6 Hz, 1 H), 5.13 (d, J = 14.1 Hz, 1 H), 3.71 (m, 4 H), 3.39 (s, 2 H), 3.22 (t, J = 6.6 Hz, 2 H), 3.03 (m, 12 H), 2.84 (m, 2 H), 2.49 (m, 1 H), 2.16 (m, 1 H).

NOTA-DNF Synthesis

2.5 mg of NOTA-DBCO were dissolved in 100 µL of a MeOH/H_2O mixture (50/50, v/v). 480 µL of azide modified RCA product, synthesized like described above, were added without further purification. The mixture was diluted with 420 µL of a buffer containing 10 mM Tris-HCl and 0.1 mM $MgCl_2$ at pH 12.2 to a final reaction volume of 1 mL and incubated at RT over night. The DNFs were separated from the reaction mixture using a Satorius Vivaspin centrifuge filter with a MWCO of 3 kDa and washed 3 times with water. After lyophilisation 0.8 mg of NOTA functionalized DNFs were obtained. DOTA-DNF synthesis was performed analogously. ^{1}H-NMR spectra of native and DOTA-DNFs in D_2O were recorded on a Bruker Avance III 400 NMR spectrometer.

Alexa Fluor 488-DNFs

The synthesis was performed analogous to the NOTA-DNFs. 10 µL of a AF488-DBCO solution (1 mg/mL) were added to a mixture, resulting in a final concentration of 12.6 µM in the final reaction volume of 1 mL.

Scaning Electron Microscopy

Samples (1-5µL) were applied to a silicon wafer and dried at room temperature over night. The wafer was attached to the sample holder using carbon tape and the sample was coated with ~3 nm carbon using a Leica EM ACE600 sputter coater. Measurements were performed on a Hitachi SU9000 electron microscope using a secondary electron detector. An acceleration voltage of 30 keV at 10 µA was used. Particle diameters were measured using ImageJ.

Dox Loading

The RCA product was lyophilized and redissolved to generate a stock solution with 2.8 mg/mL RCA product in a buffer containing 140 mM KCl, 1 mM $MgCl_2$ and 10 mM KH_2PO_4. The final volume was 200 µL and RCA concentrations were adjusted to 0.01, 0.05, 0.1, 0.5 and 1 mg/mL. 0.72 µL of a stock solution of Dox in buffer (2.76 µM) were added to reach a Dox concentration of 10 µM. Samples were incubated at RT for 30 minutes and fluorescence spectra were recorded with λ_{Ex} = 488 nm.

4. DNA Click-Functionalization with Hyperpolarizable Labels

4.1 Aim and Motivation

This chapter focusses on the development of PHIP-labeled aptamers as promising tools for the targeted MRI imaging of tumors. MRI is an appealing imaging technique, since it is non-invasive and does not rely on ionizing radiation, unlike for example CT. MRI relies on strong external magnetic fields in order to achieve sufficient contrast. These magnetic fields are usually generated by superconducting coils which are cooled with liquid helium, making MRI machines complicated and expensive to operate. An alternative way to increase MRI quality is through the use of contrast agents. The most common contrast agents are Gd^{3+}-based compounds, which are most effective during high-field MRI, due to their paramagnetic properties. For the purpose of imaging with low magnetic fields, e.g. in portable MRI machines, new contrast agents are being developed, whose nuclear magnetization is artificially increased through PHIP. Contrast agents can also be designed to accumulate in specific tissues by being conjugated to cell specific metabolites or targeting agents like aptamers or antibodies. These targeted contrast agents enable high resolution imaging of anatomical structures and help to differentiate between healthy and diseased tissues. They are especially useful during the diagnosis of cancer, since they allow an accurate assessment of the disease progression and the localization of metastases. Among targeting agents, aptamers stand out since they are cost efficient, exhibit low immunogenicity and can readily be chemically modified. While the concept of a PHIP labeled aptamer has already been demonstrated in 2023 by Brenske *et al.* [282] (see **chapter 1.6.6**), this chapter introduces a new approach to generate them. The original method employs a bottom-up synthesis strategy. It starts by attaching an alkyne function to an uracil nucleobase through Sonogashira coupling. The modified nucleobase is then functionalized with a 2'-deoxy ribose unit and a phosphoramidite group, before it is incorporated into the aptamer through solid-phase synthesis. Since this whole process needs to be repeated for each different alkyne function and aptamer sequence, this synthesis strategy is very labor intensive. In order to reduce the synthetic effort, this chapter introduces a modular approach, in which the PHIP label is conjugated post-synthetically to the DNA through Click chemistry (**Scheme 1**). This also allows for independent optimization of the PHIP label before attachment to the aptamer. To implement this strategy, a Click functionality is first introduced into the DNA. This is achieved through NHS ester coupling of a 5'-NH_2-DNA with DBCO-NHS ester (**Scheme 1a**). Instead of an aptamer, a 9-mer with the sequence 5'-$NH_2(CH_2)_6$-AACAACCAT-3' is used as a model DNA. This sequence has two important features: firstly, it forms no secondary structures and is not self-complementary, therefore eliminating these variables when evaluating the kinetics of the Click reaction and the hyperpolarization. Secondly, it includes exactly one thymine base, whose CH_3 group generates a distinct peak in the ^{1}H-NMR spectrum that can be used to obtain quantitative information about the species present in solution. The DNA is also complexed with amphiphilic amines (see **chapter 1.4.3**) to enable its solubility in organic solvents, which serves two purposes: Firstly, it allows the amine-NHS ester coupling to be performed in aprotic organic solvents (DMSO, DMF), which are the only solvents compatible with DBCO-NHS. Secondly, the DNA needs to be soluble in methanol-d_4, which is the preferred solvent for the catalytic PHIP reaction. In order to maximize its solubility in methanol, amino methoxy polyethyleneglycol (mPEG-NH_2) is the preferred

ligand for DNA complexation. But due to the presence of free amino groups, it is unclear whether the two step complexation method with ANI-HCl and mPEG-NH_2 is compatible with the amine-NHS coupling step. As an alternative surfactant, which does not contain a primary amino group, didodecyldimethylammonium bromid (DDAB) is also used in this work. Terminal functionalization through amino-NHS coupling has already been demonstrated in the literature for DDAB-complexed DNA.[306]

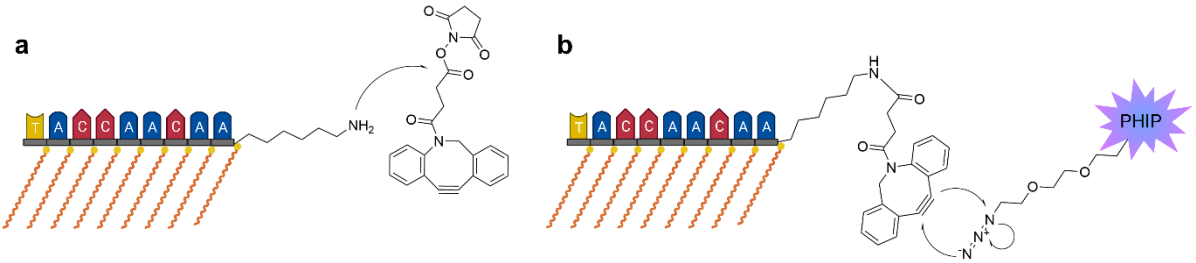

Scheme 1. DNA Click labeling strategy. (**a**) 5'-DBCO functionalization of DNA surfactant complex through amine-NHS coupling. (**b**) Click labeling of DBCO functionalized DNA with azide bearing PHIP tag. Created in BioRender. Rath, W. (2025) https://BioRender.com/u04j119.

4.2 Results

4.2.1 DBCO functionalization of mPEG-DNA complexes

First, the NH_2-DNA 9-mer was obtained through standard solid-phase synthesis with commercial phosphoramidites. The NH_2-DNA was precipitated from aqueous solution with the help of ANI-HCl. The DNA-ANI complexes were then dissolved in DMSO and reacted with DBCO-NHS ester. Afterwards the ligand exchange was performed with mPEG-NH_2 (MW: 550 Da) and the complex was purified using a centrifugal concentrator. Notably, the NHS coupling was performed before the addition of mPEG-NH_2, since this large excess of a primary amine compound would compete with the coupling to the DNA. After purification, ^{1}H-^{13}C-HSQC spectra of the native mPEG-DNA complexes and the DBCO-NHS treated mPEG-DNA complexes were recorded. **Figure 46** shows the ^{1}H-^{13}C-HSQC spectrum of the native mPEG-DNA complex recorded in methanol-d_4. The spectrum exhibits sharp peaks that can all be assigned to the structural features of the mPEG-DNA complex. The peaks that correspond to nuclei at the periphery of the complex are especially distinct, indicating excellent mobility in the solvent. For example, the peaks corresponding to the 5'-alkyl chain (^{1}H: 1.5 ppm, ^{13}C: 30 ppm, approx.) allow the differentiation between CH_2 units with slightly different chemical environment. On the other hand, the peak corresponding to the 5'-CH_2 unit of the ribose exhibits some broadening, indicating that rotation around this bond at the center of the complex is slightly hindered. The high quality of peaks for nuclei at the periphery of the complex allows for accurate integration of the thymine CH_3 peak and the mPEG CH_3 peak (**Figure 47**). A ratio of 1:9 between these integrals can be observed, which confirms quantitative complexation, since the NH_2-DNA 9-mer contains 9 phosphate groups.

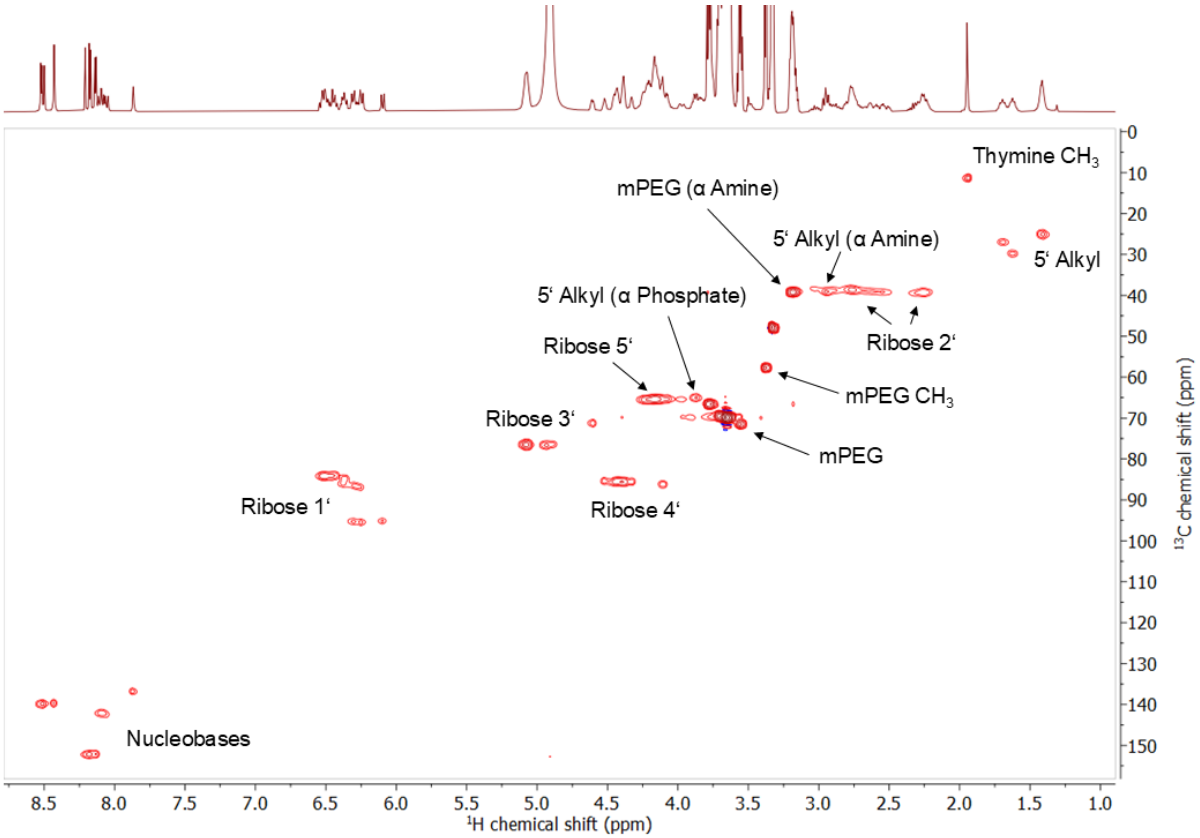

Figure 46. ^{1}H-^{13}C-HSQC spectrum (600 MHz) of native mPEG-DNA complex in methanol-d_4 with peak assignments.

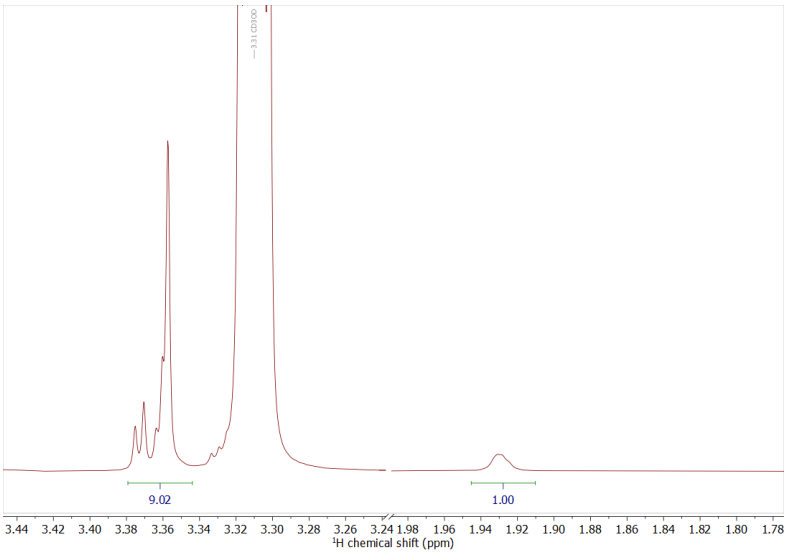

Figure 47. ^{1}H-NMR spectrum (600 MHz) of native mPEG-DNA complex in methanol-d_4 with integrals for the thymine CH_3 peak (1.9 ppm) and the mPEG CH_3 peak (3.4 ppm).

Figure 48 shows the superimposed ^{1}H-^{13}C-HSQC spectra of the native mPEG-DNA complex and the DBCO-NHS treated mPEG-DNA complex in methanl-d_4. Surprisingly, no difference between the spectra can be observed, indicating that no reaction took place. The most likely explanation for this is that the primary NH_2 group at the 5’-end of the DNA got protonated by the ANI-HCl. Protonated NH_2 groups do not contain a lone electron pair, consequently they cannot react as a nucleophile. Since the amine group in ANI-HCl is protonated, a direct competition reaction of ANI-HCl with the amine-NHS ester coupling can be ruled out. Since primary amines are more basic than aromatic amines, and ANI-HCl got added in a large excess, it is likely that the 5’-NH_2 group of the DNA got fully protonated and could not react as a nucleophile.

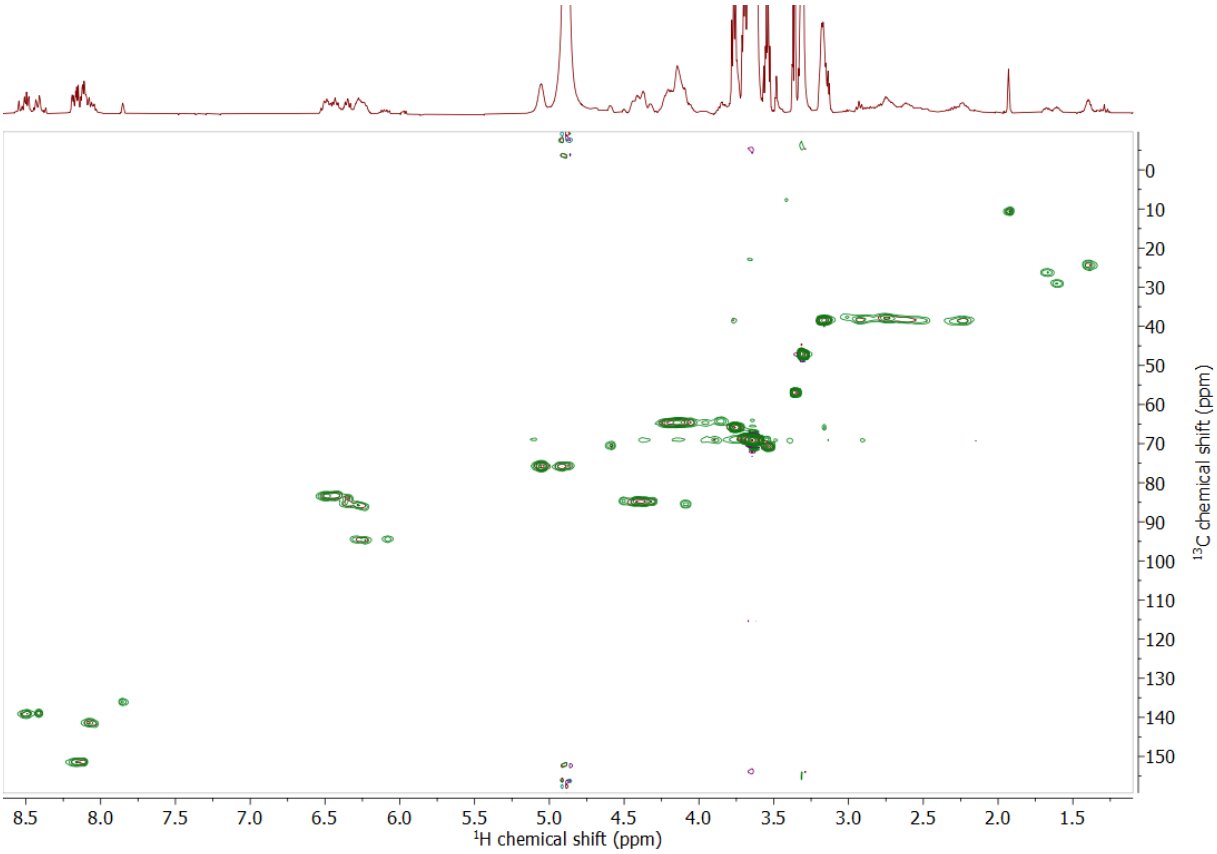

Figure 48. Superimposed ^{1}H-^{13}C-HSQC spectra (600 MHz) of native mPEG-DNA complex (green) and DBCO-NHS treated mPEG-DNA complex (red) in methanol-d_4.

4.2.2 DBCO functionalization of DDAB-DNA complexes

Since the precipitation of the DNA with ANI-HCl interferes with the amine-NHS ester coupling, the surfactant for the complexation was changed to DDAB, which is quaternary ammonium compound that cannot transfer protons. The ^{1}H-^{13}C-HSQC spectrum of the native DDAB-DNA complex recorded in $CDCl_3$ is shown in **Figure 49**. This spectrum is heavily dominated by the signals corresponding to DDAB (compare **Figure 50**), and DNA signals are hardly visible. This hints at an excess of DDAB still being present in the precipitate, which is hard to remove through centrifugation and washing alone, since the DDAB-DNA precipitate is much finer than the ANI-DNA precipitate. Nevertheless, the precipitate was dissolved in DMF, reacted with DBCO-NHS and purified with a centrifugal concentrator. The superimposed ^{1}H-^{13}C-HSQC spectra of the native and functionalized DDAB-DNA complex in $CDCl_3$ are shown in **Figure 51**. In the HSQC spectrum of the DBCO-NHS treated DDAB-DNA complex, peaks corresponding to the DNA are clearly visible (^{1}H: 3.0 ppm, ^{13}C: 40 ppm; ^{1}H: 4.5-3.5 ppm, ^{13}C: 65 ppm; ^{1}H: 4.5-4.0 ppm, ^{13}C: 85 ppm; ^{1}H: 6.5 ppm, ^{13}C: 85 ppm;), but significantly broadened. This indicates limited mobility of the DNA chain, which might be caused by the formation of micelles that limit DNA-solvent interactions. Micelle formation could also possibly cause the large excess of DDAB after precipitation (**Figure 49**). The DDAB signals are still dominating the spectrum, likely because DDAB is more mobile, by virtue of being positioned at the periphery of the complex and its larger compatibility with the unpolar solvent. Different NMR solvents (acetone-d_6, acetonitrile-d_3, THF-d_8, cyclohexane-d_{12}) were tested with the aim of improving signal quality, but the complex was only soluble in $CDCl_3$ and CD_2Cl_2.

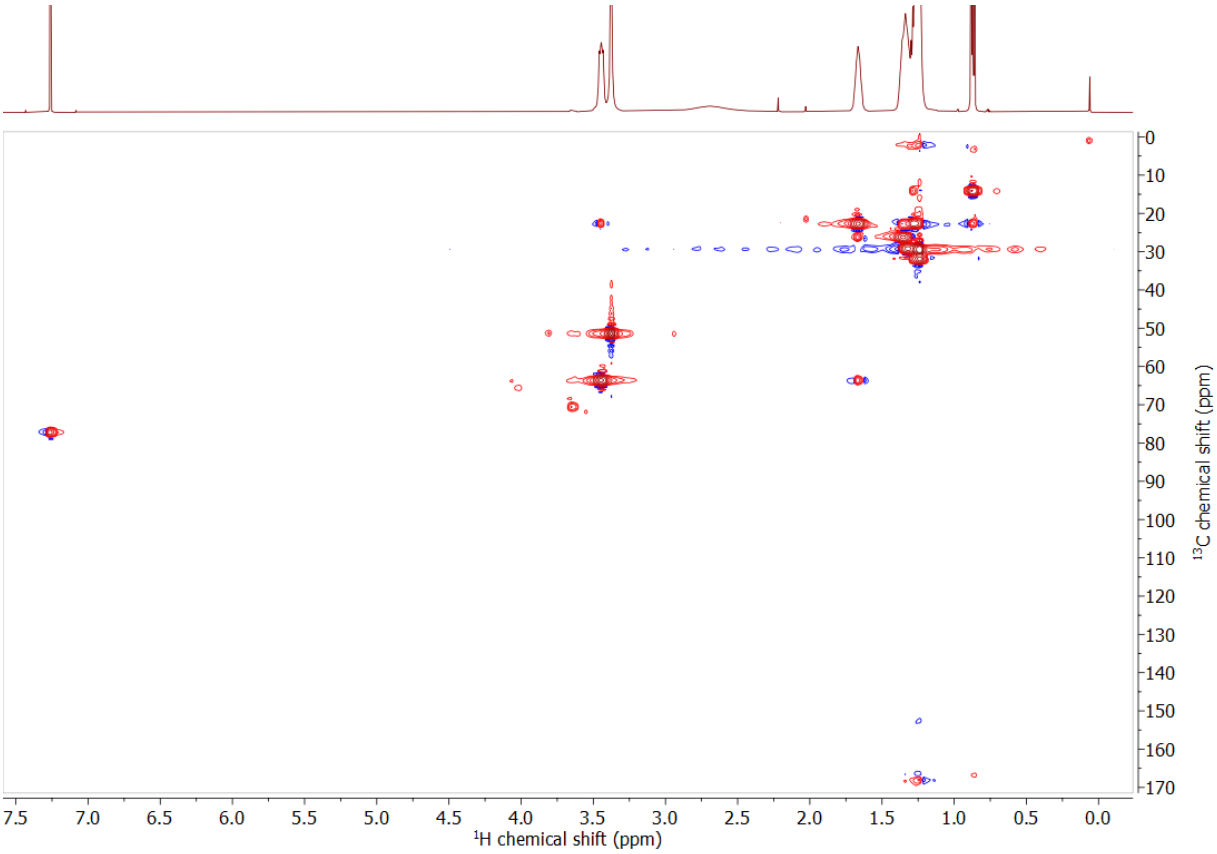

Figure 49. ^{1}H-^{13}C-HSQC spectrum (600 MHz) of native DDAB-DNA complex in $CDCl_3$.

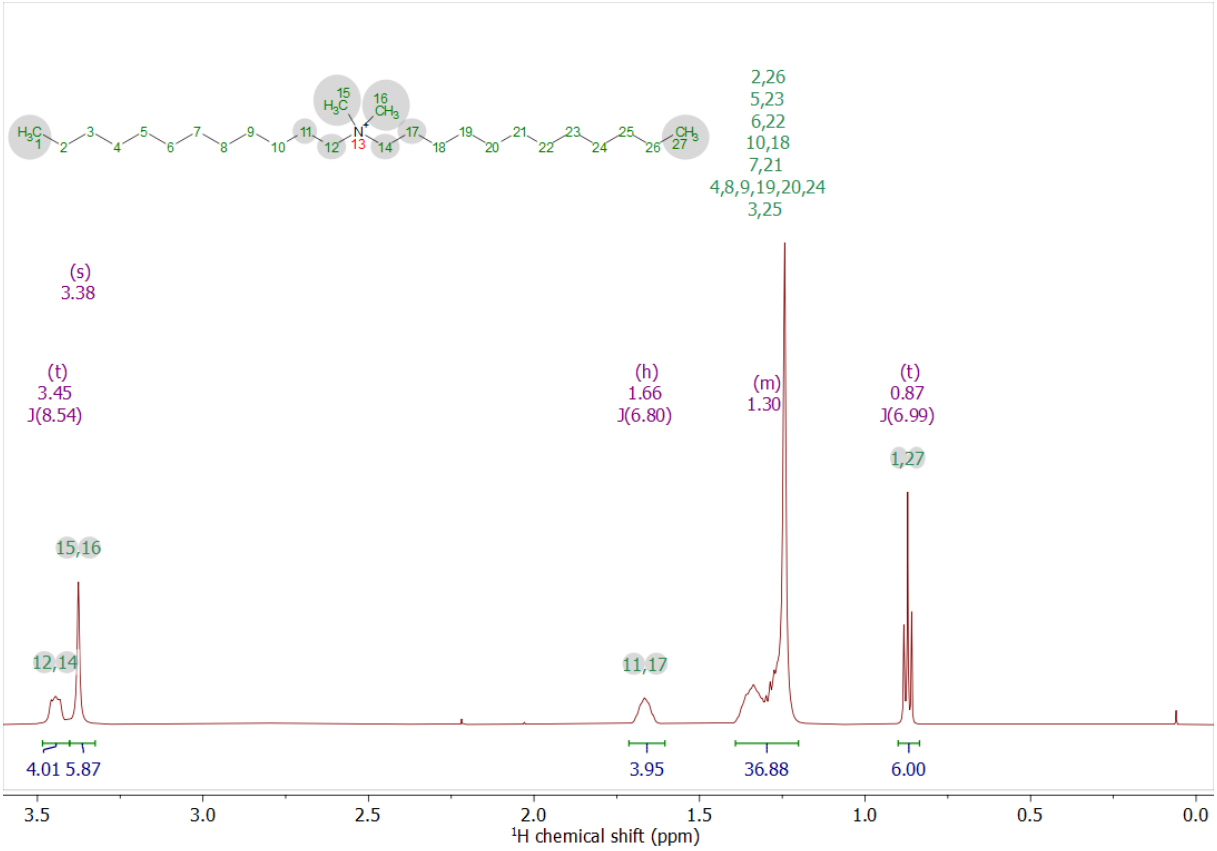

Figure 50. ^{1}H-NMR spectrum (600 MHz) of DDAB in $CDCl_3$ with peak assignments.

Due to the poor signal quality, the thymine CH_3 peak is not visible, and therefore the degree of DDAB complexation cannot be determined. Furthermore, the distinction of aromatic signals in the HSQC spectrum originating from DNA or DBCO is not possible. However, the successful functionalization of the DNA with DBCO can be confirmed through the presence of two characteristic signals, which correspond to the CH_2 unit of the cyclooctyne ring (compare **Figure 52** and **53**). This CH_2 signal is splitting up, since the two corresponding protons are locked in a specific conformation and are therefore not chemically equivalent. In **Figure 51** two different populations of these characteristic signals with different chemical shifts can be observed. This could hint at the presence of a different DDAB-DNA species in solution, for example the formation of micelles. Another possible source of these signals might be reacted DBCO, originating from an unknown side reaction. The labeling efficiency cannot be determined from the HSQC spectrum, since the α-amine hexyl peak is not visible. High-resolution denaturing PAGE was attempted, but no bands were observed, likely because the 9mer was too small for the pores and diffused out of the gel. MALDI-MS requires DDAB to be removed from the DNA backbone through the addition of NaCl, followed by an additional desalting step through a centrifugal concentrator. Since this additional purification step would be associated with a significant loss of limited material, it was not performed. The labelling efficiency was investigated through MALDI-MS by Xinpei Li as part of his Master's thesis "Development of DNA-labels for highly sensitive targeted Magnetic Resonance Imaging", during which no unreacted 5'-NH_2-DNA was found. In the literature, labelling efficiencies of approximately 70 % have been reported.[306]

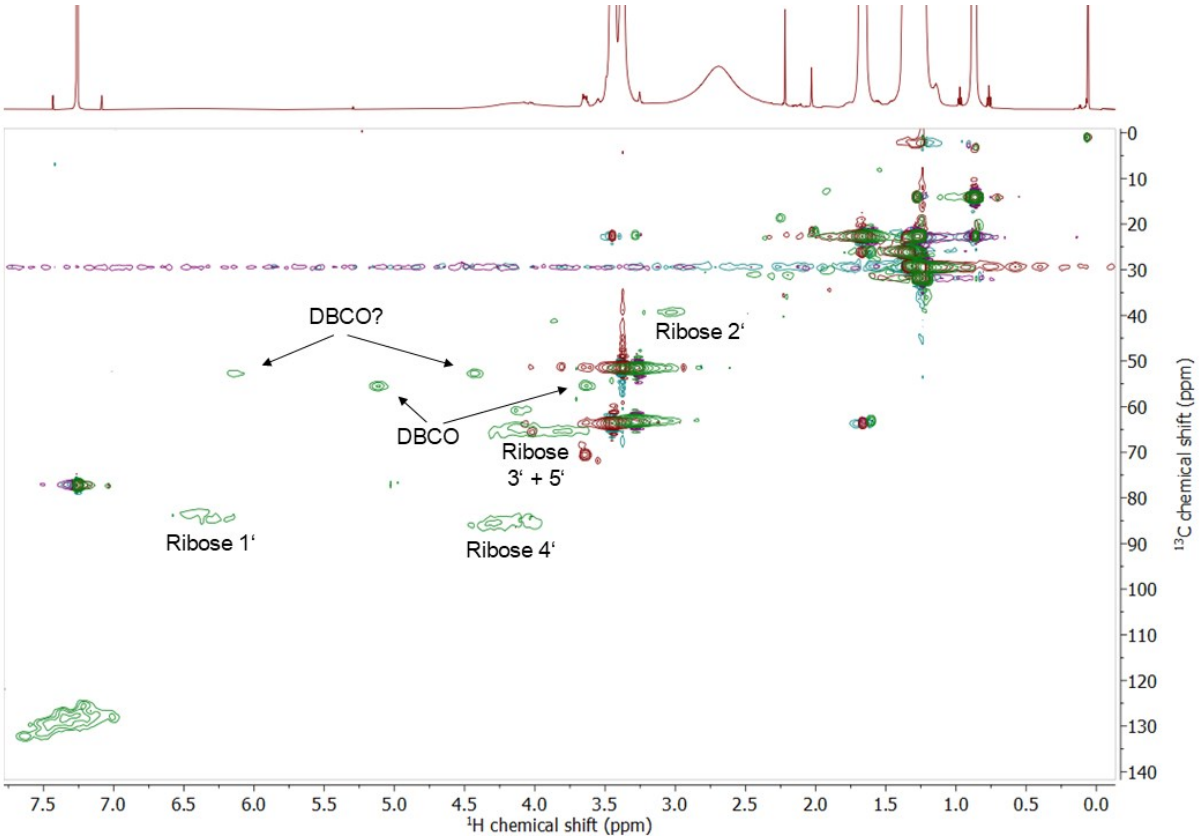

Figure 51. Superimposed ^{1}H-^{13}C-HSQC spectra (600 MHz) of native DDAB-DNA complex (red) and DBCO-NHS treated DDAB-DNA complex (green) in $CDCl_3$.

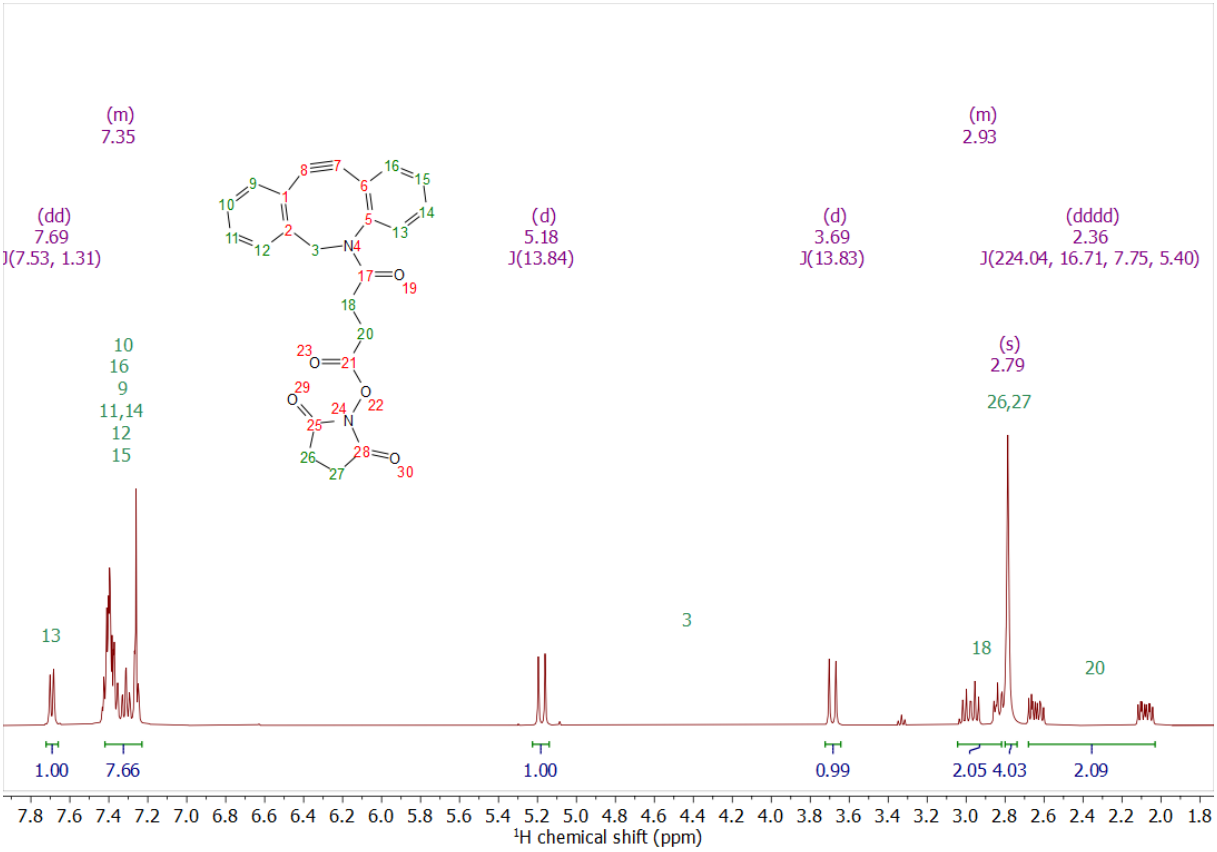

Figure 52. ^{1}H-NMR spectrum (600 MHz) of DBCO-NHS in $CDCl_3$ with peak assignments.

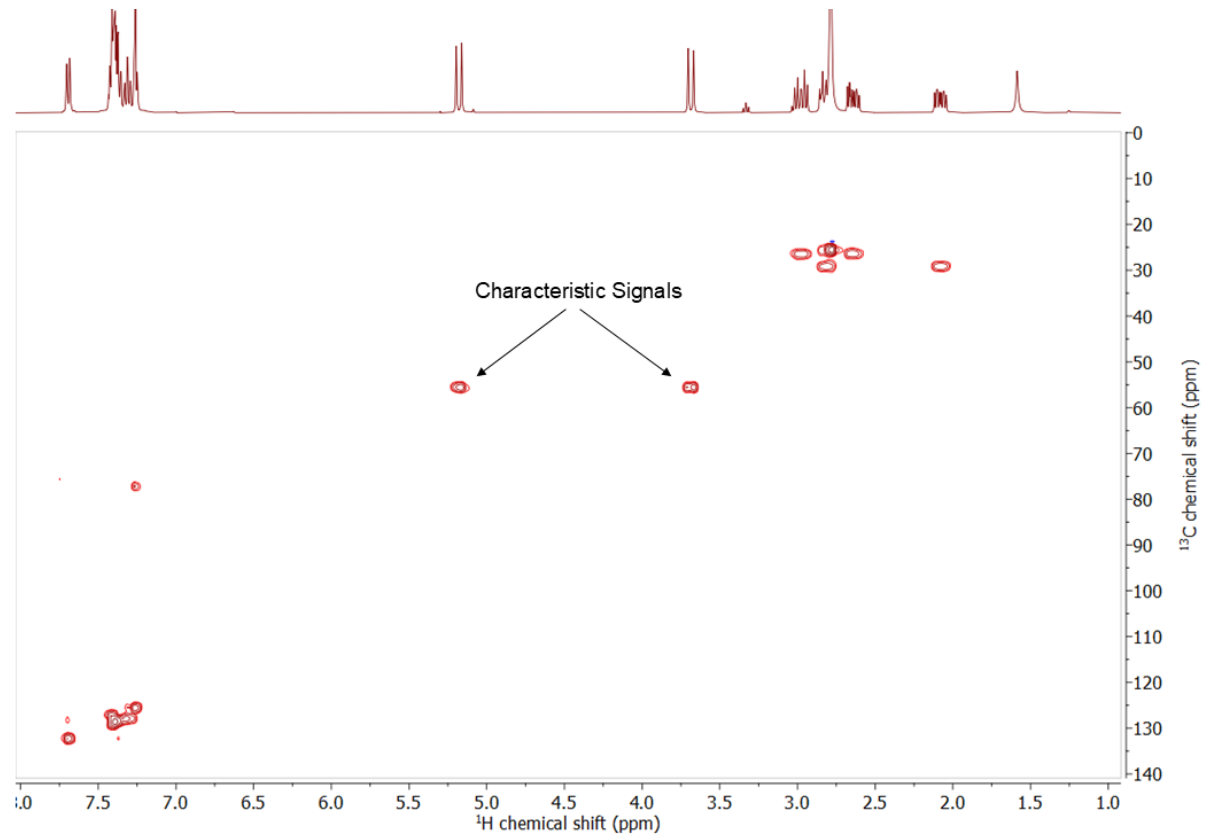

Figure 53. ^{1}H-^{13}C-HSQC spectrum (600 MHz) of DBCO-NHS in $CDCl_3$ highlighting the characteristic peaks corresponding to position 3 (compare **Figure 53**).

4.2.3 Design and synthesis of PHIP labels

In the larger context of this project, two different azide functionalized PHIP labels were designed and synthesized. Firstly, a $^{15}N_2$-diazirine Click label for SABRE based hyperpolarization was investigated by Xinpei Li in his master's thesis "Development of DNA-labels for highly sensitive targeted Magnetic Resonance Imaging". $^{15}N_2$-diazirines exhibit long T_1 relaxation times and exceptional singlet lifetimes[375], making them ideal candidates to solve the problem of short magnetization lifetimes, which was observed in the 2023 study by Brenske *et al*.[282] They also enable continuous hyperpolarization. The synthesis route for this SABRE label is shown in **Scheme 2**. The design for this label is based on a 2019 study, which reported a method of obtaining $^{15}N_2$-diazirines from amino acids through the use of phenyliodonium diacetate (PIDA) and $^{15}NH_3$.[404] In the same study, the authors also demonstrated the potential use of $^{15}N_2$-diazirines as SABRE compounds. The amino acid that was chosen for the design of the SABRE label for this project was tyrosine. The phenyl rest of tyrosine increases the boiling point of the diazirine, which is necessary to retain the product during the removal of solvents. Tyrosine's OH-group can also be deprotonated quite easily (pK_a = 10), which enables a straightforward nucleophilic substitution to attach a PEG linker with an azide function. The PEG linker serves to increase hydrophilicity and the accessibility of the azide function for the Click reaction. During his master's thesis, Xinpei Li successfully synthesized this molecule and subsequently performed the SABRE experiments, during which a signal enhancement factor of approximately 6000 and a T_1 relaxation time of 32 s were achieved for the $^{15}N_2$-group.

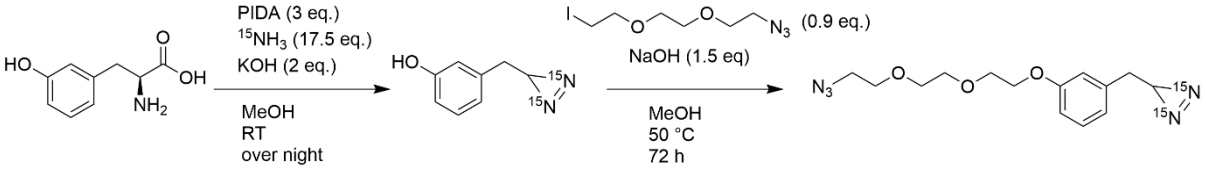

Scheme 2: Synthesis route for azide functionalized SABRE label.

Secondly, a ^{29}Si-based label for hydrogenative PHIP was designed and synthesized by Dr. Jens Köhler and Janko Stoffels (DWI-Leibniz Institute for Interactive Materials). The chemical structure of this PHIP label is shown in **Figure 54**. The design of this label is inspired by the 2023 study by Brenske *et al.*, which concluded that a DNA label for hydrogenative PHIP ideally should incorporate nuclei with long-lived spin states, in order to increase the T_1 relaxation time of the hyperpolarization.[282] The newly designed PHIP label features similar structural elements as the SABRE label, including an aromatic ring and a PEG spacer. The actual PHIP function is comprised of a terminal alkyne group, which can be catalytically hydrogenated, and an adjacent ^{29}Si nucleus, onto which the magnetization can be transferred to increase the T_1 relaxation time. At the time of writing, signal enhancement and T_1 time for this label have not been tested, but its Click reaction with the DBCO functionalized DDAB-DNA is shown below.

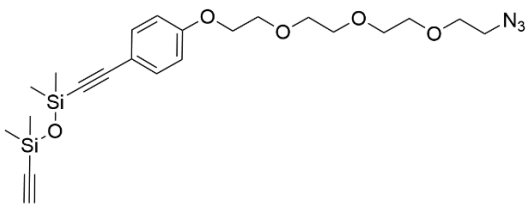

Figure 54. Structure of hydrogenative PHIP label featuring ^{29}Si heteronuclei.

4.2.4 Click-functionalization of DNA with PHIP label

Figure 55 shows the ^{1}H-NMR spectrum of the freshly synthesized PHIP label in $CDCl_3$. After storage, some triazole formation was observed (see **Figure 56**), even though the azide and alkyne function should not be able to react without a Cu catalyst. The most likely explanation for this observation is trace Cu contamination of the laboratory equipment.

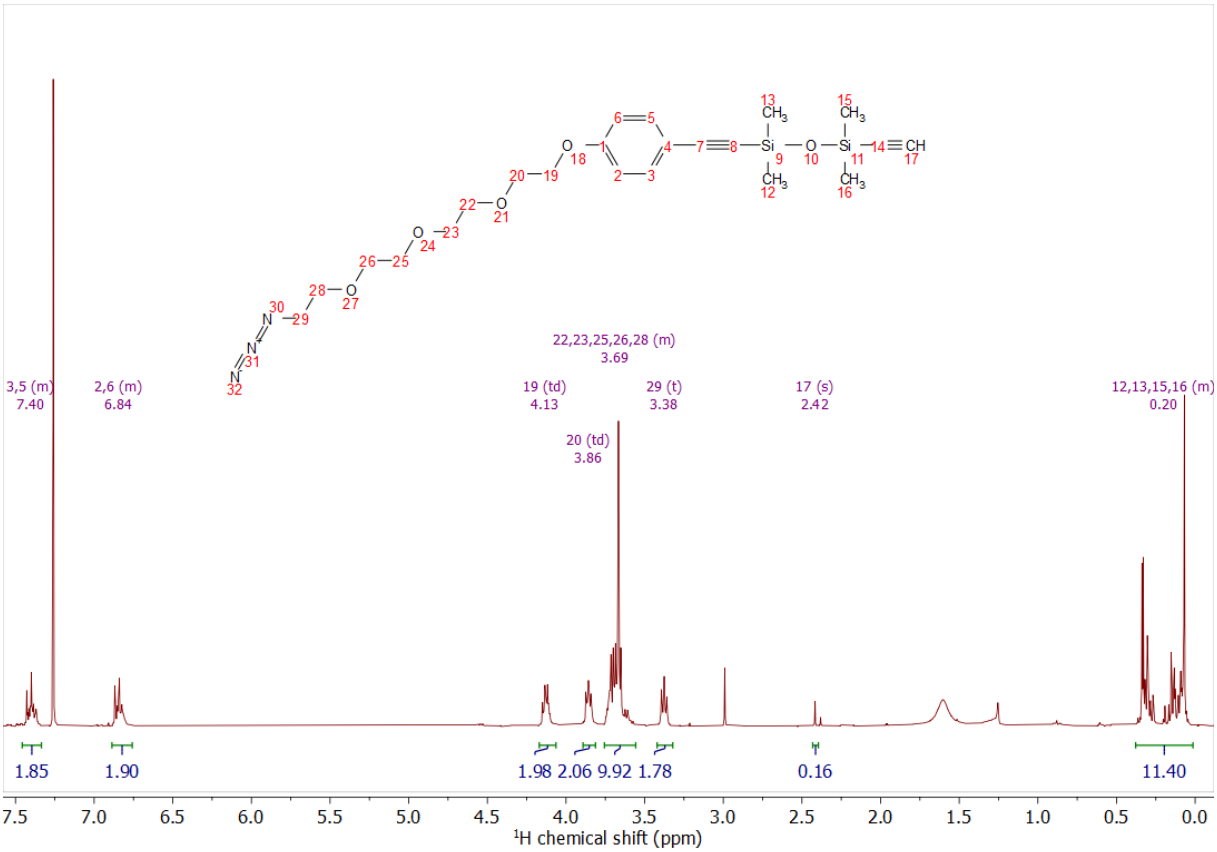

Figure 55. ^{1}H-NMR spectrum (600 MHz) of freshly synthesized PHIP label in $CDCl_3$ with peak assignments.

The freshly synthesized PHIP label was mixed with the DBCO functionalized DDAB-DNA in a 2:1 excess in $CDCl_3$. After the addition, ^{1}H kinetic spectra were recorded every 4 min, and after approximately 208 min a final ^{1}H-^{13}C-HSQC spectrum was recorded, which is shown in **Figure 57**. All new signals (compared to **Figure 51**) can be assigned to the PHIP label. The signal corresponding to the CH_2 group in α-position to the azide (position 29 in **Figure 57**) confirms the formation of the triazole. The original α-azide signal (^{1}H: 3.35 ppm,^{13}C: 70.5 ppm) is still present, since the PHIP label was added in excess, but additionally, the α-triazole signal can be clearly observed (^{1}H: 4.55 ppm,^{13}C: 50.4 ppm). In conjunction with this, the

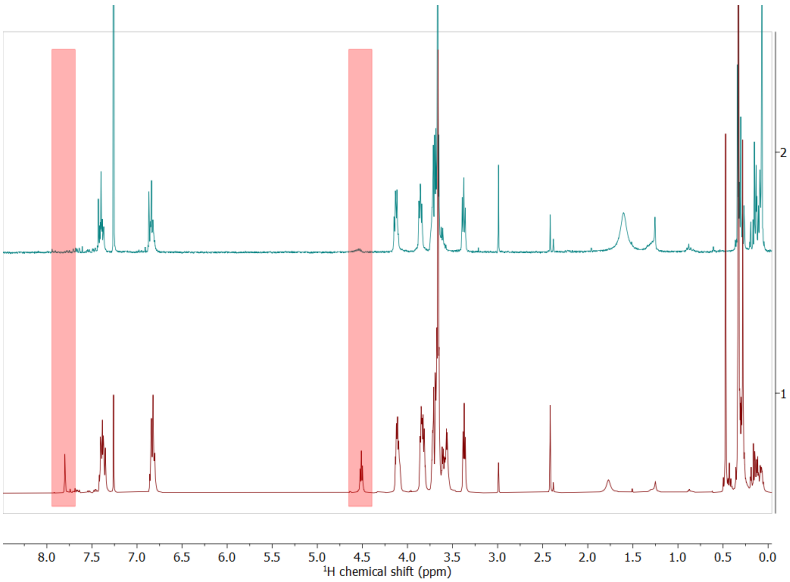

Figure 56. Stacked ^{1}H-NMR spectra (600 MHz) of PHIP label in $CDCl_3$ before (top) and after (bottom) storage.

characteristic DBCO signals (see **Figure 53**) disappear, meaning all DBCO was converted after 208 min. Contrary to this, the intensity of the signals corresponding to the unidentified DBCO species increased. This supports the hypothesis that they originate from reacted DBCO, whose presence in **Figure 51** can be explained by DBCO undergoing some side reaction during storage or amine-NHS coupling (compare **chapter 4.2.2**).

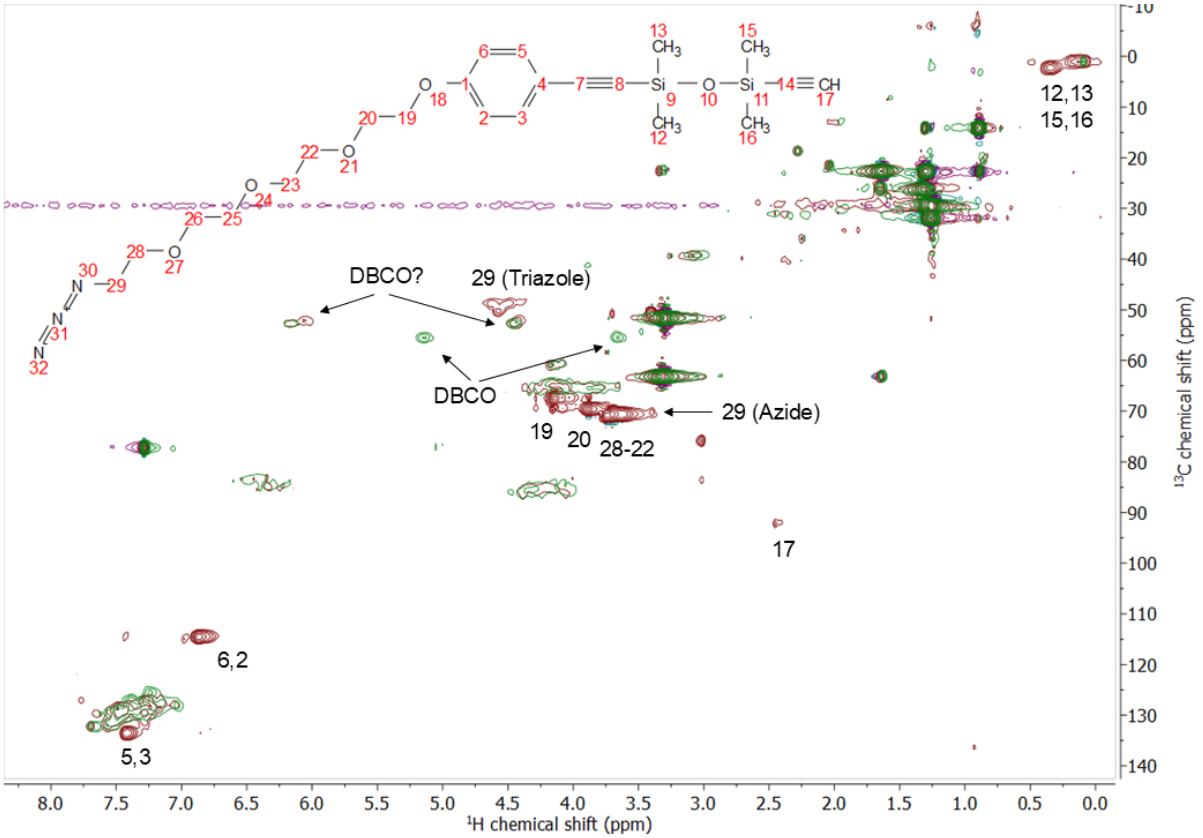

Figure 57. Superimposed ^{1}H-^{13}C-HSQC spectra (600 MHz) of DDAB-DNA complex in $CDCl_3$ before (green) and after (red) Click reaction with peak assignment for the PHIP label.

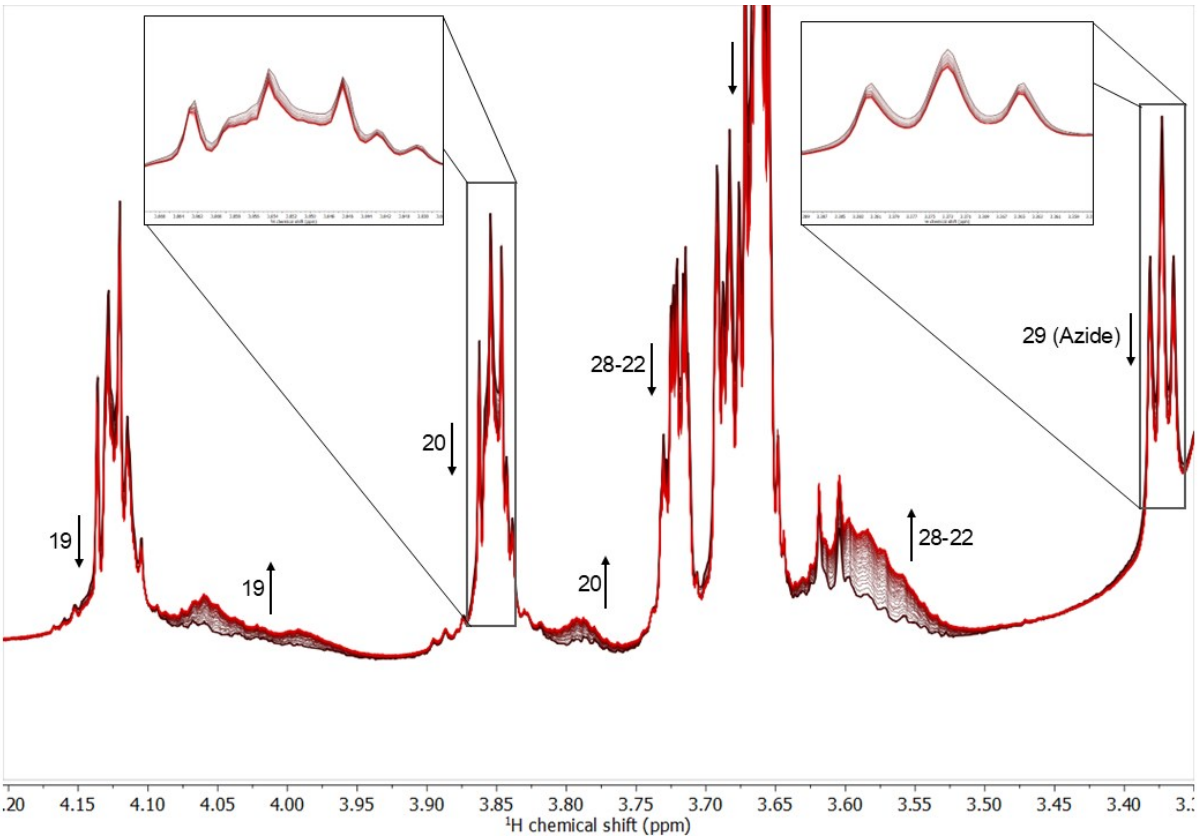

Figure 58. Stacked ^{1}H Click kinetic spectra (600 MHz) in $CDCl_3$ monitoring changes of signals corresponding to PEG spacer of PHIP label.

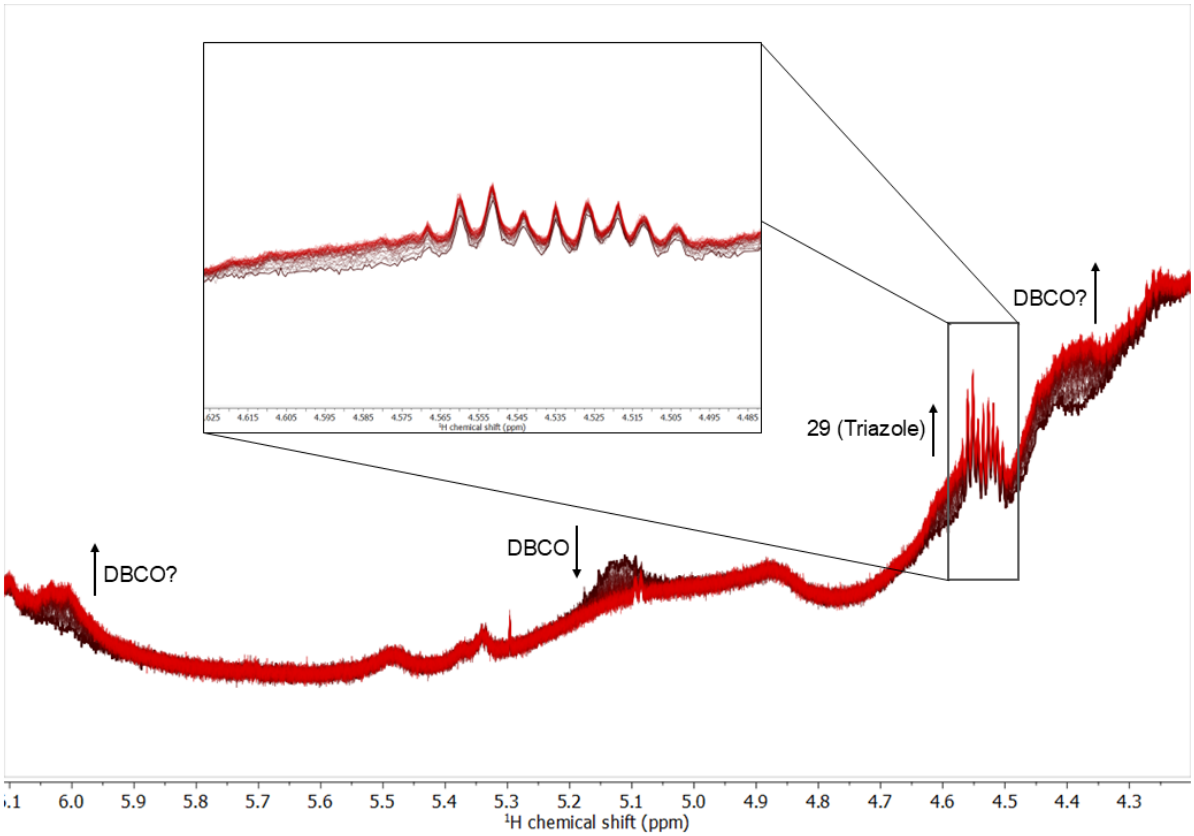

Figure 59. Stacked ^{1}H Click kinetic spectra (600 MHz) in $CDCl_3$ monitoring changes of signals corresponding to DBCO and α-triazole PEG unit.

The ^{1}H kinetic spectra of the Click reaction in $CDCl_3$ are shown in **Figure 58** and **59**. Here the progress of the reaction can clearly be observed with the help of the signals between 3.3 ppm and 6.1 ppm. The substrate peaks between 4.15 ppm and 3.3 ppm, which correspond to the nuclei of the PEG spacer, all decrease in intensity over time, while the product peaks at slightly lower ppm simultaneously increase. Additionally, some broadening of the product peaks compared to the substrate peaks can be observed, likely due to the decreased mobility of the nuclei after being attached to the DDAB-DNA complex. Around 3.35 ppm a decrease in intensity over time can be observed for the α-azide peak, while the α-triazole peak at 4.55 ppm increases in intensity. Lastly, at 5.1 ppm the intensity of the DBCO peak can be seen to decrease with time, while at 6.0 ppm and 4.35 ppm two peaks increase in intensity, which likely correspond to the reacted DBCO. The direction of these changes in intensity over time indicate that the peaks in the HSQC spectrum (**Figure 57**) were correctly assigned to the substrates and the product respectively. The labelling efficiency of the Click reaction can also be estimated from the HSQC spectrum (**Figure 57**). The full disappearance of the characteristic DBCO peaks indicates full conversion of DBCO, although this could not be confirmed through PAGE or MALDI-MS, due to the same problems described in **chapter 4.2.2**.

4.3 Discussion and Outlook

In this chapter, the post-synthetic, terminal Click functionalization of DNA with a hyperpolarizable label in organic solvents was successfully demonstrated. First, a 5'-NH_2-DNA 9-mer was functionalized with a DBCO group at the 5'-end by amino-NHS coupling. To enable DNA solubility in organic solvents for the DBCO coupling reaction, it was complexed with amphiphilic amines. The two step complexation method with ANI-HCl, followed by mPEG-NH_2, was first investigated, since it also enables DNA solubility in methanol for the hyperpolarization reaction. DBCO-NHS was added after the precipitation step with ANI-HCl, but ^{1}H-^{13}C-HSQC spectra showed that the amine-NHS coupling did not take place. The most likely explanation for this is, that the 5-NH_2-group of the DNA was protonated by ANI-HCl and therefore was not able to react as a nucleophile. Generally, the two step complexation method using ANI-HCl and mPEG-NH_2 seems to not be well compatible with the amine-NHS coupling reaction. If DBCO-NHS would have been added at a later step during the complexation process, the large excess of mPEG-NH_2 in the mixture might compete with the coupling reaction. To prevent this, the complex would need to be purified before and after the reaction with DBCO-NHS. This double purification would drastically reduce the yield. A possible way to sidestep this problem would be to functionalize the DNA in the aqueous phase with a water-soluble DBCO compound, for example DBCO-sulfo-NHS, before precipitating it with ANI-HCl. With this method, the degree of functionalization could easily be determined through MALDI-MS before precipitating the DNA. Another solution would be to use another coupling reaction that is unaffected by the presence of ANI-HCl, for example thiol-maleimide coupling, although amine-NHS coupling is very appealing due to the formation of a stable amide product.

The solution that was employed in this chapter was to use DDAB as a surfactant for the precipitation of the DNA, which is a quaternary ammonium compound that does not protonate the 5'-NH_2-group. ^{1}H-^{13}C-HSQC spectra showed that DBCO was successfully coupled to the DNA through the presence of two characteristic peaks, although the quality of the NMR spectra was much lower compared to the mPEG-DNA complexes. This could be explained by the low mobility of the complex in solution, likely caused by the formation of micelles or by strong hydrophobic interactions between the dodecyl chains of the DDAB ligands. In an effort to improve the quality of the NMR signal, different NMR solvents (acetone-d_6, acetonitrile-d_3,

THF-d_8, cyclohexane-d_{12}) were screened, but $CDCl_3$ and CD_2Cl_2 were the only suitable solvents. This leads to two problems, which might hinder this approach in the future: Firstly, the low quality of the NMR spectra prevents a comprehensive NMR analysis of the DDAB-DNA complexes. For example, due to the thymine CH_3 peak not being visible, it is impossible to confirm the quantitative complexation of the DNA phosphate groups through NMR. Secondly, the small number of suitable solvents limits the range of catalysts that can be used for the hyperpolarization reaction, which is typically performed in methanol. For these reasons, future work might focus on the DBCO-functionalization of mPEG-DNA complexes, as discussed in the paragraph above.

Despite these potential future problems, the DDAB-DNA complexes were successfully functionalized with DBCO and the Click reaction with the PHIP label was performed. A ^{1}H-NMR kinetic and an endpoint ^{1}H-^{13}C-HSQC spectrum were recorded, which confirmed the completion of the reaction after approximately 3 h. This highlights the reliability and speed of the DBCO-azide coupling reaction. While this is a promising result, it is still worth noting that 3 h is much longer than the T_1 relaxation time of the hyperpolarization. This necessitates that the Click reaction is performed before the hyperpolarization, which will lead to slower hyperpolarization kinetics and therefore a decrease in signal enhancement. Furthermore, it will be interesting to observe how the kinetics of the Click reaction are influenced by switching to mPEG-DNA complexes. Since the DBCO is attached at the DNA with a $(CH_2)_6$-spacer, it seems plausible that hydrophobic interactions with the dodecyl chains of the DDAB could reduce the accessibility of the DBCO, and therefore slow the kinetics of the Click reaction. This would not be the case when switching to mPEG ligands, on the other hand these could form stronger interactions with the PEG spacer of the PHIP label.

In the future, the yields of the amine-NHS coupling as well as the Click reaction need to be investigated in more detail. MALDI-MS, high-resolution PAGE and HPLC are appealing options for this, but they require the functionalized DNA to be free of salts and surfactants. Additionally, PAGE would necessitate the use of a larger DNA strand (14+ nucleotides).[306] As mentioned above, performing the amine-NHS coupling before precipitating the DNA with ANI would make sample preparation much easier. To assess the yield of the Click reaction through these methods, it might be necessary to utilize a different desalting method, since purification with a centrifuge concentrator is associated with large losses of material, which can also vary greatly between batches.

This study demonstrates that hyperpolarizable aptamers can be obtained with relatively low synthetic effort through a Click labeling approach. In order to transfer these findings to a clinical setting, firstly the 9-mer model DNA needs to be replaced with an aptamer sequence. Switching the DNA sequence will likely affect the kinetics of the Click labeling due to the formation of secondary and tertiary DNA structures, as well as increased size of the DNA. The aptamer sequence can also be freely changed with minimal synthetic effort, which is arguably the biggest strength of this modular labeling approach. Another big priority in the future will be the development of rapid purification techniques to reduce the time between hyperpolarization and application. For example, through the addition of salt, the hyperpolarized DNA could be precipitated from the organic phase and transferred to an aqueous medium. Catalyst immobilization could also speed up the purification process and increase cost efficiency. The water-soluble catalysts that are available at this point are limited by their slow hyperpolarization kinetics, but in the future, they might be a great option for clinical PHIP applications. They would remove the necessity for the DNA to be complexed with amphiphilic amines and

eliminate toxic solvents. Biocompatible hyperpolarization MRI techniques are still in their infancy, but the first *in vivo* applications that were demonstrated very recently[405] exemplify the great potential these techniques have to transform MRI imaging.

4.4 Experimental

General materials

All experiments were performed with ultrapure water (18.2 MΩ cm) from a PURELAB Chorus 1 system by Elga. Unless stated otherwise, all regular solvents were purchased from Fisher Scientific. Deuterated NMR solvents were purchased from Deutero.

5'-amino DNA 9-mer synthesis

DNA synthesis was kindly performed by Mark Loznik (DWI-Leibniz Institute for Interactive Materials) using an ÄKTA OligoPilot Plus oligonucleotide synthesizer by Cytiva. 5G Unylinker 350 by Cytiva was used as solid support. All phosphoramidites, including the 5'-TFA-amino-C_6-phosphoramidite, were purchased from Biosearch Technologies. Phosphoramidites were diluted to 150 mM in acetonitrile (VWR) and coupling was performed with 3 eq. of phosphoramidite. A 250 mM solution of 5-ethylthio tetrazole (ChemGenes) in acetonitrile (VWR) was used as a coupling activator. Detrytilation was performed with a 3 % solution of dichloracetic acid (Sigma) in toluene (TH Geyer). For capping, CapA solution (Sigma) and a 50:50 mixture of CapB1:CapB2 solutions (Sigma) were used. Oxidation was performed with a 50 mM solution of I_2 (TCI) in a 10:90 mixture of water:pyridine (Sigma). After synthesis, the DNA was deprotected and cleaved from the solid support by incubating for 2 h in a 15:20:65 mixture of ammonium hydroxide (Merck):methylamine (Sigma):water. The solution was filtered and washed with a 50:50 mixture of water:ethanol (Höfer Chemie). The ethanol was removed *in vacuo* and the crude DNA was purified through anion exchange chromatography using an ÄKTA Pure 25M chromatograph by Cytiva equipped with a 5 mL HiTrap Q HP column by Cytiva. Buffer A contained 25 mM Tris-base (Fisher Scientific) (pH 8.0), buffer B contained 1 M NaCl (Fisher Scientific), 25 mM Tris base (Fisher Scientific) (pH 8.0) and a gradient from 40 % to 75 % buffer B in 8 column volumes was employed. The DNA was concentrated and desalted using the ÄKTA Pure 25M chromatograph equipped with a HiPrep 26/10 desalting column by Cytiva, employing an isocratic flow of a 80:20 mixture of water:ethanol (Höfer Chemie). Finally, the ethanol was removed *in vacuo* and the DNA was concentrated.

DBCO-DNA PEG complexes

After synthesis, the concentration of 5'-amino DNA solution was determined via absorbance at 260 nm, measured with a Nanodrop One C by ThermoFisher Scientific. 4-(hexyloxy)anilinium hydrochloride (ANI-HCl) was obtained by dissolving 4-(hexyloxy)anilinium (Fisher Scientific) in diethyl ether, then HCl solution (4 M) in dioxane (Sigma) was added until no more precipitation was observed. The precipitate was filtered, washed with diethyl ether end dried. 74.4 mg ANI (324 µmol) were dissolved in 5 mL water, then 5 mL 5'-amino DNA solution (12 µmol) were added, resulting in a 3-fold excess of ANI compared to DNA phosphate groups. After mixing, a fluffy, pink precipitate started forming and the mixture was shaken overnight. The precipitate was centrifuged, washed with water 3 times and lyophilized, resulting in quantitative yield. The DNA-ANI complex was dissolved in 5 mL dry DMSO under Schlenk conditions, 15.5 mg (36 µmol, 3 eq.) of DBCO-NHS ester (abcr) were added and the mixture was stirred at RT overnight. The DMSO was removed *in vacuo*, then 178.2 mg (324 µmol) methoxy PEG amine (MW: 550 Da, Laysan Bio Inc.) were dissolved in 5 mL methanol and added to the DNA-ANI complex. The mixture was stirred at RT overnight. The DNA complex was purified using a Vivaspin centrifugal concentrator (MWCO 3 kDa) by Sartorius.

For this, the membrane of the concentrator was wetted with methanol, then the reaction mixture was centrifuged through the concentrator, washed 3 times with methanol, 2 times with water and lyophilized, yielding 4.7 mg (0.79 µmol, 8 %) DNA-PEG complex. The native DNA-PEG complexes without DBCO-functionalization were prepared analogously, except the DBCO-NHS reaction was skipped.

DBCO-DNA DDAB complexes

149.9 mg on DDAB (324 µmol) (Sigma) were dissolved overnight in 5 mL water. Then 5 mL 5'-amino-DNA (12 µmol) were added, resulting in a 3-fold excess of DDAB compared to DNA phosphate groups. After mixing, a fine, white precipitate started forming and the mixture was shaken overnight. The precipitate was centrifuged, washed 3 times with water and lyophilized, resulting in quantitative yield. The DNA-DDAB complex was dissolved in 5 mL dry DMF under Schlenk conditions, 15.5 mg (36 µmol, 3 eq.) of DBCO-NHS ester (abcr) were added and the mixture was stirred at RT overnight. The DMF was removed *in vacuo*, and the residue was dissolved in ethanol (Höfer Chemie). The functionalized DNA-DDAB complex was purified using a Microsep Advance centrifugal concentrator (MWCO 1 kDa) by Pall. The membrane of the concentrator was wetted with ethanol (Höfer Chemie), then the reaction mixture was centrifuged through the concentrator, washed 5 times with ethanol (Höfer Chemie), and dried *in vacuo*, yielding 29.8 mg (4.53 µmol, 38 %) functionalized DNA-DDAB complex.

NMR measurements

All measurements were performed on a BRUKER Avance Neo 600 spectrometer. Samples were prepared with a DNA concentration of 1.8 µmol/mL. DNA-PEG complexes were dissolved in methanol-d_4. DNA-DDAB complexes were dissolved in $CDCl_3$. Standard spectra were recorded with 32 scans, HSQC spectra were recorded with 128 scans. For the kinetic studies, one ^1H spectrum was recorded with 32 scans every 4 min, up to 208 min.

5. Conclusion

FNAs offer a versatile platform for the development of biomedical applications, due to their high biocompatibility and the ability to directly interface with biological systems on the molecular level. They offer the possibility to target specific cells by interacting with receptors on their surface and they can influence intracellular processes, for example protein expression. Opposed to other biomacromolecules like proteins, FNAs can easily be chemically modified and can be fully synthesized in a bottom-up process. This thesis highlights three different applications that all exploit these specific features of FNAs.

In **chapter 2**, the US controlled activation of a DNAzyme with help of a DNF based carrier system was demonstrated. The deactivation of the DNAzyme was achieved by hybridization to a reverse complementary RCA strand. Additionally, the condensation of the hybridized DNA into highly condensed DNFs with the help of $Mg_2P_2O_7$ also seemed to play a big role in the deactivation process. The deactivation process was tuned by introducing mismatches between the RCA and DNAzyme strand to reduce the energy barrier for DNAzyme release. The activation process was demonstrated using 20 kHz US and 660 kHz HIFU, which resulted in a different release profile compared to thermal release. This provided some insight into the mechanism of the US mediated release, which seems to be of mechanochemical nature and not thermal. This mechanochemical release process was characterized by fracturing of the RCA strand, which promoted constant rebinding of the DNAzyme to the RCA fragments and eventual sequestering of the DNAzyme strand. Beyond being a model system for the mechanochemical activation of a DNAzyme, this system might in the future be used for *in vivo* detection of heavy metals or gene therapy.

Chapter 3 introduced a novel DNF based DDS for the targeted imaging and therapy of glioblastoma. To introduce a glioblastoma targeting function, the AS1411 aptamer sequence was encoded onto the RCA template. The DNFs were also post-synthetically labeled with the radiochelator NOTA through a copper-free Click reaction. This allowed the DNFs to be radiolabeled with the radioactive isotopes ^{68}Ga, which enabled PET imaging and quantification of DNF uptake into cells via γ-counter, and ^{177}Lu for endogenous radiotherapy. DNFs could also be loaded with Dox through intercalation into AS1411's G-quadruplex structure. The selective uptake of the resulting DNFs into U87-IDH^{wt} and U87-IDH^{mut} glioblastoma cells was demonstrated with *in vitro* cell culture. Additionally, the biodistribution of the DNFs was tested in an *in ovo* chicken embryo model, and the tumor uptake was tested with a CAM xenograft model. Finally, the cytotoxicity of DNFs loaded with both Dox and ^{177}Lu was tested *in vitro*, which demonstrated the exceptional therapeutic potential of these dual-loaded DNFs. In the future, the efficacy of dual-loaded DNFs should be tested in a mouse model, to determine whether similar results can be achieved in mammals.

In **chapter 4**, the post-synthetic Click functionalization of an oligonucleotide with a PHIP label was demonstrated. Due to their ability to be artificially polarized, these PHIP labels have high potential to act as MRI contrast agents, especially at low magnetic field strength. During the labeling process, a 5'-amino functionalized DNA 9-mer was complexed with a lipid to facilitate its 5'-functionalization with DBCO. This DBCO moiety was subsequently coupled with the azide-bearing PHIP label. In the future, this synthesis route can be applied for the PHIP labeling of aptamers, which could act as targeted contrast agents for MRI.

This thesis especially highlights the potential of two techniques, which have been utilized multiple times: RCA and the copper-free Click reaction. As demonstrated here, these are excellent tools to assemble multifunctional systems in a modular fashion.

6. Appendix

6.1 List of Abbrevations

6-FAM	6-Carboxyfluorescein
AF488	AlexaFluor488
ANI-HCl	4-(hexyloxy)anilinium Hydrochloride
ATP	Adenosine Triphosphate
BBB	Blood-Brain Barrier
BHQ-1	Black Hole Quencher 1
CAM	Chorioallantoic Membrane
CEM	Crude Extracellular Matrix
CT	Computer Tomography
dATP	Deoxyadenosine Triphosphate
DAPI	4'-6-Diamidin-2-phenylindol
DBCO	Dibenzocyclooctyne
DDAB	Didoceyldimethylammonium Bromide
DDS	Drug Delivery System
DMF	Dimethylformamide
DMSO	Dimethylsulfoxide
DNA	Deoxyribonucleic Acid
DNF	DNA Nanoflower
DOTA	1,4,7,10-tetraazacyclododecane-1,4,7,10-tetraacetic acid
Dox	Doxorubicin
DTT	Dithiothreitol
EDTA	Ethylenediaminetetraacetic Acid
EGF	Endothelial Growth Factor
EPR	Enhanced Permeability and Retention
FNAs	Functional Nucleic Acids
GE	Gel Electrophoresis
HIFU	High Intensity Focussed Ultrasound
HSQC	Heteronuclear Single Quantum Correlation
ICL	Interstrand Cross-Links
IDH	Isocitrate Dehydrogenase
LDH	Lactate Dehydrogenase
LNA	Locked Nucleic Acid
MDR	Multi Drug Resistance
miRNA	Micro Ribonucleic Acid
MRI	Magnetic Resonance Imaging
NA	Nucleic Acid
NHS	N-Hydroxysuccinimide
NMR	Nuclear Magnetic Resonance
NOTA	2,2',2-(1,4,7-triazacyclononane-1,4,7-triyl)triacetic Acid
PASADENA	Parahydrogen and Synthesis Allow Dramatically Enhanced Nuclear Alignment
PCR	Polymerase Chain Reaction
PEG	Polyethylene Glycol
PET	Positron Emission Tomography
PHIP	Para-hydrogen Induced Polarization
PIDA	Phenyliodonium Diacetate
PLA	Polylactic Acid
PSMA	Prostate Specific Membrane Antigen
PTC	Polarization Transfer Complex
RCA	Rolling Circle Amplification
RCY	Radiochemical Yield
RNA	Ribonucleic Acid
ROS	Reactive Oxygen Species
SABRE	Signal Amplification by Reversible Exchange
SD	Standard Deviation
SELEX	Systematic Evolution of Ligands by Exponential Enrichment

SEM	Scanning Electron Microscopy
shRNA	Small Hairpin Ribonucleic Acid
siRNA	Small Interfering Ribonucleic Acid
THF	Tetrahydrofurane
TLC	Thin-layer Chromatography
TNF	Tumor Necrosis Factor
Tris	Tris(hydroxymethyl)aminomethane
tRNA	Transfer Ribonucleic Acid
US	Ultrasound
VEGF	Vascular Endothelial Growth Factor
XNA	Xenobiotic Nucleic Acids

6.2 List of Figures

Figure 1. Watson-Crick and Hoogsteen base pairing modes……3

Figure 2. Examples of non-canonical base pairing modes……4

Figure 3. Examples of aptamer based systems for imaging (left) and therapeutic (right) applications. Created in BioRender. Rath, W. (2025) https://BioRender.com/s17w753……6

Figure 4. Reaction mechanism of 8-17-catalyzed RNA cleavage. (**a**) Orientation of nucleobases and cofactor at the catalytic site of the DNAzyme. (**b**) Nucleophilic attack of 2'-OH group at phosphate leads to formation of a cyclic intermediate, which is subsequently hydrolyzed……7

Figure 5. Padlock ligation, RCA and the subsequent formation of DNFs. Created in BioRender. Rath, W. (2025) https://BioRender.com/a26j677……9

Figure 6. Conformations of polymer chains during stretching. Created in BioRender. Rath, W. (2025) https://BioRender.com/p39q383……10

Figure 7. Cavitation bubble nucleation, growth and collapse in response to the US pressure wave. Created in BioRender. Rath, W. (2025) https://BioRender.com/o76e095……11

Figure 8. Different features of the tumor microenvironment, which hinder the delivery of drugs into the tumor cells. Created in BioRender. Rath, W. (2025) https://BioRender.com/z79d908……15

Figure 9. Architecture of the BBB and its disruption through glioblastoma. Created in BioRender. Rath, W. (2025) https://BioRender.com/b49x088……17

Figure 10. Examples of various chemical modifications of DNA……20

Figure 11. Complexes of DOTA with (**a**) Ga^{3+} ion or (**b**) Lu^{3+} ion……23

Figure 12. Nuclear magnetization of ^{1}H nuclei resulting from exposure to external magnetic field B_0. (**a**) Spin state α is parallel to B_0, spin state β is antiparallel. The magnetic moment vector M of the nucleus precesses around B_0. (**b**) The α spin state is more populated and the precession of M is phase incoherent. This results in a net magnetization parallel to B_0. Created in BioRender. Rath, W. (2025) https://BioRender.com/i83h987……24

Figure 13. Nuclear resonance and relaxation. (**a**) When B_1 is applied, nuclear resonance occurs and M precesses around B_1. After B_1 is removed, M undergoes longitudinal relaxation (**b**) and transversal relaxation (**c**). Created in BioRender. Rath, W. (2025) https://BioRender.com/x51i344……25

Figure 14. Net nuclear magnetization M under (**a**) thermal equilibrium conditions purely due to Zeeman effect or (**b**) PHIP conditions. Created in BioRender. Rath, W. (2025) https://BioRender.com/i75e551……27

Figure 15. Spin state transitions in an AX spin system and their corresponding spectral lines under (**a**) thermal equilibrium conditions and (**b**) PHIP conditions. Created in BioRender. Rath, W. (2025) https://BioRender.com/n62h032…….28

Figure 16. Strategy for controlling DNAzyme activity through US. (**a**) Padlock ligation of RCA template. (**b**) RCA reaction and hybridization of DNAzyme to RCA strand. (**c**) US induced cavitation generates shear forces on RCA strand to release DNAzyme. (**d**) DNAzyme cleaves fluorophore-quencher-labeled substrate, which turns on fluorescence. Created in BioRender. Rath, W. (2025) https://BioRender.com/s99o814.....31

Figure 17. Agarose GE of padlock ligation and RCA reaction. (**a**) Circularized RCA templates with different template:primer ratios before and after addition of T4 ligase, 4 % agarose, ladder: GeneRuler ULR. Lane i: linear template; ii 2:1 ratio, no ligase; iii: 2:1 ratio, after ligation; iv 1.5:1 ratio, no ligase; v: 1.5:1 ratio, after ligation; vi 1:1 ratio, no ligase; vii: 1:1 ratio, after ligation; viii 1:1.5 ratio, no ligase; ix: 1:1.5 ratio, after ligation; x 1:2 ratio, no ligase; xi: 1:2 ratio, after ligation. (**b**) RCA reaction with different template:primer ratios, 0.8 % agarose, ladder: GeneRuler 1kb plus. Lane i: 2:1 ratio, lane ii: 1.5:1 ratio, lane iii: 1:1 ratio, lane iv: 1:1.5 ratio, lane v: 1:2 ratio…….32

Figure 18. Free DNAzyme kinetics, 2 µM substrate, all data presented as mean ± SD, N = 3 experiments. (**a**) Substrate cleavage kinetics at different DNAzyme:substrate ratios. (**b**) Photobleaching of cleaved substrate during long-time fluorescence measurement……..33

Figure 19. DNAzyme deactivation through loading onto DNFs, 2 µM substrate, 8 µM DNAzyme, all data presented as mean ± SD, N = 3 experiments. (**a**) Fluorescence kinetics after loading DNAzyme onto DNFs during or after synthesis. (**b**) Influence of RCA reaction time on DNAzyme deactivation…….34

Figure 20. Influence of mismatches on DNAzyme deactivation, 2 µM substrate, 8 µM DNAzyme, all data presented as mean ± SD, N = 3 experiments. (**a**) 2, 6, 10 or 14 mismatches. (**b**) 3, 4 or 5 mismatches……...34

Figure 21. DNAzyme deactivation after loading increasing amounts of DNAzyme, 2 µM substrate, all data presented as mean ± SD, N = 3 experiments. (**a**) 2 mismatches. (**b**) 6 mismatches……...35

Figure 22. Representative SEM images of loaded DNFs before sonication. (**a**) 10 000 x magnification. (**b**) 5 000 x magnification. (**c**) 2 500 x magnification. (**d**) Particle size histogram, diameter presented as mean ± SD, N = 160 particles…….36

Figure 23. Influence of 20 kHz sonication on DNFs. (**a**) Thermal image of reaction mixture directly after sonication. (**b**) Agarose GE of DNFs after sonication, 0.8 % agarose, ladder: GeneRuler 1kb plus, lane i: 0 min sonication, ii: 2 min, iii: 5 min, iv: 10 min, v: 20 min. (**c**) Normalized intensity of GE bands plotted against pixels in elution direction (y-axis). (**d**) Calibration curve correlating pixels in elution direction to DNA chain length, local maxima after sonication were found at 647 bp (2 min), 338 bp (5 min), 301 bp (10 min) and 225 bp (20 min)…….37

Figure 24. Representative SEM images of loaded DNFs after 20 kHz sonication. (**a-c**) 10 000 x magnification. (**d**) Particle size histogram, diameter presented as mean ± SD, N = 100 particles…….38

Figure 25. DNAzyme activation through 20 kHz sonication, 2 µM substrate, 8 µM DNAzyme, all data presented as mean ± SD, N = 3 experiments. (**a**) Fluorescence kinetics after increasing sonication time. (**b**) Maximum observed fluorescence after increasing sonication time, 2 mismatches. (**c**) Maximum observed fluorescence after increasing sonication time, 6 mismatches. (**d**) Maximum observed fluorescence after increasing sonication time, 3, 4, 5 mismatches……...39

Figure 26. DNAzyme activation through heating, 2 µM substrate, 8 µM DNAzyme, all data presented as mean ± SD, N = 3 experiments. (**a**) 50 °C. (**b**) 100 °C……..40

Figure 27. DNAzyme activation through 0.66 MHz sonication, 2 µM substrate, 8 µM DNAzyme, all data presented as mean ± SD, N = 3 experiments, p = 0.047, calculated through an unpaired two sample t-test, *p ≤ 0.05. (**a**) DNAzyme kinetics after HIFU sonication. (**b**) Maximum fluorescence intensity after HIFU sonication……41

Figure 28. Synthesis strategy for Dox loaded, radiolabeled ^{Apt}DNFs and pre-clinical studies using *in vitro* cell culture and a CAM xenograft tumor model. (**a**) DNF synthesis through RCA. (**b**) Encoding of AS1411 aptamer sequence onto RCA template. (**c**) Loading of Dox through intercalation into AS1411's G-quadruplex structure. (**d**) Click-functionalization of ^{Apt}DNFs with DBCO-NOTA. (**e**) Radiolabeling of NOTA with ^{68}Ga for PET imaging or ^{177}Lu for endogenous radiotherapy. (**f**) *In vitro* uptake and toxicity studies using glioblastoma cells. (**g**) Biodistribution, tumor accumulation and therapy studies in glioblastoma CAM xenograft tumor model. Created in BioRender. Rath, W. (2025) https://BioRender.com/g57y464……44

Figure 29. Synthesis of azide-bearing ^{Apt}DNFs, analyzed by agarose GE. (**a**) Padlock ligation of linear RCA template with different template:primer ratios, 4 % agarose, ladder: GeneRuler ULR. Lane i: linear template, lane ii: 2:1 ratio, lane iii: 1.5:1 ratio, lane iv: 1:1 ratio, lane v: 1:1.5 ratio, lane vi: 1:2 ratio. (**b**) RCA products synthesized with different template:primer ratios, 0.8 % agarose, ladder: GeneRuler 1kb plus. Lane i: circularized template, lane ii: 2:1 ratio, lane iii: 1.5:1 ratio, lane iv: 1:1 ratio, lane v: 1:1.5 ratio, lane vi: 1:2 ratio. (**c**) RCA products synthesized with 1:1 template primer ratio and different amounts of dATP replaced by N^6-(6-azido)hexyl-dATP, 0.8 % agarose, ladder: GeneRuler 1kb plus. Lane i: circularized template, lane ii: 25 % dATP replaced, lane iii: 50 % dATP replaced, lane iv: 100 % dATP replaced……45

Figure 30. Superimposed ^{1}H-^{13}C-HSQC spectra of native ^{Apt}DNFs (green) and N^6-(6-azido)hexyl-modified ^{Apt}DNFs (red) in D_2O with peak assignments……46

Figure 31. Representative SEM images of azide-bearing ^{Apt}DNFs. (**a**) 20 000 x magnification. (**b**) 5 000 x magnification. (**c**) 2 500 x magnification. (**d**) Particle size histogram and mean diameter ± SD from the mean, N = 150 particles……47

Figure 32. Quantification of ^{Apt}DNF Click-labeling efficiency at different pH and temperature. (**a**) UV-Vis absorbance spectra confirming equal DNA concentration. (**b**) Fluorescence spectra (λ_{Ex} = 485 nm) quantifying the amount of 5/6-FAM bound to the ^{Apt}DNFs……48

Figure 33. Superimposed ^{1}H-NMR spectra of N^6-(6-azido)hexyl-modified ^{Apt}DNFs (red) and DOTA-functionalized N^6-(6-azido)hexyl-modified ^{Apt}DNFs (blue) in D_2O……48

Figure 34. Radiolabeling of DOTA-^{Apt}DNFs with ^{68}Ga. (**a**) Radio-TLC after radiolabeling at RT and pH 4.5, showing very little ^{68}Ga bound to the ^{Apt}DNFs. (**b**) Radio-TLC after radiolabeling at 85 °C and pH 4.5, indicating ^{68}Ga was fully bound to DOTA but a significant amount of DOTA was removed from the ^{68}Ga bound to the ^{Apt}DNFs through depurination……49

Figure 35. ^{1}H-NMR spectrum of NOTA-DBCO in methanol-d_4 with peak-assignments……50

Figure 36. ESI-MS spectrum of NOTA-DBCO……50

Figure 37. Radio-TLC after radiolabeling of NOTA-^{Apt}DNFs at RT and pH 4.5, indicating a majority of ^{68}Ga was bound to the ^{Apt}DNFs with marginal amounts of free ^{68}Ga and depurination fragments……..50

Figure 38. Dox loading of ^{Apt}DNFs. (**a**) Fluorescence spectra (λ_{Ex} = 488 nm) of 10 µM Dox after incubation for 30 min at RT with different concentrations of ^{Apt}DNFs. (**b**) Fluorescence kinetics (λ_{Em} = 595 nm) of Dox loaded ^{Apt}DNFs at pH 7.4 and pH 5.0……51

Figure 39. RCY and radiochemical purity of NOTA-^{Apt}DNFs radiolabeled with ^{68}Ga and ^{177}Lu as determined by radio-TLC. (**a,b**) RCY after incubation of ^{68}Ga (**a**) and ^{177}Lu (**b**) (1 GBq) with different amounts of NOTA-^{Apt}DNFs at RT and pH 4.5. (**c,d**) Representative radio-TLC of NOTA-^{Apt}DNFs radiolabeled with ^{68}Ga (**c**) and ^{177}Lu (**d**) demonstrating their high radiochemical purity. (**e,f**) Time dependent RCY as determined by radio-TLC of NOTA-^{Apt}DNFs radiolabeled with ^{68}Ga (**e**) and ^{177}Lu (**f**) in PBS buffer and human serum. Data presented as mean ± SD, N = 9……52

Figure 40. Time dependent *in vitro* cell uptake of ^{68}Ga-^{Apt}DNFs into U87 glioblastoma cells quantified by γ-counter. (**a**) ^{68}Ga-^{Apt}DNFs uptake into U87 IDH^{wt} glioblastoma cells compared to ^{68}Ga-^{Ctr}DNFs after 1 and 4 h. (**b**) ^{68}Ga-^{Apt}DNFs uptake into U87 IDH^{mut} glioblastoma cells compared to ^{68}Ga-^{Ctr}DNFs after 1 and 4 h. (**c**) Comparison of uptake rate of ^{68}Ga-^{Apt}DNFs into U87 IDH^{wt} and U87 IDH^{mut} glioblastoma cells after 1 and 4 h. Data presented as mean ± SD, N = 18. Statistical analysis was performed with two-way ANOVA followed by multiple comparison tests and *post-hoc* Turkey test, ***p < 0.001……53

Figure 41. Immunocytochemical co-staining of U87 IDH^{wt} glioblastoma cells with DAPI (blue) and phalloidin (red) after incubation with AF488-^{Apt}DNFs for different times……..…54

Figure 42. Biodistribution of ^{68}Ga-^{Apt}DNFs in non-tumor-bearing chicken embryo after 30 and 60 mins circulation time. (**a**) PET-CT images visualizing the biodistribution of ^{68}Ga-^{Apt}DNFs in the healthy chicken embryo after 30 mins (left) and 60 mins (right). (**b**) Post-mortem quantification of ^{68}Ga-^{Apt}DNF accumulation in the individual organs after 30 mins circulation time, determined through γ-counter (decay corrected). (**c**) Post-mortem quantification of ^{68}Ga-^{Apt}DNF accumulation in the individual organs after 60 mins circulation time, determined through γ-counter (decay corrected). (**d**) Post-mortem quantification of time dependent accumulation of ^{68}Ga-^{Apt}DNFs in the brain after 30 and 60 mins circulation time, determined through γ-counter (decay corrected). (**e**) Representative images of resected organs……55

Figure 43. Biodistribution of ^{68}Ga-^{Apt}DNFs in chicken embryo bearing a CAM xenograft glioblastoma after 30 and 60 mins circulation time. (**a**) PET-CT images visualizing the biodistribution of ^{68}Ga-^{Apt}DNFs after 30 mins (left) and 60 mins (right), white arrows highlighting xenograft tumor. (**b**) Post-mortem quantification of ^{68}Ga-^{Apt}DNF accumulation in the tumor after 30 mins circulation time, determined through γ-counter. (**c**) Post-mortem quantification of ^{68}Ga-^{Apt}DNF accumulation in the tumor after 60 mins circulation time, determined through γ-counter. (**d**) Post-mortem quantification of time dependent accumulation of ^{68}Ga-^{Apt}DNFs in the tumor after 30 and 60 mins circulation time, determined through γ-counter (decay corrected). (**e**) Representative images of resected tumor and remaining carcass……...56

Figure 44. LDH release assay of U87 IDH^{wt} (left) and U87 IDH^{mut} (right) glioblastoma cells after different incubation times with unloaded ^{Apt}DNFs (grey), 10 µM free Dox (pink), ^{Apt}DNF[Dox] (pink-black), ^{177}Lu-^{Apt}DNF[Dox] (yellow-red) or 0.1 % H_2O_2 (black), compared to LDH release after lysis……..….57

Figure 45. Metabolic activity of U87 IDH^{wt} (left) and U87 IDH^{mut} (right) glioblastoma cells determined through cell titer blue (resazurin) assay after different incubation times with unloaded ^{Apt}DNFs (grey), 10 µM free Dox (pink), ^{Apt}DNF[Dox] (pink-black), ^{177}Lu-^{Apt}DNF[Dox] (yellow-red) or 0.1 % H_2O_2 (black), normalized to negative control (white)……..……57

Figure 46. ^{1}H-^{13}C-HSQC spectrum of native mPEG-DNA complex in methanol-d_4 with peak assignments……..…65

Figure 47. ^{1}H-NMR spectrum of native mPEG-DNA complex in methanol-d_4 with integrals for the thymine CH_3 peak (1.9 ppm) and the mPEG CH_3 peak (3.4 ppm)……..65

Figure 48. Superimposed ^{1}H-^{13}C-HSQC spectra of native mPEG-DNA complex (green) and DBCO-NHS treated mPEG-DNA complex (red) in methanol-d_4……66

Figure 49. ^{1}H-^{13}C-HSQC spectrum of native DDAB-DNA complex in $CDCl_3$……..……67

Figure 50. ^{1}H-NMR spectrum of DDAB in $CDCl_3$ with peak assignments……..……67

Figure 51. Superimposed ^{1}H-^{13}C-HSQC spectra of native DDAB-DNA complex (red) and DBCO-NHS treated DDAB-DNA complex (green) in $CDCl_3$……68

Figure 52. ^{1}H-NMR spectrum of DBCO-NHS in $CDCl_3$ with peak assignments……..69

Figure 53. ^{1}H-^{13}C-HSQC spectrum of DBCO-NHS in $CDCl_3$ highlighting the characteristic peaks corresponding to position 3 (compare **Figure 53**)……..……69

Figure 54. Structure of hydrogenative PHIP label featuring ^{29}Si heteronuclei……...71

Figure 55. ^{1}H-NMR spectrum of freshly synthesized PHIP label in $CDCl_3$ with peak assignments……71

Figure 56. Stacked ^{1}H-NMR spectra of PHIP label in $CDCl_3$ before (top) and after (bottom) storage….72

Figure 57. Superimposed ^{1}H-^{13}C-HSQC spectra of DDAB-DNA complex in $CDCl_3$ before (green) and after (red) Click reaction with peak assignment for the PHIP label……..…72

Figure 58. Stacked ^{1}H Click kinetic spectra in $CDCl_3$ monitoring changes of signals corresponding to PEG spacer of PHIP label……...…73

Figure 59. Stacked ^{1}H Click kinetic spectra in $CDCl_3$ monitoring changes of signals corresponding to DBCO and α-triazole PEG unit……..……73

6.3 List of Schemes

Scheme 1. DNA Click labeling strategy. (**a**) 5'-DBCO functionalization of DNA surfactant complex through amine-NHS coupling. (**b**) Click labeling of DBCO functionalized DNA with azide bearing PHIP tag. Created in BioRender. Rath, W. (2025) https://BioRender.com/u04j119……...……..64

Scheme 2: Synthesis route for azide functionalized SABRE label……..……70

6.4 List of Tables

Table 1. DNA sequences **chapter 2**……42

Table 2. DNA sequences **chapter 3**……60

7. References

[1] D. Caballero, C. M. Abreu, A. C. Lima, N. M. Neves, R. L. Reis, S. C. Kundu, "Precision biomaterials in cancer theranostics and modelling"*, Biomater.* **2022**, *280*, 121299. DOI: 10.1016/j.biomaterials.2021.121299

[2] H. Kang, S. Hu, M. H. Cho, S. H. Hong, Y. Choi, H. S. Choi, "Theranostic nanosystems for targeted cancer therapy"*, Nano Today* **2018**, *23*, 59-72. DOI: 10.1016/j.nantod.2018.11.001

[3] T. Mo, X. Liu, Y. Luo, L. Zhong, Z. Zhang, T. Li, L. Gan, X. Liu, L. Li, H. Wang, "Aptamer-based biosensors and application in tumor theranostics"*, Cancer Sci.* **2022**, *113* (1), 7-16. DOI: 10.1111/cas.15194

[4] Y. Morita, M. Leslie, H. Kameyama, D. E. Volk, T. Tanaka, "Aptamer therapeutics in cancer: current and future"*, Cancers* **2018**, *10* (3), 80. DOI: 10.3390/cancers10030080

[5] P. Mi, "Stimuli-responsive nanocarriers for drug delivery, tumor imaging, therapy and theranostics"*, Theranostics* **2020**, *10* (10), 4557. DOI: 10.1021/acsnano.3c06019

[6] G. Cravotto, E. C. Gaudino, P. Cintas, "On the mechanochemical activation by ultrasound"*, Chem. Soc. Rev.* **2013**, *42* (18), 7521-7534. DOI: 10.1039/C2CS35456J

[7] P. Lavalle, F. Boulmedais, P. Schaaf, L. Jierry, "Soft-mechanochemistry: mechanochemistry inspired by nature"*, Langmuir* **2016**, *32* (29), 7265-7276. DOI: 10.1021/acs.langmuir.6b01768

[8] J. D. Watson, F. H. Crick, "Molecular structure of nucleic acids: a structure for deoxyribose nucleic acid"*, Nature* **1953**, *171* (4356), 737-738. DOI: 10.1038/171737a0

[9] K. Hoogsteen, "The structure of crystals containing a hydrogen-bonded complex of 1-methylthymine and 9-methyladenine"*, Acta Cryst.* **1959**, *12* (10), 822-823. DOI: 10.1107/S0365110X59002389

[10] S. Takahashi, N. Sugimoto, "Watson–Crick versus Hoogsteen base pairs: chemical strategy to encode and express genetic information in life"*, Acc. Chem. Res.* **2021**, *54* (9), 2110-2120. DOI: 10.1021/acs.accounts.0c00734

[11] J. Spiegel, S. M. Cuesta, S. Adhikari, R. Hänsel-Hertsch, D. Tannahill, S. Balasubramanian, "G-quadruplexes are transcription factor binding hubs in human chromatin"*, Genome Biol.* **2021**, *22* (1), 117. DOI: 10.1186/s13059-021-02324-z

[12] P. K. Zuber, I. Artsimovitch, M. NandyMazumdar, Z. Liu, Y. Nedialkov, K. Schweimer, P. Rösch, S. H. Knauer, "The universally-conserved transcription factor RfaH is recruited to a hairpin structure of the non-template DNA strand"*, elife* **2018**, *7*, e36349. DOI: 10.7554/eLife.36349

[13] L. A. Sanz, S. R. Hartono, Y. W. Lim, S. Steyaert, A. Rajpurkar, P. A. Ginno, X. Xu, F. Chédin, "Prevalent, dynamic, and conserved R-loop structures associate with specific epigenomic signatures in mammals"*, Mol. Cell* **2016**, *63* (1), 167-178. DOI: 10.1016/j.molcel.2016.05.032

[14] L. Westin, P. Blomquist, J. F. Milligan, Ö. Wrange, "Triple helix DNA alters nucleosomal histone-DNA interactions and acts as a nucleosome barrier"*, Nucleic Acids Res.* **1995**, *23* (12), 2184-2191. DOI: 10.1093/nar/23.12.2184

[15] R. G. Thys, C. E. Lehman, L. CT Pierce, Y.-H. Wang, "DNA secondary structure at chromosomal fragile sites in human disease"*, Curr. Genomics* **2015**, *16* (1), 60-70. DOI: 10.2174/1389202916666150114223205

[16] I. Georgakopoulos-Soares, S. Morganella, N. Jain, M. Hemberg, S. Nik-Zainal, "Noncanonical secondary structures arising from non-B DNA motifs are determinants of mutagenesis"*, Genome Res.* **2018**, *28* (9), 1264-1271. DOI: 10.1101/gr.231688.117

[17] J. Das, S. Mukherjee, A. Mitra, D. Bhattacharyya, "Non-canonical base pairs and higher order structures in nucleic acids: crystal structure database analysis"*, J. Biomol. Struct. Dyn.* **2006**, *24* (2), 149-161. DOI: 10.1080/07391102.2006.10507108

[18] A. D. Ellington, J. W. Szostak, "In vitro selection of RNA molecules that bind specific ligands"*, Nature* **1990**, *346* (6287), 818-822. DOI: 10.1038/346818a0

[19] C. Tuerk, L. Gold, "Systematic evolution of ligands by exponential enrichment: RNA ligands to bacteriophage T4 DNA polymerase"*, Science* **1990**, *249* (4968), 505-510. DOI: 10.1126/science.2200121
[20] M. Darmostuk, S. Rimpelova, H. Gbelcova, T. Ruml, "Current approaches in SELEX: An update to aptamer selection technology"*, Biotechnol. Adv.* **2015**, *33* (6), 1141-1161. DOI: 10.1016/j.biotechadv.2015.02.008
[21] D. Morrison, M. Rothenbroker, Y. Li, "DNAzymes: selected for applications"*, Small Methods* **2018**, *2* (3), 1700319. DOI: 10.1002/smtd.201700319
[22] J. Wondergem, H. Schiessel, M. Tompitak, "Performing SELEX experiments in silico"*, J. Chem. Phys.* **2017**, *147* (17). DOI: 10.1063/1.5001394
[23] M. Famulok, G. n. Mayer, "Aptamer modules as sensors and detectors"*, Acc. Chem. Res.* **2011**, *44* (12), 1349-1358. DOI: 10.1021/ar2000293
[24] A. Futane, V. Narayanamurthy, P. Jadhav, A. Srinivasan, "Aptamer-based rapid diagnosis for point-of-care application"*, Microfluid. Nanofluidics* **2023**, *27* (2), 15. DOI: 10.1007/s10404-022-02622-3
[25] M. Shahdordizadeh, S. M. Taghdisi, N. Ansari, F. A. Langroodi, K. Abnous, M. Ramezani, "Aptamer based biosensors for detection of Staphylococcus aureus"*, Sens. Actuators B: Chem.* **2017**, *241*, 619-635. DOI: 10.1016/j.snb.2016.10.088
[26] S. Srivastava, P. R. Abraham, S. Mukhopadhyay, "Aptamers: An emerging tool for diagnosis and therapeutics in tuberculosis"*, Front. Cell. Infect. Microbiol.* **2021**, *11*, 656421. DOI: 10.3389/fcimb.2021.656421
[27] J. Bala, S. Chinnapaiyan, R. K. Dutta, H. Unwalla, "Aptamers in HIV research diagnosis and therapy"*, RNA Biol.* **2018**, *15* (3), 327-337. DOI: 10.1080/15476286.2017.1414131
[28] S. M. Kim, J. Kim, S. Noh, H. Sohn, T. Lee, "Recent development of aptasensor for influenza virus detection"*, Biochip J.* **2020**, *14*, 327-339. DOI: 10.1007/s13206-020-4401-2
[29] M. Moreno, V. M. Gonzalez, "Advances on aptamers targeting Plasmodium and trypanosomatids"*, Curr. Med. Chem.* **2011**, *18* (32), 5003-5010. DOI: 10.2174/092986711797535218
[30] Y.-J. Kim, Y. S. Kim, J. H. Niazi, M. B. Gu, "Electrochemical aptasensor for tetracycline detection"*, Bioprocess Biosyst. Eng.* **2010**, *33*, 31-37. DOI: 10.1007/s00449-009-0371-4
[31] M. Jo, J.-Y. Ahn, J. Lee, S. Lee, S. W. Hong, J.-W. Yoo, J. Kang, P. Dua, D.-k. Lee, S. Hong, "Development of single-stranded DNA aptamers for specific bisphenol A detection"*, Oligonucleotides* **2011**, *21* (2), 85-91. DOI: 10.1089/oli.2010.0267
[32] G. K. Mishra, V. Sharma, R. K. Mishra, "Electrochemical aptasensors for food and environmental safeguarding: A review"*, Biosensors* **2018**, *8* (2), 28. DOI: 10.3390/bios8020028
[33] L. Madianos, G. Tsekenis, E. Skotadis, L. Patsiouras, D. Tsoukalas, "A highly sensitive impedimetric aptasensor for the selective detection of acetamiprid and atrazine based on microwires formed by platinum nanoparticles"*, Biosens. Bioelectron.* **2018**, *101*, 268-274. DOI: 10.1016/j.bios.2017.10.034
[34] Y. Li, W. W. Tam, Y. Yu, Z. Zhuo, Z. Xue, C. Tsang, X. Qiao, X. Wang, W. Wang, Y. Li, "The application of Aptamer in biomarker discovery"*, Biomark. Res.* **2023**, *11* (1), 70. DOI: 10.1186/s40364-023-00510-8
[35] X. Ni, Y. Zhang, J. Ribas, W. H. Chowdhury, M. Castanares, Z. Zhang, M. Laiho, T. L. DeWeese, S. E. Lupold, "Prostate-targeted radiosensitization via aptamer-shRNA chimeras in human tumor xenografts"*, J. Clin. Invest.* **2011**, *121* (6), 2383-2390. DOI: 10.1172/JCI45109
[36] J. O. McNamara, E. R. Andrechek, Y. Wang, K. D. Viles, R. E. Rempel, E. Gilboa, B. A. Sullenger, P. H. Giangrande, "Cell type–specific delivery of siRNAs with aptamer-siRNA chimeras"*, Nat. Biotechnol.* **2006**, *24* (8), 1005-1015. DOI: 10.1038/nbt1223
[37] F. Pastor, D. Kolonias, J. O. McNamara II, E. Gilboa, "Targeting 4-1BB costimulation to disseminated tumor lesions with bi-specific oligonucleotide aptamers"*, Mol. Ther.* **2011**, *19* (10), 1878-1886. DOI: 10.1038/mt.2011.145
[38] T. C. Chu, K. Y. Twu, A. D. Ellington, M. Levy, "Aptamer mediated siRNA delivery",

Nucleic Acids Res. **2006**, *34* (10), e73-e73. DOI: 10.1093/nar/gkl388
[39] T. C. Chu, J. W. Marks III, L. A. Lavery, S. Faulkner, M. G. Rosenblum, A. D. Ellington, M. Levy, "Aptamer: toxin conjugates that specifically target prostate tumor cells"*, Cancer Res.* **2006**, *66* (12), 5989-5992. DOI: 10.1158/0008-5472.CAN-05-4583
[40] Y. F. Huang, D. Shangguan, H. Liu, J. A. Phillips, X. Zhang, Y. Chen, W. Tan, "Molecular assembly of an aptamer–drug conjugate for targeted drug delivery to tumor cells"*, ChemBioChem* **2009**, *10* (5), 862-868. DOI: 10.1002/cbic.200800805
[41] G. Zhu, S. Cansiz, M. You, L. Qiu, D. Han, L. Zhang, L. Mei, T. Fu, Z. Chen, W. Tan, "Nuclease-resistant synthetic drug-DNA adducts: programmable drug-DNA conjugation for targeted anticancer drug delivery"*, NPG Asia Mater.* **2015**, *7* (3), e169-e169. DOI: 10.1038/am.2015.19
[42] R. Wang, G. Zhu, L. Mei, Y. Xie, H. Ma, M. Ye, F.-L. Qing, W. Tan, "Automated modular synthesis of aptamer–drug conjugates for targeted drug delivery"*, J. Am. Chem. Soc.* **2014**, *136* (7), 2731-2734. DOI: 10.1021/ja4117395
[43] V. Bagalkot, O. C. Farokhzad, R. Langer, S. Jon, "An aptamer-doxorubicin physical conjugate as a novel targeted drug-delivery platform"*, Angew. Chem. Int. Ed.* **2006**, *45* (48), 8149-8152. DOI: 10.1002/anie.200602251
[44] O. C. Farokhzad, S. Jon, A. Khademhosseini, T.-N. T. Tran, D. A. LaVan, R. Langer, "Nanoparticle-aptamer bioconjugates: a new approach for targeting prostate cancer cells"*, Cancer Res.* **2004**, *64* (21), 7668-7672. DOI: 10.1158/0008-5472.CAN-04-2550
[45] J. Lopes-Nunes, A. S. Agonia, T. Rosado, E. Gallardo, R. Palmeira-de-Oliveira, A. Palmeira-de-Oliveira, J. Martinez-de-Oliveira, J. Fonseca-Moutinho, M. P. C. Campello, A. Paiva, "Aptamer-functionalized gold nanoparticles for drug delivery to gynecological carcinoma cells"*, Cancers* **2021**, *13* (16), 4038. DOI: 10.3390/cancers13164038
[46] J. S. Lee, M. Kim, H. Jin, M. Kwak, E. Cho, K.-S. Kim, D.-E. Kim, "DNA aptamer-conjugated lipid nanoparticle for targeted PTEN mRNA delivery to prostate cancer cells"*, Int. J. Pharm.* **2024**, *662*, 124519. DOI: 10.1016/j.ijpharm.2024.124519
[47] C. Bell, E. Lynam, D. J. Landfair, N. Janjic, M. E. Wiles, "Oligonucleotide NX1838 inhibits VEGF 165-mediated cellular responses in vitro"*, In Vitro Cell. Dev. Biol. Anim.* **1999**, *35*, 533-542. DOI: 10.1007/s11626-999-0064-y
[48] J. O. McNamara, D. Kolonias, F. Pastor, R. S. Mittler, L. Chen, P. H. Giangrande, B. Sullenger, E. Gilboa, "Multivalent 4-1BB binding aptamers costimulate CD8+ T cells and inhibit tumor growth in mice "*, J. Clin. Invest.* **2008**, *118* (1), 376-386. DOI: 10.1172/JCI33365
[49] J. Ruckman, L. S. Green, J. Beeson, S. Waugh, W. L. Gillette, D. D. Henninger, L. Claesson-Welsh, N. Janjic, "2'-Fluoropyrimidine RNA-based aptamers to the 165-amino acid form of vascular endothelial growth factor (VEGF165): Inhibition of receptor binding and VEGF-induced vascular permeability through interactions requiring the exon 7-encoded domain"*, J. Biol. Chem.* **1998**, *273* (32), 20556-20567. DOI: 10.1074/jbc.273.32.20556
[50] M. Kuwahara, S. Obika, "In vitro selection of BNA (LNA) aptamers"*, Artif. DNA PNA XNA* **2013**, *4* (2), 39-48. DOI: 10.4161/adna.25786
[51] Q. W. Hughes, B. T. Le, G. Gilmore, R. I. Baker, R. N. Veedu, "Construction of a bivalent thrombin binding aptamer and its antidote with improved properties"*, Molecules* **2017**, *22* (10), 1770. DOI: 10.3390/molecules22101770
[52] M. Kuwahara, N. Sugimoto, "Molecular evolution of functional nucleic acids with chemical modifications"*, Molecules* **2010**, *15* (8), 5423-5444. DOI: 10.3390/molecules15085423
[53] M. Nerantzaki, C. Loth, J.-F. Lutz, "Chemical conjugation of nucleic acid aptamers and synthetic polymers"*, Polym. Chem.* **2021**, *12* (24), 3498-3509. DOI: 10.1039/D1PY00516B
[54] C. H. Lee, S.-H. Lee, J. H. Kim, Y.-H. Noh, G.-J. Noh, S.-W. Lee, "Pharmacokinetics of a cholesterol-conjugated aptamer against the hepatitis C virus (HCV) NS5B protein"*, Mol. Ther. Nucleic Acids* **2015**, *4* (10), e254. DOI: 10.1038/mtna.2015.30
[55] M. Lin, J. Zhang, H. Wan, C. Yan, F. Xia, "Rationally designed multivalent aptamers

targeting cell surface for biomedical applications", *ACS Appl. Mater. Interfaces* **2020**, *13* (8), 9369-9389. DOI: 10.1021/acsami.0c15644
[56] G. Zhou, G. Wilson, L. Hebbard, W. Duan, C. Liddle, J. George, L. Qiao, "Aptamers: A promising chemical antibody for cancer therapy", *Oncotarget* **2016**, *7* (12), 13446. DOI: 10.18632/oncotarget.7178
[57] S. Agrawal, M. Joshi, J. B. Christoforidis, "Vitreous Inflammation Associated with Intravitreal Anti-VEGF Pharmacotherapy", *Mediators Inflamm.* **2013**, *2013* (1), 943409. DOI: 10.1155/2013/943409
[58] C. A. Farman, D. J. Kornbrust, "Oligodeoxynucleotide studies in primates: antisense and immune stimulatory indications", *Toxicol. Pathol.* **2003**, *31* (1_suppl), 119-122. DOI: 10.1080/01926230390174995
[59] E. E. Swayze, A. M. Siwkowski, E. V. Wancewicz, M. T. Migawa, T. K. Wyrzykiewicz, G. Hung, B. P. Monia, Bennett, C. Frank, "Antisense oligonucleotides containing locked nucleic acid improve potency but cause significant hepatotoxicity in animals", *Nucleic Acids Res.* **2007**, *35* (2), 687-700. DOI: 10.1093/nar/gkl1071
[60] Y. Lee, J. H. Urban, L. Xu, B. A. Sullenger, J. Lee, "2′ Fluoro modification differentially modulates the ability of RNAs to activate pattern recognition receptors", *Nucleic Acid Ther.* **2016**, *26* (3), 173-182. DOI: 10.1089/nat.2015.0575
[61] N. J. Ganson, T. J. Povsic, B. A. Sullenger, J. H. Alexander, S. L. Zelenkofske, J. M. Sailstad, C. P. Rusconi, M. S. Hershfield, "Pre-existing anti–polyethylene glycol antibody linked to first-exposure allergic reactions to pegnivacogin, a PEGylated RNA aptamer", *J. Allergy Clin. Immunol.* **2016**, *137* (5), 1610-1613. e1617. DOI: 10.1016/j.jaci.2015.10.034
[62] K. Kruger, P. J. Grabowski, A. J. Zaug, J. Sands, D. E. Gottschling, T. R. Cech, "Self-splicing RNA: autoexcision and autocyclization of the ribosomal RNA intervening sequence of Tetrahymena", *Cell* **1982**, *31* (1), 147-157. DOI: 10.1016/0092-8674(82)90414-7
[63] R. R. Breaker, G. F. Joyce, "A DNA enzyme that cleaves RNA", *Chem. Biol.* **1994**, *1* (4), 223-229. DOI: 10.1016/1074-5521(94)90014-0
[64] S. K. Silverman, "Deoxyribozymes: selection design and serendipity in the development of DNA catalysts", *Acc. Chem. Res.* **2009**, *42* (10), 1521-1531. DOI: 10.1021/ar900052y
[65] M. Hollenstein, "DNA catalysis: the chemical repertoire of DNAzymes", *Molecules* **2015**, *20* (11), 20777-20804. DOI: 10.3390/molecules201119730
[66] S. K. Silverman, "Catalytic DNA: scope, applications, and biochemistry of deoxyribozymes", *Trends Biochem. Sci.* **2016**, *41* (7), 595-609. DOI: 10.1016/j.tibs.2016.04.010
[67] S. W. Santoro, G. F. Joyce, "A general purpose RNA-cleaving DNA enzyme", *Proc. Natl. Acad. Sci.* **1997**, *94* (9), 4262-4266. DOI: 10.1073/pnas.94.9.4262
[68] M. Cepeda-Plaza, A. Peracchi, "Insights into DNA catalysis from structural and functional studies of the 8-17 DNAzyme", *Org. Biomol. Chem.* **2020**, *18* (9), 1697-1709. DOI: 10.1039/C9OB02453K
[69] G. F. Joyce, "Directed evolution of nucleic acid enzymes", *Annu. Rev. Biochem.* **2004**, *73* (1), 791-836. DOI: 10.1146/annurev.biochem.73.011303.073717
[70] K. Schlosser, Y. Li, "A versatile endoribonuclease mimic made of DNA: characteristics and applications of the 8–17 RNA-cleaving DNAzyme", *ChemBioChem* **2010**, *11* (7), 866-879. DOI: 10.1002/cbic.200900786
[71] P. J. J. Huang, D. de Rochambeau, H. F. Sleiman, J. Liu, "Target self-enhanced selectivity in metal-specific DNAzymes", *Angew. Chem. Int. Ed.* **2020**, *132* (9), 3601-3605. DOI: 10.1002/ange.201915675
[72] W. Ren, P.-J. J. Huang, D. de Rochambeau, W. J. Moon, J. Zhang, M. Lyu, S. Wang, H. Sleiman, J. Liu, "Selection of a metal ligand modified DNAzyme for detecting Ni2+", *Biosens. Bioelectron.* **2020**, *165*, 112285. DOI: 10.1016/j.bios.2020.112285
[73] J. Li, Y. Lu, "A highly sensitive and selective catalytic DNA biosensor for lead ions", *J. Am. Chem. Soc.* **2000**, *122* (42), 10466-10467. DOI: 10.1021/ja0021316
[74] J. Liu, Y. Lu, "A colorimetric lead biosensor using DNAzyme-directed assembly of gold

nanoparticles", *J. Am. Chem. Soc.* **2003**, *125* (22), 6642-6643. DOI: 10.1021/ja034775u
[75] Y. Xiao, A. A. Rowe, K. W. Plaxco, "Electrochemical detection of parts-per-billion lead via an electrode-bound DNAzyme assembly", *J. Am. Chem. Soc.* **2007**, *129* (2), 262-263. DOI: 10.1021/ja067278x
[76] W. Yun, N. Li, R. Wang, L. Yang, L. Chen, Y. Tang, "Proximity ligation assay induced hairpin to DNAzyme structure switching for entropy-driven amplified detection of thrombin", *Anal. Chim. Acta* **2019**, *1064*, 104-111. DOI: 10.1016/j.aca.2019.03.007
[77] T. Yan, L. Zhu, H. Ju, J. Lei, "DNA-walker-induced allosteric switch for tandem signal amplification with palladium nanoparticles/metal–organic framework tags in electrochemical biosensing", *Anal. Chem.* **2018**, *90* (24), 14493-14499. DOI: 10.1016/j.snb.2020.129078
[78] K. Yang, J. C. Chaput, "REVEALR: a multicomponent XNAzyme-based nucleic acid detection system for SARS-CoV-2", *J. Am. Chem. Soc.* **2021**, *143* (24), 8957-8961. DOI: 10.1021/jacs.1c02664
[79] W. Huo, X. Li, B. Wang, H. Zhang, J. Zhang, X. Yang, Y. Jin, "Recent advances of DNAzyme-based nanotherapeutic platform in cancer gene therapy", *Biophys. Rep.* **2020**, *6*, 256-265. DOI: 10.1007/s41048-020-00123-w
[80] L. Meng, W. Ma, S. Lin, S. Shi, Y. Li, Y. Lin, "Tetrahedral DNA nanostructure-delivered DNAzyme for gene silencing to suppress cell growth", *ACS Appl. Mater. Interfaces* **2019**, *11* (7), 6850-6857. DOI: 10.1021/acsami.8b22444
[81] E. Zokaei, A. Badoei-Dalfrad, M. Ansari, Z. Karami, T. Eslaminejad, S. N. Nematollahi-Mahani, "Therapeutic potential of DNAzyme loaded on chitosan/cyclodextrin nanoparticle to recovery of chemosensitivity in the MCF-7 cell line", *Appl. Biochem. Biotechnol.* **2019**, *187*, 708-723. DOI: 10.1007/s12010-018-2836-x
[82] L. Zhang, W. Zhao, C. Liang, X. Yi, Y. Pei, Y. Lin, J. He, W. Li, "VEGFR-1 targeted DNAzyme via transcatheter arterial delivery influences tumor vasculature assessed through dynamic contrast-enhanced magnetic resonance imaging", *Oncol. Rep.* **2016**, *36* (3), 1339-1344. DOI: 10.3892/or.2016.4933
[83] A. I. Taylor, V. B. Pinheiro, M. J. Smola, A. S. Morgunov, S. Peak-Chew, C. Cozens, K. M. Weeks, P. Herdewijn, P. Holliger, "Catalysts from synthetic genetic polymers", *Nature* **2015**, *518* (7539), 427-430. DOI: 10.1038/nature13982
[84] A. A. Fokina, M. I. Meschaninova, T. Durfort, A. G. Venyaminova, J.-C. François, "Targeting insulin-like growth factor I with 10–23 DNAzymes: 2′-O-methyl modifications in the catalytic core enhance mRNA cleavage", *Biochemistry* **2012**, *51* (11), 2181-2191. DOI: 10.1021/bi201532q
[85] S. Schubert, D. C. GuÈl, H. P. Grunert, H. Zeichhardt, V. A. Erdmann, J. Kurreck, "RNA cleaving '10-23'DNAzymes with enhanced stability and activity", *Nucleic Acids Res.* **2003**, *31* (20), 5982-5992. DOI: 10.1093/nar/gkg791
[86] C. WS Chan, L. M. Khachigian, "DNAzyme delivery approaches in biological settings", *Curr. Med. Chem.* **2013**, *20* (28), 3448-3455. DOI: 10.2174/09298673113209990033
[87] K. Hwang, P. Wu, T. Kim, L. Lei, S. Tian, Y. Wang, Y. Lu, "Photocaged DNAzymes as a general method for sensing metal ions in living cells", *Angew. Chem. Int. Ed.* **2014**, *53* (50), 13798-13802. DOI: 10.1002/anie.201408333
[88] Q. Zhang, Y. Liang, H. Xing, "Caging-decaging strategies to realize spatiotemporal control of DNAzyme activity for biosensing and bioimaging", *Chem. Res. Chin. Univ.* **2022**, *38* (4), 902-911. DOI: 10.1007/s40242-022-2137-3
[89] Q. Wang, Z. Wang, Y. He, B. Xiong, Y. Li, F. Wang, "Chemical and structural modification of RNA-cleaving DNAzymes for efficient biosensing and biomedical applications", *Trends Anal. Chem.* **2023**, *159*, 116910. DOI: 10.1016/j.trac.2022.116910
[90] Z. Yang, K. Y. Loh, Y.-T. Chu, R. Feng, N. S. R. Satyavolu, M. Xiong, S. M. Nakamata Huynh, K. Hwang, L. Li, H. Xing, "Optical control of metal ion probes in cells and zebrafish using highly selective DNAzymes conjugated to upconversion nanoparticles", *J. Am. Chem. Soc.* **2018**, *140* (50), 17656-17665. DOI: 10.1021/jacs.8b09867
[91] W. Wang, N. S. R. Satyavolu, Z. Wu, J. R. Zhang, J. J. Zhu, Y. Lu, "Near-Infrared

Photothermally Activated DNAzyme–Gold Nanoshells for Imaging Metal Ions in Living Cells", *Angew. Chem. Int. Ed.* **2017**, *129* (24), 6902-6906. DOI: 10.1002/ange.201701325
[92] R. Gao, L. Xu, C. Hao, C. Xu, H. Kuang, "Circular polarized light activated chiral satellite nanoprobes for the imaging and analysis of multiple metal ions in living cells", *Angew. Chem. Int. Ed.* **2019**, *131* (12), 3953-3957. DOI: 10.1002/ange.201814282
[93] D. Yi, J. Zhao, L. Li, "An enzyme-activatable engineered DNAzyme sensor for cell-selective imaging of metal ions", *Angew. Chem. Int. Ed.* **2021**, *60* (12), 6300-6304. DOI: 10.1002/anie.202015979
[94] L. Xiao, C. Gu, Y. Xiang, "Orthogonal Activation of RNA-Cleaving DNAzymes in Live Cells by Reactive Oxygen Species", *Angew. Chem. Int. Ed.* **2019**, *58* (40), 14167-14172. DOI: 10.1002/anie.201908105
[95] X. Wang, G. Kim, J. L. Chu, T. Song, Z. Yang, W. Guo, X. Shao, M. L. Oelze, K. C. Li, Y. Lu, "Noninvasive and spatiotemporal control of DNAzyme-based imaging of metal ions in vivo using high-intensity focused ultrasound", *J. Am. Chem. Soc.* **2022**, *144* (13), 5812-5819. DOI: 10.1021/jacs.1c11543
[96] M. M. Ali, F. Li, Z. Zhang, K. Zhang, D.-K. Kang, J. A. Ankrum, X. C. Le, W. Zhao, "Rolling circle amplification: a versatile tool for chemical biology, materials science and medicine", *Chem. Soc. Rev.* **2014**, *43* (10), 3324-3341. DOI: 10.1039/C3CS60439J
[97] M. G. Mohsen, E. T. Kool, "The discovery of rolling circle amplification and rolling circle transcription", *Acc. Chem. Res.* **2016**, *49* (11), 2540-2550. DOI: 10.1021/acs.accounts.6b00417
[98] G. A. S. Minero, J. Fock, B. Tian, G. Rizzi, F. Neumann, N. Madaboosi, M. Nilsson, M. Fougt Hansen, "Real-time analysis of switchable nanocomposites of magnesium pyrophosphates and rolling circle amplification products", *ChemNanoMat* **2020**, *6* (8), 1276-1282. DOI: 10.1002/cnma.202000135
[99] E. Kim, S. Agarwal, N. Kim, F. S. Hage, V. Leonardo, A. Gelmi, M. M. Stevens, "Bioinspired fabrication of DNA–inorganic hybrid composites using synthetic DNA", *ACS Nano* **2019**, *13* (3), 2888-2900. DOI: 10.1021/acsnano.8b06492
[100] Y. Lv, R. Hu, G. Zhu, X. Zhang, L. Mei, Q. Liu, L. Qiu, C. Wu, W. Tan, "Preparation and biomedical applications of programmable and multifunctional DNA nanoflowers", *Nat. Protoc.* **2015**, *10* (10), 1508-1524. DOI: 10.1038/nprot.2015.078
[101] J. Li, L. Lin, J. Yu, S. Zhai, G. Liu, L. Tian, "Fabrication and biomedical applications of “polymer-like” nucleic acids enzymatically produced by rolling circle amplification", *ACS Appl. Bio Mater.* **2019**, *2* (10), 4106-4120. DOI: 10.1021/acsabm.9b00622
[102] Y. Xu, Z. Lv, C. Yao, D. Yang, "Construction of rolling circle amplification-based DNA nanostructures for biomedical applications", *Biomat. Sci.* **2022**, *10* (12), 3054-3061. DOI: 10.1039/D2BM00445C
[103] Y. Jin, Z. Li, H. Liu, S. Chen, F. Wang, L. Wang, N. Li, K. Ge, X. Yang, X.-J. Liang, "Biodegradable, multifunctional DNAzyme nanoflowers for enhanced cancer therapy", *NPG Asia Mater.* **2017**, *9* (3), e365-e365. DOI: 10.1038/am.2017.34
[104] G. Zhu, R. Hu, Z. Zhao, Z. Chen, X. Zhang, W. Tan, "Noncanonical self-assembly of multifunctional DNA nanoflowers for biomedical applications", *J. Am. Chem. Soc.* **2013**, *135* (44), 16438-16445. DOI: 10.1021/ja406115e
[105] Z. Zhang, M. M. Ali, M. A. Eckert, D.-K. Kang, Y. Y. Chen, L. S. Sender, D. A. Fruman, W. Zhao, "A polyvalent aptamer system for targeted drug delivery", *Biomaterials* **2013**, *34* (37), 9728-9735. DOI: 10.1016/j.biomaterials.2013.08.079
[106] M. P. Stevens, *Polymer Chemistry: An Introduction*, 3rd ed., Oxford University Press, New York, **2009**.
[107] M. E. Launey, R. O. Ritchie, "On the fracture toughness of advanced materials", *Adv. Mater.* **2009**, *21* (20), 2103-2110. DOI: 10.1002/adma.200803322
[108] H. Staudinger, *Die Hochmolekularen Organischen Verbindungen - Kautschuk und Cellulose*, Springer, **1932**.
[109] T. Q. Nguyen, "Dynamics of flexible polymer chains in elongational flow", *Chimia* **2001**, *55* (3), 147-147. DOI: 10.2533/chimia.2001.147
[110] G. Ryskin, "Calculation of the effect of polymer additive in a converging flow", *J. Fluid*

Mech. **1987**, *178*, 423-440. DOI: 10.1017/S0022112087001290
[111] Y. Rabin, "Polymer fracture in steady and transient elongational flows"*, J. Chem. Phys.* **1987**, *86* (9), 5215-5216. DOI: 10.1063/1.452645
[112] D. E. Smith, S. Chu, "Response of flexible polymers to a sudden elongational flow"*, Science* **1998**, *281* (5381), 1335-1340. DOI: 10.1126/science.281.5381.1335
[113] A. Horn, E. Merrill, "Midpoint scission of macromolecules in dilute solution in turbulent flow"*, Nature* **1984**, *312* (5990), 140-141. DOI: 10.1038/312140a0
[114] E. Merrill, P. Leopairat, "Scission of non-interpenetrating macromolecules in transient extensional flows"*, Polym. Eng. Sci.* **1980**, *20* (7), 505-511. DOI: 10.1002/pen.760200711
[115] J. Mondal, R. Lakkaraju, P. Ghosh, M. Ashokkumar, "Acoustic cavitation-induced shear: a mini-review"*, Biophys. Rev.* **2021**, 1-15. DOI: 10.1007/s12551-021-00896-5
[116] E. Stride, C. Coussios, "Cavitation and contrast: the use of bubbles in ultrasound imaging and therapy"*, Proc. Inst. Mech. Eng. H.* **2010**, *224* (2), 171-191. DOI: 10.1243/09544119JEIM622
[117] S. K. Bhangu, M. Ashokkumar, "Theory of Sonochemistry"*, Top. Curr. Chem.* **2016**, *374* (56). DOI: 10.1007/s41061-016-0054-y
[118] R. Pecha, B. Gompf, "Microimplosions: cavitation collapse and shock wave emission on a nanosecond time scale"*, Phys. Rev. Lett.* **2000**, *84* (6), 1328. DOI: 10.1103/PhysRevLett.84.1328
[119] Y.-H. Chen, L. I, "Dynamics of impacting a bubble by another pulsed-laser-induced bubble: Jetting, fragmentation, and entanglement"*, Phys. Rev. E* **2008**, *77* (2), 026304. DOI: 10.1103/PhysRevE.77.026304
[120] M. Doulah, "A proposed mechanism for the degradation of addition polymers in cavitating ultrasonic fields"*, J. Appl. Polym. Sci.* **1978**, *22* (6), 1735-1743. DOI: 10.1002/app.1978.070220622
[121] G. Gooberman, "Ultrasonic degradation of polystyrene. Part 1. A proposed mechanism for degradation"*, J. Polym. Sci.* **1960**, *42* (139), 25-33. DOI: 10.1002/pol.1960.1204213904
[122] J. Lighthill, "Acoustic streaming"*, J. Sound Vib.* **1978**, *61* (3), 391-418. DOI: 10.1016/0022-460X(78)90388-7
[123] J. Jalal, T. S. Leong, "Microstreaming and its role in applications: A mini-review"*, Fluids* **2018**, *3* (4), 93. DOI: 10.3390/fluids3040093
[124] V. A. Henglein, "Die Reaktion des α, α-diphenyl-β-pikryl-hydrazyls mit langkettigen freien Radikalen, die beim Ultraschallabbau von Polymethacrylsäuremethylester gebildet werden"*, Macromol. Chem. Phys.* **1955**, *15* (1), 188-210. DOI: 10.1002/macp.1955.020150115
[125] K. L. Berkowski, S. L. Potisek, C. R. Hickenboth, J. S. Moore, "Ultrasound-induced site-specific cleavage of azo-functionalized poly (ethylene glycol)"*, Macromolecules* **2005**, *38* (22), 8975-8978. DOI: 10.1021/ma051394n
[126] T. Q. Nguyen, Q. Z. Liang, H.-H. Kausch, "Kinetics of ultrasonic and transient elongational flow degradation: a comparative study"*, Polymer* **1997**, *38* (15), 3783-3793. DOI: 10.1016/S0032-3861(96)00950-0
[127] M. Schaefer, B. Icli, C. Weder, M. Lattuada, A. F. Kilbinger, Y. C. Simon, "The role of mass and length in the sonochemistry of polymers"*, Macromolecules* **2016**, *49* (5), 1630-1636. DOI: 10.1021/acs.macromol.5b02362
[128] P. A. May, N. F. Munaretto, M. B. Hamoy, M. J. Robb, J. S. Moore, "Is molecular weight or degree of polymerization a better descriptor of ultrasound-induced mechanochemical transduction?"*, ACS Macro Lett.* **2016**, *5* (2), 177-180. DOI: 10.1021/acsmacrolett.5b00855
[129] G. I. Peterson, T.-L. Choi, "The influence of polymer architecture in polymer mechanochemistry"*, Chem. Comm.* **2021**, *57* (53), 6465-6474. DOI: 10.1039/D1CC02501E
[130] T. Q. Nguyen, H. H. Kausch, "Effects of solvent viscosity on polystyrene degradation in transient elongational flow"*, Macromolecules* **1990**, *23* (24), 5137-5145. DOI: 10.1021/ma00226a017

[131] T. Nguyen, H. Kausch, "Degradation of a polymer solution in transient elongational flow: effect of temperature", *Colloid Polym. Sci.* **1986**, *264*, 764-772. DOI: 10.1007/BF01500751
[132] G. J. Price, P. F. Smith, "Ultrasonic degradation of polymer solutions—III. The effect of changing solvent and solution concentration", *Eur. Polym. J.* **1993**, *29* (2-3), 419-424. DOI: 10.1016/0014-3057(93)90114-U
[133] G. Madras, S. Chattopadhyay, "Effect of solvent on the ultrasonic degradation of poly (vinyl acetate)", *Polym. Degrad. Stab.* **2001**, *71* (2), 273-278. DOI: 10.1016/S0141-3910(00)00174-9
[134] S. Chattopadhyay, G. Madras, "Influence of temperature on the ultrasonic degradation of poly (vinyl acetate) and poly (vinyl chloride)", *J. Appl. Polym. Sci.* **2003**, *88* (12), 2818-2822. DOI: 10.1002/app.12130
[135] G. J. Price, P. F. Smith, "Ultrasonic degradation of polymer solutions: 2. The effect of temperature, ultrasound intensity and dissolved gases on polystyrene in toluene", *Polymer* **1993**, *34* (19), 4111-4117. DOI: 10.1016/0032-3861(93)90675-Z
[136] G. Antti, P. Pentti, K. Hanna, "Ultrasonic degradation of aqueous carboxymethylcellulose: effect of viscosity, molecular mass, and concentration", *Ultrason. Sonochemistry* **2008**, *15* (4), 644-648. DOI:10.1016/j.ultsonch.2007.09.005
[137] V. Desai, M. A. Shenoy, P. R. Gogate, "Degradation of polypropylene using ultrasound-induced acoustic cavitation", *Chem. Eng. J.* **2008**, *140* (1-3), 483-487. DOI: 10.1016/j.cej.2007.11.030
[138] J. Odell, A. Keller, Y. Rabin, "Flow-induced scission of isolated macromolecules", *J. Chem. Phys.* **1988**, *88* (6), 4022-4028. Doi: 10.1063/1.453855
[139] J. A. Odell, A. J. Muller, K. A. Narh, A. Keller, "Degradation of polymer solutions in extensional flows", *Macromolecules* **1990**, *23* (12), 3092-3103. DOI: 10.1021/ma00214a011
[140] M. Encina, E. Lissi, M. Sarasua, L. Gargallo, D. Radic, "Ultrasonic degradation of polyvinylpyrrolidone: Effect of peroxide linkages", *J. Polym. Sci.* **1980**, *18* (12), 757-760. DOI: 10.1002/pol.1980.130181201
[141] F. Neufingerl, A. Palka, *Chemie 1: Allgemeine und anorganische Chemie*, 4th ed., Jugend & Volk, Wien, **2015**.
[142] C. R. Hickenboth, J. S. Moore, S. R. White, N. R. Sottos, J. Baudry, S. R. Wilson, "Biasing reaction pathways with mechanical force", *Nature* **2007**, *446* (7134), 423-427. DOI: 10.1038/nature05681
[143] D. A. Davis, A. Hamilton, J. Yang, L. D. Cremar, D. Van Gough, S. L. Potisek, M. T. Ong, P. V. Braun, T. J. Martínez, S. R. White, "Force-induced activation of covalent bonds in mechanoresponsive polymeric materials", *Nature* **2009**, *459* (7243), 68-72. DOI: 10.1038/nature07970
[144] P. Cordier, F. Tournilhac, C. Soulié-Ziakovic, L. Leibler, "Self-healing and thermoreversible rubber from supramolecular assembly", *Nature* **2008**, *451* (7181), 977-980. DOI: 10.1038/nature06669
[145] F. Donati, A. Pucci, C. Cappelli, B. Mennucci, G. Ruggeri, "Modulation of the optical response of polyethylene films containing luminescent perylene chromophores", *J. Phys. Chem. B* **2008**, *112* (12), 3668-3679. DOI: 10.1021/jp711193u
[146] J. M. Paulusse, R. P. Sijbesma, "Reversible mechanochemistry of a PdII coordination polymer", *Angew. Chem. Int. Ed.* **2004**, *43* (34), 4460-4462. DOI: 10.1002/anie.200460040
[147] A. M. Kushner, V. Gabuchian, E. G. Johnson, Z. Guan, "Biomimetic design of reversibly unfolding cross-linker to enhance mechanical properties of 3D network polymers", *J. Am. Chem. Soc.* **2007**, *129* (46), 14110-14111. DOI: 10.1021/ja0742176
[148] S.-J. Kim, D. Reneker, "A mechanochromic smart material", *Polym. Bull.* **1993**, *31*, 367-374. DOI: /10.1007/BF00692965
[149] H. Traeger, Y. Sagara, D. J. Kiebala, S. Schrettl, C. Weder, "Folded perylene diimide loops as mechanoresponsive motifs", *Angew. Chem. Int. Ed.* **2021**, *133* (29), 16327-16335. DOI: 10.1002/ange.202105219
[150] N. Huebsch, C. J. Kearney, X. Zhao, J. Kim, C. A. Cezar, Z. Suo, D. J. Mooney,

"Ultrasound-triggered disruption and self-healing of reversibly cross-linked hydrogels for drug delivery and enhanced chemotherapy", *Proc. Natl. Acad. Sci.* **2014**, *111* (27), 9762-9767. DOI: 10.1073/pnas.1405469111
[151] R. Merindol, G. Delechiave, L. Heinen, L. H. Catalani, A. Walther, "Modular design of programmable mechanofluorescent DNA hydrogels", *Nat. Comm.* **2019**, *10* (1), 528. DOI: 10.1038/s41467-019-08428-2
[152] K. Sakakibara, T. Fujisawa, J. P. Hill, K. Ariga, "Conformational interchange of a carbohydrate by mechanical compression at the air–water interface", *Phys. Chem. Chem. Phys.* **2014**, *16* (22), 10286-10294. DOI: 10.1039/C3CP55078H
[153] V. Vogel, "Mechanotransduction involving multimodular proteins: converting force into biochemical signals", *Annu. Rev. Biophys. Biomol. Struct.* **2006**, *35* (1), 459-488. DOI: 10.1146/annurev.biophys.35.040405.102013
[154] P. N. Wells, "Ultrasound imaging", *Phys. Med. Bio.* **2006**, *51* (13), R83. DOI: 10.1088/0031-9155/51/13/R06
[155] T. J. Mason, "Therapeutic ultrasound an overview", *Ultrason. Sonochemistry* **2011**, *18* (4), 847-852. DOI: 10.1016/j.ultsonch.2011.01.004
[156] M. Zou, P. Zhao, J. Fan, R. Göstl, A. Herrmann, "Microgels as drug carriers for sonopharmacology", *J. Polym. Sci.* **2022**, *60* (12), 1864-1870. DOI: 10.1002/pol.20210874
[157] L. Tu, Z. Liao, Z. Luo, Y. L. Wu, A. Herrmann, S. Huo, "Ultrasound-controlled drug release and drug activation for cancer therapy", *Exploration* **2021**, *1* (3), 20210023. DOI: 10.1002/EXP.20210023
[158] D. Yildiz, R. Göstl, A. Herrmann, "Sonopharmacology: controlling pharmacotherapy and diagnosis by ultrasound-induced polymer mechanochemistry", *Chem. Sci.* **2022**, *13* (46), 13708-13719. DOI: 10.1039/D2SC05196F
[159] J. Hahmann, A. Ishaqat, T. Lammers, A. Herrmann, "Sonogenetics for monitoring and modulating biomolecular function by ultrasound", *Angew. Chem. Int. Ed.* **2024**, *63* (13), e202317112. DOI: 10.1002/anie.202317112
[160] W. L. Nyborg, "Biological effects of ultrasound: development of safety guidelines. Part II: general review", *Ultrasound Med. Biol.* **2001**, *27* (3), 301-333. DOI: 10.1016/S0301-5629(00)00333-1
[161] C. J. Diederich, K. Hynynen, "Ultrasound technology for hyperthermia", *Ultrasound Med. Biol.* **1999**, *25* (6), 871-887. DOI: 10.1016/S0301-5629(99)00048-4
[162] C. Wright, K. Hynynen, D. Goertz, "In vitro and in vivo high-intensity focused ultrasound thrombolysis", *Investig. Radiol.* **2012**, *47* (4), 217-225. DOI: 10.1097/RLI.0b013e31823cc75c
[163] D. L. Miller, N. B. Smith, M. R. Bailey, G. J. Czarnota, K. Hynynen, I. R. S. Makin, B. C. o. t. A. I. o. U. i. Medicine, "Overview of therapeutic ultrasound applications and safety considerations", *J. Ultrasound Med.* **2012**, *31* (4), 623-634. DOI: 10.7863/jum.2012.31.4.623
[164] T. Şen, O. Tüfekçioğlu, Y. Koza, "Mechanical index", *Anatol. J. Cardiol.* **2015**, *15* (4), 334. DOI: 10.5152/akd.2015.6061
[165] S. Paliwal, S. Mitragotri, "Ultrasound-induced cavitation: applications in drug and gene delivery", *Expert Opin. Drug Deliv.* **2006**, *3* (6), 713-726. DOI: 10.1517/17425247.3.6.713
[166] S. Mitragotri, J. Kost, "Low-frequency sonophoresis: a review", *Adv. Drug Deliv. Rev.* **2004**, *56* (5), 589-601. DOI: 10.1016/j.addr.2003.10.024
[167] G. Kim, V. M. Lau, A. J. Halmes, M. L. Oelze, J. S. Moore, K. C. Li, "High-intensity focused ultrasound-induced mechanochemical transduction in synthetic elastomers", *Proc. Natl. Acad. Sci.* **2019**, *116* (21), 10214-10222. 10.1073/pnas.1901047116
[168] G. Kim, Q. Wu, J. L. Chu, E. J. Smith, M. L. Oelze, J. S. Moore, K. C. Li, "Ultrasound controlled mechanophore activation in hydrogels for cancer therapy", *Proc. Natl. Acad. Sci.* **2022**, *119* (4), e2109791119. DOI: 10.1073/pnas.2109791119
[169] J. Fan, M. Xuan, K. Zhang, R. Vinokur, L. Zheng, R. Göstl, A. Herrmann, "Accelerated Mechanophore Activation and Drug Release in Network Core-Structured Star Polymers Using High-Intensity Focused Ultrasound", *Small Sci.* **2024**, *4* (8), 2400082. DOI:

10.1002/smsc.202400082
[170] Y. Yao, M. E. McFadden, S. M. Luo, R. W. Barber, E. Kang, A. Bar-Zion, C. A. Smith, Z. Jin, M. Legendre, B. Ling, "Remote control of mechanochemical reactions under physiological conditions using biocompatible focused ultrasound", *Proc. Natl. Acad. Sci.* **2023**, *120* (39), e2309822120. DOI: 10.1073/pnas.2309822120
[171] L. Xu, J. Duan, J. Chen, S. Ding, W. Cheng, "Recent advances in rolling circle amplification-based biosensing strategies-A review", *Anal. Chim. Acta* **2021**, *1148*, 238187. doi. 10.1016/j.aca.2020.12.062
[172] P. Zhao, S. Huo, J. Fan, J. Chen, F. Kiessling, A. J. Boersma, R. Göstl, A. Herrmann, "Activation of the catalytic activity of thrombin for fibrin formation by ultrasound", *Angew. Chem. Int. Ed.* **2021**, *60* (26), 14707-14714. DOI: 10.1002/anie.202105404
[173] S. Huo, P. Zhao, Z. Shi, M. Zou, X. Yang, E. Warszawik, M. Loznik, R. Göstl, A. Herrmann, "Mechanochemical bond scission for the activation of drugs", *Nat. Chem.* **2021**, *13* (2), 131-139. DOI: 10.1038/s41557-020-00624-8
[174] S. L. Grokhovsky, I. A. Il'icheva, M. Golovkin, Y. Nechipurenko, D. Nechipurenko, L. Panchenko, R. Polozov, "Mechanochemical cleavage of DNA by ultrasound", *Adv. Eng. Res* **2014**, *213*, 1-24
[175] A. Ishaqat, J. Hahmann, C. Lin, X. Zhang, C. He, W. H. Rath, P. Habib, S. E. Sahnoun, K. Rahimi, R. Vinokur, "In vivo polymer mechanochemistry with polynucleotides", *Adv. Mater.* **2024**, *36* (32), 2403752. DOI: 10.1002/adma.202403752
[176] L. S. Goodman, M. M. Wintrobe, W. Dameshek, M. J. Goodman, A. Gilman, M. T. McLennan, "Nitrogen mustard therapy: Use of methyl-bis (beta-chloroethyl) amine hydrochloride and tris (beta-chloroethyl) amine hydrochloride for hodgkin's disease, lymphosarcoma, leukemia and certain allied and miscellaneous disorders", *Jama* **1984**, *251* (17), 2255-2261. DOI: 10.1001/jama.1984.03340410063036
[177] A. Gilman, "The initial clinical trial of nitrogen mustard", *Am. J. Surg.* **1963**, *105* (5), 574-578. DOI: 10.1016/0002-9610(63)90232-0
[178] S. M. Rink, M. S. Solomon, M. J. Taylor, S. B. Rajur, L. W. McLaughlin, P. B. Hopkins, "Covalent structure of a nitrogen mustard-induced DNA interstrand cross-link: an N7-to-N7 linkage of deoxyguanosine residues at the duplex sequence 5'-d (GNC)", *J. Am. Chem. Soc.* **1993**, *115* (7), 2551-2557. DOI: 10.1021/ja00060a001
[179] C. Heidelberger, N. Chaudhuri, P. Danneberg, D. Mooren, L. Griesbach, R. Duschinsky, R. Schnitzer, E. Pleven, J. Scheiner, "Fluorinated pyrimidines, a new class of tumour-inhibitory compounds", *Nature* **1957**, *179* (4561), 663-666. DOI: 10.1038/179663a0
[180] R. M. Whittington, H. P. Close, "Clinical experience with mitomycin C (NSC-26980)", *Cancer Chemother. Rep.* **1970**, *54* (3), 195-198
[181] V. Cepeda, M. A. Fuertes, J. Castilla, C. Alonso, C. Quevedo, J. M. Pérez, "Biochemical mechanisms of cisplatin cytotoxicity", *Anti-Cancer Agents Med. Chem.* **2007**, *7* (1), 3-18. DOI: 10.2174/187152007779314044
[182] P. F. Zipfel, C. Skerka, "From magic bullets to modern therapeutics: Paul Ehrlich, the German immunobiologist and physician coined the term 'complement'", *Mol. Immunol.* **2022**, *150*, 90-98. DOI: 10.1016/j.molimm.2022.08.002
[183] D. Hanahan, R. A. Weinberg, "The hallmarks of cancer", *Cell* **2000**, *100* (1), 57-70. DOI: 10.1016/s0092-8674(00)81683-9
[184] A. Arora, E. M. Scholar, "Role of tyrosine kinase inhibitors in cancer therapy", *J. Pharmacol. Exp. Ther.* **2005**, *315* (3), 971-979. DOI: 10.1124/jpet.105.084145
[185] C. Vernieri, S. Casola, M. Foiani, F. Pietrantonio, F. de Braud, V. Longo, "Targeting cancer metabolism: dietary and pharmacologic interventions", *Cancer Discov.* **2016**, *6* (12), 1315-1333. DOI: 10.1158/2159-8290.CD-16-0615
[186] L. Leanza, A. Managò, M. Zoratti, E. Gulbins, I. Szabo, "Pharmacological targeting of ion channels for cancer therapy: in vivo evidences", *Biochim. Biophys. Acta* **2016**, *1863* (6), 1385-1397. DOI: 10.1016/j.bbamcr.2015.11.032
[187] N. W. Mabe, J. A. Perry, C. F. Malone, K. Stegmaier, "Pharmacological targeting of the cancer epigenome", *Nat. Cancer* **2024**, *5* (6), 844-865. DOI: 10.1038/s43018-024-00777-2

[188] P. Carmeliet, R. K. Jain, "Angiogenesis in cancer and other diseases", *Nature* **2000**, *407* (6801), 249-257. DOI: 10.1038/35025220
[189] N. Ferrara, H.-P. Gerber, J. LeCouter, "The biology of VEGF and its receptors", *Nat. Med.* **2003**, *9* (6), 669-676. DOI: 10.1038/nm0603-669
[190] J. W. Baish, R. K. Jain, "Fractals and Cancer", *Cancer Res.* **2000**, *60* (14), 3683-3688
[191] L. E. Benjamin, D. Golijanin, A. Itin, D. Pode, E. Keshet, "Selective ablation of immature blood vessels in established human tumors follows vascular endothelial growth factor withdrawal", *J. Clin. Investig.* **1999**, *103* (2), 159-165. DOI: 10.1172/JCI5028
[192] H. Hashizume, P. Baluk, S. Morikawa, J. W. McLean, G. Thurston, S. Roberge, R. K. Jain, D. M. McDonald, "Openings between defective endothelial cells explain tumor vessel leakiness", *Am. J. Pathol.* **2000**, *156* (4), 1363-1380. DOI: 10.1016/S0002-9440(10)65006-7
[193] W. G. Roberts, G. E. Palade, "Neovasculature induced by vascular endothelial growth factor is fenestrated", *Cancer Res.* **1997**, *57* (4), 765-772
[194] G. Helmlinger, P. A. Netti, H. C. Lichtenbeld, R. J. Melder, R. K. Jain, "Solid stress inhibits the growth of multicellular tumor spheroids", *Nat. Biotechnol.* **1997**, *15* (8), 778-783. DOI: 10.1038/nbt0897-778
[195] C.-H. Heldin, K. Rubin, K. Pietras, A. Östman, "High interstitial fluid pressure—an obstacle in cancer therapy", *Nat. Rev. Cancer* **2004**, *4* (10), 806-813. DOI: 10.1038/nrc1456
[196] S. M. Kim, P. H. Faix, J. E. Schnitzer, "Overcoming key biological barriers to cancer drug delivery and efficacy", *J. Control. Release* **2017**, *267*, 15-30. DOI: 10.1016/j.jconrel.2017.09.016
[197] R. K. Jain, "Normalizing tumor vasculature with anti-angiogenic therapy: a new paradigm for combination therapy", *Nat. Med.* **2001**, *7* (9), 987-989. DOI: 10.1038/nm0901-987
[198] A. Rapisarda, G. Melillo, "Overcoming disappointing results with antiangiogenic therapy by targeting hypoxia", *Nat. Rev. Clin. Oncol.* **2012**, *9* (7), 378-390. DOI: 10.1038/nrclinonc.2012.64
[199] T. Donnem, J. Hu, M. Ferguson, O. Adighibe, C. Snell, A. L. Harris, K. C. Gatter, F. Pezzella, "Vessel co-option in primary human tumors and metastases: an obstacle to effective anti-angiogenic treatment?", *Cancer Med.* **2013**, *2* (4), 427-436. DOI: 10.1002/cam4.105
[200] J. A. Nagy, H. F. Dvorak, "Heterogeneity of the tumor vasculature: the need for new tumor blood vessel type-specific targets", *Clin. Exp. Metastasis* **2012**, *29*, 657-662. DOI: 10.1007/s10585-012-9500-6
[201] S. T. Pan, Z. L. Li, Z. X. He, J. X. Qiu, S. F. Zhou, "Molecular mechanisms for tumour resistance to chemotherapy", *Clin. Exp. Pharmacol. Physiol.* **2016**, *43* (8), 723-737. DOI: 10.1111/1440-1681.12581
[202] S. G. Aller, J. Yu, A. Ward, Y. Weng, S. Chittaboina, R. Zhuo, P. M. Harrell, Y. T. Trinh, Q. Zhang, I. L. Urbatsch, "Structure of P-glycoprotein reveals a molecular basis for poly-specific drug binding", *Science* **2009**, *323* (5922), 1718-1722. DOI: 10.1126/science.1168750
[203] Y. Fan, K. Ma, J. Jing, C. Wang, Y. Hu, Y. Shi, E. Li, Q. Geng, "Recombinant dual-target MDM2/MDMX inhibitor reverses doxorubicin resistance through activation of the TAB1/TAK1/p38 MAPK pathway in wild-type p53 multidrug-resistant breast cancer cells", *J. Cancer* **2020**, *11* (1), 25. DOI: 10.7150/jca.32765
[204] C. Xu, Y. Wang, Z. Guo, J. Chen, L. Lin, J. Wu, H. Tian, X. Chen, "Pulmonary delivery by exploiting doxorubicin and cisplatin co-loaded nanoparticles for metastatic lung cancer therapy", *J. Control. Release* **2019**, *295*, 153-163. DOI: 10.1016/j.jconrel.2018.12.013
[205] Y. Wei, L. Gao, L. Wang, L. Shi, E. Wei, B. Zhou, L. Zhou, B. Ge, "Polydopamine and peptide decorated doxorubicin-loaded mesoporous silica nanoparticles as a targeted drug delivery system for bladder cancer therapy", *Drug Deliv.* **2017**, *24* (1), 681-691. DOI: 10.1080/10717544.2017.1309475
[206] Y. Malinovskaya, P. Melnikov, V. Baklaushev, A. Gabashvili, N. Osipova, S. Mantrov,

Y. Ermolenko, O. Maksimenko, M. Gorshkova, V. Balabanyan, "Delivery of doxorubicin-loaded PLGA nanoparticles into U87 human glioblastoma cells", *Int. J. Pharm.* **2017**, *524* (1-2), 77-90. DOI: 10.1016/j.ijpharm.2017.03.049

[207] S. Y. van der Zanden, X. Qiao, J. Neefjes, "New insights into the activities and toxicities of the old anticancer drug doxorubicin", *FEBS J.* **2021**, *288* (21), 6095-6111. DOI: 10.1111/febs.15583

[208] J. Liu, M. Zhu, Y. Feng, Q. Tang, M. Xu, "The multidrug resistance can be reversed for the decrease of P-gp and LRP by inhibiting PI3K/Akt/NF-κB signal pathway in nasopharynx carcinoma", *Biosci. Rep.* **2020**, *40* (5), BSR20190239. doi. 10.1042/BSR20190239

[209] I.-g. Ryoo, G. Kim, B.-h. Choi, S.-h. Lee, M.-K. Kwak, "Involvement of NRF2 signaling in doxorubicin resistance of cancer stem cell-enriched colonospheres", *Biomol. Ther.* **2016**, *24* (5), 482. DOI: 10.4062/biomolther.2016.145

[210] A. C. Tan, D. M. Ashley, G. Y. López, M. Malinzak, H. S. Friedman, M. Khasraw, "Management of glioblastoma: State of the art and future directions", *CA: Cancer J. Clin.* **2020**, *70* (4), 299-312. DOI: 10.3322/caac.21613

[211] B. C. Prager, S. Bhargava, V. Mahadev, C. G. Hubert, J. N. Rich, "Glioblastoma stem cells: driving resilience through chaos", *Trends Cancer* **2020**, *6* (3), 223-235. DOI: 10.1016/j.trecan.2020.01.009

[212] S. Han, Y. Liu, S. J. Cai, M. Qian, J. Ding, M. Larion, M. R. Gilbert, C. Yang, "IDH mutation in glioma: molecular mechanisms and potential therapeutic targets", *Br. J. Cancer* **2020**, *122* (11), 1580-1589. DOI: 10.1038/s41416-020-0814-x

[213] F. Mo, A. Pellerino, R. Soffietti, R. Rudà, "Blood–brain barrier in brain tumors: biology and clinical relevance", *Int. J. Mol. Sci.* **2021**, *22* (23), 12654. DOI: 10.3390/ijms222312654

[214] P. Ballabh, A. Braun, M. Nedergaard, "The blood–brain barrier: an overview: structure, regulation, and clinical implications", *Neurobiol. Dis.* **2004**, *16* (1), 1-13. DOI: 10.1016/j.nbd.2003.12.016

[215] A. Ou, W. A. Yung, N. Majd, "Molecular mechanisms of treatment resistance in glioblastoma", *Int. J. Mol. Sci.* **2020**, *22* (1), 351. DOI: 10.3390/ijms22010351

[216] A. Tsuji, T. Terasaki, Y. Takabatake, Y. Tenda, I. Tamai, T. Yamashima, S. Moritani, T. Tsuruo, J. Yamashita, "P-glycoprotein as the drug efflux pump in primary cultured bovine brain capillary endothelial cells", *Life Sci.* **1992**, *51* (18), 1427-1437. DOI: 10.1016/0024-3205(92)90537-Y

[217] C. Zhao, H. Wang, C. Xiong, Y. Liu, "Hypoxic glioblastoma release exosomal VEGF-A induce the permeability of blood-brain barrier", *Biochem. Biophys. Res. Commun.* **2018**, *502* (3), 324-331. DOI: 10.1016/j.bbrc.2018.05.140

[218] E. A. Neuwelt, E. P. Frenkel, J. Diehl, L. Vu, S. Rapoport, S. Hill, "Reversible osmotic blood-brain barrier disruption in humans: implications for the chemotherapy of malignant brain tumors", *Neurosurgery* **1980**, *7* (1), 44-52. DOI: 10.1227/00006123-198007000-00007

[219] S. Kunwar, S. Chang, M. Westphal, M. Vogelbaum, J. Sampson, G. Barnett, M. Shaffrey, Z. Ram, J. Piepmeier, M. Prados, "Phase III randomized trial of CED of IL13-PE38QQR vs Gliadel wafers for recurrent glioblastoma", *Neuro-Oncol.* **2010**, *12* (8), 871-881. DOI: 10.1093/neuonc/nop054

[220] K.-T. Chen, Y.-J. Lin, W.-Y. Chai, C.-J. Lin, P.-Y. Chen, C.-Y. Huang, J. S. Kuo, H.-L. Liu, K.-C. Wei, "Neuronavigation-guided focused ultrasound (NaviFUS) for transcranial blood-brain barrier opening in recurrent glioblastoma patients: Clinical trial protocol", *Ann. Transl. Med.* **2020**, *8* (11), 673. DOI: 10.21037/atm-20-344

[221] D. Liu, D. T. Auguste, "Cancer targeted therapeutics: From molecules to drug delivery vehicles", *J. Control. Release* **2015**, *219*, 632-643. DOI: 10.1016/j.jconrel.2015.08.041

[222] H. S. Choi, W. Liu, P. Misra, E. Tanaka, J. P. Zimmer, B. I. Ipe, M. G. Bawendi, J. V. Frangioni, "Renal clearance of nanoparticles", *Nat. Biotechnol.* **2007**, *25* (10), 1165. DOI: 10.1038/nbt1340

[223] G. Arturson, G. Wallenius, "The renal clearance of dextran of different molecular sizes in normal humans", *Scand. J. Clin. Lab. Investig.* **1964**, *16* (1), 81-86. DOI:

10.3109/00365516409060486
[224] S. Jain, D. Hirst, J. O'Sullivan, "Gold nanoparticles as novel agents for cancer therapy", *Br. J. Radiol.* **2012**, *85* (1010), 101-113. DOI: 10.1259/bjr/59448833
[225] Z. Li, J. C. Barnes, A. Bosoy, J. F. Stoddart, J. I. Zink, "Mesoporous silica nanoparticles in biomedical applications", *Chem. Soc. Rev.* **2012**, *41* (7), 2590-2605. DOI: 10.1039/C1CS15246G
[226] K. Maruyama, "Intracellular targeting delivery of liposomal drugs to solid tumors based on EPR effects", *Adv. Drug Deliv. Rev.* **2011**, *63* (3), 161-169. DOI: 10.1016/j.addr.2010.09.003
[227] H. Maeda, G. Bharate, J. Daruwalla, "Polymeric drugs for efficient tumor-targeted drug delivery based on EPR-effect", *Eur. J. Pharm. Biopharm.* **2009**, *71* (3), 409-419. DOI: 10.1016/j.ejpb.2008.11.010
[228] M. Gaumet, A. Vargas, R. Gurny, F. Delie, "Nanoparticles for drug delivery: the need for precision in reporting particle size parameters", *Eur. J. Pharm. Biopharm.* **2008**, *69* (1), 1-9. DOI: 10.1016/j.ejpb.2007.08.001
[229] M. R. Dreher, W. Liu, C. R. Michelich, M. W. Dewhirst, F. Yuan, A. Chilkoti, "Tumor vascular permeability, accumulation, and penetration of macromolecular drug carriers", *J. Natl. Cancer Inst.* **2006**, *98* (5), 335-344. doi. 10.1093/jnci/djj070
[230] C. He, Y. Hu, L. Yin, C. Tang, C. Yin, "Effects of particle size and surface charge on cellular uptake and biodistribution of polymeric nanoparticles", *Biomaterials* **2010**, *31* (13), 3657-3666. DOI: 10.1016/j.biomaterials.2010.01.065
[231] J. A. Champion, Y. K. Katare, S. Mitragotri, "Particle shape: a new design parameter for micro-and nanoscale drug delivery carriers", *J. Control. Release* **2007**, *121* (1-2), 3-9. DOI: 10.1016/j.jconrel.2007.03.022
[232] M. Sun, T. Wang, L. Li, X. Li, Y. Zhai, J. Zhang, W. Li, "The application of inorganic nanoparticles in molecular targeted cancer therapy: EGFR targeting", *Front. Pharmacol.* **2021**, *12*, 702445. DOI: 10.3389/fphar.2021.702445
[233] H. Takahashi, G. Yoshimatsu, D. L. Faustman, "The roles of TNFR2 signaling in cancer cells and the tumor microenvironment and the potency of TNFR2 targeted therapy", *Cells* **2022**, *11* (12), 1952. DOI: 10.3390/cells11121952
[234] S. D. Jayasena, "Aptamers: an emerging class of molecules that rival antibodies in diagnostics", *Clin. Chem.* **1999**, *45* (9), 1628-1650. DOI: 10.1093/clinchem/45.9.1628
[235] M. S. Nabavinia, A. Gholoobi, F. Charbgoo, M. Nabavinia, M. Ramezani, K. Abnous, "Anti-MUC1 aptamer: a potential opportunity for cancer treatment", *Med. Res. Rev.* **2017**, *37* (6), 1518-1539. DOI: 10.1002/med.21462
[236] E. Sicco, J. Baez, M. Ibarra, M. Fernández, P. Cabral, M. Moreno, H. Cerecetto, V. Calzada, "Sgc8-c aptamer as a potential theranostic agent for hemato-oncological malignancies", *Cancer Biother. Radiopharm.* **2020**, *35* (4), 262-270. DOI: 0.1089/cbr.2019.3402
[237] P. J. Bates, D. A. Laber, D. M. Miller, S. D. Thomas, J. O. Trent, "Discovery and development of the G-rich oligonucleotide AS1411 as a novel treatment for cancer", *Exp. Mol. Pathol.* **2009**, *86* (3), 151-164. DOI: 10.1016/j.yexmp.2009.01.004
[238] C. Riccardi, D. Musumeci, I. R. Krauss, M. Piccolo, C. Irace, L. Paduano, D. Montesarchio, "Exploring the conformational behaviour and aggregation properties of lipid-conjugated AS1411 aptamers", *Int. J. Biol. Macromol.* **2018**, *118*, 1384-1399. DOI: 10.1016/j.ijbiomac.2018.06.137
[239] S. Soundararajan, L. Wang, V. Sridharan, W. Chen, N. Courtenay-Luck, D. Jones, E. K. Spicer, D. J. Fernandes, "Plasma membrane nucleolin is a receptor for the anticancer aptamer AS1411 in MV4-11 leukemia cells", *Mol. Pharmacol.* **2009**, *76* (5), 984-991. DOI: 10.1124/mol.109.055947
[240] J. E. Rosenberg, R. M. Bambury, E. M. Van Allen, H. A. Drabkin, P. N. Lara, A. L. Harzstark, N. Wagle, R. A. Figlin, G. W. Smith, L. A. Garraway, "A phase II trial of AS1411 (a novel nucleolin-targeted DNA aptamer) in metastatic renal cell carcinoma", *Investig. New Drugs* **2014**, *32*, 178-187. DOI: 10.1007/s10637-013-0045-6
[241] T. L. Trinh, G. Zhu, X. Xiao, W. Puszyk, K. Sefah, Q. Wu, W. Tan, C. Liu, "A synthetic aptamer-drug adduct for targeted liver cancer therapy", *PLoS One* **2015**, *10* (11),

e0136673. DOI: 10.1371/journal.pone.0136673
[242] S. H. Rajabnejad, A. Mokhtarzadeh, K. Abnous, S. M. Taghdisi, M. Ramezani, B. M. Razavi, "Targeted delivery of melittin to cancer cells by AS1411 anti-nucleolin aptamer", *Drug Dev. Ind. Pharm.* **2018**, *44* (6), 982-987. doi. 10.1080/03639045.2018.1427760
[243] F. S. M. Tekie, M. Soleimani, A. Zakerian, M. Dinarvand, M. Amini, R. Dinarvand, E. Arefian, F. Atyabi, "Glutathione responsive chitosan-thiolated dextran conjugated miR-145 nanoparticles targeted with AS1411 aptamer for cancer treatment", *Carbohydr. Polym.* **2018**, *201*, 131-140. DOI: 10.1016/j.carbpol.2018.08.060
[244] S. Vandghanooni, M. Eskandani, J. Barar, Y. Omidi, "AS1411 aptamer-decorated cisplatin-loaded poly (lactic-co-glycolic acid) nanoparticles for targeted therapy of miR-21-inhibited ovarian cancer cells", *Nanomedicine* **2018**, *13* (21), 2729-2758. DOI: 10.2217/nnm-2018-0205
[245] Y. Li, Y. Duo, J. Bi, X. Zeng, L. Mei, S. Bao, L. He, A. Shan, Y. Zhang, X. Yu, "Targeted delivery of anti-miR-155 by functionalized mesoporous silica nanoparticles for colorectal cancer therapy", *Int. J. Nanomed.* **2018**, 1241-1256. DOI: 10.2147/IJN.S158290
[246] L. Li, J. Hou, X. Liu, Y. Guo, Y. Wu, L. Zhang, Z. Yang, "Nucleolin-targeting liposomes guided by aptamer AS1411 for the delivery of siRNA for the treatment of malignant melanomas", *Biomaterials* **2014**, *35* (12), 3840-3850. DOI: 10.1016/j.biomaterials.2014.01.019
[247] X. Liu, L. Wu, L. Wang, W. Jiang, "A dual-targeting DNA tetrahedron nanocarrier for breast cancer cell imaging and drug delivery", *Talanta* **2018**, *179*, 356-363. DOI: 10.1016/j.talanta.2017.11.034
[248] X. Li, X. Wu, H. Yang, L. Li, Z. Ye, Y. Rao, "A nuclear targeted Dox-aptamer loaded liposome delivery platform for the circumvention of drug resistance in breast cancer", *Biomed. Pharmacother.* **2019**, *117*, 109072. DOI: 10.1016/j.biopha.2019.109072
[249] R. Tuteja, N. Tuteja, "Nucleolin: a multifunctional major nucleolar phosphoprotein", *Crit. Rev. Biochem. Mol. Biol.* **1998**, *33* (6), 407-436. DOI: 10.1080/10409239891204260
[250] B. Giles, M. Nakhjavani, A. Wiesa, T. Knight, S. Shigdar, R. M. Samarasinghe, "Unravelling the glioblastoma tumour microenvironment: Can aptamer targeted delivery become successful in treating brain cancers?", *Cancers* **2023**, *15* (17), 4376. DOI: /10.3390/cancers15174376
[251] Y. Zeng, L. Zhao, K. Li, J. Ma, D. Chen, C. Liu, W. Zhan, Y. Zhan, "Aptamer-functionalized nanoplatforms overcoming temozolomide resistance in synergistic chemo/photothermal therapy through alleviating tumor hypoxia", *Nano Res.* **2023**, *16* (7), 9859-9872. DOI: 10.1007/s12274-023-5742-7
[252] Z. Luo, Z. Yan, K. Jin, Q. Pang, T. Jiang, H. Lu, X. Liu, Z. Pang, L. Yu, X. Jiang, "Precise glioblastoma targeting by AS1411 aptamer-functionalized poly (l-γ-glutamylglutamine)–paclitaxel nanoconjugates", *J. Colloid Interface Sci.* **2017**, *490*, 783-796. DOI: 10.1016/j.jcis.2016.12.004
[253] K. Seo, K. Hwang, K. M. Nam, M. J. Kim, Y.-K. Song, C.-Y. Kim, "Nucleolin-Targeting AS1411 Aptamer-Conjugated Nanospheres for Targeted Treatment of Glioblastoma", *Pharmaceutics* **2024**, *16* (4), 566. doi. 10.3390/pharmaceutics16040566
[254] H. Gao, J. Qian, S. Cao, Z. Yang, Z. Pang, S. Pan, L. Fan, Z. Xi, X. Jiang, Q. Zhang, "Precise glioma targeting of and penetration by aptamer and peptide dual-functioned nanoparticles", *Biomaterials* **2012**, *33* (20), 5115-5123. DOI: 10.1016/j.biomaterials.2012.03.058
[255] H. Wang, Z. Zhu, G. Zhang, F. Lin, Y. Liu, Y. Zhang, J. Feng, W. Chen, Q. Meng, L. Chen, "AS1411 aptamer/hyaluronic acid-bifunctionalized microemulsion co-loading shikonin and docetaxel for enhanced antiglioma therapy", *J. Pharm. Sci.* **2019**, *108* (11), 3684-3694. DOI: 10.1016/j.xphs.2019.08.017
[256] P. M. Friden, L. R. Walus, G. F. Musso, M. A. Taylor, B. Malfroy, R. M. Starzyk, "Anti-transferrin receptor antibody and antibody-drug conjugates cross the blood-brain barrier", *Proc. Natl. Acad. Sci.* **1991**, *88* (11), 4771-4775. DOI: 10.1073/pnas.88.11.4771

[257] J. H. Lee, J. A. Engler, J. F. Collawn, B. A. Moore, "Receptor mediated uptake of peptides that bind the human transferrin receptor"*, Eur. J. Biochem.* **2001**, *268* (7), 2004-2012. DOI: 10.1046/j.1432-1327.2001.02073.x

[258] J.-W. Choi, M. Seo, K. Kim, A.-R. Kim, H. Lee, H.-S. Kim, C. G. Park, S. W. Cho, J. H. Kang, J. Joo, "Aptamer nanoconstructs crossing human blood–brain barrier discovered via microphysiological system-based SELEX technology"*, ACS Nano* **2023**, *17* (9), 8153-8166. DOI: 10.1021/acsnano.2c11675

[259] W. Fu, C. You, L. Ma, H. Li, Y. Ju, X. Guo, S. Shi, T. Zhang, R. Zhou, Y. Lin, "Enhanced efficacy of temozolomide loaded by a tetrahedral framework DNA nanoparticle in the therapy for glioblastoma"*, ACS Appl. Mater. Interfaces* **2019**, *11* (43), 39525-39533. DOI: 10.1021/acsami.9b13829

[260] J. Macdonald, J. Henri, L. Goodman, D. Xiang, W. Duan, S. Shigdar, "Development of a bifunctional aptamer targeting the transferrin receptor and epithelial cell adhesion molecule (EpCAM) for the treatment of brain cancer metastases"*, ACS Chem. Neurosci.* **2017**, *8* (4), 777-784. DOI: 10.1021/acschemneuro.6b00369

[261] E. Moradi, T. Zavvar, M. Alibolandi, M. Ramezani, K. Abnous, S. M. Taghdisi, "Targeted delivery of epirubicin to breast cancer cells using poly-aptamer DNA nanocarriers prepared by the RCA method with multiple repeats of aptamers of FOXM1 and AS1411"*, Drug Dev. Ind. Pharm.* **2023**, *49* (3), 260-270. DOI: 10.1080/03639045.2023.2199075

[262] H. Liao, Y. Cao, C. Hu, S. Shen, Z. Zhang, D. Li, Y. Du, "Oxygen-producing and pH-responsive targeted DNA nanoflowers for enhanced chemo-sonodynamic therapy of lung cancer"*, Mater. Today Bio* **2024**, *25*, 101005. DOI: 10.1016/j.mtbio.2024.101005

[263] J. Tannenbaum, B. T. Bennett, "Russell and Burch's 3Rs then and now: the need for clarity in definition and purpose"*, J. Am. Assoc. Lab. Anim. Sci.* **2015**, *54* (2), 120-132

[264] M. Ravi, V. Paramesh, S. Kaviya, E. Anuradha, F. P. Solomon, "3D cell culture systems: advantages and applications"*, J. Cell. Physiol.* **2015**, *230* (1), 16-26. DOI: 10.1002/jcp.24683

[265] L. A. Low, C. Mummery, B. R. Berridge, C. P. Austin, D. A. Tagle, "Organs-on-chips: into the next decade"*, Nat. Rev. Drug. Discov.* **2021**, *20* (5), 345-361. DOI: 10.1038/s41573-020-0079-3

[266] J. M. Ayuso, R. Monge, A. Martínez-González, M. Virumbrales-Muñoz, G. A. Llamazares, J. Berganzo, A. Hernández-Laín, J. Santolaria, M. Doblaré, C. Hubert, "Glioblastoma on a microfluidic chip: Generating pseudopalisades and enhancing aggressiveness through blood vessel obstruction events"*, Neuro-Oncol.* **2017**, *19* (4), 503-513. DOI: 10.1093/neuonc/now230

[267] Z. Xie, M. Chen, J. Lian, H. Wang, J. Ma, "Glioblastoma-on-a-chip construction and therapeutic applications"*, Front. Oncol.* **2023**, *13*, 1183059. DOI: 10.3389/fonc.2023.1183059

[268] S. I. Ahn, Y. J. Sei, H.-J. Park, J. Kim, Y. Ryu, J. J. Choi, H.-J. Sung, T. J. MacDonald, A. I. Levey, Y. Kim, "Microengineered human blood–brain barrier platform for understanding nanoparticle transport mechanisms"*, Nat. Comm.* **2020**, *11* (1), 175. DOI: 10.1038/s41467-019-13896-7

[269] A. Sarnella, Y. Ferrara, C. Terlizzi, S. Albanese, S. Monti, L. Licenziato, M. Mancini, "The Chicken Embryo: An Old but Promising Model for In Vivo Preclinical Research"*, Biomedicines* **2024**, *12* (12), 2835. DOI: 10.3390/biomedicines12122835

[270] S. C. Süß, J. Werner, A. M. Saller, L. Weiss, J. Reiser, J. M. Ondracek, Y. Zablotski, S. Kollmansperger, M. Anders, H. Potschka, "Nociception in chicken embryos, Part III: Analysis of movements before and after application of a noxious stimulus"*, Animals* **2023**, *13* (18), 2859. DOI: 10.3390/ani13182859

[271] C. A. Aventurado, J. B. Billones, R. D. Vasquez, A. L. Castillo, "In ovo and in silico evaluation of the anti-angiogenic potential of syringin"*, Drug Des. Dev. Ther.* **2020**, 5189-5204. DOI: 10.2147/DDDT.S271952

[272] E. Grambow, H. Sorg, C. G. Sorg, D. Strüder, "Experimental models to study skin wound healing with a focus on angiogenesis"*, Med: Sci:* **2021**, *9* (3), 55. DOI: 10.3390/medsci9030055

[273] A. K. Mapanao, P. P. Che, P. Sarogni, P. Sminia, E. Giovannetti, V. Voliani, "Tumor grafted–chick chorioallantoic membrane as an alternative model for biological cancer research and conventional/nanomaterial-based theranostics evaluation"*, Expert Opin. Drug Metab. Toxicol.* **2021**, *17* (8), 947-968. DOI: 10.1080/17425255.2021.1879047
[274] P. Garcia, Y. Wang, J. Viallet, Z. Macek Jilkova, "The chicken embryo model: a novel and relevant model for immune-based studies"*, Front. Immunol.* **2021**, *12*, 791081. DOI: 10.3389/fimmu.2021.791081
[275] A. Senrung, T. Tripathi, D. Janjua, S. K. Yadav, A. Chhokar, N. Aggarwal, J. Yadav, A. Chaudhary, U. Joshi, P. Sethi, "Chick chorioallantoic membrane: a valuable 3D in vivo model for screening nanoformulations for tumor antiangiogenic therapeutics"*, Int. J. Dev. Biol.* **2024**, *67* (4), 115-135. DOI: 10.1387/ijdb.230198pb
[276] K. Mitrevska, M. A. M. Rodrigo, N. Cernei, H. Michalkova, Z. Splichal, D. Hynek, O. Zitka, Z. Heger, P. Kopel, V. Adam, "Chick chorioallantoic membrane (CAM) assay for the evaluation of the antitumor and antimetastatic activity of platinum-based drugs in association with the impact on the amino acid metabolism"*, Mater. Today Bio* **2023**, *19*, 100570. DOI: 10.1016/j.mtbio.2023.100570
[277] K. S. Butler, C. J. Brinker, H. S. Leong, "Bridging the in vitro to in vivo gap: using the chick embryo model to accelerate nanoparticle validation and qualification for in vivo studies"*, ACS Nano* **2022**, *16* (12), 19626-19650. DOI: 10.1021/acsnano.2c03990
[278] B. Li, Z. Jiang, D. Xie, Y. Wang, X. Lao, "Cetuximab-modified CuS nanoparticles integrating near-infrared-II-responsive photothermal therapy and anti-vessel treatment"*, Int. J. Nanomed.* **2018**, 7289-7302. DOI: 10.2147/IJN.S175334
[279] N. Babae, M. Bourajjaj, Y. Liu, J. R. Van Beijnum, F. Cerisoli, P. V. Scaria, M. Verheul, M. P. Van Berkel, E. H. Pieters, R. J. Van Haastert, "Systemic miRNA-7 delivery inhibits tumor angiogenesis and growth in murine xenograft glioblastoma"*, Oncotarget* **2014**, *5* (16), 6687. DOI: 10.18632/oncotarget.2235
[280] E. Eremeeva, M. Abramov, L. Margamuljana, P. Herdewijn, "Base-modified nucleic acids as a powerful tool for synthetic biology and biotechnology"*, Chem. Euro. J.* **2017**, *23* (40), 9560-9576. DOI: 10.1002/chem.201700679
[281] J. Balintová, J. Špaček, R. Pohl, M. Brázdová, L. Havran, M. Fojta, M. Hocek, "Azidophenyl as a click-transformable redox label of DNA suitable for electrochemical detection of DNA–protein interactions"*, Chem. Sci.* **2015**, *6* (1), 575-587. DOI: 10.1039/C4SC01906G
[282] K. O. Brenske, M. Emondts, S. T. Hörnig, S. Panitz, M. I. Pieper, A. Ligori, A. Schacht, J. Henkel, J. Klankermayer, A. Herrmann, "Parahydrogen-Induced Polarization of a Labeled, Cancer-Targeting DNA Aptamer"*, Angew. Chem. Int. Ed.* **2023**, *62* (22), e202300531. DOI: 10.1002/anie.202300531
[283] C. Höbartner, C. Kreutz, E. Flecker, E. Ottenschläger, W. Pils, K. Grubmayr, R. Micura, "The synthesis of 2′-O-[(triisopropylsilyl) oxy] methyl (TOM) phosphoramidites of methylated ribonucleosides (m 1 G, m 2 G, m 2 2 G, m 1 I, m 3 U, m 4 C, m 6 A, m 6 2 A) for use in automated RNA solid-phase synthesis"*, Monatsh. Chemie* **2003**, *134*, 851-873. DOI: 10.1007/s00706-003-0592-1
[284] T. P. Prakash, "An overview of sugar-modified oligonucleotides for antisense therapeutics"*, Chem. Biodiversity* **2011**, *8* (9), 1616-1641. DOI: 10.1002/cbdv.201100081
[285] Á. Somoza, "Protecting groups for RNA synthesis: an increasing need for selective preparative methods"*, Chem. Soc. Rev.* **2008**, *37* (12), 2668-2675. DOI: 10.1039/B809851D
[286] X. Wei, "Coupling activators for the oligonucleotide synthesis via phosphoramidite approach"*, Tetrahedron* **2013**, *69* (18), 3615-3637. DOI: 10.1016/j.tet.2013.03.001
[287] G. P. Miller, E. T. Kool, "Versatile 5 ‘-Functionalization of Oligonucleotides on Solid Support: Amines, Azides, Thiols, and Thioethers via Phosphorus Chemistry"*, J. Org. Chem.* **2004**, *69* (7), 2404-2410. DOI: 10.1021/jo035765e
[288] G. Goel, A. Kumar, A. Puniya, W. Chen, K. Singh, "Molecular beacon: a multitask probe"*, J. Appl. Microbiol.* **2005**, *99* (3), 435-442. DOI: 10.1111/j.1365-2672.2005.02663.x

[289] K. Bartosik, K. Debiec, A. Czarnecka, E. Sochacka, G. Leszczynska, "Synthesis of nucleobase-modified RNA oligonucleotides by post-synthetic approach", *Molecules* **2020**, *25* (15), 3344. DOI: 10.3390/molecules25153344
[290] V. A. Korshun, D. A. Stetsenko, M. J. Gait, "Novel uridin-2′-yl carbamates: synthesis, incorporation into oligodeoxyribonucleotides, and remarkable fluorescence properties of 2′-pyren-1-ylmethylcarbamate", *J. Chem. Soc.* **2002** (8), 1092-1104. DOI: /10.1039/B111434B
[291] K. Yamana, H. Zako, K. Asazuma, R. Iwase, H. Nakano, A. Murakami, "Fluorescence detection of specific RNA sequences using 2′-pyrene-modified oligoribonucleotides", *Angew. Chem. Int. Ed.* **2001**, *113* (6), 1138-1140. DOI: 10.1002/1521-3773(20010316)40:6<1104::AID-ANIE11040>3.0.CO;2-2
[292] H. Krishna, M. H. Caruthers, "Alkynyl phosphonate DNA: a versatile “click” able backbone for DNA-based biological applications", *J. Am. Chem. Soc.* **2012**, *134* (28), 11618-11631. DOI: 10.1021/ja3026714
[293] A. Hottin, A. Marx, "Structural insights into the processing of nucleobase-modified nucleotides by DNA polymerases", *Acc. Chem. Res.* **2016**, *49* (3), 418-427. DOI: 10.1021/acs.accounts.5b00544
[294] J. A. Brown, Z. Suo, "Unlocking the sugar “steric gate” of DNA polymerases", *Biochemistry* **2011**, *50* (7), 1135-1142. DOI: 10.1021/bi101915z
[295] E. Eremeeva, P. Herdewijn, "Reprint of: non canonical genetic material", *Curr. Opin. Biotechnol.* **2019**, *60*, 259-267. DOI: 10.1016/j.copbio.2018.12.001
[296] R. Padilla, R. Sousa, "A Y639F/H784A T7 RNA polymerase double mutant displays superior properties for synthesizing RNAs with non-canonical NTPs", *Nucleic Acids Res.* **2002**, *30* (24), e138-e138. DOI: 10.1093/nar/gnf138
[297] Y. J. Seo, D. A. Malyshev, T. Lavergne, P. Ordoukhanian, F. E. Romesberg, "Site-specific labeling of DNA and RNA using an efficiently replicated and transcribed class of unnatural base pairs", *J. Am. Chem. Soc.* **2011**, *133* (49), 19878-19888. DOI: 10.1021/ja207907d
[298] S. H. Weisbrod, A. Marx, "Novel strategies for the site-specific covalent labelling of nucleic acids", *Chem. Comm.* **2008** (44), 5675-5685. DOI: 10.1039/B809528K
[299] S. S. Ghosh, P. M. Kao, A. W. McCue, H. L. Chappelle, "Use of maleimide-thiol coupling chemistry for efficient syntheses of oligonucleotide-enzyme conjugate hybridization probes", *Bioconjugate Chem.* **1990**, *1* (1), 71-76
[300] S. Rajur, C. Roth, J. Morgan, M. Yarmush, "Covalent Protein− Oligonucleotide Conjugates for Efficient Delivery of Antisense Molecules", *Bioconjugate Chem.* **1997**, *8* (6), 935-940. DOI: 10.1021/bc970172u
[301] P. Schelté, C. Boeckler, B. Frisch, F. Schuber, "Differential reactivity of maleimide and bromoacetyl functions with thiols: application to the preparation of liposomal diepitope constructs", *Bioconjugate Chem.* **2000**, *11* (1), 118-123. DOI: 10.1021/bc990122k
[302] A. Okamoto, T. Taiji, K. Tainaka, I. Saito, "Oligonucleotides containing 7-vinyl-7-deazaguanine as a facile strategy for expanding the functional diversity of DNA", *Bioorg. Med. Chem. Lett.* **2002**, *12* (15), 1895-1896. DOI: 10.1016/S0960-894X(02)00334-7
[303] N. Z. Fantoni, A. H. El-Sagheer, T. Brown, "A hitchhiker’s guide to click-chemistry with nucleic acids", *Chem. Rev.* **2021**, *121* (12), 7122-7154. DOI: 10.1021/acs.chemrev.0c00928
[304] C. C.-Y. Wang, T. S. Seo, Z. Li, H. Ruparel, J. Ju, "Site-specific fluorescent labeling of DNA using Staudinger ligation", *Bioconjugate Chem.* **2003**, *14* (3), 697-701. DOI: 10.1021/bc0256392
[305] K. Ijiro, Y. Okahata, "A DNA–lipid complex soluble in organic solvents", *J. Chem. Soc.* **1992** (18), 1339-1341. DOI: 10.1039/C39920001339
[306] K. Liu, L. Zheng, Q. Liu, J. W. de Vries, J. Y. Gerasimov, A. Herrmann, "Nucleic acid chemistry in the organic phase: from functionalized oligonucleotides to DNA side chain polymers", *J. Am. Chem. Soc.* **2014**, *136* (40), 14255-14262. DOI: 10.1021/ja5080486
[307] W. Chen, J. Y. Gerasimov, P. Zhao, K. Liu, A. Herrmann, "High-density noncovalent functionalization of DNA by electrostatic interactions", *J. Am. Chem. Soc.* **2015**, *137*

(40), 12884-12889. DOI: 10.1021/jacs.5b05432
[308] G. Chakraborty, K. Balinin, G. Portale, M. Loznik, E. Polushkin, T. Weil, A. Herrmann, "Electrostatically PEGylated DNA enables salt-free hybridization in water"*, Chem. Sci.* **2019**, *10* (43), 10097-10105. DOI: 10.1039/C9SC02598G
[309] G. Chakraborty, K. Balinin, R. del Villar-Guerra, M. Emondts, G. Portale, M. Loznik, W. J. N. Klement, L. Zheng, T. Weil, J. B. Chaires, "Supramolecular DNA-based catalysis in organic solvents"*, Iscience* **2024**, *27* (5). doi. 10.1016/j.isci.2024.109689
[310] L. K. Griffeth, "Use of PET/CT scanning in cancer patients: technical and practical considerations"*, Bayl. Univ. Med. Cent. Proc.* **2005**, *18* (4), 321-330. DOI: 10.1080/08998280.2005.11928089
[311] M. Fani, J. P. André, H. R. Maecke, "68Ga-PET: a powerful generator-based alternative to cyclotron-based PET radiopharmaceuticals"*, Contrast Media Mol. Imaging* **2008**, *3* (2), 53-63. DOI: 10.1002/cmmi.232
[312] L. Farzin, M. Shamsipur, M. E. Moassesi, S. Sheibani, "Clinical aspects of radiolabeled aptamers in diagnostic nuclear medicine: A new class of targeted radiopharmaceuticals"*, Bioorg. Med. Chem.* **2019**, *27* (12), 2282-2291. DOI: 10.1016/j.bmc.2018.11.031
[313] P. Spang, C. Herrmann, F. Roesch, "Bifunctional gallium-68 chelators: Past, present, and future"*, Semin. Nucl. Med.* **2016**, *46* (5), 373-394. DOI: 10.1053/j.semnuclmed.2016.04.003
[314] H. Stetter, W. Frank, "Complex formation with tetraazacycloalkane-N, N′, N ″, N‴-tetraacetic acids as a function of ring size"*, Angew. Chem. Int. Ed.* **1976**, *15* (11), 686-686. DOI: 10.1002/anie.197606861
[315] V. Kubicek, J. Havlickova, J. Kotek, G. Tircso, P. Hermann, E. Toth, I. Lukes, "Gallium (III) complexes of DOTA and DOTA− monoamide: kinetic and thermodynamic studies"*, Inorg. Chem.* **2010**, *49* (23), 10960-10969. DOI: 10.1021/ic101378s
[316] M. R. Lewis, J. Y. Kao, A.-L. J. Anderson, J. E. Shively, A. Raubitschek, "An improved method for conjugating monoclonal antibodies with N-hydroxysulfosuccinimidyl DOTA"*, Bioconjugate Chem.* **2001**, *12* (2), 320-324. DOI: 10.1021/bc0000886
[317] A. Ghai, B. Singh, P. P. Hazari, M. K. Schultz, A. Parmar, P. Kumar, S. Sharma, D. Dhawan, A. K. Mishra, "Radiolabeling optimization and characterization of 68Ga labeled DOTA–polyamido-amine dendrimer conjugate–animal biodistribution and PET imaging results"*, Appl. Radiat. Isot.* **2015**, *105*, 40-46. DOI: 10.1016/j.apradiso.2015.07.021
[318] E. Blom, B. Långström, I. Velikyan, "68Ga-labeling of biotin analogues and their characterization"*, Bioconjugate Chem.* **2009**, *20* (6), 1146-1151. DOI: 10.1021/bc800538s
[319] W. Mier, J. Hoffend, S. Krämer, J. Schuhmacher, W. E. Hull, M. Eisenhut, U. Haberkorn, "Conjugation of DOTA using isolated phenolic active esters: the labeling and biodistribution of albumin as blood pool marker"*, Bioconjugate Chem.* **2005**, *16* (1), 237-240. DOI: 10.1021/bc034216c
[320] H. L. Evans, L. Carroll, E. O. Aboagye, A. C. Spivey, "Bioorthogonal chemistry for 68Ga radiolabelling of DOTA-containing compounds"*, J. Label. Compd. Radiopharm.* **2014**, *57* (4), 291-297. DOI: 10.1002/jlcr.3153
[321] N. J. Baumhover, M. E. Martin, S. G. Parameswarappa, K. C. Kloepping, M. S. O'Dorisio, F. C. Pigge, M. K. Schultz, "Improved synthesis and biological evaluation of chelator-modified α-MSH analogs prepared by copper-free click chemistry"*, Bioorg. Med. Chem. Lett.* **2011**, *21* (19), 5757-5761. DOI: 10.1016/j.bmcl.2011.08.017
[322] A. E. Martell, R. J. Motekaitis, E. T. Clarke, R. Delgado, Y. Sun, R. Ma, "Stability constants of metal complexes of macrocyclic ligands with pendant donor groups"*, Supramol. Chem.* **1996**, *6* (3-4), 353-363. DOI: 10.1080/10610279608032555
[323] J. R. Nedrow, A. G. White, J. Modi, K. Nguyen, A. J. Chang, C. J. Anderson, "Positron emission tomographic imaging of copper 64–and gallium 68–labeled chelator conjugates of the somatostatin agonist Tyr3-octreotate"*, Mol. Imaging* **2014**, *13* (7), 7290.2014. 00020. DOI: 10.2310/7290.2014.00020
[324] S. V. Gudkov, N. Y. Shilyagina, V. A. Vodeneev, A. V. Zvyagin, "Targeted radionuclide

therapy of human tumors", *Int. J. Mol. Sci.* **2015**, *17* (1), 33. DOI: 10.3390/ijms17010033
[325] A. Jang, A. T. Kendi, G. B. Johnson, T. R. Halfdanarson, O. Sartor, "Targeted alpha-particle therapy: a review of current trials", *Int. J. Mol. Sci.* **2023**, *24* (14), 11626. DOI: 10.3390/ijms241411626
[326] F. Lacoeuille, N. Arlicot, A. Faivre-Chauvet, "Targeted alpha and beta radiotherapy: An overview of radiopharmaceutical and clinical aspects", *Med. Nucl.* **2018**, *42* (1), 32-44. DOI: 10.1016/j.mednuc.2017.12.002
[327] J. L Parus, D. Pawlak, R. Mikolajczak, A. Duatti, "Chemistry and bifunctional chelating agents for binding 177Lu", *Curr. Radiopharm.* **2015**, *8* (2), 86-94. DOI: 10.2174/1874471008666150312160440
[328] E. W. Price, C. Orvig, "Matching chelators to radiometals for radiopharmaceuticals", *Chem. Soc. Rev.* **2014**, *43* (1), 260-290. DOI: 10.1039/C3CS60304K
[329] B. J. Hicke, A. W. Stephens, T. Gould, Y.-F. Chang, C. K. Lynott, J. Heil, S. Borkowski, C.-S. Hilger, G. Cook, S. Warren, "Tumor targeting by an aptamer", *J. Nucl. Med.* **2006**, *47* (4), 668-678
[330] Z. Noaparast, S. J. Hosseinimehr, M. Piramoon, S. M. Abedi, "Tumor targeting with a 99mTc-labeled AS1411 aptamer in prostate tumor cells", *J. Drug Target.* **2015**, *23* (6), 497-505. DOI: 10.3109/1061186X.2015.1009075
[331] Y. Qiu, Q. Yang, Y. Zhang, L. Song, X. Sun, Z. Chen, W. Qiu, W. Huang, H. Jiao, Q. Jiang, "Technetium-99m radiolabeled nucleolin-targeted aptamer for glioma tumor imaging in murine models", *Colloids Surf.* **2023**, *657*, 130587. DOI: 10.1016/j.colsurfa.2022.130587
[332] J. Li, H. Zheng, P. J. Bates, T. Malik, X.-F. Li, J. O. Trent, C. K. Ng, "Aptamer imaging with cu-64 labeled as1411: Preliminary assessment in lung cancer", *Nucl. Med. Biol.* **2014**, *41* (2), 179-185. DOI: 10.1016/j.nucmedbio.2013.10.008
[333] P. Li, C. Wang, W. Wang, X. Duan, J. Li, "Preliminary evaluation of a 64Cu-labeled DNA aptamer for PET imaging of glioblastoma", *J. Radioanal. Nucl. Chem.* **2023**, *332* (6), 2279-2284. DOI: 10.1007/s10967-023-08835-2
[334] P. Desai, R. Rimal, S. E. Sahnoun, F. M. Mottaghy, M. Möller, A. Morgenroth, S. Singh, "Radiolabeled nanocarriers as theranostics—Advancement from peptides to nanocarriers", *Small* **2022**, *18* (25), 2200673. DOI: 10.1002/smll.202200673
[335] Y. R. Baker, L. Yuan, J. Chen, R. Belle, R. Carlisle, A. H. El-Sagheer, T. Brown, "Expanding the chemical functionality of DNA nanomaterials generated by rolling circle amplification", *Nucleic Acids Res.* **2021**, *49* (16), 9042-9052. DOI: 10.1093/nar/gkab720
[336] K.-R. Kim, P. Röthlisberger, S. J. Kang, K. Nam, S. Lee, M. Hollenstein, D.-R. Ahn, "Shaping rolling circle amplification products into DNA nanoparticles by incorporation of modified nucleotides and their application to in vitro and in vivo delivery of a photosensitizer", *Molecules* **2018**, *23* (7), 1833. DOI: 10.3390/molecules23071833
[337] A. Tampieri, M. Szabó, F. Medina, H. Gulyás, "A brief introduction to the basics of NMR spectroscopy and selected examples of its applications to materials characterization", *Phys. Sci. Rev.* **2021**, *6* (1), 20190086. DOI: 10.1515/psr-2019-0086
[338] J. C. McGowan, "Basic principles of magnetic resonance imaging", *Neuroimaging Clin. N. Am.* **2008**, *18* (4), 623-636. DOI: 10.1016/j.nic.2008.06.004
[339] A. L. Scherzinger, W. R. Hendee, "Basic principles of magnetic resonance imaging--an update", *West. J. Med.* **1985**, *143* (6), 782-792
[340] T. A. Bley, O. Wieben, C. J. François, J. H. Brittain, S. B. Reeder, "Fat and water magnetic resonance imaging", *J. Magn. Reson. Imaging* **2010**, *31* (1), 4-18. DOI: 10.1002/jmri.21895
[341] G. J. Stanisz, E. E. Odrobina, J. Pun, M. Escaravage, S. J. Graham, M. J. Bronskill, R. M. Henkelman, "T1, T2 relaxation and magnetization transfer in tissue at 3T", *Magn. Reson. Med.* **2005**, *54* (3), 507-512. DOI: 10.1002/mrm.20605
[342] M. E. Ladd, "High-field-strength magnetic resonance: potential and limits", *Top. Magn. Reson. Imaging* **2007**, *18* (2), 139-152. DOI: 10.1097/RMR.0b013e3180f612b3
[343] L. L. Wald, P. C. McDaniel, T. Witzel, J. P. Stockmann, C. Z. Cooley, "Low-cost and

portable MRI", *J. Magn. Reson. Imaging* **2020**, *52* (3), 686-696. DOI: 10.1002/jmri.26942
[344] J. Wahsner, E. M. Gale, A. Rodríguez-Rodríguez, P. Caravan, "Chemistry of MRI contrast agents: current challenges and new frontiers", *Chem. Rev.* **2018**, *119* (2), 957-1057. DOI: 10.1021/acs.chemrev.8b00363
[345] L. Yang, I. Krefting, A. Gorovets, L. Marzella, J. Kaiser, R. Boucher, D. Rieves, "Nephrogenic systemic fibrosis and class labeling of gadolinium-based contrast agents by the Food and Drug Administration", *Radiology* **2012**, *265* (1), 248-253. DOI: 10.1148/radiol.12112783
[346] T. Kanda, T. Fukusato, M. Matsuda, K. Toyoda, H. Oba, J. i. Kotoku, T. Haruyama, K. Kitajima, S. Furui, "Gadolinium-based contrast agent accumulates in the brain even in subjects without severe renal dysfunction: evaluation of autopsy brain specimens with inductively coupled plasma mass spectroscopy", *Radiology* **2015**, *276* (1), 228-232. DOI: 10.1148/radiol.2015142690
[347] R. Buyanov, A. Zel'Dovich, Y. K. Pilipenko, "A liquefier for producing para-hydrogen and catalysts for the ortho-para conversion of hydrogen", *Cryogenics* **1962**, *2* (3), 143-144. DOI: 10.1016/0011-2275(62)90031-0
[348] T. Das, S.-C. Kweon, I. W. Nah, S. W. Karng, J.-G. Choi, I.-H. Oh, "Spin conversion of hydrogen using supported iron catalysts at cryogenic temperature", *Cryogenics* **2015**, *69*, 36-43. DOI: 10.1016/j.cryogenics.2015.03.003
[349] J. H. Kim, S. W. Karng, I.-H. Oh, I. W. Nah, "Ortho-para hydrogen conversion characteristics of amorphous and mesoporous Cr2O3 powders at a temperature of 77 K", *Int. J. Hydrog. Energy* **2015**, *40* (41), 14147-14153. DOI: 10.1016/j.ijhydene.2015.08.105
[350] M. S. Haberbusch, C. T. Nguyen, R. J. Stochl, T. Y. Hui, "Development of No-Vent™ liquid hydrogen storage system for space applications", *Cryogenics* **2010**, *50* (9), 541-548. DOI: 10.1016/j.cryogenics.2010.02.025
[351] C. R. Bowers, D. P. Weitekamp, "Transformation of symmetrization order to nuclear-spin magnetization by chemical reaction and nuclear magnetic resonance", *Phys. Rev. Lett.* **1986**, *57* (21), 2645. DOI: 10.1103/PhysRevLett.57.2645
[352] C. R. Bowers, D. P. Weitekamp, "Parahydrogen and synthesis allow dramatically enhanced nuclear alignment", *J. Am. Chem. Soc.* **1987**, *109* (18), 5541-5542. DOI: 10.1021/ja00252a049
[353] J. Natterer, J. Bargon, "Parahydrogen induced polarization", *Prog. Nucl. Magn. Reson. Spectrosc.* **1997**, *31* (4), 293-315. DOI: 10.1016/S0079-6565(97)00007-1
[354] R. U. Kirss, R. Eisenberg, "Para-hydrogen-induced polarization in rhodium complex-catalyzed hydrogenation reactions", *J. Organomet. Chem.* **1989**, *359* (1), C22-C26. DOI: 10.1016/0022-328X(89)85265-9
[355] F. Reineri, S. Aime, R. Gobetto, C. Nervi, "Role of the reaction intermediates in determining PHIP (parahydrogen induced polarization) effect in the hydrogenation of acetylene dicarboxylic acid with the complex [Rh (dppb)]+(dppb: 1, 4-bis (diphenylphosphino) butane)", *J. Chem. Phys.* **2014**, *140* (9). DOI: 10.1063/1.4867269
[356] J. Barkemeyer, M. Haake, J. Bargon, "Hetero-NMR enhancement via parahydrogen labeling", *J. Am. Chem. Soc.* **1995**, *117* (10), 2927-2928. DOI: 10.1021/ja00115a028
[357] S. Aime, R. Gobetto, F. Reineri, D. Canet, "Polarization transfer from para-hydrogen to heteronuclei: Effect of H/D substitution. The case of AA′ X and A2A2′ X spin systems", *J. Magn. Reson.* **2006**, *178* (2), 184-192. DOI: 10.1016/j.jmr.2005.09.008
[358] M. J. Cowley, R. W. Adams, K. D. Atkinson, M. C. Cockett, S. B. Duckett, G. G. Green, J. A. Lohman, R. Kerssebaum, D. Kilgour, R. E. Mewis, "Iridium N-heterocyclic carbene complexes as efficient catalysts for magnetization transfer from para-hydrogen", *J. Am. Chem. Soc.* **2011**, *133* (16), 6134-6137. DOI: 10.1021/ja200299u
[359] J.-B. Hövener, N. Schwaderlapp, T. Lickert, S. B. Duckett, R. E. Mewis, L. A. Highton, S. M. Kenny, G. G. Green, D. Leibfritz, J. G. Korvink, "A hyperpolarized equilibrium for magnetic resonance", *Nat. Comm.* **2013**, *4* (1), 2946. DOI: 10.1038/ncomms3946
[360] H. Zeng, J. Xu, J. Gillen, M. T. McMahon, D. Artemov, J.-M. Tyburn, J. A. Lohman, R. E. Mewis, K. D. Atkinson, G. G. Green, "Optimization of SABRE for polarization of the

tuberculosis drugs pyrazinamide and isoniazid", *J. Magn. Res.* **2013**, *237*, 73-78. DOI: 10.1016/j.jmr.2013.09.012

[361] D. A. Barskiy, R. V. Shchepin, A. M. Coffey, T. Theis, W. S. Warren, B. M. Goodson, E. Y. Chekmenev, "Over 20% 15N hyperpolarization in under one minute for metronidazole, an antibiotic and hypoxia probe", *J. Am. Chem. Soc.* **2016**, *138* (26), 8080-8083. DOI: 10.1021/jacs.6b04784

[362] M. T. Huynh, Z. Kovacs, "Homogeneous Catalysts for Hydrogenative PHIP Used in Biomedical Applications", *Anal. Sens.* **2025**, *5* (1), e202400044. DOI: 10.1002/anse.202400044

[363] J.-B. Hövener, E. Y. Chekmenev, K. C. Harris, W. H. Perman, T. T. Tran, B. D. Ross, P. Bhattacharya, "Quality assurance of PASADENA hyperpolarization for 13 C biomolecules", *Magn. Reson. Mater. Phys. Biol. Med.* **2009**, *22*, 123-134. DOI: 10.1007/s10334-008-0154-y

[364] J. F. Colell, M. Emondts, A. W. Logan, K. Shen, J. Bae, R. V. Shchepin, G. X. Ortiz Jr, P. Spannring, Q. Wang, S. J. Malcolmson, "Direct hyperpolarization of nitrogen-15 in aqueous media with parahydrogen in reversible exchange", *J. Am. Chem. Soc.* **2017**, *139* (23), 7761-7767. DOI: 10.1021/jacs.7b00569

[365] F. Shi, P. He, Q. A. Best, K. Groome, M. L. Truong, A. M. Coffey, G. Zimay, R. V. Shchepin, K. W. Waddell, E. Y. Chekmenev, "Aqueous NMR signal enhancement by reversible exchange in a single step using water-soluble catalysts", *J. Phys. Chem. C* **2016**, *120* (22), 12149-12156. DOI: 10.1021/acs.jpcc.6b04484

[366] B. E. Kidd, J. L. Gesiorski, M. E. Gemeinhardt, R. V. Shchepin, K. V. Kovtunov, I. V. Koptyug, E. Y. Chekmenev, B. M. Goodson, "Facile removal of homogeneous SABRE catalysts for purifying hyperpolarized metronidazole, a potential hypoxia sensor", *J. Phys. Chem. C* **2018**, *122* (29), 16848-16852. DOI: 10.1021/acs.jpcc.8b05758

[367] K. V. Kovtunov, I. E. Beck, V. I. Bukhtiyarov, I. V. Koptyug, "Observation of parahydrogen-induced polarization in heterogeneous hydrogenation on supported metal catalysts", *Angew. Chem. Int. Ed.* **2008**, *47* (8), 1492-1495. DOI: 10.1002/anie.200704881

[368] L. B. Bales, K. V. Kovtunov, D. A. Barskiy, R. V. Shchepin, A. M. Coffey, L. M. Kovtunova, A. V. Bukhtiyarov, M. A. Feldman, V. I. Bukhtiyarov, E. Y. Chekmenev, "Aqueous, heterogeneous para-hydrogen-induced 15N polarization", *J. Phys. Chem. C* **2017**, *121* (28), 15304-15309. DOI: 10.1021/acs.jpcc.7b05912

[369] K. V. Kovtunov, D. A. Barskiy, O. G. Salnikov, R. V. Shchepin, A. M. Coffey, L. M. Kovtunova, V. I. Bukhtiyarov, I. V. Koptyug, E. Y. Chekmenev, "Toward production of pure 13 C hyperpolarized metabolites using heterogeneous parahydrogen-induced polarization of ethyl [1-13 C] acetate", *RSC Adv.* **2016**, *6* (74), 69728-69732. DOI: 10.1039/C6RA15808K

[370] K. V. Kovtunov, L. M. Kovtunova, M. E. Gemeinhardt, A. V. Bukhtiyarov, J. Gesiorski, V. I. Bukhtiyarov, E. Y. Chekmenev, I. V. Koptyug, B. M. Goodson, "Heterogeneous microtesla SABRE enhancement of 15N NMR signals", *Angew. Chem. Int. Ed.* **2017**, *129* (35), 10569-10573. DOI: 10.1002/anie.201705014

[371] W. Iali, A. M. Olaru, G. G. Green, S. B. Duckett, "Achieving high levels of NMR-hyperpolarization in aqueous media with minimal catalyst contamination using SABRE", *Chem. Euro. J.* **2017**, *23* (44), 10491-10495. DOI: 10.1002/chem.201702716

[372] R. V. Shchepin, A. M. Coffey, K. W. Waddell, E. Y. Chekmenev, "PASADENA hyperpolarized 13C phospholactate", *J. Am. Chem. Soc.* **2012**, *134* (9), 3957-3960. DOI: 10.1021/ja210639c

[373] P. Bhattacharya, E. Y. Chekmenev, W. H. Perman, K. C. Harris, A. P. Lin, V. A. Norton, C. T. Tan, B. D. Ross, D. P. Weitekamp, "Towards hyperpolarized 13C-succinate imaging of brain cancer", *J. Magn. Res.* **2007**, *186* (1), 150-155. DOI: 10.1016/j.jmr.2007.01.017

[374] F. Reineri, A. Viale, S. Ellena, D. Alberti, T. Boi, G. B. Giovenzana, R. Gobetto, S. S. Premkumar, S. Aime, "15N Magnetic resonance hyperpolarization via the reaction of parahydrogen with 15N-propargylcholine", *J. Am. Chem. Soc.* **2012**, *134* (27), 11146-11152. DOI: 10.1021/ja209884h

[375] T. Theis, G. X. Ortiz Jr, A. W. Logan, K. E. Claytor, Y. Feng, W. P. Huhn, V. Blum, S. J. Malcolmson, E. Y. Chekmenev, Q. Wang, "Direct and cost-efficient hyperpolarization of long-lived nuclear spin states on universal 15N2-diazirine molecular tags"*, Sci. Adv.* **2016**, *2* (3), e1501438. DOI: 10.1126/sciadv.1501438
[376] S. Ellena, A. Viale, R. Gobetto, S. Aime, "Para-hydrogen induced polarization of Si-29 NMR resonances as a potentially useful tool for analytical applications"*, Mag. Res. Chem.* **2012**, *50* (8), 529-533. DOI: 10.1002/mrc.3832
[377] M. J. Burns, P. J. Rayner, G. G. Green, L. A. Highton, R. E. Mewis, S. B. Duckett, "Improving the hyperpolarization of 31P nuclei by synthetic design"*, J. Phys. Chem. B* **2015**, *119* (15), 5020-5027. DOI: 10.1021/acs.jpcb.5b00686
[378] S. J. Nelson, J. Kurhanewicz, D. B. Vigneron, P. E. Larson, A. L. Harzstark, M. Ferrone, M. Van Criekinge, J. W. Chang, R. Bok, I. Park, "Metabolic imaging of patients with prostate cancer using hyperpolarized [1-13C] pyruvate"*, Sci. Transl. Med.* **2013**, *5* (198), 198ra108-198ra108. DOI: 10.1126/scitranslmed.3006070
[379] N. M. Zacharias, C. R. McCullough, S. Wagner, N. Sailasuta, H. R. Chan, Y. Lee, J. Hu, W. H. Perman, C. Henneberg, B. D. Ross, "Towards real-time metabolic profiling of cancer with hyperpolarized succinate"*, J. Mol. Imaging Dyn.* **2016**, *6* (1), 123. DOI: 10.4172/2155-9937.1000123
[380] R. V. Shchepin, W. Pham, E. Y. Chekmenev, "Dephosphorylation and biodistribution of 1-13C-phospholactate in vivo"*, J. Label. Compd. Radiopharm.* **2014**, *57* (8), 517-524. DOI: 10.1002/jlcr.3207
[381] M. Körner, G. Sauer, A. Heil, D. Nasu, M. Empting, D. Tietze, S. Voigt, H. Weidler, T. Gutmann, O. Avrutina, "PHIP-label: parahydrogen-induced polarization in propargylglycine-containing synthetic oligopeptides"*, Chem. Comm.* **2013**, *49* (71), 7839-7841. DOI: 10.1039/C3CC43978J
[382] A. S. Kiryutin, G. Sauer, D. Tietze, M. Brodrecht, S. Knecht, A. V. Yurkovskaya, K. L. Ivanov, O. Avrutina, H. Kolmar, G. Buntkowsky, "Ultrafast Single-Scan 2D NMR Spectroscopic Detection of a PHIP-Hyperpolarized Protease Inhibitor"*, Chem. Euro. J.* **2019**, *25* (16), 4025-4030. DOI: 10.1002/chem.201900079
[383] T. Ratajczyk, T. Gutmann, P. Bernatowicz, G. Buntkowsky, J. Frydel, B. Fedorczyk, "NMR signal enhancement by effective SABRE labeling of oligopeptides"*, Chem. Euro. J.* **2015**, *21* (36), 12616-12619. DOI: 10.1002/chem.201501552
[384] T. Ratajczyk, G. Buntkowsky, T. Gutmann, B. Fedorczyk, A. Mames, M. Pietrzak, Z. Puzio, P. G. Szkudlarek, "Magnetic resonance signal amplification by reversible exchange of selective PyFALGEA oligopeptide ligands towards epidermal growth factor receptors", *ChemBioChem* **2021**, *22* (5), 855-860. DOI: 10.1002/cbic.202000711
[385] W. Zhou, Q. Chen, P.-J. J. Huang, J. Ding, J. Liu, "DNAzyme hybridization, cleavage, degradation, and sensing in undiluted human blood serum"*, Anal. Chem.* **2015**, *87* (7), 4001-4007. DOI: 10.1021/acs.analchem.5b00220
[386] J. Chen, Y. R. Baker, A. Brown, A. H. El-Sagheer, T. Brown, "Enzyme-free synthesis of cyclic single-stranded DNA constructs containing a single triazole, amide or phosphoramidate backbone linkage and their use as templates for rolling circle amplification and nanoflower formation"*, Chem. Sci.* **2018**, *9* (42), 8110-8120. DOI: 10.1039/C8SC02952K
[387] R. An, Y. Jia, B. Wan, Y. Zhang, P. Dong, J. Li, X. Liang, "Non-enzymatic depurination of nucleic acids: factors and mechanisms"*, PloS One* **2014**, *9* (12), e115950. DOI: 10.1371/journal.pone.0115950
[388] A. Larenkov, I. Mitrofanov, E. Pavlenko, M. Rakhimov, "Radiolysis-associated decrease in radiochemical purity of 177Lu-radiopharmaceuticals and comparison of the effectiveness of selected quenchers against this process"*, Molecules* **2023**, *28* (4), 1884. DOI: 10.3390/molecules28041884
[389] P. Kumar, A. Nagarajan, P. D. Uchil, "Analysis of cell viability by the lactate dehydrogenase assay"*, Cold Spring Harb. Protoc.* **2018**, *2018* (6), pdb. prot095497. DOI: 10.1101/pdb.prot095497
[390] J. Petiti, L. Revel, C. Divieto, "Standard operating procedure to optimize resazurin-based viability assays"*, Biosensors* **2024**, *14* (4), 156. DOI: 10.3390/bios14040156

[391] J. Willibald, J. Harder, K. Sparrer, K.-K. Conzelmann, T. Carell, "Click-modified anandamide siRNA enables delivery and gene silencing in neuronal and immune cells"*, J. Am. Chem. Soc.* **2012**, *134* (30), 12330-12333. DOI: 10.1021/ja303251f
[392] N. Hüsken, G. Gasser, S. D. Köster, N. Metzler-Nolte, ""Four-potential" ferrocene labeling of PNA oligomers via click chemistry"*, Bioconjugate Chem.* **2009**, *20* (8), 1578-1586. DOI: 10.1021/bc9001272
[393] A. Das, B. K. Banik, "Advances in heterocycles as DNA intercalating cancer drugs"*, Phys. Sci. Rev.* **2023**, *8* (9), 2473-2521. DOI: 10.1515/psr-2021-0065
[394] K. Du, Q. Xia, H. Heng, F. Feng, "Temozolomide–doxorubicin conjugate as a double intercalating agent and delivery by apoferritin for glioblastoma chemotherapy"*, ACS Appl. Mater. Interfaces* **2020**, *12* (31), 34599-34609. DOI: 10.1021/acsami.0c08531
[395] A. Koudrina, E. M. McConnell, J. A. Zurakowski, G. O. Cron, S. Chen, E. C. Tsai, M. C. DeRosa, "Exploring the unique contrast properties of aptamer–gadolinium conjugates in magnetic resonance imaging for targeted imaging of thrombi"*, ACS Appl. Mater. Interfaces* **2021**, *13* (8), 9412-9424. DOI: 10.1021/acsami.0c16666
[396] G. Solomou, A. Finch, A. Asghar, C. Bardella, "Mutant IDH in gliomas: role in cancer and treatment options"*, Cancers* **2023**, *15* (11), 2883. DOI: 10.3390/cancers15112883
[397] S. Wakai, N. Hirokawa, "Development of the blood-brain barrier to horseradish peroxidase in the chick embryo"*, Cell Tissue Res.* **1978**, *195*, 195-203. DOI: 10.1007/BF00236719
[398] M. Chauhan, S. Shekhar, B. Yadav, V. Garg, R. Dutt, A. K. Mehata, P. Goswami, B. Koch, M. S. Muthu, R. P. Singh, "AS1411 aptamer/RGD dual functionalized theranostic chitosan-PLGA nanoparticles for brain cancer treatment and imaging"*, Biomater. Adv.* **2024**, *160*, 213833. DOI: 10.1016/j.bioadv.2024.213833
[399] H. Ma, Z. Gao, P. Yu, S. Shen, Y. Liu, B. Xu, "A dual functional fluorescent probe for glioma imaging mediated by blood-brain barrier penetration and glioma cell targeting"*, Biochem. Biophys. Res. Commun.* **2014**, *449* (1), 44-48. DOI: 10.1016/j.bbrc.2014.04.148
[400] M. Chauhan, R. P. Singh, B. Yadav, S. Shekhar, L. Kumar, A. K. Mehata, V. Jhawat, R. Dutt, V. Garg, V. Kailashiya, "Dual-targeted transferrin and AS1411 aptamer conjugated micelles for improved therapeutic efficacy and imaging of brain cancer"*, Colloids Surf. B: Biointerfaces* **2023**, *231*, 113544. DOI: 10.1016/j.colsurfb.2023.113544
[401] I. Monaco, S. Camorani, D. Colecchia, E. Locatelli, P. Calandro, A. Oudin, S. Niclou, C. Arra, M. Chiariello, L. Cerchia, "Aptamer functionalization of nanosystems for glioblastoma targeting through the blood–brain barrier"*, J. Med. Chem.* **2017**, *60* (10), 4510-4516. DOI: 10.1021/acs.jmedchem.7b00527
[402] X. Li, Y. Yang, H. Zhao, T. Zhu, Z. Yang, H. Xu, Y. Fu, F. Lin, X. Pan, L. Li, "Enhanced in vivo blood–brain barrier penetration by circular tau–transferrin receptor bifunctional aptamer for tauopathy therapy"*, J. Am. Chem. Soc.* **2020**, *142* (8), 3862-3872. DOI: 10.1021/jacs.9b11490
[403] Y. Liang, X. Jiang, R. Yuan, Y. Zhou, C. Ji, L. Yang, H. Chen, Q. Wang, "Metabolism-based click-mediated platform for specific imaging and quantification of cell surface sialic acids"*, Anal. Chem.* **2017**, *89* (1), 538-543. DOI: 10.1021/acs.analchem.6b04141
[404] T. Glachet, H. Marzag, N. Saraiva Rosa, J. F. Colell, G. Zhang, W. S. Warren, X. Franck, T. Theis, V. Reboul, "Iodonitrene in Action: Direct transformation of amino acids into terminal diazirines and 15N2-diazirines and their application as hyperpolarized markers"*, J. Am. Chem. Soc.* **2019**, *141* (34), 13689-13696. DOI: 10.1021/jacs.9b07035
[405] A. B. Schmidt, E. Y. Chekmenev, H. de Maissin, P. R. Groß, S. Petersen, L. Nagel, F. Schilling, I. Schwartz, T. Reinheckel, J. B. Hövener, "Signal amplification by reversible exchange and its translation to hyperpolarized magnetic resonance imaging in biomedicine"*, Anal. Sens.* **2024**, *4* (6), e202400039. DOI: 10.1002/anse.202400039